UNIVERSITY OF COPENHAGEN
NIELS BOHR INSTITUTE

PhD Thesis

Source-driven black hole relaxation: imprint of the two-body dynamics

Marina De Amicis

Supervisors:

Prof. Gregorio Carullo

Prof. Vitor Cardoso

Submitted 05/06/2025

This thesis has been submitted to the PhD School of The Faculty of Science, University of Copenhagen.

Acknowledgments

First and foremost, I am deeply grateful to my supervisor Professor Gregorio Carullo, for having "adopted" me as his padawan. A year into my PhD, I decided to switch research topic and I felt initially lost, unsure of what research direction to follow. Gregorio believed in me from the start: he presented me with stimulating problems and a contagious enthusiasm that after countless discussions (and a great deal of patience on his part), ultimately shaped the material in this thesis. Thanks to his support, I went from feeling lost to achieving the proudest and most fulfilling work of my life. I cannot express how thankful I am for his mentorship. Beyond physics itself, Gregorio guided me in every little aspect of research life: from preparing talks to engaging productively with colleagues, he invested countless hours in helping me develop as a scientist. In an academic environment that can be challenging to navigate, Gregorio has always been a role model for how to be an honest researcher and, more in general, a good human being. One of the best aspects of this job is the possibility to work with friends, I really hope we will keep on collaborating for many years to come – we sure don't lack ideas!

I am also profoundly grateful to my supervisor Professor Vitor Cardoso. When I switched my research topic, Vitor was always there with unyielding support and remarkable patience, giving me the time to choose a topic that truly engaged me. Vitor encouraged me to pursue my own ideas, while always being available for discussions to provide constructive criticism and sharpen my intuition, making sure I was on the right path to have a successful PhD. It is rare to have a supervisor that allows for this freedom, but incredibly valuable: it is thanks to Vitor that I am now an independent researcher.

The PhD marked the first time I left my home, my life-long friends and family, to move abroad. I can genuinely say that, albeit excited, I was initially terrified. This fear quickly dissipated as I met the amazing people that I am about to mention.

Damiano Fiorillo and Ersilia Guarini, you made my days in this (often dark and cloudy) city dazzling with joy. From our "everything can happen" Friday nights, to improvised karaoke sessions and tea (and gossip) time you were the first friends I made in this new place, and soon became my closest. I can't wait to visit you again, be it in Copenhagen, Berlin or wherever you will live, ready to scream the latest Taylor Swift album at the top of my lungs with you.

Juno Chun Lung Chan, you are one of my very best friends in the whole world, making me realize how surprisingly similar the chaotic culture of Hong Kong and Rome can be. My loyal partner in mischief, we both know that the world will be a safer place with us not living in the same city, but rest assured that I will keep on bothering you forever, no matter where we end up.

Tania Pitik, Antonio Capanema, Kevin Urquía, Daniele Pica and Enrico Peretti, I will always cherish all the memories we made together: be it at parties, brunches, playing music together or just chilling at Reffen, you made my time in Copenhagen unforgettable.

When Vitor gave me the amazing opportunity to join the Strong group, I knew I was about to meet some of the most brilliant people in our field, but I could not imagine how enriching this journey would be. Interacting every day with people from all over the world literally changed how my brain works for the better. Every day during my PhD, I learned something new, recognized each cultural bias I had, and then had those biases challenged. It is difficult now to think about living in any other setting. But the Strong group is even more special, and soon became for me a family away from home. I want to thank my fellow PhDs for always supporting each other. Thomas Spieksma for being my "daily dose of caffeine", Jaime Redondo Yuste for always being open to debate everything with me, Conor Dyson and Luka Vujeva for being the most sweet and wholesome people in the group, Juno Chun Lung Chan and Evelyn-Andreea Ester for being as work alcoholic as me. I am grateful to all the postdocs and professors in the group for teaching me on a daily basis how to be a good physicist. In particular, I want to thank: Marica Minucci, Rodrigo Panosso Macedo, David Pereñiguez, Maarten van de Meent, Lorena Magana Zertuche, Takuya Katagiri for letting me bother them constantly with way too many physics questions. The most special thanks go to Julie de Molade, the Strong group coordinator, without whom I would probably not have survived long in Denmark. Julie helped me (and the whole group) adjust to life in Copenhagen, and soon became a friend I knew I could always count on here.

I am deeply grateful to Alessandro Nagar, Simone Albanesi, and Thibault Damour. Your guidance and our (fierce) discussions helped me conceive many of the ideas explored in this thesis.

I am thankful to many other people I have met and worked with, in particular Diego Blas, Laura Sberna, Enrico Cannizzaro, Marta Cocco, and Elisa Grilli.

Se sono arrivata qui, è grazie alla mia incredibile famiglia. A mia madre Maria e mia nonna Pinuccia, per essere le persone più forti e determinate che abbia mai incontrato: avervi come modello mi da' la sicurezza necessaria per affrontare qualsiasi cosa. A mio nonno Luigi e mio zio Giovanni per avermi fatto appassionare alla scienza, in particolare alla fisica, fin da quando ero bambina: grazie per avermi trasmesso quella che è diventata la mia più grande passione. A Silvia, Chiara, Matteo, Moira, Francesco e Peppe, la mia famiglia acquisita e i migliori amici in cui si possa sperare. Ogni volta che torno a Roma mi fate sentire come se non me ne fossi mai andata e ripartire è sempre più difficile. Mi avete supportato nei momenti più difficili di questi anni e avete gioito con me di ogni vittoria, questo traguardo non sarebbe stato possibile senza di voi.

Abstract

This thesis summarises the candidate contributions in advancing the understanding of how the remnant of a black hole binary merger relaxes towards equilibrium. In the past, significant effort has been dedicated to studying the response of a black hole perturbed by initial-data. A posteriori analyses of perturbative (extreme mass-ratio) and fully non-linear (comparable masses) binary mergers numerical waveforms hint towards a strong imprint of the inspiral two-body dynamics on the waveform emitted after a common horizon is formed. However, to date, attention to address the analytical modeling of this problem has been sparse. This is the focus of the thesis.

After introducing basic techniques in perturbation theory and the analytical modeling of the two-body problem, we first reproduce past phenomenological results on the imprint of the inspiral on black hole relaxation. We present a battery of inference tests performed on non-linear waveforms using the Bayesian inference algorithm `bayRing`, and analyze the post-merger signal of simulations of non-spinning progenitors in quasi-circular binaries. We validate past results obtained by fitting the numerical data through powerful tools of Bayesian data analysis. We show that unmodeled features in the post-peak waveform preclude confidently extracting more than one overtone harmonic in the black hole relaxation spectrum. This results hints at the presence of non-modal physical features of the waveform comparable or larger in magnitude than high overtones. In agreement with past literature, we find a linear dependence of the fundamental quadrupolar mode amplitude on the progenitors symmmetric mass-ratio. We then extend for the first time this approach to electrically-charged progenitors, by introducing an effective charge able to parametrize the fundamental mode amplitude, remnant mass and spin at the merger.

Having consolidated the physical picture arising in the post-merger waveform, we turn our attention to a first principles description of its features in the perturbative, extreme-mass-ratio limit. We derive an analytical model able to describe the late-time tails emitted by a test-particle infalling in a Schwarzschild black hole through generic orbits. The model is an integral over the system's entire past history, obtained by convolution of the test-particle source with Price's law Green's function, thereby highlighting tails' hereditary nature. We validate the model against a set of perturbative numerical evolutions, considering quasi-circular and eccentric mergers, dynamical captures, radial infalls and a scattering configuration. Our model yields an accurate prediction of the late-times waveform for bounded orbit with intermediate to high eccentricities. The model explains the several orders-of-magnitude increase in tail amplitude with orbital eccentricity, and shows that the tail emission is maximized when the motion is at large distances. Fast angular motion induces destructive interference among subsequent tail signals, hence the total tail

emission is enhanced along the portion of the trajectory with small angular velocity. This understanding predicts that for an eccentric merger, the late-time tail observed right after the ringdown is generated at the last apastron before the merger. We validate this hypothesis with a series of numerical experiments, showcasing the ability of tails to probe the spacetime large scale structure. We show that the late-time signal is a superposition of an infinite number of inverse power laws in the retarded time, with Price's law as slowest decaying contribution. As a consequence, in a binary merger, a large number of faster decaying corrections is excited giving rise to a long lived transient with lenght comparable to the inspiral duration. Price's law, i.e. vacuum perturbation theory prediction, can only be obtained in the limit of very late times.

We leverage the obtained analytical understanding of late-time tails excited by a two-body problem, to investigate this effect in fully non-linear numerical evolutions. We focus on head-on collisions of comparable masses, non-spinning progenitors. For the first time, we uncover the presence of late-time tails in non-linear simulations, by carefully handling extrapolation methods and outer-boundary placement. Comparison between non-linear results and perturbative prediction yields an excellent agreement, from the peak of the waveforms to late times. The relative amplitude of the tail with respect to the peak is consistent among the perturbative and non-linear cases. However, the non-linear tail decays slower than the perturbative prediction, yielding the first evidence of non-modal non-linear effects in the late-times portion of the signal.

Finally, we study the dynamical excitation of black hole quasi-normal modes. This is a problem of key importance both to extend black hole spectroscopy to the near-peak signal, containing the largest amount of signal power, and to avoid modeling systematics that might induce overfitting in phenomenological templates. We show how quasi-normal-mode signals propagate within the light cone and derive a causality condition selecting the retarded part of their Green's function. This allows to build the first analytical model for the dynamical excitation of the ringdown, that can be smoothly connected to the inspiral portion of the waveform. We derive this model for generic planar orbits of a test-particle on a Schwarzschild background. The quasi-normal modes amplitudes behave as activating functions, growing during the inspiral-plunge and saturating to constant values near the light-ring crossing. The causality prescription regularizes the quasi-normal modes Green's function, otherwise divergent once the test-particle reaches the horizon. The apparent location of the test-particle as observed at null infinity reaches the horizon in an infinite amount of time. As a consequence, the observer receives signals emitted by the test-particle source even at late-times after the light-ring crossing, and the signal is quenched with the horizon redshift. In particular, we show that this new feature of the post-peak waveform is described by a superposition of non-oscillating, exponentially decaying terms with decay-rate given by multiples of the horizon redshift.

Our model for the ringdown excitation does not completely reproduce the near-peak evolution observed in numerical waveforms. Other components of the Schwarzschild background spectral response must be taken into account to predict the waveform at such early times. However, we are able for the first time to predict the inspiral imprint on the stationary ringdown response, as we explicitly show by computing the amplitude and phase dependence on the eccentricity.

This thesis initiates a program of first-principles analytical modeling of the post-peak waveform. We detail future efforts required to fully achieve this goal, in light of the results obtained.

Abstract (Danish version)

Denne afhandling opsummerer kandidatens bidrag til at fremme forståelsen af, hvordan resterne af en sort hul binær fusion går mod ligevægt. Der er tidligere blevet lagt betydelig indsats i at studere responsen af et sort hul forstyrret af initialdata. A-posteriori analyser af perturbative (ekstrem masseforhold) og fuldt non-lineære (sammenlignelige masser) numeriske bølgeformer udsendt af binære fusioner peger på et stærkt aftryk af inspiral-to-legeme problem i den udsendte bølgeform efter dannelsen af en fælles horisont. Derimod har opmærksomheden på at adressere den analytiske modellering af problemet været sparsom. Dette er fokus for afhandlingen.

Efter at have introduceret grundlæggende teknikker i perturbationsteori og den analytiske modellering af to-legeme problemet, replikerer vi først tidligere fænomenologiske resultater om inspiralens aftryk på sort hul afslapning. Vi præsenterer en række inference-tests udført på non-lineære bølgeformer ved hjælp af den Bayesianske inference-algoritme BAYRING og analyserer post-merger signalet fra simuleringer af ikke-roterende progenitorer i quasi-cirkulære binære systemer. Vi validerer tidligere resultater opnået ved at tilpasse de numeriske data gennem kraftfulde værktøjer til Bayesiansk dataanalyse. Vi viser, at umodelerede træk i bølgeformen efter toppen forhindrer en pålidelig udtrækning af mere end én harmonisk overtone i sort hul afslapningsspektret. Dette resultat peger på tilstedeværelsen af ikke-modale fysiske træk i bølgeformen, som er sammenlignelige med eller større end de høje overtoner. I overensstemmelse med tidligere litteratur finder vi en lineær afhængighed af den fundamentale quadrupole mode amplitude på progenitorernes symmetriske masseforhold. Vi udvider derefter for første gang denne tilgang til elektrisk ladede progenitorer ved at introducere en effektiv ladning, der kan parametrisere den fundamentale mode amplitude, restmassen og spinnen ved fusionen.

Efter at have analyseret det fysiske billede, der opstår i bølgeformen efter fusionen, retter vi vores opmærksomhed mod en først-principper beskrivelse af dens træk i den perturbative, ekstreme-masseforholds grænse.

Vi udleder en analytisk model, der kan beskrive de sene tids haler, der udsendes af en test-partikel, der falder ind i et Schwarzschild-sort hul gennem generiske baner. Modellen er et integral over systemets samlede historik, opnået ved konvolution af test-partikelkilden med Price's lov Green's funktion, hvilket fremhæver halernes arvelige natur. Vi validerer modellen mod et sæt af perturbative numeriske evolutioner, der omfatter quasi-cirkulære og eksentriske fusioner, dynamiske fangster, radiale indfald og en spredningskonfiguration. Vores model giver en præcis forudsigelse af bølgeformens sene opførsel for bundne baner med mellemlange til høje ekscentriciteter. Modellen forklarer den flere størrelsesordener store stigning i haleamplitude med orbital ekscentricitet og viser, at haleemissionen er maksimeret, når bevægelsen er på store afstande. Hurtig vinkelbevægelse inducerer destruktiv interferens blandt de efterfølgende halesignaler, hvorfor den totale haleemission forstærkes langs den del af banen med lille vinkelhastighed. Denne forståelse forudser, at for en eksentrisk fusion, vil den sene tids hale, der observeres lige efter ringdown, blive genereret ved den sidste apastron før fusionen. Vi validerer denne hypotese med en række numeriske eksperimenter, der viser halernes evne til at undersøge rumtidens stor-skala struktur. Vi viser, at den sene tids signal er en superposition af et uendeligt antal inverse potenslove i den retarderede tid, hvor Price's lov giver det langsomste dæmpende bidrag. Som en konsekvens bliver et stort antal hurtigere

dæmpende korrektioner i en binær fusion exciteret, hvilket giver anledning til en langlivet transiente med længde sammenlignelig med inspiralens varighed. Price's lov, dvs. vacuum-perturbationsteoriens forudsigelse, kan kun opnås i grænsen af meget sene tidspunkter.

Vi udnytter den opnåede analytiske forståelse af sene tids haler, exciteret af et to-legeme problem, til at undersøge denne effekt i fuldt non-lineære numeriske evolutioner. Vi fokuserer på direkte kollisioner af sammenlignelige masser, ikke-roterende progenitorer. For første gang afslører vi tilstedeværelsen af sene tids haler i non-lineære simuleringer ved omhyggeligt at håndtere ekstrapolationsmetoder og placeringen af ydre grænser. Sammenligning mellem non-lineære resultater og perturbative forudsigelser giver en fremragende overensstemmelse, fra bølgeformernes top til sene tider. Den relative amplitude af halen i forhold til toppen er konsekvent mellem de perturbative og non-lineære tilfælde. Dog aftager den non-lineære hale langsommere end den perturbative forudsigelse, hvilket giver den første evidens for ikke-modale non-lineære effekter i den sene tids del af signalet.

Endelig studerer vi den dynamiske excitering af sorte hulers quasi-normal modes. Dette er et problem af afgørende betydning både for at udvide sort hul spektroskopi til signalet nær toppen, som indeholder den største mængde signalstyrke, og for at undgå modellering systematikker, der kunne inducere overfitting i fænomenologiske skabeloner. Vi viser, hvordan quasi-normal-mode signaler propagerer inden for lysets konus og udleder en kausalitetsbetingelse, der vælger den retarderede del af deres Green's funktion. Dette gør det muligt at bygge den første analytiske model for den dynamiske excitation af ringdown, som kan forbindes glat med inspiral-delen af bølgeformen. Vi udleder denne model for generiske planbaner af en test-partikel på en Schwarzschild baggrund. Quasi-normal modes amplituder opfører sig som aktiveringsfunktioner, der vokser under inspiral-plunge og mætter til konstante værdier nær lys-ring krydsningen. Kausalitet medføre at quasi-normal modes Green's funktionen er regulariseret, som ellers ville være divergent, når test-partiklen når horisonten. Den tilsyneladende placering af test-partiklen, som observeres ved null uendelighed, når horisonten på efter en uendelig mængde tid. Som en konsekvens modtager observatøren signaler udsendt af test-partikelkilden selv ved sene tider efter lys-ring krydsningen, og signalet dæmpes med horisontens rødforskydning. Især viser vi, at denne nye funktion af bølgeformen efter toppen beskrives af en superposition af ikke-oscillerende, eksponentielt aftagende termer med en dæmpningsrate givet ved multipla af horisontens rødforskydning.

Vores model for ringdown excitationer er ikke i stand til fuldt ud at reproducere den nær-toppe udvikling i amplitude og øjeblikkelig frekvens, der observeres i numeriske bølgeforme. Andre komponenter af Schwarzschild baggrundens spektrale respons skal tages i betragtning for at forudsige bølgeformen på så tidlige tidspunkter. Vi er dog i stand til for første gang at forudsige inspiralens aftryk på den stationære ringdown respons, som vi eksplicit viser ved at beregne amplitude- og faseafhængigheden af ekscentriciteten.

Denne afhandling initierer et program for først-principper analytisk modellering af bølgeformen efter toppen. Vi beskriver fremtidige indsatsområder, der kræves for fuldt ud at opnå dette mål, på baggrund af de opnåede resultater.

Danish translation revised by Leart Sabani

Summary

In Chapter 1, we outline the problem addressed in this thesis and highlight its relevance within the context of past literature. We provide intuition and briefly discuss the methods used to derive the original results of this manuscript.

In Chapter 2, we introduce the basic elements of black hole perturbation theory, focusing on a Schwarzschild background. We review the derivation of the non-homogeneous Regge-Wheeler and Zerilli equations, dictating the behavior of the gravitational perturbations multipoles driven by a generic stress-energy matter tensor. We discuss the Green's function approach as a framework to solve for the perturbations and we detail its spectral decomposition in a prompt, quasi-normal modes and tail components, following past literature. We conclude the chapter by reviewing some results on initial-data driven perturbations in vacuum, useful for the original results presented in this manuscript.

In Chapter 3, we discuss the basics of the relativistic two-body problem. After introducing the geodesics equations of motion via the Hamiltonian formalism, we review the characteristics of different bounded orbits. We discuss radiation-reaction effective forces driving the dynamics through inspiral and plunge, providing a broad overview of well-known methods. We conclude by discussing the specific radiation-reaction forces used to compute the original results of this thesis.

In Chapter 4, we review past efforts devoted to modeling the ringdown signal through a posteriori analyses of numerical evolutions and discuss phenomenological models that describe the waveform near its peak. In the second part of the chapter, we present original results. We investigate the ringdown emitted by non-spinning progenitors in quasi-circular orbits through a Bayesian inference algorithm. Our results validate previous studies based on fitting algorithms. We then generalize the investigation to electrically charged progenitors.

In Chapter 5, we investigate late-time tails in the post-peak signal emitted by a test particle infalling in a Schwarzschild black hole, presenting our novel tails model. This Chapter is based on the work in Ref. [1].

In Chapter 6, we uncover late-time tails in fully non-linear mergers, focusing on head-on collisions of equal masses black holes. The results are compared with perturbative ones hinting at the presence of non-linear effects in the late-times portion of the signal. This Chapter is an adaptation of the project Ref. [2].

In Chapter 7, we investigate the dynamical excitation of quasi-normal modes for a test-particle infalling in a Schwarzschild black hole. We derive a causality condition for the propagation of the quasi-normal

modes, from first principles. We present an analytical model for the ringdown, smoothly connected with the plunge-merger portion of the evolution. This chapter contains original results from ongoing efforts.

In Chapter 8, we summarize the main findings of the thesis and discuss future extension of this work.

In Appendix A, we present the expression of the source term in the Regge-Wheeler/Zerilli equations, for perturbations driven by a test-particle. In Appendix B, we discuss the convergence of the RWZHyp code used to obtain the results in Chapters 5, 6, 7. In Appendix C we discuss the Chandrasekhar's transformations relating Regge-Wheeler and Zerilli modes. In Appendix D we review regularization techniques used in the literature to compute the excitation coefficients of the quasi-normal modes excited by a source which extends towards the horizon.

Declaration of authorship

This thesis is based on and partially consists in reprints of the following publications and on-going efforts:

- *Inspiral-inherited ringdown tails*;
  Authors: Marina De Amicis, Simone Albanesi, Gregorio Carullo;
  Journal: Physical Review D, 110, 104005, (2024);
  DOI: 10.1103/PhysRevD.110.104005;
  Preprint: arXiv:2406.17018;
  Comments: Chapter 5, Appendix B and Sec. 7.1 consist in a reprint of this paper or portions of, with minor adjustments.

- *Late-time tails in nonlinear evolutions of merging black holes*;
  Authors: Marina De Amicis, Hannes Rüter, Gregorio Carullo, Simone Albanesi, C. Melize Ferrus, Keefe Mitman, Leo C. Stein, Vitor Cardoso;
  Software Authors: Sebastiano Bernuzzi, Michael Boyle, Nils Deppe, Lawrence E. Kidder, Jordan Moxon, Alessandro Nagar, Kyle C. Nelli, Harald P. Pfeiffer, Mark A. Scheel, William Throwe, Nils L. Vu, Anıl Zenginoğlu;
  Journal: Submitted to Physical Review Letters;
  Preprint: arXiv:2412.06887;
  Comments: Chapter 6 consists in a reprint of this paper, with minor adjustments.

- *Dynamical quasinormal modes excitation*;
  Authors: Marina De Amicis, Enrico Cannizzaro, Gregorio Carullo, Laura Sberna;
  Preprint: arXiv:2506.21668;
  Comments: Chapter 7, Appendix C, D consist in a reprint of this paper or portions of, with minor adjustments.

- Section 4.3.3 and Section 4.3.4 are based on on-going research efforts of the candidate Marina De Amicis, in collaboration with Gregorio Carullo and Vitor Cardoso.

- Section 4.3.5 is based on on-going research efforts of the candidate Marina De Amicis, in collaboration with Gabriele Bozzola, Gregorio Carullo and Vitor Cardoso.

The publications and on-going efforts listed above are outcomes of the research I carried at the Niels Bohr Institute, University of Copenhagen, between March 2022 and June 2025.

Contents

Chapter 1

Introduction

Gravitational waves are a clear prediction of Einstein's General Relativity. Working in the simplest setting, we consider a flat spacetime described by the Minkowski metric $\eta_{\mu\nu}$ with small perturbations $h_{\mu\nu}$ [3, 4]

$$g_{\mu\nu} = \eta_{\mu\nu} + h_{\mu\nu} \quad , \quad |h_{\mu\nu}| \ll 1 \, . \tag{1.1}$$

We substitute the above ansatz into Einstein's equations, expand in $h_{\mu\nu}$ and neglect all terms beyond linear order. This yields a set of ten equations governing the evolution of $h_{\mu\nu}$. A fundamental principle of General Relativity is gauge invariance: solutions of Einstein's equations remain valid under coordinate (gauge) transformations. This freedom allows us to impose four constraint equations on $h_{\mu\nu}$. For the sake of this example, it is convenient to adopt the harmonic gauge (also known as the De Donder or Lorentz gauge) [3, 4]

$$\partial^\mu \left(h_{\mu\nu} - \frac{1}{2} \eta_{\mu\nu} \eta^{\alpha\beta} h_{\alpha\beta} \right) = 0 \, . \tag{1.2}$$

In this gauge, the linearized Einstein's equations governing $h_{\mu\nu}$ read

$$\Box_{\mathrm{F}} \left(h_{\mu\nu} - \frac{1}{2} \eta_{\mu\nu} \eta^{\alpha\beta} h_{\alpha\beta} \right) = - \frac{16\pi G}{c^4} T_{\mu\nu} \, , \tag{1.3}$$

where $T_{\mu\nu}$ is the stress-energy tensor sourcing the gravitational perturbations, and $\Box_{\mathrm{F}} \equiv \eta^{\mu\nu} \partial_\mu \partial_\nu$ is the flat space d'Alambert operator. This equation predicts the existence of wave-like spacetime perturbations, which we call *gravitational waves*. Einstein [5] was the first to derive this result, but he erroneously argued that gravitational waves were a "gauge artifact" removable by choosing an appropriate coordinate frame. Later, it was shown that a gravitational wave passing through a collection of test particles alters their relative proper distance, which is a physical observable. In particular, gravitational waves possess two physical degrees of freedom, corresponding to two observable polarizations [3, 4].

A rough estimate of the gravitational waves' amplitude generated by a source $T_{\mu\nu}$, can be obtained from the prefactor on the right-hand side of Eq. (1.3)

$$\Box_F h \sim \frac{G}{c^4} \times T \sim 8 \cdot 10^{-50} \frac{\mathrm{s}^2}{\mathrm{g\,cm}} \times T \, . \tag{1.4}$$

Gravitational wave emission is extremely weak, so these signals are generally difficult to observe except via secular effects or from extremely massive and compact sources. The first evidence for gravitational

waves was, in fact, indirect: precise timing of the Hulse–Taylor binary pulsar revealed a decreasing orbital period, consistent with the orbital energy loss due to gravitational wave emission predicted by general relativity [6]. The first direct detection of gravitational waves was instead achieved in 2015, by the *LIGO-Virgo collaboration* [7], using Michelson interferometry.

Binary black hole mergers generalities

Since the first direct detection, many more binary black hole mergers have been observed, thanks also to upgrades that improved the detectors' sensitivity [8]. Gravitational waves coming from these systems can be divided into three main stages. A schematic representation of these phases is shown in Fig. 1.1, taken from Ref. [7]. Initially, the two black holes orbit each other on a bound trajectory that gradually decays as energy and angular momentum are carried away by gravitational radiation. We denote this portion of the binary evolution and the gravitational signal it emits *inspiral*. Because the gravitational emission is weak, its back-reaction on the orbit is small and acts over long timescales. As a consequence, the trajectory slowly evolves through a sequence of stable bounded orbits. After a critical separation is reached, stable orbits able to osculate the trajectory no longer exist. The relative motion of the two objects becomes much faster and is unaffected by back-reaction [9, 10]. This portion of the orbital evolution, known as the *plunge*, culminates in the formation of a common horizon, the *merger*. During the *plunge-merger* stage, the waveform exhibits a *transient* behavior: its amplitude peaks, and then starts to decay exponentially. Its instantaneous frequency grows until it saturates to a constant. This transient lasts for about $\approx 15M$ [11, 12] and ends when the waveform is well described by a superposition of exponentially damped sinusoids (at leading order) [13], a regime denoted as the *ringdown*.

In the ringdown phase, a common horizon has already formed, and a perturbed black hole geometry approximates the spacetime. Black hole perturbations in vacuum have been studied by analytical and numerical means, mainly evolving Gaussian-like initial data in an exact geometry, e.g. Schwarzschild or Kerr. These studies decompose the black hole response into three different spectral components [14, 15, 16, 17, 18]: a prompt signal, propagating the initial data directly towards the observer, a superposition of exponentially damped sinusoids (the *quasi-normal modes*) and a late-time inverse power-law decay (the *tail*). Analyses of numerical waveforms [13] showed that, for each multipole, the amplitude and instantaneous frequency of the ringdown signal match the least-damped quasi-normal mode frequency of the remnant black hole, as computed by perturbation theory. This motivated modeling the post-merger phase as a superposition of constant-amplitude quasi-normal modes

$$h^{\rm ring}(t,r,\theta,\varphi) = \frac{1}{r}\theta(t-t_{\rm start})\sum_{\ell\geq 2}\sum_{|m|\leq\ell}\sum_{n=0}\sum_{s=\pm} A_{\ell mns}e^{i\phi_{\ell mns}}\times e^{-i\omega_{\ell mns}t - t/\tau_{\ell mns}}\times {}_{-2}Y_{\ell m}(\theta,\varphi)\,, \tag{1.5}$$

where $A_{\ell mns}$, $\phi_{\ell mns}$ are the real amplitude and phase of each mode, while $\omega_{\ell mns}$, $\tau_{\ell mns}$ denote its real frequency and damping time. The indices (ℓm) label different components in the spin weight -2 spherical harmonics ${}_{-2}Y_{\ell m}$ basis (note that also spin weight -2 spheroidal harmonics can be used), n is the overtone number and s distinguishes "regular" and "mirror" modes. $t_{\rm start}$ defines the ringdown starting time, i.e. the time after which Eq. (1.5) can accurately describe the signal.

The current sensitivity of the LIGO-Virgo detectors spans approximately the range $\sim 20-10^3$ Hz, allowing the detection of binaries with total mass in the stellar and intermediate mass intervals $\sim 2-10^3\,M_\odot$ [8].

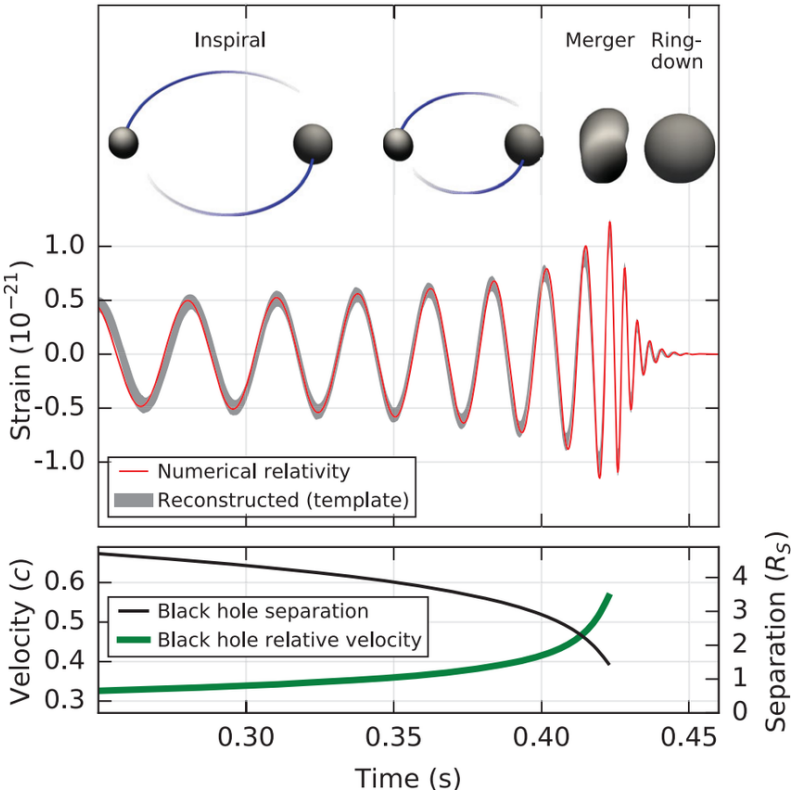

Figure 1.1: Numerical waveform emitted from a black-hole binary merger with an artistic rendering of each different stage. Figure taken from Ref. [7].

The fundamental quadrupolar mode $(\ell mn) = (220)$ of a Schwarzschild black hole has frequency $\omega_{220+} \simeq 0.37/M$, hence, the ringdown is in the LIGO-Virgo band for total mass in the intermediate regime $\sim 10^2 - 10^3 M_\odot$. The first gravitational wave detection marked also the first ringdown observation; to date, ~ 20 ringdown events have been catalogued [8] (see Ref. [19] for the full list). This sample is expected to grow extensively in future observing runs, as the LIGO–Virgo detectors undergo further upgrades.

To extract information from observations, we compare the data against predictions derived under different hypothesis, enclosed in waveform *models*. Such models do not need to cover the full inspiral-merger-ringdown signal, but can be restricted to different evolution phases or even to selected features. For instance, the template in Eq. (1.5) is a *parametrized model* for extracting quasi-normal mode content from the post-merger waveform, treating the (complex) amplitudes and frequencies as free parameters. In General Relativity, the *no-hair conjecture* implies that the complex quasi-normal frequencies depend only on the black hole's mass, spin, electric and magnetic charge [20, 21, 22, 23, 24, 25, 26, 27, 28, 29, 30, 31, 32]. Hence, detecting a single quasi-normal mode lets us infer the remnant's mass and spin, whereas observing multiple modes enables tests of general relativity and its coupling to other fundamental fields.

This line of research, denoted as *black hole spectroscopy* [33, 34, 35, 36, 37, 38], holds great potential to discover new physics, motivating further investigations aimed at computing accurate plunge-merger-ringdown models that more closely match General Relativity's predictions.

Defining the problem

The ringdown template in Eq. (1.5) has several limitations. To begin with, its functional form was computed from first principles, solving linearized Einstein's equations for narrow Gaussian initial data with small amplitude, localized far from the black hole, and is only valid at late times for an observer at large distances [39, 14, 15]. It is not immediate to deduce that a model constructed under such simplifications can be applied to binary mergers. To start with, comparison of non-linear and perturbative waveforms hints at a suppression of non-linear effects at later times [40]. Therefore, enough time after a common horizon has formed, the signal emitted seems to be well-modeled as a linear initial-value problem on a fixed background geometry, at leading order. Also, for real detections, we can always assume the observer to be at large distances. Hence, two of the above hypotheses are expected to be valid. However, realistic initial data are not a narrow Gaussian localized far from the black hole. Relaxing this assumption yields a more complex phenomenology than Eq. (1.5) [41]. Further, although at late times non-linear effects are suppressed, the plunge-merger and post-merger portion of the signal does contain such beyond-linear effects. Some appear as exponentially damped sinusoids: the *quadratic* quasi-normal modes deriving from second-order couplings in the Einstein equations [42, 43, 44, 45, 46, 47, 48, 40, 49], which can easily be incorporated into Eq. (1.5). Other non-linear phenomena are non-modal [50, 51, 52, 53, 54, 55, 56, 57] and cannot be captured by Eq. (1.5).

Equation (1.5) does not predict how the constant-amplitude quasi-normal response is excited, hence it cannot be smoothly connected to the transient signal and requires an additional free parameter, the starting time $t_{\rm start}$. Without clear predictions on $t_{\rm start}$ and the plunge-merger transient, ringdown analyses of real data could, in principle, be performed at any time, even near the waveform peak. At such early times and only for specific systems, the (numerical) waveform may be approximated by a superposition of many overtones [13, 58, 59]. This result, however, is not a prediction but rather an *a posteriori* observation, derived by fitting numerical relativity waveforms with many free parameters, assuming a fixed black hole geometry (while the remnant is dynamical), and without properly addressing overfitting. Lacking an accurate plunge-merger-ringdown waveform model could lure one into repeating such analysis on real data [60], potentially yielding unphysical conclusions [61, 40, 62].

The ringdown signal decays fast: for a remnant black hole of mass $\sim 100M_\odot$ and zero spin, the fundamental mode in the quadrupole has lifetime $\tau_{220+} \sim 5.54\,\mathrm{ms}\ \mathrm{M}/(100\mathrm{M}_\odot)$. If the model restricts our analyses to times well after the peak, the rapidly decaying nature of the signal leads to a loss in *signal to noise ratio*, reducing our ability to disentangle gravitational waves from the detector noise. Pushing modeling abilities closer to the waveform peak would imply following the merger-ringdown evolution for a longer duration, improving parameter estimation.

Current closed-form plunge-merger models are purely *phenomenological*, built by fitting heuristic templates to numerical relativity waveforms. Alternatively, it is possible to use numerical waveforms directly as models. In this case, we have a *first-principles* model, since it is obtained by solving the full Einstein's equations describing the two-body problem until the remnant reaches an equilibrium configuration. Since generating a waveform for every binary configuration and progenitors' parameters is computationally challenging, numerical relativity based models typically interpolate across a catalog of numerical waveforms,

creating *numerical surrogates* [63, 64, 65, 66, 67, 68, 69]. Both numerical surrogates and phenomenological models are valuable because they enable the identification of gravitational-wave signals within detector noise and facilitate the extraction of some physical parameters. However, these models have downsides. They only allow us to quantify the total agreement or mismatch between the data and a set of predictions on different portions of the signal, in which all parameters are fixed a priori. In this process, the inability to disentangle different waveform features and parametrize them in terms of fundamental observables of our theory of gravity limits the ability to isolate specific physical contributions and infer new physics from observations.

We wish instead to have analytical models derived by first principles, able to describe different waveform features, in the form of closed templates parametrized by observables. If we consider binaries initialized in different configurations, modify the underlying theory of gravity, assume the presence of an environment, etc., such models should yield precise predictions on how each observable is affected, while often retaining a similar underlying functional expression. By comparison with observations, we would then be able to make theory-agnostic tests on these observables, later evaluating them against existing predictions or formulating new ones as needed.

First-principles analytical models have been computed through perturbative expansions for the inspiral part of the waveform, through the Effective-One-Body approach [70, 71] for generic mass ratios and by the self-force program [72] for extreme and intermediate mass ratios of the progenitors. In these frameworks, given a theory (e.g. general relativity in vacuum or electrovacuum, extensions to this theory), it is possible to derive semi-analytic solutions to the two-body problem, describing both the objects' motion and the gravitational radiation they emit. This thesis employs black-hole perturbation theory to derive first-principles analytic models of the plunge–merger and post-merger phases of the gravitational-wave signal.

Intuition and starting points

An intuition on how to tackle this problem can be built by analyzing and comparing perturbative and non-linear numerical waveforms, exploiting the features uncovered by phenomenological ansatzes. Below, we briefly sketch such intuition, which will be tested and made rigorous in the remainder of the thesis. For instance, it is possible to describe the transient and ringdown phase in each multipole through a single quasi-normal mode, the least damped one, with time dependent amplitudes $A_{\ell m}(t)$ and phases $\phi_{\ell m}(t)$, modeled as smooth activation functions [73]. The templates for $A_{\ell m}(t)$, $\phi_{\ell m}(t)$ are heuristic functions of parameters fitted from numerical waveforms. The key idea, however, is that the quasi-normal mode response must switch on over a finite timescale, rather than instantaneously as assumed in Eq. (1.5).

The picture behind this intuition is the following (see also Fig. 1.2). During the inspiral, the instantaneous frequency of the multipole (ℓm) is approximately $m\Omega(t)$, where $\Omega(t)$ is the binary orbital frequency. This behavior still holds in the early plunge, until the maximum orbital frequency is reached $\Omega_{\rm max}$. Afterwards, $\Omega(t)$ falls rapidly, while the multipolar instantaneous gravitational-wave frequency continues to increase, until it saturates to the fundamental quasi-normal frequency. In the extreme mass-ratio limit, the binary system reduces to a test particle evolving on a fixed black hole background, and the orbital frequency has

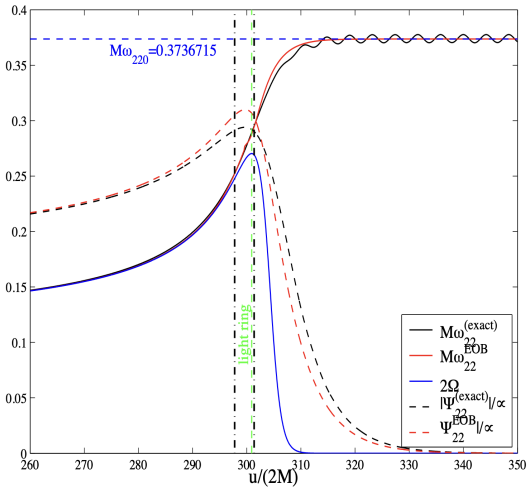

Figure 1.2: In black, the quadrupolar instantaneous frequency emitted by a test particle infalling in a Schwarzschild BH. In blue, its instantaneous orbital frequency, rescaled with respect to the multipole number $m = 2$. Figure taken from Ref. [74].

a peak when the light-ring is crossed. The light-ring is located near the peak of the background effective potential barrier. Studies of black hole perturbations in vacuum identify the generation of quasi-normal modes as a scattering process off the potential barrier peak. Hence, we heuristically expect the ringdown response to be "activated" as the test particle approaches and crosses the light-ring.

The quasi-normal mode response is a solution of a second-order partial differential equation in (t, r_*). When a test particle drives the perturbations, this equation is non-homogeneous, with a source term oscillating with frequency well approximated by $\approx m\Omega(t)$. Then, the quasi-normal mode excitation can be viewed as a driven, damped harmonic oscillator [74, 75]. The fundamental mode ($n = 0$) has the longest life-time and the largest real frequency $\omega_{\ell m 0+}$, satisfying $\omega_{\ell m 0+} > m\Omega_{\rm max}$. Overtones are characterized by a shorter life-time and a smaller real frequency. In the limit $n \gg 1$ the quasi-normal modes share the same real frequency $\ll 1$, while the decay-rate grows linearly in n [15]. As the test particle plunges, $m\Omega(t)$ either sweeps or approaches each real quasi-normal frequency $\omega_{\ell mn+}$, progressively driving the excitation of the respective mode. This cumulative ("quasi-resonant") effect is most efficient for the least damped modes, $n \gtrsim 0$, corresponding to frequencies $\omega_{\ell mn+} \gtrsim \Omega_{\rm max}$ and, as a consequence, it contributes the most when the test particle is close to the light-ring. Once the test particle crosses the light-ring, $\Omega(t)$ drops quickly to zero. The "driving force" disappears, the quasi-normal mode excitation can be modeled as a free oscillator, and we expect the quasi-normal amplitudes to be approximately constant.

Even though this intuition is derived under the extreme mass-ratio limit, it can be generalized to comparable masses by stating that the quasi-normal mode response is progressively excited near the peak of the binary orbital frequency. Phenomenological models employed to describe the post-peak waveform [73], share the same functional form in both the perturbative, extreme mass-ratio limit and the fully non-linear, comparable-mass one. The non-linear content of the waveform is encapsulated in the free parameters of these phenomenological templates. This feature showcases how perturbative and non-linear post-merger

waveforms are characterized by similar features, hinting at a common underlying mechanism to describe them at leading order.

The heuristic picture sketched above offers an intuition on how to connect the ringdown template in Eq. (1.5) with the inspiral portion of the waveform. Moreover, it hints at the fact that the ringdown response begins to accumulate before a common horizon has formed, when two distinct objects are still present. As a consequence, we expect that the quasi-normal mode amplitudes will carry information on inspiral features. This is indeed observed in numerical relativity waveforms: fits of numerical data performed with template Eq. (1.5) and fixed quasi-normal frequencies yield amplitudes and phases which carry clear imprints of the progenitors' binary [76, 77, 11, 78, 12, 79, 49, 80, 69, 81, 82, 83].

Interestingly, a posteriori analyses of numerical waveforms can robustly identify up to the first few overtones, while higher overtones are not parametrically stable [40, 84]. Agnostic studies, in which both complex amplitudes and frequencies are fitted from the data, hint at the presence of low-frequency features in the post-merger waveform comparable in magnitude with overtones $n \geq 2$ [40]. These features could be either unmodeled numerical noise or unmodeled physical signals not captured by Eq. (1.5), which, as aforementioned, is derived under oversimplified conditions. A possible low-frequency contamination in the waveform at intermediate times, is given by tails, an inverse power-law decay dominating the signal at late times. This signal is small by the time it starts dominating the strain, however, its functional behavior hints it could be louder at earlier times, enough to potentially compete in magnitude with overtones. Due to the current lack of a first principles understanding of how overtones and tails are excited, this picture remains speculative. There are hints that the late-time tails could bear imprints of the inspiral two-body problem and be potentially magnified by certain binary features [75]. However, contrary to the quasi-normal mode case, there is no intuition behind the mechanism of tail excitation. These results warrant deeper investigations.

A better understanding of tails is important not only in the context of ringdown studies. The several orders of magnitude enhancement of late-time tails with the progenitors' binary eccentricity observed in Ref. [75] brings tails into the realm of observational physics and is relevant for current (LIGO-Virgo-KAGRA) and future (LISA) detections. Several channels for eccentric mergers are being investigated (see e.g. [85, 86]); moreover, there is evidence that an eccentric merger has already been observed by the LIGO-Virgo-KAGRA collaboration [87, 88]. A tail detection would have significant implications both in the foundations of general relativity and in astrophysics. On one side, tails have the potential to complement small-scale information obtained through the ringdown with information on the spacetime asymptotic structure [89, 90] and peeling behavior (or lack thereof) [91]. At the same time, the strong dependence on eccentricity offers a unique way to measure this parameter through gravitational waves, which is relevant in the context of population studies and binary formation scenarios.

Methods

We have outlined the problem we want to solve and sketched our intuition on how the post-merger response is excited. Now, we identify the methods required to translate such intuition into a rigorous calculation. We will see that, although the overall qualitative picture is correct, several other features

contribute to the dynamical excitation of the black hole relaxation.

The main focus of this thesis will be on binaries in which one of the black holes is much smaller than the other, so that it can be approximated by a test particle. To derive these results, we will consider a decomposition of the gravitational perturbation in spin weight -2 spherical harmonics, and solve for the Regge-Wheeler and the Zerilli differential equations [92, 3, 4], driven by a source localized at the particle trajectory. We will present semi-analytical results, obtained through the convolution of the source, fed with a numerical trajectory, with different components of the retarded Green's function associated with the Regge-Wheeler/Zerilli differential operator. The results will then be compared with numerical perturbative evolutions, computed with the RWZHYP code [93, 94]. For some fine-tuned configurations, we analyze fully non-linear numerical evolutions, computed with the SPEC code [95, 96, 97, 98, 99], relative to comparable-masses BH binaries.

We will mainly consider a test particle evolving along trajectories driven by radiation reaction through the inspiral, plunge, and merger phases. At each time before the plunge, it is possible to find a geodesic osculating the trajectory, while, once the test particle enters the plunge, the effect of radiation reaction on the orbit becomes negligible, and the trajectory approaches a geodesic [9, 10]. This non-linear trajectory will be fed into the source term on the right-hand side of the Regge–Wheeler and Zerilli equations. This approach has been widely used in the literature [100, 74, 101, 75] to compute inspiral–plunge–ringdown waveforms for small mass ratios; however, it is not formally consistent with a first-order perturbative expansion. To be consistent with first-order perturbation theory, we should restrict our treatment to geodesic trajectories. Instead, we introduce dissipative second-order effects in the particle-dependent source driving the perturbations. Below, we justify this approach based on results and arguments present in the literature.

The heuristic argument behind our framework is that, due to the long timescale over which radiation reaction affects the orbital evolution, we expect it to be effectively (though not formally) equivalent to the *adiabatic approximation* approach in Ref. [102]. In this reference, the inspiral-plunge waveform emitted by the test particle is computed by allowing its amplitude and instantaneous frequency to have a slow time evolution. At each time step, these quantities are fixed to values relative to a motion along the osculating geodesic. The resulting waveform then "stitches together" first-order waveforms and is formally consistent with a perturbative expansion.

A formal argument supporting the approach used in this thesis was presented in Ref. [100]. In this reference, the Regge–Wheeler and Zerilli equations with the non-linear trajectory fed into the source are solved numerically. The resulting angular momentum flux at future null infinity is then compared with an analytical prediction of the binary's angular momentum loss, computed through a resummed Post-Newtonian expansion. This analytical quantity, derived within a consistent perturbative framework, shows good agreement with the numerical angular momentum flux at infinity during the inspiral (see Fig. 4 of Ref. [100]). As discussed in Ref. [100], a mismatch appears in the final stages of the plunge. However, in this regime, the motion becomes approximately geodesic, and the numerical framework thus becomes consistent with first-order perturbation theory. This result suggests that the error introduced by the inconsistent use of perturbation theory stays small throughout the orbital evolution.

Ref. [103] provided another test of the validity of our approach. This work compares test-particle numerical waveforms obtained using the "perturbatively inconsistent" framework with fully non-linear numerical evolutions computed for several mass ratios in the intermediate regime, the largest being $q = 128$. The amplitudes at merger, where non-linear effects are expected to be most relevant, are compared after rescaling by the leading dependence on the symmetric mass ratio. Ref. [103] found excellent agreement between the test-particle and fully non-linear results for all the multipoles considered in the present work, i.e., $(\ell, m) = (2, 2), (3, 2), (4, 4)$ (see Fig. 2 of Ref. [103]). This direct comparison with the full solution of Einstein's equations further validates the approach used in this thesis, suggesting that non-linearities in wave generation are subleading, at least for the aforementioned multipoles.

Unless specified, we will always use geometric units, for which $G = c = 1$.

Chapter 2

Schwarzschild black hole perturbations

A Schwarzschild black hole (BH) is a spherically symmetric, asymptotically flat solution of Einstein's equations in vacuum, characterized by the presence of a null hypersurface, known as the *horizon*. Let $g^0_{\mu\nu}$ denote the Schwarzschild metric and $R^0_{\mu\nu}$, R^0 be the Ricci tensor and the Ricci scalar constructed from this metric, Einstein's equations read

$$R^0_{\mu\nu} - \frac{1}{2} g^0_{\mu\nu} R^0 = 0 \,. \tag{2.1}$$

In Schwarzschild coordinates (t, r, θ, φ), the line element describing this solution is

$$ds^2 = g^0_{\mu\nu} dx^\mu dx^\nu = -A(r) dt^2 + \frac{1}{A(r)} dr^2 + r^2 \left(d\theta^2 + \sin^2 \varphi d\varphi^2 \right) \quad , \quad A(r) = \left(1 - \frac{2}{r} \right) , \tag{2.2}$$

where we have rescaled $r \to r/M$, with M BH mass. We adopt this convention throughout the chapter. It is also useful to introduce the tortoise coordinate r_* as a function of r, with the following convention

$$\frac{dr_*}{dr} = A^{-1}(r) \quad , \quad r_*(r) = r + 2 \log \left(\frac{r}{2} - 1 \right) , \tag{2.3}$$

and the Eddington-Finkelstein coordinates (u, v) (also referred to as retarded and advanced time, respectively)

$$u = t - r_* \quad , \quad v = t + r_* \,. \tag{2.4}$$

We will consider linear perturbations on top of $g^0_{\mu\nu}$; thanks to the spherical symmetry of the background, the equations governing the evolution of these perturbations *separate* into an angular part and a (t, r) part. The angular sector is solved using tensor spherical harmonics. The (t, r) sector is governed by second-order partial differential equations known as *master* equations. These equations will be derived in Sec. 2.1 assuming the presence of matter driving the perturbations. However, in this chapter, we will focus on a vacuum problem, studying the evolution of initial data imposed on the Cauchy hypersurface $t = t_0$. In Sec. 2.2, we will introduce a framework to study these perturbations, based on the Green's function technique. In Sec. 2.3, we will review previous results in the literature, on which the results of Chapters 7 and 5 are based. The non-vacuum case will be discussed in detail in Chapters 3 and 4.

The discussion of Sec. 2.1 is based on Refs. [92, 3, 4] and references therein, as stated in the text. Sec. 2.2 is mainly based on Refs. [104, 14, 105, 15, 106, 107, 18].

The discussion in Sec. 2.3.2 is based on Ref. [108].

2.1 Master equations

We consider small perturbations on top of a Schwarzschild background $g^0_{\mu\nu}$, kept fixed, driven by the presence of a stress-energy tensor $T_{\mu\nu} \sim O(\varepsilon)$, where ε is a small book-keeping parameter. The perturbed metric is expanded in $O(\varepsilon)$ and Einstein's equations are solved iteratively, order by order. At the linear level, we have

$$g_{\mu\nu} = g^0_{\mu\nu} + \varepsilon h_{\mu\nu} + \dots , \tag{2.5}$$

with $h_{\mu\nu}$ solution of the linearized Einstein's equations

$$R^1_{\mu\nu} - \frac{1}{2} g^0_{\mu\nu} R^1 = 8\pi T_{\mu\nu} . \tag{2.6}$$

$R^1_{\mu\nu}$ and R^1 are the linearized (order $\sim \varepsilon$) Ricci tensor and Ricci scalar [92].

Following Refs. [92, 3, 4], we proceed to separate the perturbations into an angular and a (t, r)-sector, independent from each other.

We exploit the spherical symmetry of the background and decompose the Schwarzschild manifold as $\mathcal{M} = \mathrm{M}^2 \times \mathrm{S}^2$, where M^2 is the 2-dimensional Lorentzian manifold covered by the coordinates (t, r), while S^2 is the 2-sphere with coordinates (θ, φ). We will use capital Roman letters to denote components on M^2, and lowercase for components on S^2. We denote the metric on S^2 as $\gamma_{ab} \equiv \mathrm{diag}(1, \sin^2\theta)$, with inverse $\gamma^{ab} = \mathrm{diag}\left(1, \sin^{-2}\theta\right)$. ∇_a is the covariant derivative on S^2.

We can rewrite $h_{\mu\nu}$ as [92, 4]

$$h_{\mu\nu} = \begin{pmatrix} h_{AB} & h_{Aa} \\ h_{aA} & h_{ab} \end{pmatrix} \quad , \quad A, B = t, r \quad , \quad a, b = \theta, \varphi . \tag{2.7}$$

Each of the components h_{AB} for A, B fixed is a scalar under rotations on S^2, h_{Aa} for A fixed is a vector and h_{ab} is a rank-2 tensor. As a consequence, it is possible to expand h_{AB}, h_{Aa} and h_{ab} in scalar, vector and tensor spherical harmonics, respectively. We denote the scalar spherical harmonics by $Y^{\ell m}(\theta, \varphi)$ with $\ell \geq 0$, $|m| \leq \ell$, as the solutions of the following eigenvalue problem

$$\gamma^{ab} \nabla_a \nabla_b Y^{\ell m}(\theta, \varphi) = -\lambda\, Y^{\ell m}(\theta, \varphi) , \tag{2.8}$$

where we have defined $\lambda \equiv \ell(\ell + 1)$.

The vector spherical harmonics on S^2 are defined for $\ell \geq 1$, $|m| \leq \ell$ as

$$\begin{aligned} Y^{\ell m}_a &= \nabla_a Y^{\ell m} = \left(\partial_\theta Y^{\ell m}, \partial_\varphi Y^{\ell m}\right) , \\ S^{\ell m}_a &= -\epsilon_{ab} \gamma^{bc} \nabla_c Y^{\ell m} = \left(-\frac{1}{\sin\theta}\, \partial_\varphi Y^{\ell m}, \sin\theta\, \partial_\theta Y^{\ell m}\right) . \end{aligned} \tag{2.9}$$

In the above, ϵ_{ab} is the Levi-Civita symbol on S^2 defined as $\epsilon_{23} = -\epsilon_{32} = \sin\theta$.

For tensor spherical harmonics, we use the orthonormal set introduced by Zerilli-Mathews [109, 110], defined for $\ell \geq 2$ as

$$\begin{aligned} A^{\ell m}_{ab} &= \gamma_{ab} Y^{\ell m} = \mathrm{diag}\left(Y^{\ell m}, \sin^2\theta\, Y^{\ell m}\right), \\ Z^{\ell m}_{ab} &= \nabla_a \nabla_b Y^{\ell m} + \frac{\lambda}{2}\gamma_{ab} Y^{\ell m} = \frac{1}{2}\begin{pmatrix} W^{\ell m} & X^{\ell m} \\ X^{\ell m} & -\sin^2\theta\, W^{\ell m}\end{pmatrix}, \\ S^{\ell m}_{ab} &= \frac{1}{2}\left(\nabla_b S^{\ell m}_{\ a} + \nabla_b S^{\ell m}_{\ a}\right) = \frac{1}{2}\begin{pmatrix} -\frac{1}{\sin\theta} X^{\ell m} & \sin\theta\, W^{\ell m} \\ \sin\theta\, W^{\ell m} & \sin\theta\, X^{\ell m}\end{pmatrix}, \end{aligned} \tag{2.10}$$

where we have introduced the functions $W^{\ell m}$, $X^{\ell m}$ as follows

$$W^{\ell m}(\theta,\varphi) \equiv \partial^2_\theta Y^{\ell m} - \cot\theta\, \partial_\theta Y^{\ell m} - \frac{1}{\sin^2\theta}\partial^2_\varphi Y^{\ell m} \quad , \quad X^{\ell m}(\theta,\varphi) \equiv 2\partial_\theta\partial_\varphi Y^{\ell m} - 2\cot\theta\, \partial_\varphi Y^{\ell m}\,. \tag{2.11}$$

The harmonics just introduced are eigenstates of the parity operator, whose action maps $\theta \to -\theta + \pi$, $\varphi \to \varphi + \pi$. In particular, $Y^{\ell m}$, $Y^{\ell m}_a$, $A^{\ell m}_{ab}$ and $Z^{\ell m}_{ab}$ have eigenvalue $(-1)^\ell$ and are denoted as *even* or *polar*. The *odd* or *axial* harmonics $S^{\ell m}_{\ a}$ and $S^{\ell m}_{\ ab}$ have eigenvalues $(-1)^{\ell+1}$. It follows that we can separate the first-order perturbations $h_{\mu\nu}$ in Eq. (2.7) into even and odd, as [92, 4]

$$h_{\mu\nu} = \sum_{\ell,|m|\leq\ell} \left(h^{\ell m,(\mathrm{e})}_{\mu\nu} + h^{\ell m,(\mathrm{o})}_{\mu\nu}\right). \tag{2.12}$$

The even sector is decomposed as [92, 4]

$$h^{\ell m,(\mathrm{e})}_{\mu\nu} = \begin{pmatrix} h^{\ell m,(\mathrm{e})}_{AB}(t,r)\, Y^{\ell m}(\theta,\varphi) & h^{\ell m,(\mathrm{e})}_{A}(t,r)\, Y^{\ell m}_a(\theta,\varphi) \\ h^{\ell m,(\mathrm{e})}_{A}(t,r)\, Y^{\ell m}_a(\theta,\varphi) & r^2\left[K_{\ell m}(t,r) A^{\ell m}_{ab}(\theta,\varphi) + H_{\ell m}(t,r) Z^{\ell m}_{ab}(\theta,\varphi)\right]\end{pmatrix}, \tag{2.13}$$

while the odd perturbations have components [92, 4]

$$h^{\ell m,(\mathrm{o})}_{\mu\nu} = \begin{pmatrix} 0 & h^{\ell m,(\mathrm{o})}_{A}(t,r)\, S^{\ell m}_{\ a}(\theta,\varphi) \\ h^{\ell m,(\mathrm{o})}_{A}(t,r)\, S^{\ell m}_{\ a}(\theta,\varphi) & \bar{h}^{\ell m,(\mathrm{o})}(t,r)\, S^{\ell m}_{\ ab}(\theta,\varphi)\end{pmatrix}. \tag{2.14}$$

The stress-energy tensor of the external perturbations $T_{\mu\nu}$ can also be decomposed in scalar, vector and tensor spherical harmonics, and then separated into even and odd sectors [92]

$$T_{\mu\nu} = \sum_{\ell,|m|\leq\ell} \left(T^{\ell m,(\mathrm{e})}_{\mu\nu} + T^{\ell m,(\mathrm{o})}_{\mu\nu}\right), \tag{2.15}$$

where the even and odd sectors are defined as [92]

$$T^{\ell m,(\mathrm{e})}_{\mu\nu} \begin{pmatrix} T^{\ell m,(\mathrm{e})}_{AB}(t,r)\, Y^{\ell m}(\theta,\varphi) & T^{\ell m,(\mathrm{e})}_{A}(t,r)\, Y^{\ell m}_a(\theta,\varphi) \\ T^{\ell m,(\mathrm{e})}_{A}(t,r)\, Y^{\ell m}_a(\theta,\varphi) & r^2 T^{\ell m}_3(t,r) A^{\ell m}_{ab}(\theta,\varphi) + T^{\ell m}_2(t,r) Z^{\ell m}_{ab}(\theta,\varphi)\end{pmatrix}, \tag{2.16}$$

$$T^{\ell m,(\mathrm{o})}_{\mu\nu} = \begin{pmatrix} 0 & T^{\ell m,(\mathrm{o})}_{A}(t,r)\, S^{\ell m}_{\ a}(\theta,\varphi) \\ T^{\ell m,(\mathrm{o})}_{A}(t,r)\, S^{\ell m}_{\ a}(\theta,\varphi) & \bar{T}^{\ell m,(\mathrm{o})}(t,r)\, S^{\ell m}_{\ ab}(\theta,\varphi)\end{pmatrix}. \tag{2.17}$$

2.1.1 Sourced Regge-Wheeler equation

We substitute the linear-order odd perturbations Eq. (2.14) and stress-energy tensor Eq. (2.17) into the linearized Einstein's equations Eq. (2.6). Following [92], we redefine the function $\partial_t h_r^{\ell m,(\mathrm{o})}$ in terms of the *Regge-Wheeler master function* $\Psi_{\ell m}^{(\mathrm{o})}$ as

$$\partial_t h_r^{\ell m,(\mathrm{o})} = \frac{(\lambda-2)}{r}\Psi_{\ell m}^{(\mathrm{o})} + r^2\partial_r\left(\frac{h_t^{\ell m,(\mathrm{o})}}{r^2}\right), \tag{2.18}$$

and substitute this expression into the linearized Einstein's equations for the odd sector. The $(t\phi)$-component is a function of the following variables

$$\delta \mathrm{G}_{t\phi}^{\ell m,(\mathrm{o})}\left[r, \Psi_{\ell m}^{(\mathrm{o})}, \partial_r\Psi_{\ell m}^{(\mathrm{o})}, h_t^{\ell m,(\mathrm{o})}, \partial_r h_t^{\ell m,(\mathrm{o})}, \partial_r^2 h_t^{\ell m,(\mathrm{o})}, \partial_t \bar{h}^{\ell m}\right] = 8\pi T_{t\phi}^{\ell m,(\mathrm{o})}\left[r, T_t^{\ell m,(\mathrm{o})}\right], \tag{2.19}$$

where we used the notation $\delta \mathrm{G}_{\mu\nu} = R^1_{\mu\nu} - (1/2) g^0_{\mu\nu} R^1$. We differentiate the $(r\phi)$-component of the linearized Einstein's equations with respect to the t-coordinate, then substitute the expression for $\partial_t \bar{h}^{\ell m}$ obtained solving Eq. (2.19). Finally, we rewrite the equation in terms of the r_* coordinate, as defined in Eq. (2.3). The result is a partial differential equation in the variables (t, r_*) only, independent of the angular variables (θ, φ). This equation, governing the odd-parity perturbations, is denoted *Regge-Wheeler master equation* and reads

$$\left[\partial_t^2 - \partial_{r_*}^2 + V_{\ell m}^{RW}(r_*)\right]\Psi_{\ell m}^{(\mathrm{o})}(t, r_*) = S_{\ell m}^{(\mathrm{o})}(t, r_*), \tag{2.20}$$

where the Regge-Wheeler potential and source have been defined, respectively, as [92, 3, 4]

$$V_{\ell m}^{RW}(r_*) \equiv A(r)\left(\frac{\lambda}{r^2} - \frac{6}{r^3}\right), \tag{2.21}$$

and [92]

$$S_{\ell m}^{(\mathrm{o})}(t, r_*) \equiv \frac{16\pi r}{\lambda - 2}\left[A(r)\,\partial_t T_r^{\ell m,(\mathrm{o})}(t, r_*) - \partial_{r_*} T_t^{\ell m,(\mathrm{o})}(t, r_*)\right]. \tag{2.22}$$

2.1.2 Sourced Zerilli equation

Following Refs. [92], we introduce the *Zerilli master function* as

$$\Psi_{\ell m}^{(e)}(t, r_*) = \frac{r}{\lambda\left[r(\lambda-2)+6\right]}\left(r\lambda\,\kappa_1 + 4rA^2(r)\,\kappa_2\right), \tag{2.23}$$

where the functions $\kappa_{1,2}$ are defined as

$$\begin{aligned}
\kappa_1 &\equiv K_{\ell m} + \frac{\lambda}{2}H_{\ell m} + A(r)\left(r\partial_r H_{\ell m} - \frac{2}{r}h_r^{\ell m,(e)}\right), \\
\kappa_2 &\equiv \frac{1}{2}h_{rr}^{\ell m,(e)} - A^{-1/2}(r)\partial_r\left[rA^{-1/2}(r)\left(K_{\ell m} + \frac{\lambda}{2}H_{\ell m}\right)\right].
\end{aligned} \tag{2.24}$$

Manipulating the linearized Einstein's equations Eq. (2.6) for the even-sector, it is possible to find that $\Psi_{\ell m}^{(\mathrm{e})}$ is solution of a second order partial differential equation in the variables (t, r_*), the *Zerilli master equation* [92]

$$\left[\partial_t^2 - \partial_{r_*}^2 + V_{\ell m}^{Z}(r_*)\right]\Psi_{\ell m}^{(\mathrm{e})}(t, r_*) = S_{\ell m}^{(\mathrm{e})}(t, r_*) \tag{2.25}$$

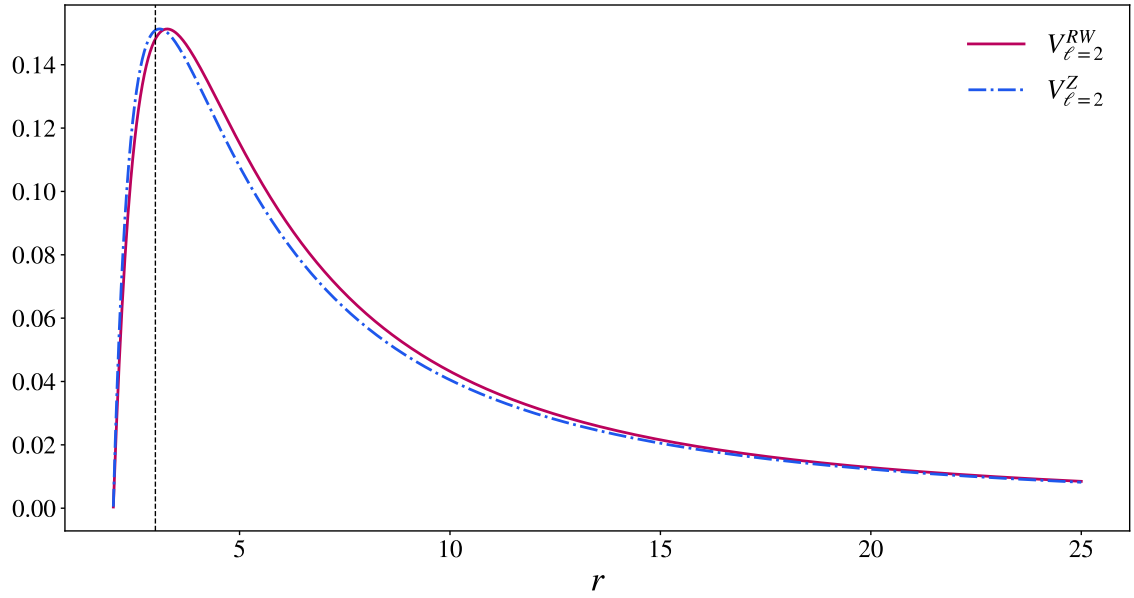

Figure 2.1: Regge-Wheeler (purple), Eq. (2.21), and Zerilli (blue, dot-dashed), Eq. (2.26), potentials vs the r-coordinate for $\ell = 2$, $\lambda = 6$.

where we have introduced the Zerilli potential as [92, 3, 4]

$$V^{Z}_{\ell m}(r_*) \equiv A(r)\frac{\lambda(\lambda-2)^2 r^3 + 6(\lambda-2)^2 r^2 + 36(\lambda-2)r + 72}{r^3\left[r(\lambda-2)+6\right]^2}\,, \tag{2.26}$$

and the source [92]

$$\begin{aligned} S^{(e)}_{\ell m}(t, r_*) \equiv -\frac{8\pi}{\lambda\left[r(\lambda-2)+6\right]}\Big\{ & A^2(r) r\left[2 + r(\lambda-4)\right] T^{\ell m,(e)}_{rr} + 2r^3 \partial_{r_*} T^{\ell m,(e)}_{tt} + \\ & \frac{2\lambda(3r-8)r - r^2\lambda^2 - 8r^2 + 68r - 108}{r(\lambda-2)+6} r T^{\ell m,(e)}_{tt} - 2r^3 A^2(r)\partial_{r_*} T^{\ell m,(e)}_{rr} + \\ & 4\lambda r A^2(r) T^{\ell m,(e)}_{r} + A^2(r)\left[2\left(1-\frac{3}{r}\right) - \lambda\right]\lambda T^{\ell m,(e)}_{2} + 4r^2 A^2(r) T^{\ell m,(e)}_{3}\Big\}\,. \end{aligned} \tag{2.27}$$

The Regge-Wheeler and Zerilli potentials, Eq. (2.21) and Eq. (2.26) respectively, share similar features, as shown in Fig. 2.1 for the case $\ell = 2$, $\lambda = 6$. Both $V^{\rm RW,Z}_{\ell m}$ are potential barriers with a peak near the light-ring $r \sim 3$, vanishing exponentially towards the horizon. Neither potential is compact at large distances; in fact, both decay as inverse polynomials in $r \gg 1$, with leading behavior given by the centrifugal barrier λr^{-2}.

2.1.3 Metric reconstruction

We consider an observer at rest in the *wave zone*, i.e. very far away from the source emitting the gravitational perturbation. Following Ref. [92], we define the tetrad e^{μ}_{a}, projecting into the observer's local inertial frame, as $\eta_{ab} = e^{\mu}_{a} e^{\nu}_{b} g^{0}_{\mu\nu}$ with $e^{\mu}_{a} = \text{diag}\left[-A^{-1/2}(r), A^{1/2}(r), r^{-1}, (r\sin\theta)^{-1}\right]$. Then, we apply this projection to the gravitational perturbations $h^{\ell m}_{\mu\nu}$. The goal is to write the master functions $\Psi^{(\rm e/o)}_{\ell m}(t, r)$ as

functions of the two polarizations $h_{+,\times}(t, r, \theta, \varphi)$ measured by the observer in the *transverse-traceless (TT) gauge*.

By definition, a TT tensor satisfies the following properties [111]

$$h^{(\mathrm{TT})}_{\mu 0} = 0 \ , \quad h^{(\mathrm{TT})}_{kk} = 0 \ , \quad h^{(\mathrm{TT})}_{ij} = h^{(\mathrm{TT})}_{ji} \ , \quad \partial_i h^{(\mathrm{TT})}_{ij} = 0 \, . \tag{2.28}$$

Only the radiative components of the metric perturbation can be written in a TT form. These components are characterized by the behavior $h \sim r^{-1}$ in the wave zone [111]. Hence, in the TT gauge it must hold, for $r \gg 1$

$$h^{\mathrm{TT}}_{\theta\phi} = h^{\mathrm{TT}}_{\theta\theta} = h^{\mathrm{TT}}_{\phi\phi} \sim \frac{1}{r} \ , \quad h^{\mathrm{TT}}_{\theta\theta} + h^{\mathrm{TT}}_{\phi\phi} \sim O(r^{-2}) \ , \quad h^{(\mathrm{TT})}_{\mu t}, h^{(\mathrm{TT})}_{\mu r} \sim O(r^{-2}) \, , \tag{2.29}$$

The TT-tensor components are related to the strain polarizations as [111]

$$h_+ = h^{(\mathrm{TT})}_{\theta\theta} = -h^{(\mathrm{TT})}_{\varphi\varphi} \ , \quad h_\times = h^{(\mathrm{TT})}_{\theta\varphi} = h^{(\mathrm{TT})}_{\varphi\theta} \, . \tag{2.30}$$

With these considerations, following Ref. [92], we can reconstruct the metric perturbation for the odd-sector perturbations.

We apply e^μ_a to the odd perturbations tensor $h^{\ell m,(\mathrm{o})}_{\mu\nu}$ in Eq. (2.14), yielding

$$h^{\ell m,(\mathrm{o})}_{ab} = \begin{pmatrix} 0 & 0 & -\frac{h^{\ell m,(\mathrm{o})}_0}{r} S_2(\theta,\varphi) & -\frac{h^{\ell m,(\mathrm{o})}_0}{r\sin\theta} S_2(\theta,\varphi) \\ * & 0 & \frac{h^{\ell m,(\mathrm{o})}_1}{r} S_2(\theta,\varphi) & \frac{h^{\ell m,(\mathrm{o})}_1}{r\sin\theta} S_2(\theta,\varphi) \\ * & * & -2\bar{h}^{\ell m} \frac{X^{\ell m}(\theta,\varphi)}{r^2\sin\theta} & \bar{h}^{\ell m} \frac{W^{\ell m}(\theta,\varphi)}{r^2} \\ * & * & * & 2\bar{h}^{\ell m} \frac{X^{\ell m}(\theta,\varphi)}{r^2\sin\theta} \end{pmatrix} + O\left(r^{-2}\right) . \tag{2.31}$$

Comparing the above with the conditions in Eq. (2.29), it must hold

$$h^{\ell m,(\mathrm{o})}_t, h^{\ell m,(\mathrm{o})}_r \sim O(r^{-1}) \ , \quad \bar{h}^{\ell m} \sim O(r) \, , \tag{2.32}$$

while the two polarizations in Eq. (2.30) can be found as

$$h^{\ell m,(\mathrm{o})}_\times = \frac{\bar{h}^{\ell m}(t, r_*)}{r^2} W^{\ell m}(\theta,\varphi) \ , \quad h^{\ell m,(\mathrm{o})}_+ = -\frac{\bar{h}^{\ell m}(t, r_*)}{r^2} \frac{X^{\ell m}(\theta,\varphi)}{\sin\theta} \, . \tag{2.33}$$

We have now related the variable $\bar{h}^{\ell m}$ to the $\times, +$ polarizations in the TT gauge. We are left with the task of relating the $\bar{h}^{\ell m}$ variable to the Regge-Wheeler master function $\Psi^{(o)}_{\ell m}$. To do so, we expand in $O(r^{-n})$ the $(t\phi)$-component of the linearized Einstein's equation in the odd sector, Eq. (2.19). At lowest order in $r \gg 1$ it holds

$$\partial_t \bar{h}^{\ell m} = A(r)\partial_r \left(r\Psi^{(\mathrm{o})}_{\ell m}\right) + h^{\ell m,(\mathrm{o})}_t \sim \partial_r \left(r\Psi^{(\mathrm{o})}_{\ell m}\right) + O\left(r^{-1}\right) . \tag{2.34}$$

Note that we have assumed a compact source for the stress-energy tensor, which vanishes at large distances from the BH. At large distances, we expect the gravitational perturbation to be a function of the retarded time $t - r_* \approx t - r$. As a consequence, it will hold $\partial_t \bar{h}^{\ell m} \approx -\partial_r \bar{h}^{\ell m}$. Since $\bar{h}^{\ell m} \sim O(r)$, we can neglect the subleading term $O(r^{-1})$ in Eq. (2.34) and write $\bar{h}^{\ell m} \simeq -r\Psi^{(\mathrm{o})}_{\ell m}$. We can then construct the odd-parity strain in terms of the two polarizations $h_{\times,+}$ from the master function $\Psi^{(\mathrm{o})}_{\ell m}$ as

$$\left(h^{\ell m,(\mathrm{o})}_+ - i h^{\ell m,(\mathrm{o})}_\times\right) = i\sqrt{\frac{(\ell+2)!}{(\ell-1)!}} \frac{\Psi^{(\mathrm{o})}_{\ell m}(t, r_*)}{r} {}_{-2}Y^{\ell m}(\theta,\varphi) + O\left(r^{-2}\right) , \tag{2.35}$$

where we have introduced the spin-weight −2 spherical harmonics as

$$ {}_{-2}Y^{\ell m}(\theta,\varphi) = \sqrt{\frac{(\ell-2)!}{(\ell+2)!}}\left(W^{\ell m} - i\frac{X^{\ell m}}{\sin\theta}\right). \tag{2.36} $$

We now repeat this procedure for the even sector. We apply the tetrad e^{μ}_{a} to the even perturbations tensor $h^{\ell m,(\mathrm{e})}_{\mu\nu}$ and we impose Eq. (2.29), yielding

$$ h^{\ell m,(\mathrm{e})}_{tt},\, h^{\ell m,(\mathrm{e})}_{rr},\, h^{\ell m,(\mathrm{e})}_{tr} \sim O(r^{-2}) \;\;,\;\; h^{\ell m,(\mathrm{e})}_{t},\, h^{\ell m,(\mathrm{e})}_{r} \sim O(r^{-1}) \;\;,\;\; H^{\ell m} \sim O(r^{-1}) \;\;,\;\; K^{\ell m} \sim O(r^{-2}). \tag{2.37} $$

The two polarizations can be written in terms of the quantity $H^{\ell m}$ as

$$ h^{\ell m,(\mathrm{e})}_{\times} = H^{\ell m}(t,r_*)\,\frac{X_{\ell m}(\theta,\varphi)}{2\sin\theta} \;\;,\;\; h^{\ell m,(\mathrm{e})}_{+} = H^{\ell m}(t,r_*)\,\frac{W_{\ell m}(\theta,\varphi)}{2}. \tag{2.38} $$

We expand $\kappa_{1,2}$ as defined in Eqs. (2.24) assuming the wave-zone behaviors in Eq. (2.37), yielding

$$ \begin{aligned} \kappa_1 &\simeq \frac{\lambda}{2}H^{\ell m} + r\partial_r H^{\ell m}, \\ \kappa_2 &\simeq -\frac{\lambda}{4}\partial_r(rH^{\ell m}). \end{aligned} \tag{2.39} $$

Substituting into Eq. (2.23), it is possible to find $\Psi^{(\mathrm{e})}_{\ell m} \simeq rH^{\ell m}$. Then, the Zerilli master function $\Psi^{(\mathrm{e})}_{\ell m}$ and the +, × polarizations are related through the following equation

$$ \left(h^{\ell m,(\mathrm{e})}_{+} - i\,h^{\ell m,(\mathrm{e})}_{\times}\right) = \sqrt{\frac{(\ell+2)!}{(\ell-2)!}}\frac{\Psi^{(\mathrm{e})}_{\ell m}(t,r_*)}{r}\,{}_{-2}Y^{\ell m}(\theta,\varphi) + O(r^{-2}). \tag{2.40} $$

Results for the odd, Eq. (2.35), and the even, Eq. (2.40), sectors can be combined to yield

$$ (h_+ - i\,h_\times) = \sum_{\ell,|m|\le\ell}\sqrt{\frac{(\ell+2)!}{(\ell-2)!}}\frac{1}{r}\left(\Psi^{(\mathrm{e})}_{\ell m} + i\,\Psi^{(\mathrm{o})}_{\ell m}\right){}_{-2}Y^{\ell m}(\theta,\varphi) + O(r^{-2}). \tag{2.41} $$

2.1.4 Energy and angular momentum fluxes

To define energy and angular momentum carried by the gravitational perturbation $h_{\mu\nu}$, a separation in the typical scales of $g^0_{\mu\nu}$, $h_{\mu\nu}$ is needed [111, 3, 4]. For instance, let L be the characteristic length of the background $g^0_{\mu\nu}$ and Λ the typical wavelength of the GWs perturbation $h_{\mu\nu}$, such that the condition $\Lambda/L \ll 1$ holds. It is then possible to define the gravitational-wave energy density through the tensor [3, 4] $\langle t^{\mu\nu}\rangle$, obtained by averaging the Landau-Lifshits stress-energy pseudo-tensor $t^{\mu\nu}$ [112] over several wavelengths Λ.

The energy flux dE/dt through a 2-sphere at $r \gg 1$ carried by the gravitational waves, can be written as [3, 4]

$$ \frac{dE}{dt} = \int d\Omega \left\langle t^{00}\right\rangle = \frac{r^2}{16\pi}\int d\Omega \left\langle |\dot{h}_+(t,r_*)|^2 + |\dot{h}_\times(t,r_*)|^2\right\rangle, \tag{2.42} $$

where the integration is performed along the full solid angle and we have denoted with $(\dot{\cdot})$ differentiation with respect to the time coordinate t. Substituting Eq. (2.41) into Eq. (2.42), we can rewrite the energy flux in terms of the Regge-Wheeler and Zerilli master functions [92]

$$\frac{dE}{dt} = \frac{1}{16\pi} \sum_{\ell,|m|\leq\ell} \frac{(\ell+2)!}{(\ell-2)!} \left\langle |\dot{\Psi}^{(\mathrm{e})}_{\ell m}(t, r_*)|^2 + |\dot{\Psi}^{(\mathrm{o})}_{\ell m}(t, r_*)|^2 \right\rangle . \tag{2.43}$$

The angular momentum flux dJ/dt is related to the $(r\phi)$-component of the GWs stress-energy tensor $\langle t^{\mu\nu} \rangle$, in particular it is possible to write [92]

$$\frac{dJ}{dt} = \frac{1}{32\pi} \sum_{\ell,|m|\leq\ell} \frac{(\ell+2)!}{(\ell-2)!} \left\langle im \left[\dot{\Psi}^{(\mathrm{e})}_{\ell m} \left(\Psi^{(\mathrm{e})}_{\ell m}\right)^* + \dot{\Psi}^{(\mathrm{o})}_{\ell m} \left(\Psi^{(\mathrm{o})}_{\ell m}\right)^* \right] + \text{c.c.} \right\rangle , \tag{2.44}$$

where we have used $(\,\cdot\,)$ + c.c. to denote that we sum the quantity $(\,\cdot\,)$ with its complex conjugate $(\,\cdot\,)^*$.

2.2 Green's function method

We define the Green's function (GF) associated with the Regge-Wheeler/Zerilli differential operators $\partial_t^2 - \partial_{r_*}^2 - V_{\ell m}(r)$ through

$$\left[\partial_t^2 - \partial_{r_*}^2 + V_{\ell m}(r_*)\right] G_{\ell m}(t - t'; r_*, r'_*) = \delta(t - t')\delta(r_* - r'_*) . \tag{2.45}$$

with the condition $G(t - t'; r_*, r'_*) = 0$ if $t < t'$, due to causality. The GF gives information on how a perturbation which is impulsive in both variables of the partial differential equation, i.e. localized at a certain event (t', r'_*), *propagates* on the curved (fixed) background towards the observer at (t, r_*). Assume now to have a superposition of N impulsive contributions localized at different events (t^i, r^i_*), each with a different amplitude $S(t^i, r^i_*)$. The contribution of each source propagates towards the observer in a different way, as encoded in the relative GF, $G(t - t^i; r_*, r^i_*)$. The general solution will then be a sum of the source impulsive contributions, each weighted with the corresponding GF.

Heuristically, we can consider a generic, extended source as a superposition of $N \to \infty$ impulsive sources, each with a different amplitude $S(t', r')$ and localized at different locations (t', r'). The general solution, then, as we take the continuous limit $N \to \infty$, can be written in terms of the convolution integral

$$\Psi(t, r_*) = \int_{-\infty}^{\infty} dt' \int_{-\infty}^{\infty} dr'_* G(t - t'; r_*, r'_*) S(t', r'_*) . \tag{2.46}$$

To solve Eq. (2.45), it is convenient to define a Fourier (anti-)transform and switch to (time t) frequency ω domain as

$$\mathcal{F}\phi = \tilde{\phi}(\omega, r) \equiv \int_{-\infty}^{\infty} dt\, e^{i\omega(t-t')} \phi(t, r) \quad , \quad \mathcal{F}^{-1}\tilde{\phi} = \phi(t, r) = \frac{1}{2\pi} \int_{-\infty}^{\infty} d\omega\, e^{-i\omega(t-t')} \tilde{\phi}(\omega, r) . \tag{2.47}$$

Note that, from now on, we will label with a $(\tilde{\cdot})$ the quantities in the ω-domain. We apply the transform operator $\mathcal{F}$ on Eq. (2.45) to reduce the partial differential equation to an ordinary differential equation. Remembering that the Dirac delta function can be represented as $\delta(t - t') = (2\pi)^{-1} \int_{-\infty}^{\infty} d\omega\, e^{-i\omega(t-t')}$, we obtain

$$\left[-\partial_{r_*}^2 - \omega^2 + V_{\ell m}(r)\right] \tilde{G}_{\ell m}(\omega; r_*, r'_*) = \delta(r_* - r'_*) . \tag{2.48}$$

The general solution of the above equation can be written as

$$\tilde{G}_{\ell m}(\omega; r_*, r'_*) = \theta(r_* - r'_*)\tilde{u}^{\rm out}_{\ell m}(\omega; r_*)\frac{\tilde{u}^{\rm in}_{\ell m}(\omega; r'_*)}{\mathrm{W}_{\ell m}(\omega; r'_*)} + \theta(r'_* - r_*)\tilde{u}^{\rm in}_{\ell m}(\omega; r_*)\frac{\tilde{u}^{\rm out}_{\ell m}(\omega; r'_*)}{\mathrm{W}_{\ell m}(\omega; r'_*)}\,, \tag{2.49}$$

where $\tilde{u}^{\rm in,out}_{\ell m}(\omega; r_*)$ are solutions of the homogeneous problem associated with Eq. (2.48), i.e.

$$\left[-\partial^2_{r_*} - \omega^2 + V_{\ell m}(r)\right]\tilde{u}_{\ell m}(\omega; r_*) = 0\,, \tag{2.50}$$

with the following boundary conditions

$$\tilde{u}^{\rm in}_{\ell m}(\omega, r_*) = \begin{cases} e^{-i\omega r_*} \quad , & r_* \to -\infty \\ A_{\rm in}(\omega)e^{-i\omega r_*} + A_{\rm out}(\omega)e^{i\omega r_*} \quad , & r_* \to \infty \end{cases}\,, \tag{2.51}$$

$$\tilde{u}^{\rm out}_{\ell m}(\omega, r_*) = \begin{cases} B_{\rm in}(\omega)e^{-i\omega r_*} + B_{\rm out}(\omega)e^{i\omega r_*} \quad , & r_* \to -\infty \\ e^{i\omega r_*} \quad , & r_* \to \infty \end{cases}\,. \tag{2.52}$$

The Wronskian of these solutions is $\mathrm{W}_{\ell m}(\omega; r_*)$ and has the following definition

$$\mathrm{W}_{\ell m}(\omega; r_*) = \tilde{u}^{\rm out}_{\ell m}(\omega; r_*)\partial_{r_*}\tilde{u}^{\rm in}_{\ell m}(\omega; r_*) - \tilde{u}^{\rm in}_{\ell m}(\omega; r_*)\partial_{r_*}\tilde{u}^{\rm out}_{\ell m}(\omega; r_*)\,. \tag{2.53}$$

The Schwarzschild GF problem was first addressed by Leaver [14], who analytically proved that the BH spectral response in the (complex) ω domain can be divided into three distinct contributions: an infinite set of isolated simple poles, a branch cut and a high-frequency response. In the time domain, these contributions translate, respectively, into a superposition of exponentially damped oscillatory modes, the *quasi-normal modes*, an inverse power-law decay, the *tail*, and a Heaviside function-like component, the *prompt response*.

In the following sections, we will show how to compute the GF for each of the contributions mentioned above, following the seminal works [14, 15, 106, 107, 18].

2.2.1 Quasi-normal modes Green's function

As shown in Eq. (2.49), to construct the GF, it is first necessary to compute the homogeneous solutions $\tilde{u}^{\rm in,out}_{\ell m}$ associated with the problem in Eq. (2.48) with the boundary prescriptions Eqs. (2.51) and (2.52). To this end, it is useful to rewrite the homogeneous equation Eq. (2.50) in the r coordinate. Note that, to ease the notation, we will temporarily drop the $(\,\cdot\,)_{\ell m}$ indices.

Due to the simpler expression of the Regge-Wheeler potential, compared with the Zerilli one, we will focus on the former. Results for the Zerilli modes can be obtained either using the same framework, or mapping the odd results into the even sector exploiting Chandrasekhar's transformation theory [113].The homogeneous Regge-Wheeler equation in ω-domain, in terms of the r coordinate, reads [105]

$$r(r-2)\frac{d^2}{dr^2}\tilde{u}(\omega; r) + 2\frac{d}{dr}\tilde{u}(\omega; r) + \left[\frac{\omega^2 r^3}{r-2} - \lambda + \frac{6}{r}\right]\tilde{u}(\omega; r_*) = 0\,. \tag{2.54}$$

This is a generalized spheroidal wave equation, characterized by two regular and one irregular singular points, at $r = 0, 2$ and $r = \infty$ respectively [104]. Different types of solutions to this equation have been computed, as infinite expansions around different singular points; a detailed analysis on the subject was provided by Leaver [105, 14]. Here we focus on the solution proposed in Ref. [14] to describe the QNMs response as an infinite expansion near the horizon $r = 2$, characterized both by a purely ingoing wave (in r_*) behavior at the horizon and a purely outgoing one (in r_*) at infinity

$$\lim_{r\to 2} \tilde{u} \propto e^{-2i\omega \log(r/2-1)} \quad , \quad \lim_{r\to+\infty} \tilde{u} = e^{i\omega\left[r+2\log(r/2)\right]} \simeq e^{i\omega r_*} \,. \tag{2.55}$$

This solution has the following ansatz [104]

$$\tilde{u}_h(\omega; r_*(r)) = \mathrm{N}_h(\omega) e^{i\omega r_*} \left(\frac{r-2}{r}\right)^{-4i\omega} \sum_{k=0}^{\infty} a_k(\omega) \left(1 - \frac{2}{r}\right)^k \,, \tag{2.56}$$

where $\mathrm{N}_h(\omega)$ is a normalization factor reinforcing the boundary condition of outgoing plane wave with unitary amplitude $\tilde{u}_h \to e^{i\omega r_*}$ in the limit $r_* \to \infty$, and is equal to $\mathrm{N}_h(\omega) = (\sum_k a_k)^{-1}$. Moreover, in the limit $r \to 2$, it holds

$$\tilde{u}_h \simeq \left[e^{4i\omega} a_0 \mathrm{N}_h(\omega)\right] \cdot e^{-2i\omega - 2i\omega \log(r/2-1)} \simeq \left[e^{4i\omega} a_0 \mathrm{N}_h(\omega)\right] \cdot e^{-i\omega r_*} \equiv \mathrm{N}^{-1}_{h,\mathcal{H}^+} \cdot e^{-i\omega r_*} \,. \tag{2.57}$$

In the above equation, we have defined the ratio between an ingoing unitary plane wave at the horizon $e^{-i\omega r_*}$ and the solution $\tilde{u}_h$, as $\mathrm{N}_{h,\mathcal{H}^+}$.

Substituting Eq. (2.56) into Eq. (2.54) yields a recurrence equation for the expansion coefficients $\{a_k(\omega)\}_k$ [104]

$$\begin{aligned} &a_0 = 1 \,, \\ &\alpha_0 a_1 + \beta_0 a_0 = 0 \,, \\ &\alpha_k a_{k+1} + \beta_k a_k + \gamma_k a_{k-1} = 0 \quad , \quad k \geq 1 \,. \end{aligned} \tag{2.58}$$

with

$$\begin{aligned} \alpha_k(\omega) &= k^2 + (2 - 4i\omega)k - 4i\omega + 1 \,, \\ \beta_k(\omega) &= -2k^2 - (2 - 16i\omega)k + 16\omega^2 + 8i\omega - \lambda + 6 \,, \\ \gamma_k(\omega) &= k^2 - 8i\omega k - 8\omega^2 - 7 \,. \end{aligned} \tag{2.59}$$

We define the polynomial $F(\omega)$ as the *infinite continued fraction*

$$F(\omega) \equiv \cfrac{-\gamma_1}{\beta_1 - \cfrac{\alpha_1\gamma_2}{\beta_2 - \cfrac{\alpha_2\gamma_3}{\beta_3 - \dots}}} \tag{2.60}$$

It is possible to show [104, 114] that there exist a set of complex frequencies $\{\omega_n\}_n$, the quasi-normal frequencies (QNFs), such that

$$F(\omega_n) = -\frac{\beta_0(\omega_n)}{\alpha_0(\omega_n)} \,. \tag{2.61}$$

Then, substituting into the second of Eq. (2.58), a_1 can be computed, and from the third equation all the other coefficients can be derived. At the QNFs the series in Eq. (2.56) *converges uniformly* [104, 105], i.e.

as a function (at least C^0) in r. The solutions Eq. (2.56) at the QNFs $\{\omega_n\}_n$ are called quasi-normal modes (QNMs).

Following Ref. [14], we introduce two other solutions with different boundary conditions. The ansatze for these solutions are the following [14]

$$\tilde{u}_{\infty\pm}(\omega; r_*(r)) = (4\omega)^{\mp 2i\omega} e^{\pm i\phi_\pm} \left(\frac{r-2}{r}\right)^{-2i\omega} \sum_{L=-\infty}^{\infty} b_L \left[G_{L+\nu}(-2\omega, \omega r) \pm i F_{L+\nu}(-2\omega, \omega r)\right] , \tag{2.62}$$

where $F_{L+\nu}(-2\omega, \omega r)$, $G_{L+\nu}(-2\omega, \omega r)$ are Coulomb wave functions as defined in Ref. [115] with $\eta = -2\omega\,, \rho = \omega r$ and

$$\phi_\pm = \pm i \, \log\left\{ \sum_{L=-\infty}^{\infty} b_L \left[\frac{\Gamma(L+\nu+1-2i\omega)}{\Gamma(L+\nu+1+2i\omega)}\right]^{\pm 1/2} e^{\mp i\frac{L+\nu}{2}\pi} \right\} . \tag{2.63}$$

The coefficients b_L in Eq. (2.62) satisfy a three terms recursive equation similar to Eq. (2.58), but with different coefficients α_L, β_L and γ_L, now functions of $\nu(\omega)$ for each ω, whose explicit expression can be found in Ref. [14]. For a generic ω, in the limit $r \to \infty$, the Coulomb wave functions can be approximated as [115]

$$F_{L+\nu}(-2\omega, \omega r) \pm i G_{L+\nu}(-2\omega, \omega r) \simeq e^{\pm i\omega\left(r+2\log(r/2)\right)} \cdot e^{\pm i\left[2\omega\log(4\omega) - \frac{L+\nu}{2}\pi + \arg\Gamma(L+\nu-2i\omega)\right]} . \tag{2.64}$$

The solutions $\tilde{u}_{\infty\pm}$ in Eq. (2.62) are a purely outgoing ($\tilde{u}_{\infty+} \simeq e^{i\omega r_*}$) and ingoing ($\tilde{u}_{\infty-} \simeq e^{-i\omega r_*}$) unitary plane wave at $r \to \infty$, respectively. Note that the Coulomb wave function $G_{L+\nu}(-2\omega, \omega r)$ is singular for $\omega = 0$ and, when computed on complex frequencies, is a multi-valued function of ω [115]. As a consequence, to evaluate it on the complex ω plane, it is necessary to introduce a branch cut with branch point at the origin.

Following [14], we focus on the QNMs and express the solutions $\tilde{u}^{\rm in,out}(\omega; r_*)$ defined in Eqs. (2.51) and (2.52), in terms of $\tilde{u}_h$, $\tilde{u}_{\infty\pm}$ for $\omega = \omega_n$. Given the boundary prescription in Eq. (2.51), we can write

$$\tilde{u}^{\rm in}(\omega; r_*) = A_{\rm in}(\omega)\tilde{u}_{\infty-}(\omega; r_*) + A_{\rm out}(\omega)\tilde{u}_{\infty+}(\omega; r_*) \quad , \quad \tilde{u}^{\rm out}(\omega; r_*) = \tilde{u}_{\infty+}(\omega; r_*) . \tag{2.65}$$

The Wronskian Eq. (2.53), computed in the limit $r_* \to \infty$, is given by

$$\mathrm{W}(\omega) = -2i\omega A_{\rm in}(\omega) . \tag{2.66}$$

By definition, at the QNFs $\{\omega_n\}_n$ the homogeneous solution $\tilde{u}^{\rm in}$ is purely ingoing (outgoing) at the horizon (infinity) and can be expressed as in Eq. (2.56), i.e. $\tilde{u}^{\rm in}(\omega_n; r_*) \equiv \mathrm{N}_{h,\mathcal{H}^+}\tilde{u}_h(\omega_n; r_*)$. Hence, at the QNFs, the conditions $A_{\rm in}(\omega_n) = 0$ and $\mathrm{N}_{h,\mathcal{H}^+}(\omega_n)\tilde{u}_h(\omega_n; r_*) \equiv A_{\rm out}(\omega_n)\tilde{u}_{\infty+}(\omega_n; r_*)$ hold and the Wronskian vanishes. The quantity $A_{\rm out}(\omega_n)$ can be computed explicitly comparing Eqs. (2.56) and (2.62) in the limit $r \to \infty$, yielding [14]

$$A_{\rm out}(\omega_n) = \mathrm{N}_{h,\mathcal{H}^+}(\omega_n) = e^{-4i\omega_n} \sum_{k=0}^{\infty} a_k . \tag{2.67}$$

To switch to the time domain, it is necessary to perform an anti-transform as in Eq. (2.47). The integral for the t-domain GF reads

$$G(t-t'; r_*, r'_*) = \int_{\Gamma_1} d\omega \, \frac{ie^{-i\omega(t-t')}}{4\pi\omega A_{\rm in}(\omega)} \left[\theta(r_* - r'_*)\tilde{u}^{\rm in}(\omega; r'_*)\tilde{u}_{\infty+}(\omega; r_*) + \theta(r'_* - r_*)\tilde{u}^{\rm in}(\omega; r_*)\tilde{u}_{\infty+}(\omega; r'_*)\right] . \tag{2.68}$$

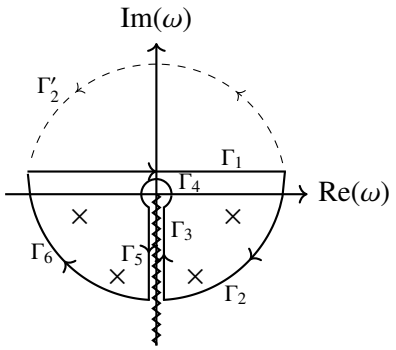

Figure 2.2: Schematic representation of the complex-frequencies plane relative to the integrand in Eq. (2.68). The zig-zagged line is the branch cut, and the crosses are the simple poles of the integrand. Thick and dashed lines represent two possible closed contours: $\Gamma_1 + \Gamma_2'$ and $\Gamma_1 + \Gamma_2 + \Gamma_3 + \Gamma_4 + \Gamma_5 + \Gamma_6$. Figure taken from Ref. [1].

In the above equation, Γ_1 indicates that we are integrating over the whole real axis, i.e. for $\omega \in (-\infty, \infty)$ with $\omega \in$ Re. However, the integrand has a singularity in $\omega = 0$; hence, to compute the integral, we perform an analytical continuation to complex frequencies ω. At an operational level, we shift Γ_1 parallel to the Re(ω) axis, at Im(ω) $= \epsilon \ll 1$, as shown in Fig. 2.2 [14, 15]. The integrand in Eq. (2.68) has a rich structure in the complex Im(ω) < 0 half plane: there is an infinite set of complex frequencies $\{\omega_n\}_n$, the QNFs, at which the Wronskian vanishes yielding isolated regular poles. Along the negative imaginary axis Re(ω) $= 0$, Im(ω) < 0, there is a branch cut, originating from the branch point in $\omega = 0$. Following Leaver [14], the time-domain GF can be separated to account for each of these different contributions

$$G(t-t';r_*,r'_*) = G_F(t-t';r_*,r'_*) + G_{\rm QNMs}(t-t';r_*,r'_*) + G_{\rm BC}(t-t';r_*,r'_*) \tag{2.69}$$

The term $G_{\rm BC}(t-t';r_*,r'_*)$ is given by the integration along the branch cut

$$G_{\rm BC}(t-t';r_*,r'_*) = -\left[\int_{\Gamma_3} d\omega\, \tilde{G}(\omega;r_*,r'_*) + \int_{\Gamma_4} d\omega\, \tilde{G}(\omega;r_*,r'_*) + \int_{\Gamma_5} d\omega\, \tilde{G}(\omega;r_*,r'_*)\right]. \tag{2.70}$$

As we will show in detail in Sec. 2.2.2, this contribution is characterized by an inverse power-law behavior in the retarded time, denoted as *late-time tail*.

The term $G_F(t-t';r_*,r'_*)$ in Eq. (2.69) is the contribution of the high-frequency arcs Γ_2 and Γ_6

$$G_{\rm F}(t-t';r_*,r'_*) = -\left[\int_{\Gamma_2} d\omega\, \tilde{G}(\omega;r_*,r'_*) + \int_{\Gamma_6} d\omega\, \tilde{G}(\omega;r_*,r'_*)\right]. \tag{2.71}$$

As detailed in Sec. 2.2.3, it is common in the literature [14, 15] to assume that this contribution is responsible for the *prompt response*, i.e. the initial propagation of the perturbation right towards an observer placed at large distances.

Finally, the $G_{\rm QNMs}(t-t';r_*,r'_*)$ term in Eq. (2.69) is the contribution to the integral given by the isolated poles in Fig. 2.2, the QNFs $\{\omega_n\}_n$. For frequencies approaching the QNFs, it is possible to Taylor expand the Wronskian as [14]

$$\mathrm{W}(\omega) = -2i\omega A_{\rm in}(\omega) \simeq -2i\omega_n(\omega-\omega_n)\frac{dA_{\rm in}(\omega_n)}{d\omega} \tag{2.72}$$

Under this expansion, the QNFs appear to be first-order isolated poles of the integrand $\tilde{G}(\omega; r_*, r'_*)$, hence, their contribution to the time-domain GF is given by the *residue theorem* [14]

$$G_{\rm QNMs}(t-t'; r_*, r'_*) = -2\pi i \sum_{n=0,s=\pm} \text{Res}\left[\tilde{G}(\omega; r_*, r'_*)\right] = \sum_{n=0,s=\pm} B_{n,s} \cdot e^{-i\omega_{n,s}(t-t')} \tilde{u}_h(\omega_{n,s}; r'_*)\tilde{u}_h(\omega_{n,s}; r_*)\,, \tag{2.73}$$

where we have defined the *geometric excitation coefficients* $B_{n,s}$ as

$$B_{n,s} \equiv \mathrm{N}_{h,\mathcal{H}^+}(\omega_{n,s}) \frac{1}{2\omega_{n,s}\,\alpha_{n,s}} \quad , \qquad \alpha_{n,s} \equiv \left.\frac{dA_{\rm in}(\omega)}{d\omega}\right|_{\omega=\omega_{n,s}} . \tag{2.74}$$

The notation in Eq. (2.73) is such that n identifies QNFs with the same imaginary component, while s differentiates between modes with positive ($s = +$) real frequency or negative ($s = -$) one, i.e. $\omega_{n,-} = -\omega^*_{n,+}$. Modes with $s = -$ are denoted *mirror modes*.

For a Schwarzschild BH, the odd and even sectors are *isospectral*: they are characterized by the same spectrum of QNFs.

2.2.2 Tails

The contribution of the branch cut in Fig. 2.2 to the time domain GF was investigated in Refs. [14, 15], under the assumptions of large distances $r \gg 1$ and small frequencies $\omega \ll 1$. Ref. [106] carried out the computation for real frequencies under the same assumptions, but without the analytical continuation in the complex plane, and obtained an equivalent result.

Starting from the homogeneous RW equation in ω-domain Eq. (2.54), we perform a field redefinition as $\tilde{u}(\omega; r_*) = A^{-1/2}(r) y(\omega; r)$ [15], yielding

$$r^2(r-2)^2 \frac{d^2}{dr^2} y_\ell(\omega; r) + \left[r^4\omega^2 - \lambda r^2 + 2r(\lambda+4) - 15\right] y_\ell(\omega; r) = 0\,, \tag{2.75}$$

We approximate this equation in the large-distance limit $r \gg 1$, neglecting all terms which decay faster than $O(r^{-2})$ [106]

$$\frac{d^2}{dr^2} y_\ell(\omega; r) + \left[\omega^2 + \frac{4\omega^2}{r} + \frac{12\omega^2 - \lambda}{r^2}\right] y_\ell(\omega; r) = 0\,, \tag{2.76}$$

Introducing the new variable $\rho = \omega r$ and expanding the equation above in the limit $\omega \ll 1$, keeping corrections up to $O(\omega)$, we obtain the following result [106]

$$\frac{d^2}{d\rho^2} y_\ell(\omega; r(\rho,\omega)) + \left[1 - \frac{2\eta}{\rho} - \frac{\lambda}{\rho^2}\right] y_\ell(\omega; r(\rho,\omega)) = 0\,, \tag{2.77}$$

with $\eta = -2\omega$. Eq. (2.77) is called *Coulomb wave equation* [115] and its solutions are the Coulomb wave functions $F_\ell(\eta;\rho)$ and $G_\ell(\eta;\rho)$. We are interested in a solution which is purely outgoing at $\rho \to \infty$, that we will denote $y^{\rm out}$, and a solution which is regular at $\rho \simeq 0$, denoted $y^{\rm in}$ [106]

$$\begin{aligned} y^{\rm in}_\ell(\omega; r(\rho,\omega)) &= F_\ell(\eta,\rho) = \frac{2^\ell |\Gamma(\ell+1+i\eta)|}{\Gamma(2\ell+2)} \rho^{\ell+1} e^{-i\rho} M(\ell+1-i\eta, 2\ell+2, 2i\rho)\,, \\ y^{\rm out}_\ell(\omega; r(\rho,\omega)) &= G_\ell(\eta,\rho) + iF_\ell(\eta,\rho)\,, \end{aligned} \tag{2.78}$$

where $M(a,b;z)$ is the Kummer's function [115].

To simplify the computation, we will assume that the initial-data, or the generic matter perturbations, are compact and do not extend towards the observer $r_* > r'_*$, in particular we will assume $r_* \gg r'_*$ and separate the scales of the observer and the source by imposing $\omega r \gg 1$ and $\omega r' \ll 1$ respectively. The $u_\ell^{\rm in,out}(\omega; r_*)$ solutions in the GF expression Eq. (2.49) are related to $y_\ell^{\rm in,out}$ through $u_\ell^{\rm in,out}(\omega; r_*) = (r-2)^{-2i\omega} r^{2i\omega} y_\ell^{\rm in,out}(\omega; r)$. Reinforcing the large distances approximation $r, r' \gg 1$ for both $\tilde{u}^{\rm in,out}$ modes, we approximate $u_\ell^{\rm in,out}(\omega; r_*) \approx y_\ell^{\rm in,out}(\omega, \omega, r)$. Note that, in doing this approximation, our formalism is no longer able to "see" the horizon at $r = 2$. The Wronskian of $\tilde{u}_\ell^{\rm in,out}(\omega; r_*)$ can be computed, in the large $r_* \to \infty$ limit, as [115]

$$\mathrm{W}(\omega) \equiv \omega \left[G_\ell(\eta,\rho) \frac{dF_\ell(\eta,\rho)}{d\rho} - F_\ell(\eta,\rho) \frac{dG_\ell(\eta,\rho)}{d\rho} \right] = \omega \,, \tag{2.79}$$

In the limits $\omega r \gg 1$ and $\omega r' \ll 1$, $u^{\rm in}(\omega; r'_*)$ and $u^{\rm out}(\omega; r_*)$ can be expanded as [14, 106]

$$\begin{aligned} u_\ell^{\rm in}(\omega; r'_*) &\simeq \frac{2^\ell e^{\pi\omega} |\Gamma(\ell+1-2i\omega)|}{\Gamma(2\ell+2)} (r'\omega)^{\ell+1} \,, \\ u_\ell^{\rm out}(\omega; r_*) &\simeq e^{i\omega r_*} \cdot e^{2i\omega \log(2\omega)} \cdot e^{-i\pi\ell/2} \cdot e^{i \arg\Gamma(\ell+1-2i\omega)} \,, \end{aligned} \tag{2.80}$$

Substituting into the GF expression in frequency domain in Eq. (2.49) and expanding in the limit $\omega \ll 1$ neglecting orders $O(\omega^2)$, it holds [106]

$$\tilde{G}(\omega; r_*, r'_*) = \frac{2^\ell (-i)^\ell \ell!}{(2\ell+1)!} \omega^\ell (r')^{\ell+1} e^{i\omega r_*} \cdot \left[1 + 2i\omega \log(4\omega) + \pi\omega - 2i\omega\gamma(\ell+1) \right] , \tag{2.81}$$

where $\gamma(\ell+1)$ is the digamma function of (integer) argument $\ell+1$. The Green's function in the time domain can be found using the anti-transform defined in Eq. (2.47)

$$G(t-t'; r_*, r'_*) = \frac{1}{2\pi} \int_{-\infty}^{\infty} d\omega \, \frac{2^\ell (-i)^\ell \ell!}{(2\ell+1)!} \omega^\ell (r')^{\ell+1} e^{-i\omega(t-t'-r_*)} \cdot \left[1 + 2i\omega \log(4\omega) - 2i\omega\gamma(\ell+1) \right] . \tag{2.82}$$

However, the logarithm $\log(\omega)$ is not defined along the full real axis, but only for $\omega > 0$, and is singular at the origin $\omega = 0$. Hence, to perform the anti-Fourier transform in Eq. (2.82), we analytically continue to complex frequencies ω. The (now complex) logarithm is a multi-valued function, introducing a branch cut along the negative imaginary axis which originates at the branch point $\omega = 0$. The structure of the integrand in Eq. (2.82) in the complex ω-plane is the same as what is shown in Fig. (2.2), with the exception that now the integrand does not have any isolated simple pole. We shift the real axis at $\mathrm{Im}(\omega) = \epsilon \ll 1$ and perform the integration by means of the residue theorem, along the thick contour shown in Fig. 2.2, under the late times assumptions $t - t' - r_* \gg 1$ [14]. Due to the absence of residuals inside the closed contour, it holds

$$\begin{aligned} G(t-t'; r_*, r'_*) = \frac{1}{2\pi} \int_{\Gamma_1} d\omega \, e^{-i\omega(t-t')} \tilde{G}(\omega; r_*, r'_*) = \\ - \frac{1}{2\pi} \left[\int_{\Gamma_3} d\omega \, e^{-i\omega(t-t')} \tilde{G}(\omega; r_*, r'_*) + \int_{\Gamma_5} d\omega \, e^{-i\omega(t-t')} \tilde{G}(\omega; r_*, r'_*) \right] . \end{aligned} \tag{2.83}$$

The contributions coming from the arcs Γ_2, Γ_6 vanish due to Jordan's lemma: the integrand asymptotes to a null value for $|\omega| \to \infty$ on the lower-half of the complex plane $\mathrm{Im}(\omega) < 0$.

The single-valued terms in Eq. (2.82) cancel out when integrated along both sides of the branch cut. The term proportional to the complex logarithm, that we denote $f(\omega)\log\omega$, becomes $f(\omega)\left(\log\omega + 2\pi i\right)$ when evaluated on the left side of the branch cut [14, 15]. As a consequence, the integral of $f(\omega)\log\omega$ along Γ_3 and Γ_5 is equal to [14, 15]

$$\begin{aligned} G(t-t';r_*,r'_*) = -\frac{1}{2\pi}\left[\int_{\Gamma_3} d\omega\, e^{-i\omega(t-t')}\tilde{G}(\omega;r_*,r'_*) + \int_{\Gamma_5} d\omega\, e^{-i\omega(t-t')}\tilde{G}(\omega;r_*,r'_*)\right] = \\ -\frac{1}{2\pi}2\pi i\int_{-i\infty}^{0} d\omega\, e^{-i\omega(t-t')}f(\omega)\,. \end{aligned} \tag{2.84}$$

This integral yields the following result [14]

$$G_{\rm BC}(t-t';r_*,r'_*) = \frac{(-1)^{\ell+1}2^{\ell+1}\ell!(\ell+1)!}{(2\ell+1)!}\frac{(r')^{\ell+1}}{(t-r_*-t')^{\ell+2}}\,. \tag{2.85}$$

This is the time-domain GF propagating the late-time response of a Schwarzschild BH to an external perturbation, usually denoted as *radiative tail* [14], as observed at very large distances $r_* \to \infty$.

It is possible to find a non-radiative tail if we place the observer closer to the source of the radiation. In particular, we still consider $r \gg 1$, but instead of assuming $\omega r \gg 1$, we impose $\omega r \ll 1$ [14]. We consider $u^{\rm in}(\omega;r'_*)$ as in Eq. (2.80), but we construct $u^{\rm out}(\omega;r_*)$ from $y^{\rm out}(\omega;r(\rho,\omega))$ in Eq. (2.78) as [14]

$$\begin{aligned} u^{\rm out}(\omega;r_*) =& G_\ell(\eta(\omega),\rho(\omega,r_*)) + iF_\ell(\eta(\omega),\rho(\omega,r_*)) \simeq \\ & -\frac{2^\ell\ell!}{(\ell+1)!}4i\omega\log(\omega)(r\omega)^{\ell+1} + O(\omega^2) + \text{single valued}\,. \end{aligned} \tag{2.86}$$

The ω-domain GF is then

$$\tilde{G}(\omega;r_*,r'_*) = -\left[\frac{2^\ell\ell!}{(\ell+1)!}\right]^2 2i\left(rr'\right)^{\ell+1}(\omega)^{2\ell+2}\log(\omega) + \text{single valued}\,. \tag{2.87}$$

The time domain GF can be found in the late times limit $t-t' \gg 1$, with the same contour used in Eq. (2.83), with the high-frequency arcs $\Gamma_{2,6}$ contributions vanishing due to Jordan's lemma. The difference along the two sides of the branch cut gives a factor $2\pi i$ in the multi-valued piece in Eq. (2.87), while the single-valued contributions cancel out and the integral reduces to [14]

$$G_{\rm BC}(t-t';r_*,r'_*) = \left[\frac{2^\ell\ell!}{(\ell+1)!}\right]^2 2(-1)^{\ell+1}(2\ell+2)!\frac{(rr')^{\ell+1}}{(t-t')^{3+2\ell}}\,. \tag{2.88}$$

This Green's function propagates the late-time response of a Schwarzschild BH to an external perturbation, as observed at a finite distance r_*. Equation (2.88) is the propagator of *Price's law* [16, 17, 14] as will be discussed in more detail in Sec. 2.3.2.

If the observer is located at $\mathcal{I}^+$, the approximation $\omega r \gg 1$ is valid at any time and, as a consequence, the late-time signal is always dominated by the radiative tail in Eq. (2.85). If the observer is placed at a finite distance, there is an initial transient δt such that $r_* \gg \delta t$ and the approximation $\omega r_* \gg 1$ holds. As a consequence, this transient is dominated by the radiative tail. At later times, however, $\omega r_* \ll 1$ and Price's law dictates the perturbed Schwarzschild spacetime relaxation. In particular, Leaver [14] estimated the radiative tail to be the dominant inverse power-law behavior until $t-t'-r_*+r'_* \ll r_*$, while for $t \gg r_*$ Price's law is dominant.

2.2.3 Prompt response

Leaver [14] suggested that the contribution to the GF coming from the high-frequencies arcs, $G_{\rm F}$ in Eq. (2.71), propagates the initial radiation observed at times $t' + |r_* - r'_*| \lesssim t \lesssim t' + r_* + r'_*$, but did not compute this contribution explicitly. Later, Andersson [15] gave a first estimate of the high-frequency arcs contribution to the full GF, working in large ω and large r, r' limit, focusing on a scalar field. As a result, he proposed [1]

$$G_{\rm F}(t - t'; r_*, r'_*) = \frac{1}{2}\theta\left(t - r_* - t' + r'_*\right) . \tag{2.89}$$

In Chapter 8, we show numerical experiments solving for the gravitational field GF, stressing that the prompt response has a non-constant functional form not captured by Eq. (2.89), even for $r, r' \gg 1$.

An interesting computation for this part of the signal was performed by Barack [107, 18] in the time domain, for an observer placed at null infinity $\mathcal{I}^+$, assuming compact initial data localized outside the potential barrier. Following Ref. [107, 18], under these assumptions, it is possible to approximate the potential in the Regge-Wheeler/Zerilli equations as

$$V_0(r_*) \equiv \begin{cases} \frac{\lambda}{4r_*^2} \ , & r_* \geq r_{*,0} \, , \\ 0 \ , & r_* < r_{*,0} \, . \end{cases} \tag{2.90}$$

In the above, $r_{*,0}$ is a typical scale set near the peak of the (real) potential, close to the light-ring. The field is then solved in an iterative expansion: the lowest order corresponds to compact initial data $\Psi(u = u_0, v) = 0$, $\Psi(u, v = 0) = \zeta(u)$ propagated by a GF approximating the prompt response one. Higher orders are sourced by corrections to the potential $\delta V \equiv V(r) - V_0(r)$. The approximated prompt response GF is the solution to the problem

$$\partial_u \partial_v G_{\rm F}(u, v; u', v') + V_0(r) G_{\rm F}(u, v; u', v') = \delta(u - u')\delta(v - v') \, , \tag{2.91}$$

where u, v are the Eddington-Finkelstein coordinates defined in Eq. (2.4).

We consider a compact initial-data source localized in the region $r_* > r_{*,0}$ and focus on the response observed at $\mathcal{I}^+$ for $u' \leq u \leq v' - 2r_0$ (I-region in Ref. [18]), corresponding to the times when the prompt-response dominate the signal according to Leaver [14], $t' + r_* - r'_* < t < t' + r'_* + r_* - 2r_{*,0}$.

Following Barack [107, 18], the GF propagating this response is $G_{\rm F}(u, v; u', v') = \theta(u - u')\theta(v - v')\bar{G}_{\rm F}(u, v; u', v')$, where

$$\partial_u \partial_v \bar{G}_{\rm F}(u, v; u', v') + \frac{\lambda}{(v - u)^2} \bar{G}_{\rm F}(u, v; u', v') = 0 \ , \quad u \geq u' \ , \quad v \geq v' \, , \tag{2.92}$$

with boundary conditions $\bar{G}_{\rm F}(u', v'; u', v') = 1$. The solution to this problem is [107, 18]

$$\bar{G}_{\rm F}(u, v; u', v') = \sum_{n=0}^{\ell} \frac{(2\ell - n)!}{n!\ell!(\ell - n)!} \frac{1}{(v' - u')^{\ell}(v - u)^{\ell - n}} \frac{d^n}{du^n} \left[(v' - u)(u - u')\right]^{\ell} \, . \tag{2.93}$$

The initial assumptions are such that the GF in Eq. (2.93) is not informed (yet) of the potential V_0 structure inside $r_{*,0}$. As a consequence, this GF is essentially Minkowski's propagator.

[1] Note that Andersson [15] assumed $t' = 0$ in his computations. Here we are considering his computations in a more generic case: while for an initial-data problem we are always free to impose $t' = 0$, if we were to convolve the GF with a generic source, it would not be possible to fix t'.

2.3 Initial data problem: numerical and analytical past results

In Sec. 2.1, we have derived the master equations governing the response of a Schwarzschild BH to an external perturbation, in terms of two field variables $\Psi^{(\mathrm{o,e})}$ directly related to the strain cross and plus polarization as observed very far away from the source. In this section, we restrict the focus on perturbations of a Schwarzschild BH (SBH) in vacuum, i.e. we assume $T^{\mu\nu} = 0$ and consider perturbations generated by some initial data (ID) imposed on a Cauchy hypersurface $t = t'$. Problem Eqs. (2.20), (2.25) translates in an homogeneous equation with ID prescriptions

$$\left[\partial_t^2 - \partial_{r_*}^2 + V(r)\right]\Psi(t, r_*) = 0\,, \tag{2.94}$$

$$\Psi(t = t', r_*) \equiv \psi(r_*) \quad , \quad \partial_t\Psi(t = t', r_*) = \zeta(r_*)\,. \tag{2.95}$$

This problem can be solved using the Green's function method. The first step is to move in the frequency domain through a Fourier transform, as defined in Eq. (2.47). Integrating by parts, it is possible to show that

$$\begin{aligned}\mathcal{F}\left[\partial_t\Psi(t, r_*)\right] &= -i\omega\tilde{\Psi}(\omega; r_*) + \psi(r_*)\,,\\ \mathcal{F}\left[\partial_t^2\Psi(t, r_*)\right] &= \zeta(r_*) - i\omega\psi(r_*) - \omega^2\tilde{\Psi}(\omega; r_*)\,.\end{aligned} \tag{2.96}$$

Hence, applying the Fourier transform operator to the homogeneous problem Eq. (2.94) with ID Eq. (2.95), yields a non-homogeneous problem in the ω-domain

$$\left[-\partial_{r_*}^2 - \omega^2 + V(r)\right]\tilde{\Psi}(\omega; r_*) = i\omega\psi(r_*) - \zeta(r_*) \tag{2.97}$$

The solution to this equation is computed by convolution of the ω-domain GF with the initial-data ω-domain source

$$\tilde{\Psi}(\omega; r_*) = \int_{-\infty}^{\infty} dr'_*\, \tilde{G}(\omega; r_*, r'_*)\left[i\omega\psi(r'_*) - \zeta(r'_*)\right]\,. \tag{2.98}$$

To switch to t-domain, it is sufficient to anti-transform Eq. (2.98), as in Eq. (2.47).

Equations. (2.94), (2.95) are equivalent to the following problem [14]

$$\left[\partial_t^2 - \partial_{r_*}^2 + V(r)\right]\Psi(t, r_*) = -\psi(r_*)\partial_t\delta(t - t') - \zeta(r_*)\delta(t - t') \equiv S^{\mathrm{ID}}(t - t', r_*)\,, \tag{2.99}$$

$$\Psi(t = t', r_*) \equiv 0 \quad , \quad \partial_t\Psi(t = t', r_*) = 0\,. \tag{2.100}$$

In fact, the general solution of Eqs. (2.99), (2.100) can be found though the t-domain GF as

$$\begin{aligned}\Psi(t, r_*) = &\int_{-\infty}^{\infty} dt'' \int_{-\infty}^{\infty} dr'_*\, G(t - t''; r_*, r'_*)\left[-\psi(r'_*)\partial_{t''}\delta(t'' - t') - \zeta(r_*)\delta(t'' - t')\right] =\\ &\int_{-\infty}^{\infty} dr'_* \left[\psi(r'_*)\partial_{t''}G(t - t''; r_*, r'_*)\Big|_{t''=t'} - \zeta(r_*)G(t - t'; r_*, r'_*)\right]\,,\end{aligned} \tag{2.101}$$

which is equivalent to the anti-Fourier transform of Eq. (2.98). This result implies that we can consider an ID problem in vacuum as a non-homogeneous problem with null ID, Eq. (2.100), driven by a source with a specific time dependence, prescribed in Eq. (2.99).

In this section, we review some important results, both numerical and analytical, for QNMs and tails in the context of initial data problems. In Chapters 7 and 5, we generalize the discussion to perturbations induced by a test-particle source.

2.3.1 Quasi-normal modes

Vishveshwara [39] studied the scattering of a Gaussian packet from a SBH, numerically at first-order in the perturbations, showing that the signal observed at $\mathcal{I}^+$ is a superposition of spaced peaks: an oscillatory response with exponentially damped amplitude. This is the first work in which QNMs have been observed. Moreover, Ref. [39] found that the spacing between the peaks (as well as the number of resolved peaks) is highly dependent on the width a of the Gaussian packet, and it saturates once this width is comparable with the BH size $a \sim 1$. This result suggests that QNMs are generated close to the BH and are strictly connected to the potential barrier *peak*.

This hypothesis was further investigated by Ferrari and Mashhoon [116, 117], under the *eikonal limit* $\ell \gg 1$ and approximating the *real* potentials of Eq. (2.20), (2.25) with a *Poshl-Teller* potential. The Poshl-Teller potential is, by definition, a symmetric potential barrier of width α centered at the maximum of the real potential, $r_{*,0}$, vanishing exponentially towards the horizon and at large distances [116, 117]

$$V_{\rm PT}(r) \equiv \frac{V_0}{\cosh^2\left[\alpha(r_* - r_{*,0})\right]}\,, \tag{2.102}$$

where the parameters α, V_0 are estimated from the real potential as [116, 117]

$$\alpha^2 \equiv -\frac{1}{2V_0}\frac{d^2V}{dr_*^2}\bigg|_{r_*=r_{*,0}}\,, \quad V_0 \equiv V_{RW/Z}(r_* = r_{*,0})\,. \tag{2.103}$$

This scheme yields the following approximated expression for the QNFs [116, 117]

$$\omega_{\ell\gg1,n} \simeq \pm\sqrt{V_0 - \frac{\alpha^2}{4}} - i\,\alpha\left(n+\frac{1}{2}\right) \simeq \frac{1}{3\sqrt{3}}\left[\pm\left(\ell+\frac{1}{2}\right) - i\left(n+\frac{1}{2}\right)\right]. \tag{2.104}$$

These results are consistent with Leaver's computations [104] for QNF with $\ell \gg 1$, reinforcing that, at least in this limit, the peak of the potential is indeed the only relevant feature.

Working with the GF formalism, Leaver [104, 14] introduced an analytical framework to isolate and investigate the ringing portion of the signal $\Psi^{\rm QNMs}$

$$\Psi^{\rm QNMs}_{\ell m}(t, r_*) = \sum_{n=0,s=\pm} c_{\ell mns}\cdot e^{-i\omega_{\ell mns}(t-r_*)}\,. \tag{2.105}$$

The terms $c_{\ell mns}$ are denoted *excitation coefficients* and yield the (constant) amplitude of each QNM present in the BH response to an external perturbation. The $c_{\ell mns}$ are factor of two terms: the geometrical excitation coefficients $B_{\ell mns}$ in Eq. (2.74), and the overlap between the QNM eigenfunction in Eq. (2.56) and the initial data source in Eq. (2.97)

$$c_{\ell mns} \equiv B_{\ell mns}\, e^{i\omega_{\ell mns}t'}\int_{-\infty}^{\infty} dr'_*\,\tilde{u}_h(\omega_{\ell mns}; r'_*)\cdot\left[i\omega_{\ell mns}\psi(r'_*) - \zeta(r'_*)\right]. \tag{2.106}$$

Note that, in Eq. (2.105), the QNMs propagation appears to be instantaneous, whereas any signal must travel on or inside the light-cone. In fact, it was argued by Leaver [14] that Eq. (2.105) is only valid after some time. In particular, given the central role of the potential barrier peak in the QNMs generation, Leaver [14] and many subsequent works, e.g. [118, 119], considered the QNMs excitation as a *scattering*

process. A Gaussian-like perturbation is initialized at r'_* outside the light-ring at time t'. A portion of this perturbation travels directly to the observer at $r_* > r'_*$, $r_* \gg 1$, yielding the signal denoted as prompt response [14, 15, 18]. A portion of the initial perturbation travels from r'_* towards the BH and, once it reaches the potential barrier peak $r_* \approx 0$, generates a QNMs response traveling towards the observer at r_*. Hence, the observer at r_* sees the QNMs response approximately after a time $t \gtrsim t' + r'_* + r_*$ [14, 118, 119]. This condition (heuristically) describes inside which portion of the curved light-cone the QNMs propagate, assuming a compact source located outside the potential barrier peak.

Refs. [14, 118] also considered the case in which an initial perturbation is extended inside the light-ring and is not compact (i.e. it does not vanish fast enough) at the horizon. In this case, the integral in the definition of the excitation coefficients $c_{\ell mns}$, Eq. (2.106), is (in general) divergent for the overtones $n > 1$, since the QNMs radial functions $\tilde{u}_h \to \infty$ for $r_* \to -\infty$. Refs. [14, 118] introduced a regularization scheme to compute this integral, but did not discuss properly how a perturbation initialized inside the light-ring can escape towards $\mathcal{I}^+$, i.e. over which portion of the light-ring this signal propagates. Following [14, 118], the first step of the regularization procedure consists of splitting the integral in Eq. (2.106) into two different contributions as

$$c_{\ell mn} = B_{\ell mn} e^{i\omega_{\ell mn} t'} \left[\int_{r_{*,0}}^{\infty} dr_* \, \tilde{u}_h(\omega_{\ell mn}; r_*) \, \tilde{S}(\omega_{\ell mn}; r_*) + \int_{-\infty}^{r_{*,0}} dr_* \, \tilde{u}_h(\omega_{\ell mn}; r_*) \, \tilde{S}(\omega_{\ell mn}; r_*) \right] . \tag{2.107}$$

In the above, we are considering a generic ω-domain source $\tilde{S}(\omega; r_*)$ for the perturbations. For an ID problem, $\tilde{S}(\omega; r_*) = i\omega\psi(r_*) - \zeta(r_*)$, however, the formalism is general and can be applied to any extended source that can be Fourier transformed. If we assume a source which is compact in the limit $r_* \to \infty$, the first term on the right-hand side of Eq. (2.107) is regular, and can be discarded from the present discussion. For simplicity, we will work with the Schwarzschild coordinate r instead of the tortoise coordinate r_*. Assuming that the source $\tilde{S}(\omega; r_*(r))$ can be expanded in series near the horizon $r = 2$, since $\tilde{u}_h$ in Eq. (2.56) is by definition a near-horizon expansion, it is possible to rewrite the second integral in Eq. (2.107) as [118]

$$\int_{-\infty}^{r_{*,0}} dr_* \, \tilde{u}_h(\omega_n; r_*) \, \tilde{S}(\omega_n; r_*) = \int_2^{r_0} dr \sum_{k=k_0}^{\infty} \xi_k(\omega_n) \, (r-2)^{k-2i\omega_n} \, . \tag{2.108}$$

In the above, k_0 is an integer and accounts for the behavior of the source near the horizon; terms in the sum with k such that $k - 2|\mathrm{Im}(\omega_n)| > 0$ are regular as $r \to 2$ and their integral is

$$\int_2^{r_0} dr \sum_{k-2|\mathrm{Im}(\omega_n)|>0} \xi_k(\omega_n) \, (r-2)^{k-2i\omega_n} = \sum_{k-2|\mathrm{Im}(\omega_n)|>0} \xi_k(\omega_n) \, \frac{(r-2)^{k+1-2i\omega_n}}{k+1-2i\omega_n} \, . \tag{2.109}$$

For the terms with $k - 2|\mathrm{Im}(\omega_n)| < 0$ the integral Eq. (2.108) can be computed though an analytical continuation of the r coordinate [14, 118]. Note, however, that there is no clear prescription describing when a signal emitted inside the light-ring, possibly extending towards the horizon, reaches $\mathcal{I}^+$. We will come back to this point in Chapter 7, where we detailed the regularization procedure in Refs. [14, 118] and compare it against some of the original results of this manuscript.

Among past ID-driven results, it is important to mention Ref. [41] as the first work that took into account the light-cone propagation of QNMs, yielding a formula with time-dependent amplitudes. This work,

however, does not consider a SBH but is restricted to a simplified geometry, in which the master function describing linear order perturbations satisfies an equation like Eqs. (2.20) and (2.25), with potential approximated by a delta-function centered at the peak of the real potential, $V_\delta \equiv V_0\delta(r_*)$. This simplified model mimics the fundamental mode excitation in the Schwarzschild case: there are no late-time tails and there is only one QNM, with frequency dictated by the height of the potential barrier $\omega = -iV_0/2$ [120, 41]. In this case, the time domain GF can be computed exactly, yielding [41]

$$G(t-t';r_*,r'_*) = G_{\rm F}(t-t';r_*,r'_*) + G_{\rm QNM}(t-t';r_*,r'_*)\,, \tag{2.110}$$

with [41]

$$\begin{aligned} G_{\rm F}(t-t';r_*,r'_*) &= -\frac{1}{2}\left[\theta\left(t-t'-|r_*-r'_*|\right)-\theta\left(t-t'-|r_*|-|r'_*|\right)\right]\,,\\ G_{\rm QNM}(t-t';r_*,r'_*) &= -\frac{1}{2}\theta\left(t-t'-|r_*|-|r'_*|\right)\,\exp\left[-\frac{1}{2}V_0\left(t-t'-|r_*|-|r'_*|\right)\right]\,. \end{aligned} \tag{2.111}$$

Given some initial data, the observable contribution to the BH response propagated by the QNMs GF $G_{\rm QNM}(t-t';r_*,r'_*)$ is given by [41]

$$\Psi_{\rm QNM}(t,r_*) = \theta\left(t-|r_*|\right)\,c_0(t,r_*)\,e^{-\frac{V_0}{2}(t-|r_*|)}\,, \tag{2.112}$$

where $c_0(t,r_*)$ is the *time-dependent QNM amplitude*, obtained from the initial data source in Eq. (2.99) as

$$c_0(t,r_*) = \frac{1}{2}\int_{|r_*|-t}^{t-|r_*|} dr'_*\left[\zeta(r'_*) - \frac{V_0}{2}\psi(r'_*)\right]\,. \tag{2.113}$$

The time dependence of the QNM amplitude originates from the Heaviside function in Eq. (2.111), necessary to reinforce causality: to see a signal at (t,r_*), the observer must wait for the initial data to propagate on the background. If the initial data is extended, it will not reach the observer all at once. As shown in Ref.[41], another interesting consequence of the causality condition in Eq.(2.111) is that the QNM portion of the signal in Eq. (2.112) asymptotes to a late-time constant, instead of a constant-amplitude QNM, for sigmoid-like initial data asymptotically constant at the horizon.

We will return to causality considerations regarding the QNM propagation in a Schwarzschild background in Chapter 7 to extend the results presented in this section to the case of a test particle infalling into a BH driving the perturbations. We will show that causality implies the automatic regularization of the retarded QNMs GF for $r_* \to -\infty$, introducing a non-oscillating new behavior strictly related to the presence of an event horizon.

2.3.2 Tails

Price was the first to analytically investigate the late-time signal emitted by a perturbed Schwarzschild BH. In Ref. [121, 17], he focused on the collapse of a scalar field into a BH and found that the late-time signal emitted by such system behaves as $t^{-2\ell-3-a}$, with $a = 0,\,1$ for an initially stationary, static scalar perturbations, commonly denoted as Price's law. Gundlach, Price and Pullin performed numerical

simulations for the scalar collapse, both linear [122] and non linear [123], verifying in both cases Price's analytical predictions.

The original result of Price [17] was re-obtained through the Green's function method by Leaver [14], who found a new, radiative, tail signal as inverse power-law in the retarded time $u^{-\ell-2-a}$ with $a = 0, 1$ for stationary, static ID, respectively. According to Leaver's analytical predictions, if the signal is observed at finite distances, the radiative tail only dominates the initial late-time response, eventually leaving place to Price's law, as discussed in Sec. 2.2.2. If the signal is observed at $\mathcal{I}^+$, the late-time response is dominated only by the radiative tail, and Price's law is not present in the signal at any time.

The radiative tail observed at $\mathcal{I}^+$ was investigated through numerical simulations first in Ref. [124] by Burko and Ori and later by Zenginoglu [125, 126]. Zenginoglu [125, 126], also studied the transition from a radiative tail-dominated behavior to Price's law as a function of the observer distance from the source of gravitational radiation. Numerical results of Refs. [125, 126] validate the predictions of Leaver [14]: the further the observer, the longer the time-scale over which the radiative tail dominates the signal before giving way to Price's law. Interestingly, Ref. [125] estimated that astrophysical sources probed by current and future detectors are located so far away that we can focus only on the radiative tail and discard Price's law contribution to the signal. This implies approximating the detectors as being placed at $\mathcal{I}^+$, as far as tail observations are concerned. For instance, Ref. [125] estimated that for a source at a distance of $\sim 10^4 M$ (close, relative to sources usually observed), the late-time response is approximated by the radiative tail over a time-scale of $\sim 10^5 M$.

Finally, it is worth mentioning other works that computed both the radiative tail and Price's law using the GF methods, but in the time domain. In particular, Barack [107, 18, 127] found the radiative tail as propagation of the O(G) corrections to the approximated background potential in Eq. (2.90), convolved with the flat space time GF in Eq. (2.93).

Poisson [89] found the GF for Price's law in the time domain, in a post-Minkowskian fashion, by means of a perturbative expansion in O(G). Notably, Ref. [89] showed that Price's law GF does not depend on the symmetries of the background but only on its asymptotic structure: the late-time tail GF is the same for a Kerr or a Schwarzschild spacetime. These results were later generalized in Ref. [128] for generic corrections to the potentials in Eq. (2.21), (2.26) behaving as $\sim r^{-\alpha}$. Ref. [128] analytically proved that any correction with $\alpha > 2$ leaves, at leading order, the late-time tail unaffected. Through a series of numerical experiments, Ref. [128] showed instead that for $0 < \alpha < 2$ the late-time signal is affected at leading order.

Other works have computed corrections to the tail propagator, either considering generic potentials as in Ref. [129, 130], or computing higher-order corrections to the large distances approximation [15, 131].

We will return to tails in Chapters 5, 6 to discuss how this signal is excited in binary black hole mergers, focusing first on the perturbative case of a test particle in a SBH and later extending the results on the late-time relaxation following a non-linear, comparable masses BH merger.

Chapter 3

Relativistic two-body problem

In this chapter, we focus on the relative motion of two black holes (BHs) of masses m_1, m_2 as predicted by General Relativity, commonly denoted as the *relativistic two-body problem*. We define the *mass-ratio* q and the *symmetric mass-ratio* η as

$$q \equiv \frac{m_2}{m_1} \quad , \quad \eta \equiv \frac{m_1 m_2}{(m_1 + m_2)^2} \quad , \quad m_1 \leq m_2 \, , \tag{3.1}$$

with $M \equiv (m_1 + m_2)$ total mass of the binary. We differentiate between two cases: the *extreme mass-ratio* (EMR) limit $q \gg 1$ and the *comparable masses* case $q \gtrsim 1$.

In the EMR limit, the small BH can be approximated, to lowest order, as a test particle of mass $\mu \equiv M\eta$ orbiting a fixed curved background, generated by the massive companion. During its evolution, the test particle emits gravitational waves: this signal is a correction to the background metric, hence it will induce corrections to the test-particle orbit. In particular, the test particle loses energy and angular momentum by gravitational waves (GWs) emission, and its (bounded) orbit shrinks in time.

During the initial stage of the binary evolution, the *back-reaction* on the trajectory acts on a large timescale with respect to the orbital motion itself. As a consequence, the orbit evolves *adiabatically* and, at each time, it is possible to find an osculating geodesic which describes the particle motion [9]. We denote this portion of the orbital evolution as *inspiral*.

At a certain distance from the black hole, depending on the test-particle initial energy and angular momentum, the trajectory is osculated by the last stable orbital configuration and, at later times, no stable configurations exist anymore. We denote this portion of the trajectory as *transition to plunge*; the *plunge* is the last segment of the orbital evolution, ending with the test particle approaching the horizon. During the plunge, the orbital motion is fast, almost unaffected by the radiation reaction and can be approximated as quasi-geodesic [9, 10] (see also e.g. Sec. III.A of [74]).

In this chapter, we review some basic techniques used to solve the general relativistic two-body problem along different portions of the orbit. We focus on the EMR limit, and investigate the motion of a test particle of mass μ on top of the background generated by a Schwarzschild BH (SBH), Eq. (5.1). Note, however, that some of the methods we will discuss are general and can be applied to comparable-mass systems.

In Sec. 3.1 we introduce the geodesics equation of motion of the test particle, through the Hamiltonian formalism. In Sec. 3.1.1, we discuss the different possible orbital configurations, depending on the initial energy and angular momentum of the test particle. In Sec. 3.2 we give an overview of the semi-analytical methods to compute the radiation reaction driving the dynamics during the inspiral, while in Sec. 3.3 we briefly discuss the transition to plunge. We will implement the methods introduced in this chapter to evolve generic planar orbits in Chapters 5 and 7. In Sec. 3.4, we give details on the specific radiation reaction used in those chapters, to obtain the original results of this thesis.

The discussion in Sec. 3.1 is based on the textbook Ref. [4], while the discussion of Sec. 3.2 and Sec. 3.3 is mainly based on Refs. [132, 133, 3].

3.1 Geodesic Hamiltonian equations of motion

We work in Schwarzschild coordinates, but we replace the r-coordinate with the tortoise one r_* as defined in Eq. (2.3) $(t, r_*, \theta, \varphi)$. The Lagrangian density governing the test-particle motion is

$$\mathcal{L}(x^\mu, \dot{x}^\mu) = \frac{\mu}{2} g^0_{\mu\nu} \frac{dx^\mu}{d\tau}\frac{dx^\nu}{d\tau} = -\frac{\mu}{2}A(r)\left(u^t\right)^2 + \frac{\mu}{2}A(r)\,(u^{r_*})^2 + \frac{\mu}{2}r^2\left(u^\theta\right)^2 + \frac{\mu}{2}r^2\sin^2\theta\,(u^\varphi)^2\,, \tag{3.2}$$

with μ mass of the test particle. In the above, τ is the affine parameter for the curve $x^\mu(\tau)$ so that $u^\mu \equiv dx^\mu/d\tau$ is the four-velocity of the test particle, $g^0_{\mu\nu}$ is the Schwarzschild metric Eq. (5.1), written in terms of r_*

$$ds^2 = -A(r)dt^2 + A(r)dr_*^2 + r^2\left(d\theta^2 + \sin\theta\, d\varphi^2\right)\,. \tag{3.3}$$

The Lagrangian density is a function of the variables x^μ and their derivatives with respect to the affine parameters u_μ. We want to move to Hamiltonian variables, i.e. x^μ and their conjugate momenta, defined as $\tilde{p}_\mu = \partial\mathcal{L}/\partial u^\mu$

$$\tilde{p}_t \equiv \frac{\partial\mathcal{L}}{\partial u^t} = -\mu\,A(r)\,u^t\;\;,\quad \tilde{p}_{r_*} \equiv \frac{\partial\mathcal{L}}{\partial u^{r_*}} = \mu\,A(r)\,u^{r_*}\;\;,\quad \tilde{p}_\theta \equiv \frac{\partial\mathcal{L}}{\partial u^\theta} = \mu\,r^2\,u^\theta\;\;,\quad \tilde{p}_\varphi \equiv \frac{\partial\mathcal{L}}{\partial u^\varphi} = \mu\,r^2\sin^2\theta\,u^\varphi\,. \tag{3.4}$$

We focus on planar orbit, hence we assume $\theta = \pi/2$, $\tilde{p}_\theta = 0$. Starting from the Lagrangian density Eq. (3.2) and the conjugate momenta in Eq. (3.4), we compute the test-particle Hamiltonian

$$\mathcal{H}(x^\mu, \tilde{p}_\mu) = u^\mu\tilde{p}_\mu - \mathcal{L}(x^\mu, u^\mu) = -\frac{1}{2\mu A(r)}\tilde{p}_t^2 + \frac{1}{2\mu A(r)}\tilde{p}_{r_*}^2 + \frac{1}{2\mu r^2}\tilde{p}_\varphi^2\,. \tag{3.5}$$

The equation of motion for the test particle, i.e. the geodesics, can be found from

$$\frac{dx^\mu}{d\tau} = \frac{\partial\mathcal{H}}{\partial\tilde{p}_\mu}\;\;,\quad \frac{d\tilde{p}_\mu}{d\tau} = -\frac{\partial\mathcal{H}}{\partial x^\mu}\,. \tag{3.6}$$

yielding

$$\frac{dt}{d\tau} = -\frac{\tilde{p}_t}{\mu A(r)}\;\;,\quad \frac{dr_*}{d\tau} = \frac{\tilde{p}_{r_*}}{\mu A(r)}\;\;,\quad \frac{d\varphi}{d\tau} = \frac{\tilde{p}_\varphi}{\mu r^2}\,, \tag{3.7}$$

for the variables, while for the momenta

$$\frac{d\tilde{p}_t}{d\tau} = 0\;\;,\quad \frac{d\tilde{p}_{r_*}}{d\tau} = \frac{1}{\mu r^2 A(r)}\left(-\tilde{p}_t^2 + \tilde{p}_{r_*}^2\right) + \frac{A(r)\tilde{p}_\varphi^2}{\mu r^3}\;\;,\quad \frac{d\tilde{p}_\varphi}{d\tau} = 0\,. \tag{3.8}$$

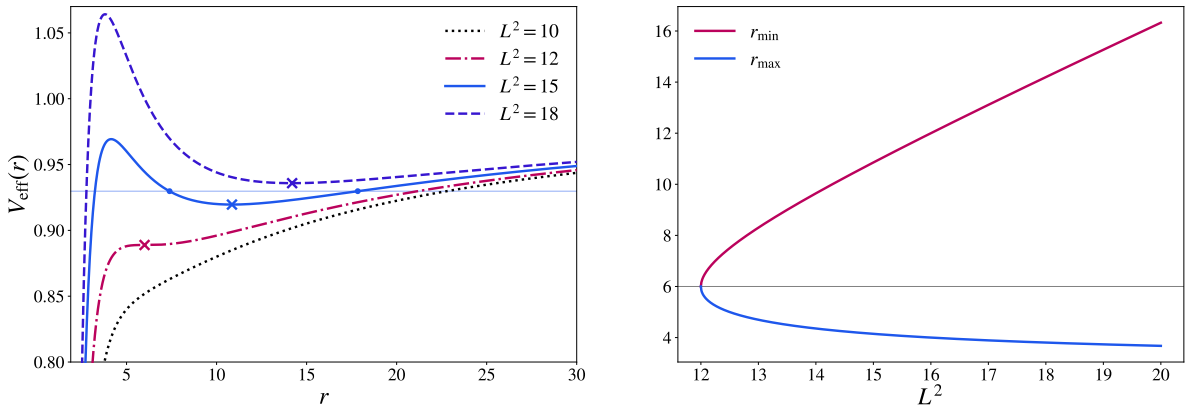

Figure 3.1: Left: Effective potential $V_{\rm eff}$ in Eq. (3.11) as function of r, for different values of L^2 as shown in the labels. Crosses indicate the minimum of the potential, if it exists. The horizontal line corresponds to the energy $\hat{H}^2$ that a test particle with $L^2 = 15$ must have to evolve along a bounded, eccentric orbit between $r_{\rm apo,peri}$, at which $V_{\rm eff}(r_{\rm apo,peri})$ takes the values indicated by the dots. Right: Location of the minimum $r_{\rm min}$ and maximum $r_{\rm max}$ of the potential with respect to the test-particle angular momentum L^2.

The quantities $\tilde{p}_t$, $\tilde{p}_\varphi$ are constants of the geodesic motion, associated with the two Killing vector fields of the Schwarzschild solution: $k^\mu = (1,0,0,0)$ and $m^\mu = (0,0,0,1)$. We will denote them as $\tilde{p}_t \equiv -H$, $\tilde{p}_\varphi \equiv \tilde{L}$ since, for a test particle very far away from the BH, these quantities can be interpreted as its energy and angular momentum, respectively.

It is possible to find a constraint equation that the momenta must satisfy, considering that a massive test particle travels along timelike curves, i.e. the four-velocity u^μ obeys the following equation

$$g^0_{\mu\nu} u^\mu u^\nu = -\frac{1}{A(r)}\left(\hat{H}^2 - p^2_{r_*}\right) + \frac{p^2_\varphi}{r^2} = -1\,. \tag{3.9}$$

where we have introduced the μ-rescaled momenta and energy as $p_\mu \equiv \tilde{p}_\mu/\mu$, $\hat{H} \equiv H/\mu$, respectively.

We can rewrite equations Eqs. (3.7) and (3.8) in terms of derivatives with respect to the time coordinate t, that we indicate through the notation $(\dot{\cdot}) \equiv d(\cdot)/dt$, as

$$\begin{aligned}
\dot{r}_* &= \frac{p_{r_*}}{\hat{H}} \equiv \frac{v_r}{A(r)}\,,\\
\dot{\varphi} &= \frac{A(r)}{r^2\hat{H}} p_\varphi \equiv \omega\,,\\
\dot{p}_{r_*} &= \frac{A(r)}{r^2\hat{H}}\left[-1 + p_\varphi \frac{-3+r}{r^2}\right],\\
\dot{p}_\varphi &= 0\,.
\end{aligned} \tag{3.10}$$

In the above, we have defined radial and angular orbital velocities as v_r and ω, respectively.

3.1.1 Planar orbits

The expression in Eq. (3.9) allows to write the energy in terms of a kinetic term and an *effective potential* $V_{\rm eff}(r)$

$$\hat{H}^2 = V_{\rm eff}(r) + p_{r_*}^2 \quad , \quad V_{\rm eff}(r) \equiv A(r)\left(1 + \frac{L^2}{r^2}\right), \tag{3.11}$$

where $L \equiv \tilde{L}/\mu$ is the angular momentum of the test particle per unit mass μ. For each L, $V_{\rm eff}(r)$ has a fixed radial profile. As an example, we show in Fig. 3.1, the shape of the effective potential $V_{\rm eff}(r)$, for $L^2 = 10, 12, 15, 18$. Then, different orbital configurations are possible depending on the test-particle energy E.

We can compute the stationary points of the potential in Eq. (3.11) by analyzing the behavior of its first derivative

$$\frac{dV_{\rm eff}(r)}{dr} = 0 \;\; \rightarrow \;\; r_{\rm min} = \frac{L^2}{2}\left(1 + \sqrt{1 - \frac{12}{L^2}}\right) \;\; , \;\; r_{\rm max} = \frac{L^2}{2}\left(1 - \sqrt{1 - \frac{12}{L^2}}\right). \tag{3.12}$$

For $L^2 < 12$, $V_{\rm eff}(r)$ has no stationary points, hence a test particle coming from infinity (i.e. $E \geq 1$) with $\dot{r} \leq 0$ is captured and falls directly into the BH.

The case $L^2 = 12$ corresponds to $r_{\rm min} \equiv r_{\rm max}$ being a stable inflection point of the effective potential $V_{\rm eff}$. As a consequence, a test particle with $\hat{H}^2 = V_{\rm eff}(r_{\rm min})$ at $r = r_{\rm min}$ moves along a stable circular orbit. A test particle initialized at finite distances with $V_{\rm eff}(r_{\rm min}) < \hat{H}^2 < 1$ and $\dot{r} \geq 0$ initially moves outwards from the BH. However, it eventually reaches a turning point, defined as

$$r \equiv r_{\rm TP} \;\; | \;\; \hat{H}^2 = V_{\rm eff}(r_{\rm TP}) \;\; , \;\; \dot{r}(r_{\rm TP}) = 0\,, \tag{3.13}$$

where it is scattered by the potential barrier back towards the BH. It the test particle initially has $\dot{r} \leq 0$ and $\hat{H}^2 > V_{\rm eff}(r_{\rm min})$ it directly falls into the BH.

We now analyze the case $L^2 > 12$, for which $r_{\rm min,max}$ are, respectively, a minimum and a maximum of the effective potential $V_{\rm eff}$. A test particle with $\dot{r} = 0$ localized at $r = r_{\rm min}$ ($/r = r_{\rm max}$), moves along a stable (/unstable) circular orbit with energy $\hat{H}^2 = V_{\rm eff}(r_{\rm min})$ ($/\hat{H}^2 = V_{\rm eff}(r_{\rm max})$).

For $L^2 = 16$, the potential satisfies $V_{\rm eff}(r_{\rm max}) = 1$; we will analyze separately the cases $12 < L^2 < 16$ and $L^2 > 16$. For $12 < L^2 < 16$, a particle either arriving from infinity with $\hat{H} \geq 1$ and $\dot{r} \leq 0$ or initialized at some finite distance with $V_{\rm eff}(r_{\rm max}) < \hat{H} < 1$ and $\dot{r} \leq 0$, falls directly into the BH. Another possibility is to initialize the particle at some finite distance with $V_{\rm eff}(r_{\rm max}) < \hat{H} < 1$ but with $\dot{r} > 0$. In this case, it will initially move outward from the BH, to be later "reflected" from the potential at the inversion point, defined as in Eq. (3.13), subsequently falling into the BH. Finally, if the test particle has energy in the interval $V_{\rm eff}(r_{\rm min}) < \hat{H}^2 < V_{\rm eff}(r_{\rm max})$, it will move between two turning points $r_\pm$, at which $\hat{H}^2 = V_{\rm eff}(r_\pm)$ and $\dot{r}(r_\pm) = 0$, i.e. the test particle is on an eccentric orbit. We will discuss later, in more detail, how to characterize such orbits.

In the case $L^2 > 16$, a test particle with $\dot{r} \leq 0$ and $\hat{H}^2 > V_{\rm eff}(r_{\rm max})$ falls directly into the BH, while a test particle with $1 < \hat{H}^2 < V_{\rm eff}(r_{\rm max})$ and $\dot{r} \leq 0$, coming towards the BH from large distances, eventually

reaches a turning point, defined as in Eq. (3.13), at which its radial velocity changes sign and is scattered back from the BH towards infinity. Instead, if $V_{\rm eff}(r_{\rm min}) < \hat{H}^2 < 1$, the particle motion is bounded between two turning points, moving in an eccentric orbit.

3.1.1.1 Circular orbits

We are interested in how the characteristics of stable and unstable circular orbits change by varying the angular momentum L of the test particle. As shown in Fig. 3.1, $r_{\rm min}$ is an increasing function of L and, for $L^2 = 12$, it holds $r_{\rm min} = r_{\rm max} = 6$ yielding the minimum size of a stable circular orbit, denoted as *innermost stable circular orbit* or ISCO.

On the other hand, $r_{\rm max}$ is a decreasing function of L^2, as can be seen in Fig. 3.1. In the limit $L^2 \to \infty$, expanding Eq. (3.12) in a Taylor series, we find

$$r_{\rm max} \simeq 3 + O(L^{-2})\,. \tag{3.14}$$

Massive test particles, in the limit $L^2 \to \infty$, can move along unstable circular orbits as close to the black hole as the *light-ring* at $r = 3$. This is related to the so-called *geometric optics limit*: a massive test particle with large angular momentum behaves as a light-ray; as a consequence, its unstable circular orbit is as close to the BH as the unstable circular orbit of massless particles (the light-ring).

3.1.1.2 Eccentric orbits

We consider now bounded orbits in which the r-coordinate of the test particle varies in time between a minimum and a maximum value, denoted as periastron $r_{\rm peri}$ and apastron $r_{\rm apo}$, respectively. We introduce the *eccentricity* e and the *semi-latus rectum* p, as

$$e = \frac{r_{\rm apo} - r_{\rm peri}}{r_{\rm apo} + r_{\rm peri}}\ , \quad p = \frac{2 r_{\rm apo} r_{\rm peri}}{r_{\rm apo} + r_{\rm peri}}\,. \tag{3.15}$$

The above equations can be inverted to yield

$$r_{\rm apo} = \frac{p}{1-e}\ , \quad r_{\rm peri} = \frac{p}{1+e}\,. \tag{3.16}$$

Being the extreme points of motion, at the apastron and at the periastron $\dot{r} = 0$ and the test-particle energy equals the effective potential $\hat{H}^2 = V_{\rm eff}(r_{\rm apo,peri})$. Inverting these equations, it is possible to find an expression of the energy and the angular momentum $\hat{H}$, L in terms of eccentricity e and semi-latus rectum p

$$\hat{H}^2 = \frac{4e^2 - (p-2)^2}{p(3+e^2-p)}\ , \quad L^2 = \frac{p^2}{p-3-e^2}\,. \tag{3.17}$$

Note that it must hold $r_{\rm apo} \geq r_{\rm peri}$, implying the condition $e \geq 0$. Moreover, $r_{\rm apo}$ is an increasing function of $\hat{H}^2$ and, considering the case $L^2 > 16$ and the limit $\hat{H}^2 \to 1$ it holds $r_{\rm apo} \to \infty$, i.e. $e \to 1$. It follows from this reasoning that the eccentricity is constrained in the interval $0 \leq e < 1$.

For $L^2 > 16$ and $\hat{H}^2 < 1$ or $12 < L^2 < 16$ and $\hat{H}^2 < V_{\rm eff}(r_{\rm max})$, the equation $\hat{H}^2 = V_{\rm eff}(r)$ has three roots: $r_{\rm apo,peri}$ and r_3, which has the following expression in terms of e, p

$$r_3 = \frac{2p}{p-4}\,. \tag{3.18}$$

It is then possible to rewrite the expression $\hat{H}^2 - V_{\rm eff}(r)$ as

$$\hat{H}^2 - V_{\rm eff}(r) = (r - r_{\rm apo})(r - r_{\rm peri})(r - r_3)\,. \tag{3.19}$$

In the case in which $\hat{H}^2 = V_{\rm eff}(r_{\rm min})$, then $r_{\rm apo} = r_{\rm peri} = r_{\rm min}$ and the test particle moves on a circular stable orbit, corresponding to $e = 0$ and $p = r_{\rm min}$.

In the case $\hat{H}^2 = V_{\rm eff}(r_{\rm max})$, then $r_{\rm peri} = r_3 = r_{\rm max}$ and the test particle is on an unstable circular orbit. From Eqs. (3.16) and (3.18), it is possible to see that $r_{\rm peri} = r_3$ has two roots: the first one is $p = 0$, which does not satisfy the condition $L^2 > 12$ so is discarded. The second root is the solution we select and corresponds to $p = 6 + 2e$. For $e = 0$, it holds $p = 6$, $L^2 = 12$ and the orbit corresponds to a stable circular orbit, while smaller values of p do not correspond to any bounded orbit. Hence, the root $p = 6 + 2e$, denoted as the *separatrix*, gives the general condition which must be satisfied for bounded orbits to exist $p \geq 6 + 2e$.

3.2 Radiation reaction driving the dynamics

In the previous section, we have considered a test particle evolving on top of a SBH geometry along a geodesic identified by two constant parameters, the energy $\hat{H}$ and angular momentum L. However, as the particle moves on the curved background, it generates gravitational waves. Since the test particle has a small mass and the gravitational emission is always weak with respect to the source (see Eq. (1.4) and related discussion), the gravitational signal it emits can be considered as a small correction of the fixed stationary background. This correction can be treated in a perturbative expansion as in Eq. (2.5). Then, from Eqs. (2.43) and (2.44), it is possible to compute the fluxes of energy and angular momentum carried by the GWs at infinity. This non-vanishing flux implies that the test-particle trajectory's energy and angular momentum $\hat{H}$, L get time-dependent corrections at order $O(h^2)$. As a consequence, the effective potential $V_{\rm eff}$ describing the possible orbital configurations for the test particle becomes a function of time. Hence, a test particle cannot move exactly along the background geodesics and, due to back-reaction effects, it moves along geodesics of the perturbed spacetime. Note that, even if the fluxes are $\sim O(h^2)$, the geodesics equations get corrected at order $\sim O(h)$ (since Christoffel symbols are modified at order $\Gamma^{\mu}_{\alpha\beta} \sim O(h)$).

Operationally, corrections to the geodesic motion manifest not only in a time dependence of the test-particle energy and angular momentum (denoted as H, p_φ), but also in the presence of *effective forces*

$\mathcal{F}_{r,\varphi}$ accounting for radiation reaction, correcting the Hamiltonian equations of motion in Eq. (3.10) as

$$\begin{aligned}
\dot{r}_* &= \frac{p_{r_*}}{\hat{H}} \equiv \frac{v_r}{A(r)}\,, \\
\dot{\varphi} &= \frac{A(r)}{r^2\hat{H}} p_\varphi \equiv \omega\,, \\
\dot{p}_{r_*} &= \frac{A(r)}{r^2\hat{H}}\left[-1 + p_\varphi \frac{-3+r}{r^2}\right] + A(r)\mathcal{F}_r\,, \\
\dot{p}_\varphi &= \mathcal{F}_\varphi\,.
\end{aligned} \tag{3.20}$$

Computing the radiation-reaction effective forces implies solving the two-body problem in General Relativity. Different approximation schemes have been introduced to solve this problem; a brief review of these methods is the topic of the current section. Note that we temporarily re-introduce physical units G, c.

We first introduce some quantities to describe the source. We define M as its mass, d as its characteristic length, and v as its characteristic velocity. Since we will focus on BH binaries, d is the size of the binary. We denote the source characteristic frequency as $\Omega \sim 2\pi v/d$ and its typical wavelength as $\lambda = 2\pi c/\Omega$.

One of the first approaches developed to solve the two-body problem in General Relativity is the *post-Newtonian* (PN) approximation scheme. The PN framework is based on the underlying approximation of a slowly moving source generating a weak gravitational field. In terms of the quantities defined above, this condition reads [3]

$$\epsilon \sim (v/c)^2 \sim GM/(c^2 d) \quad , \quad \epsilon \ll 1\,, \tag{3.21}$$

where we have used $\sim$ to denote that the quantities must be of the same order of magnitude.

The spacetime metric and the matter stress-energy tensor are expanded under the above approximation in orders $O(\epsilon^n)$. We will denote their components at different ϵ^i orders as $g^{(i)}_{\mu\nu}$ and $T^{(i)}_{\mu\nu}$, respectively; note that i is not necessary an integer. If we neglect dissipative effects (i.e. working at low PN order, as will be discussed shortly), the metric is invariant under time reversal; then, g_{00}, g_{jk} must be expanded in powers of ϵ^n, while g_{0j} in $\epsilon^{n/2}$ with $n \in \mathbb{N}$, [3]. Hence, under this condition, it is possible to PN expand $g^{\mu\nu}$ as [3]

$$\begin{aligned}
g_{00} &= -1 + g^{(1)}_{00} + g^{(2)}_{00} + ... \\
g_{0j} &= g^{(1.5)}_{0j} + g^{(2.5)}_{0j} + ... \\
g_{jk} &= \delta_{jk} + g^{(1)}_{jk} + g^{(2)}_{jk} + ...
\end{aligned} \tag{3.22}$$

Similarly, we can expand the stress-energy tensor as

$$\begin{aligned}
T^{00} &= T^{00,\,(0)} + T^{00,\,(1)} + ... \\
T^{0j} &= T^{0j,\,(0.5)} + T^{0j,\,(1.5)} + ... \\
T^{jk} &= T^{jk,\,(1)} + T^{jk,\,(2)} + ...
\end{aligned} \tag{3.23}$$

Note that the T^{jk} expansion starts at ϵ order with respect to T^{00}, while T^{0j} starts at $\epsilon^{0.5}$, as a consequence of the condition in Eq. (3.21). Substituting Eqs. (3.22), (3.23) into Einstein's equations and solving for

each ϵ^i order, it is possible to find the explicit expressions of the PN metric component. The lowest PN order corresponds to the Newtonian limit, given by the metric

$$g^{00}_{\rm Newt} = -1 + 2\frac{\Phi}{c^2} \ , \quad g^{0j}_{\rm Newt} = 0 \ , \quad g^{jk}_{\rm Newt} = \delta^{jk} \, , \tag{3.24}$$

where Φ is the Newtonian gravitational potential. We will denote this as 0PN order. The next to leading order corrections are $g^{(2)}_{00}$, $g^{(1.5)}_{0j}$ and $g^{(1)}_{jk}$ denoted as 1PN order, and so on.

Before proceeding any further, it is useful to introduce a new formalism to treat Einstein's equations. We start by defining the *gothic metric* as $\mathfrak{g}^{\mu\nu} \equiv \sqrt{-g}\, g^{\mu\nu}$, with g metric determinant. Then we move into the *harmonic gauge* by imposing the four equations [3]

$$\partial_\mu \mathfrak{g}^{\mu\nu} = 0 \, . \tag{3.25}$$

We rewrite $\mathfrak{g}^{\mu\nu}$ in terms of the quantities $h^{\mu\nu}$ as

$$\mathfrak{g}^{\mu\nu} = \eta^{\mu\nu} + h^{\mu\nu} \, . \tag{3.26}$$

Einstein's equations are then the gauge condition in Eq. (3.25), $\partial_\mu h^{\mu\nu} = 0$ in terms of $h^{\mu\nu}$, and the wave equation

$$\Box_{\rm F} h^{\mu\nu} = \frac{16\pi G}{c^4}\tau^{\mu\nu} \, , \tag{3.27}$$

denoted *relaxed Einstein field equation* [134]. In Eq. (3.27), $\Box_{\rm F} \equiv \eta^{\mu\nu}\partial_\mu\partial_\nu$ and $\tau^{\mu\nu}$ is the *effective stress-energy pseudotensor* which consists in the matter stress-energy tensor $T^{\mu\nu}$ and two pseudotensors, $t^{\mu\nu}_{\rm LL}$ and $t^{\mu\nu}_{\rm H}$, which depend only on the gravitational field [134]

$$\tau^{\mu\nu} \equiv (-g)\, \left(T^{\mu\nu} + t^{\mu\nu}_{\rm LL} + t^{\mu\nu}_{\rm H} \right) . \tag{3.28}$$

$t^{\mu\nu}_{\rm LL}$ is the Landau-Lifshifts pseudotensor while $t^{\mu\nu}_{\rm H}$ is related to the harmonic gauge choice; explicit expressions can be found in Chapter 6 of Ref. [134]. The harmonic gauge condition can be rewritten as a statement on the stress-energy pseudotensor, as

$$\partial_\mu \tau^{\mu\nu} = 0 \, , \tag{3.29}$$

and supplements the wave equation for the gravitational field Eq. (3.27), with information on how it backreacts on the matter source [134].

We consider an expansion of $h^{\mu\nu}$ analogous to Eq. (3.22), then substitute into Eq. (3.27) and iteratively solve in $O(\epsilon^i)$. The typical frequency of the gravitational radiation emitted by the system is $O(2\Omega)$, as a consequence, in the limit Eq. (3.21), time derivatives of the metric are of higher PN order than spatial derivatives, in particular $\partial_t \sim O(\epsilon^{1/2})\partial_i$ [3]. With this consideration, it is possible to see that each $O(\epsilon^i)$ perturbation is solution of the following problem [3]

$$\nabla^2 h^{(i)}_{\mu\nu} = \frac{16\pi G}{c^4}\tau^{\mu\nu,\,(i-1)} + \partial_t^2 h^{(i-1)}_{\mu\nu} \, . \tag{3.30}$$

Assuming time derivatives as subleading with respect to spatial ones corresponds to neglecting propagation effects. This approximation is valid only in the so-called *near zone*, i.e. in the region $r \ll \lambda$. At larger

distances, in the *wave zone*, Eq. (3.30) is not valid anymore, propagation effects are relevant, and the PN expansion breaks down. We will discuss this shortly.

Through the PN approximation scheme just outlined, it is possible to compute the lowest-order contributions to the effective forces correcting the geodesic dynamics in Eq. (3.20). These forces appear at $O(\epsilon^{5/2})$ or 2.5PN order, as can be shown through the simple example of a test particle in a circular orbit around a SBH. Be μ its mass, ω its angular velocity and d the radius of the orbit. We assume an observer at r far away from the source, placed along the direction $\hat{n}$, such that the angle between $\hat{n}$ and the perpendicular to the orbital plane is θ. In the (Newtonian) quadrupolar approximation, the observer measures the polarizations [3]

$$h_+ = \frac{1+\cos^2\theta}{2}\frac{G\mu}{c^2 r}\frac{4v^2}{c^2}\cos(2vt/d) \quad , \quad h_\times = \cos\theta\frac{G\mu}{c^2 r}\frac{4v^2}{c^2}\sin(2vt/d)\,. \tag{3.31}$$

where $v \equiv \omega d$. From Eq. (2.42), we can compute the flux of energy across a 2-sphere at r

$$\dot{E}_{\rm obs} = \frac{1}{10}\frac{G\mu^2}{d^2}\frac{v^6}{c^5}\,. \tag{3.32}$$

We equate the above flux with the orbital energy loss $\dot{E}_{\rm orb}$. Following Ref. [3], we argue that, at Newtonian order, $E_{\rm orb} = \mu v^2/2 + V_{\rm p}$ with $V_{\rm p}$ potential energy of the orbit, related to the kinetic energy $\mu v^2/2$ through the virial theorem $V_{\rm p} = -\mu v^2$, hence $E_{\rm orb} = -\mu v^2/2$. Differentiating with respect to time and equating to Eq. (3.32), yields

$$\frac{dv}{dt} = -\frac{1}{10}\frac{\mu}{M}\frac{GM}{d^2}(v/c)^5\,. \tag{3.33}$$

The back-reaction on the orbit of the test particle appears at $\epsilon^{5/2}$ order after the leading Newtonian order GM/d^2.

Following Refs. [135, 136, 137], for a generic system, we define back reaction forces in the equations of motion through the ansatz

$$\left.\frac{d^2x^i}{dt^2}\right|_{\rm rad-react} = -\frac{8}{5c^3}\left(\frac{\mu}{M}\right)\left(\frac{GM}{d^2}\right)\cdot\left(\frac{GM}{d}\right)\cdot\left(-A_{5/2}\dot{r}\,n^i + B_{5/2}v^i\right)\,. \tag{3.34}$$

In the expression above, GM/d^2 is the leading Newtonian order, while $GM/(c^2 d)$ is the relativistic correction due to the GWs emission $\sim O(\epsilon)$. The power of the velocity is justified by the requirement that radiation reaction is a dissipative effect and yields a correction of order $\sim O(\epsilon^{1/2})$. Since we expect radiation-reaction forces to appear at $O(\epsilon^{5/2})$, the coefficients $A_{5/2},\ B_{5/2} \sim O(\epsilon)$. These coefficients can be found through balance laws for the energy and angular momentum fluxes, following the intuition of the example above. In particular, it is imposed that the PN fluxes through a 2-sphere located far away from the source, $r \gg d$, are equal to the energy and angular momentum losses of the orbit, computed including Eq. (3.34) in the dynamics [136, 137].

In a BH spacetime, there are two dissipative boundaries: one at infinity and the other at the BH horizon. However, in the above discussion, we have completely neglected the effect of energy fluxes through the horizon. The reason is that such effects appear at high PN order. BH perturbation theory provides a

natural framework to investigate *horizon absorption* effects, as it allows probing of strong field regions. This approach applies to small perturbations $h \ll 1$ on top of a BH background, generated by a test particle of mass $\mu \ll M$ moving in this curved geometry. Using this framework, Ref. [138] computed the energy flux through the horizon for a particle on a circular orbit in SBH, finding that this effect appears at 4PN order. As argued in Ref. [138], this feature can be heuristically explained by the presence of a potential barrier surrounding the horizon. As the test particle orbits the SBH, it emits a small-frequency signal. As a consequence, when this signal reaches the potential barrier it is mainly scattered towards the observer at large distances, while transmission is suppressed. Ref. [139] extended the computation to Kerr, showing that in this case, horizon absorption effects in the energy fluxes appear at 2.5PN. These works are performed in the EMR limit, while Ref. [140] was the first to compute horizon absorption effects for a comparable-masses binary, showing that they are suppressed also for generic mass ratios.

The PN approach outlined above cannot be extended to the whole spacetime, but can only be applied close to the source since only in this region the basic assumption of the PN expansion, Eq. (3.21), is valid. This is made manifest in Eq. (3.30): in the PN framework, the gravitational interaction is instantaneous. This result automatically becomes ill-defined if extended to the whole spacetime, since it would violate causality (signals must travel locally on the curved light-cone). Moreover, if one tries to extend the PN expansion to the whole spacetime, singular integrals appear in the expansion Eq. (3.35). In particular, there are non-compact source terms on the right-hand side of Eq. (3.30), which give rise to a singular behavior at large r for PN solutions starting from the 4PN order $O(\epsilon^4)$, as shown by Ref. [141]. While the results discussed above to compute Eq. (3.34) are valid, the same framework cannot be straightforwardly applied to higher PN orders.

Blanchet and Damour [132] introduced a regular framework to compute up to generic PN order the gravitational fluxes at large distances and radiation-reaction effects on the source internal dynamics. The basic idea is to divide the spacetime into two different regions: *near zone* and *outer region*. The near zone is defined through the condition $r \ll \lambda$: it is the region of spacetime enclosing the source where propagation effects can be neglected. These effects, in fact, become important on a scale $r \gg \lambda$, which defines the *wave zone*. We introduce the outer region as the zone where the matter stress-energy tensor vanishes, i.e. $r > d$. The outer region includes the wave zone and also an overlap with the near zone, for $d < r \ll \lambda$. This overlap region depends on the nature of the source: for non-relativistic sources, it holds $v/c \sim d/\lambda \ll 1$ and the overlap region is extended.

In the Blanchet-Damour approach, [132], the PN expansion is used to study the source evolution and the gravitational signal it emits, in the inner region. Focusing on a source which generates a weak gravitational field, in the outer region $r > d$, the gothic metric $\mathfrak{g}^{\mu\nu}$ can be expanded around the flat metric $\eta^{\mu\nu}$ in the small quantity $GM/(c^2 d) \ll 1$. This expansion is denoted as *post-Minkowskian* (PM) and usually represented as

$$\mathfrak{g}^{\mu\nu} = \eta^{\mu\nu} + \sum_{i=1} \mathrm{G}^i h_i^{\mu\nu} \,. \tag{3.35}$$

where the gravitational constant G is used as book-keeping parameter, in agreement with the literature [3].

Following Ref. [132], we substitute the PM expansion, Eq. (3.35), into Eq. (3.27). Since we are outside the source, $r > d$, the matter stress-energy tensor vanishes and each order $O(G^i)$ is solution of

$$\Box_F h_i^{\mu\nu} = \Lambda^{\mu\nu}\left[h_1, h_2, ..., h_{i-1}\right] , \tag{3.36}$$

where $\Lambda^{\mu\nu}$ is given by $\tau^{\mu\nu}$ truncated at order n. Since $\Lambda^{\mu\nu}$ is at least quadratic in $h^{\mu\nu}$, is non vanishing only for $n > 1$. Eq. (3.36), together with the gauge condition $\partial_\mu h_i^{\mu\nu} = 0$, determine the solution in the outer region $r > d$, at order i.

At each order, the strain is expanded in spherical multipoles [132]

$$h_i^{\mu\nu} = \sum_{\ell\geq 0} \hat{n}_L(\theta,\varphi)\, h_{i,L}^{\mu\nu}(t,r) , \tag{3.37}$$

where we use L to indicate the collection of indices $i_1 i_2 ... i_\ell$ and we have defined $\hat{n}_L \equiv \mathrm{STF}[(x^{i_1}/r)(x^{i_2}/r)...(x^{i_\ell}/r)]$, with $\mathrm{STF}[\,\cdot\,]$ to denote the symmetric trace-free component of a tensor [3]. As a consequence, also the source on the right-hand side of Eq. (3.36) is written as an expansion in multipoles. As argued in Ref. [132], it is not trivial to integrate Eq. (3.36). The particular solution of this equation cannot be computed through the convolution of the retarded Green's function with the source, defined as $\Box_{\mathrm{F}}^{-1}\Lambda^{\mu\nu}$ with

$$(\Box_{\mathrm{F}}^{-1} f)(t,\mathbf{x}) \equiv -\frac{1}{4\pi}\int_{\mathbb{R}^3} \frac{d^3\mathbf{x}'}{|\mathbf{x}-\mathbf{x}'|}\, f(t-|\mathbf{x}-\mathbf{x}'|/c, \mathbf{x}') , \tag{3.38}$$

since we cannot extend the integral beyond $r > d$: the source $\Lambda^{\mu\nu}$ would be singular at $r = 0$ due to its multipolar structure. However, Ref. [132] presented a mathematical algorithm to circumvent this problem, allowing for the regularization of the convolution integral. This approach is valid only when the multipole expansion is truncated and is denoted as *multipolar post-Minkowskian* (MPM) expansion [3].

Once the solutions in the outer region and the near zone are computed, a matching procedure is performed in the overlap region $d < r \ll \lambda$, exploiting the possibility to expand in $(v/c) \ll 1$ (i.e. to neglect retardation effects) and in $GM/(c^2 d) \ll 1$ both. In this region, the outer region solution, written in terms of a multipoles expansion, is expanded in the limit $(v/c) \ll 1$; the near zone solution obtained through the PN approach is expanded in multipoles [132]. In this way, the multipoles of the outer region expansion are related to the matter source [132, 3].

Ref. [132] found that the general solution of Eq. (3.36), at each order, can be written as a sum of two different types of terms: instantaneous and, starting from $O(G^2)$, hereditary contributions. An *instantaneous* contribution depends only on the retarded time $t - r/c$ at which the signal reaches the observer in the outer region, while an *hereditary* term is an integral over the whole history of the source prior to the retarded time $t - r/c$. Hereditary terms derived in the outer region are, in the overlap region, of order $O\left[\epsilon^{i+2}(\log\epsilon)^{i-1}\right]$, with i identifying the PM order. This implies that the (now regular at all orders) PN expansion must contain terms of order $\sim \epsilon^n \log\epsilon^m$ other than $\sim \epsilon^n$. The first hereditary term appears at $O(G^2)$ in the outer region and is of PN order $O(\epsilon^4 \ln\epsilon)$ in the overlap region.

Through the matched PN-MPM formalism it is possible to compute the corrections to the *quadrupole formula* connecting the radiation observed at large distances in the TT-gauge h_{ij}^{TT} with the quadrupole

moment of the source I_{ij} which, at Newtonian level, is given by

$$ {}^{\rm Newt}I_{ij}(t) = \frac{1}{c^2}\int_V d^3x \left(x_i x_j - \frac{1}{3}\delta_{ij}(x^k x_k)\right)\cdot T^{00}_{\rm Newt}\,. \tag{3.39} $$

In the equation above, V is the volume enclosing the source and $T^{00}_{\rm Newt}$ is the (00)-component of the stress-energy tensor, at Newtonian order. Up to 4PN order accuracy, the quadrupole formula can be written as

$$ h^{TT}_{ij}(u) = \frac{2G}{c^4\,r}\frac{d^2}{dt^2}I_{ij}(u) + \frac{4G^2M}{c^7\,r}\int_0^\infty d\tau\,\frac{d^2}{dt^2}{}^{\rm Newt}I_{ij}(u-\tau)\left[\ln\left(\frac{\tau}{2r}\right)+\kappa_2\right] + o(\epsilon^4\ln\epsilon)\,, \tag{3.40} $$

where $u = t - r/c$ is a retarded time coordinate, I_{ij} is the quadrupole moment of the source with corrections up to $\sim O(\epsilon^4)$ order, and κ_2 is a constant, which depends on the gauge. The first term on the right-hand side of Eq. (3.40) is the usual (instantaneous) quadrupole formula, while the second term is an integral over the whole history and is the lowest PN order contribution to the *hereditary tails*. In Chapter 5 we will show that late-times tails computed in a perturbation theory framework (as introduced in Sec. 2.2.2 and 2.3.2) are hereditary effects which depend on the whole history of the system, yielding the same physical effect as tails in PM theory. However, while Eq. (3.40) focuses on the signal emitted during the inspiral regime, we will investigate these hereditary effects as observed at very late-times, after the two objects have merged into a final BH.

It is important to specify that the results derived in Ref. [132], can be applied to BHs binary systems with generic mass-ratios and are not only valid in the EMR limit. For comparable-mass systems, the test-particle mass μ translates into the binary reduced mass, related to the symmetric mass-ratio introduced in Eq. (3.1) as $\mu = M\eta$.

As a conclusive remark for this section, it is important to stress that the PN-MPM matched approach is not the only approach possible to compute radiation-reaction effects driving the motion of a test particle in a BH spacetime. Parallel efforts have been developed over the years exploiting BH perturbation theory tools, starting from the investigations in Refs. [142, 143, 138, 144, 145]. This line of research, in particular starting from Ref. [146], originated what is nowadays denoted as the *self-force* approach, see Ref. [72] for a recent review.

3.3 Transition to plunge

Since radiation-reaction corrections appear in the equations of motion only from the $\sim O(\epsilon^{5/2})$ order, this effect can only impact the orbital dynamics on a long timescale. For instance, we assume a test particle with initial energy $\hat{H}$ and angular momentum L far from the separatrix crossing values, such that at the initial time step the particle is on a bounded circular orbit. As time evolves, due to radiation reaction, the test-particle motion is not geodesic. However, at each time step, it is possible to find a geodesic that osculates the trajectory. This portion of the evolution is denoted as *adiabatic inspiral regime* [9]. The parameters $\hat{H}$, L vary smoothly and with a slow time dependence; as a consequence, also the effective potential $V_{\rm eff}$ evolves in time, while the orbital configurations span over a set of geodesics until the

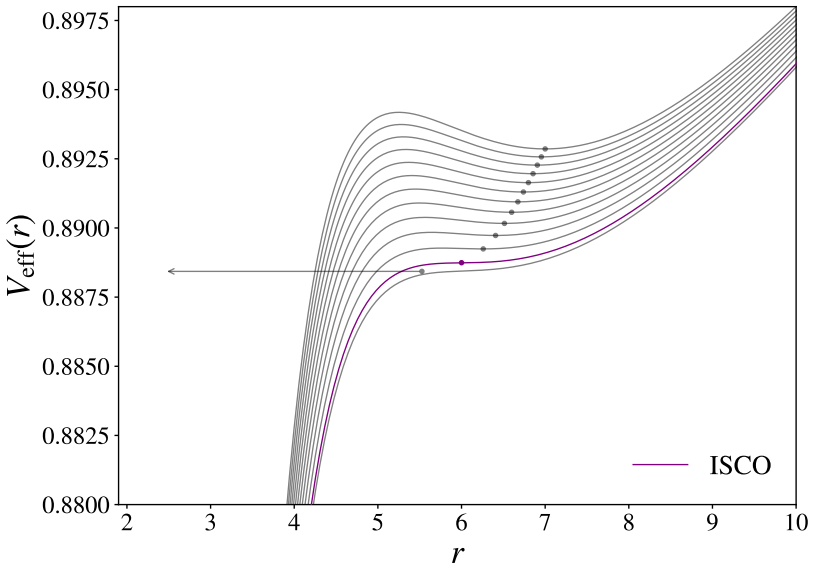

Figure 3.2: Effective potential $V_{\rm eff}$ in Eq. (3.11) as function of r. Each line corresponds to the potential build with angular momentum p_φ at a different time-step t of the orbital evolution. Dots represent the energy and location $(\hat{H}(t), r(t))$ of the test particle at that time. In purple, values at the time $t_{\rm ISCO}$ when the test particle is at the ISCO $r_{\rm ISCO} = 6$. After this time, no stable bound orbits exist, and the test particle plunges into the horizon. Results relative to a quasi-circular evolution obtained numerically solving the Hamiltonian equations of motion Eq. (3.20) with the RWZHyp code [93, 94], with effective forces $\mathcal{F}_\varphi$, $\mathcal{F}_{r_*}$ as computed in Ref. [147], discussed in Sec. 3.4.

separatrix is reached. This behavior is shown in Fig. 3.2, for a quasi-circular inspiral evolved with the radiation reaction computed in Refs. [147]. The typical size (velocity) of the orbit decreases (increases) in time, hence the parameter ϵ controlling the validity of the PN expansion progressively increases.

After the separatrix is crossed, the parameters $\hat{H}$, L are such that bounded geodesics do not exist anymore; as a consequence, the typical timescale of the dynamics becomes much faster and radiation-reaction effects can be neglected so that the motion is quasi-geodesic [9, 10, 74]. This stage is denoted *transition to plunge* and is the focus of the present section. During the plunge, the orbital motion is fast and $\epsilon \to 1$ as the test particle approaches the horizon. Hence, in this last stage of the trajectory, large PN orders might be necessary to converge towards the "real" motion.

The matched PN-MPM method developed by Ref. [132] and discussed in the previous section is an algorithm to compute a well behaved gravitational signal at $\mathcal{I}^+$ that, in turn, induces corrections in the test-particle orbit, at generic PN order $O(\epsilon^n \ln \epsilon^m)$. In particular, both the emitted gravitational radiation from the test particle in the near region and its equations of motion are computed, in this framework, as Taylor series in $\epsilon^n \log \epsilon^m$. The regularity of the Taylor expansions at each PN order, however, does not guarantee the convergence of the Taylor series towards the "real solution" for $\epsilon \lesssim 1$. In this case, we define convergence by requiring that the difference between the truncated Taylor series of a quantity and its "real value" (e.g. computed numerically) progressively and consistently decreases with the order of

truncation.

In Ref. [148], the linear perturbative waveform emitted by a test particle on a circular orbit around a SBH was computed numerically and the flux of energy at infinity was later fitted with a PN series-like template

$$\frac{dE}{dt} = \dot{E}_{\rm Newt} \cdot \sum_{k=0}^{5} a_k \, x^k \,, \tag{3.41}$$

where, following Ref. [148], $\dot{E}_{\rm Newt}$ is the Newtonian energy flux, $x \equiv r_0^{-1/2}$ with r_0 position of the test-particle circular orbit and a_k are free-parameters of the fit. Up to $k = 3$, Ref. [148] showed that the fitted PN coefficients a_k agree up to high accuracy with the theoretically computed ones and estimated that higher corrections of orders $k = 4, 5$, as inferred from the fit, are accurate up to $\sim 2\%$, 10% respectively. From $\dot{E}$ it is possible to compute the orbital frequency increase, directly related to the evolution rate of the emitted GWs frequency $\dot{\Omega}_{\rm GW}/\Omega_{\rm GW}$, hence to its phase. Be $\Delta\dot{E}$ the difference between the exact energy flux and the one computed through the PN expansion-like in Eq. (3.41). Two waveforms computed with these two different $\dot{E}$ will accumulate a phase difference of order $\Delta\phi/\phi \sim \Delta\dot{E}/\dot{E}$ [148]. Ref. [148] argued that adding more terms to the truncated expansion in Eq. (3.41) does not greatly improve this phase difference, hinting at a slow convergence of the PN Taylor expansion.

In Ref. [149], the exact expression for the energy flux of a test particle in a circular orbit around a BH was computed. This quantity was compared with Taylor expanded fluxes truncated at different PN orders, showcasing a slow and oscillating convergence towards the exact solution.

In Ref. [133], an alternative expansion was proposed in place of the usual Taylor series, able to improve convergence for large values of the PN parameter ϵ. This new expansion is based on *Padé approximants*; we introduce this mathematical tool through the example in Refs. [133, 3], focusing on the energy of a test particle in a SBH background.

The general idea behind *Padé approximants* is the following [133, 3]. Define $T_n[f, \epsilon]$ as the operator which, applied to the function f, returns its Taylor series near $\epsilon \approx 0$ truncated at order n, denoted as $T_n[f, \epsilon] = \hat{f}_n(\epsilon)$. The Padé approximant $P^m_k[f, \epsilon]$ is defined as the ratio of two polynomials in the variable ϵ, $N_m(\epsilon)$ of order m and $D_k(\epsilon)$ of order k, such that [133]

$$P^m_{k>0}[f, \epsilon] = \frac{N_m(\epsilon)}{D_{k>0}(\epsilon)} \,, \quad n = m + k \quad | \quad T_n[P^m_k[f, \epsilon]] = \hat{f}_n(\epsilon) \tag{3.42}$$

with the convention $D_k(0) = 1$. Note that we have required $k > 0$; otherwise, the Padé approximant would coincide with the Taylor expansion. Since the Taylor expansion of the Padé approximant of f is equal to the Taylor series of the function itself, it is usually said that this method consists in a *re-summation* [133].

In order to understand how Padé approximants work with respect to the usual Taylor expansion, we consider a simple example. Following Refs. [133, 3] we consider a test particle on a circular orbit around a SBH. The expression for the orbital frequency ω can be found imposing $p_{r_*} = 0$ and

$$\frac{dp_{r_*}}{d\tau} = \frac{1}{r^2 A(r)} E^2 + \frac{A(r)}{r^3} p_\varphi = -\frac{E^2}{r^2 A(r)} \left(1 - \omega^2 r^3\right) = 0 \quad \rightarrow \quad \omega = r^{-3/2} \,, \tag{3.43}$$

where we have used the definition of the orbital velocity given in Eq. (3.10). Substituting this expression

into Eq. (3.9), it is possible to compute the energy of the test particle as a function of its frequency ω

$$E_{\rm circ} = A(r)\left(1-\frac{3}{r}\right)^{-1/2} = \frac{1-2x}{\sqrt{1-3x}}\,. \tag{3.44}$$

To simplify the notation, we will use the parameter $x \equiv r^{-1}$. Following Refs. [133, 3], we introduce a new energy function $\xi(x)$ as

$$\xi(x) \equiv E^2 - 1\,. \tag{3.45}$$

Since we know the explicit expression of the test-particle energy E, $E_{\rm circ}$ in Eq. (3.44), we can compute ξ explicitly as

$$\xi_{\rm circ}(x) = x\frac{1-4x}{-1+3x}\,. \tag{3.46}$$

We perform a PN expansion of the quantity above, as a Taylor series in $x \sim \epsilon$ truncated at order $n = 2$ (2PN)

$$\xi^T_{\rm circ} = x\left(-1+x+3x^2\right) \tag{3.47}$$

Although we know the exact expression of the (new) energy function $\xi_{\rm circ}$, we assume, for the moment, to have access only to its truncated Taylor series Eq. (3.47), along with the knowledge that $\xi_{\rm circ}$ possesses a simple pole [133, 3]. We use this information to construct the Padé approximant of $E_{\rm circ}$, following the prescription in Eq. (3.42). Since the exact function has a pole, we consider the approximant $m = k = 1$ whose generic expression is given by

$$P^1_1(\xi, x) = x\frac{a+bx}{1+cx}\,. \tag{3.48}$$

To find the coefficients a, b, c we expand P^1_1/x in a Taylor series, keeping corrections up to x^2, then impose this quantity to be equal to $\xi^T_{\rm circ}/x$ in Eq. (3.47). As a result, we obtain

$$a = -1\ ,\quad b = 4\ ,\quad c = -3\,. \tag{3.49}$$

Substituting the above result in Eq. (3.48), we see that the Padé approximant, given only a perturbative Taylor expansion of the real function and the knowledge of its pole structure, yields the *exact* expression for the energy in Eq. (3.44), [133, 3].

In the simplified example presented above, the exact expression of the energy was known, in general, this is not the case: for instance, an explicit expression for the energy flux at infinity in the test-particle limit is not known, and only Taylor expansions of this quantity in the PN limit are available. As argued in Ref. [149, 133], these Taylor expansions appear to converge slowly to numerically computed fluxes, oscillating in the PN truncation order around the real (numerically computed) solution. Ref. [133] applied the Padé approximants framework to this problem, showing that a Padé expansion for the flux yields a result converging monotonically towards the numerical results.

Thanks to its convergent behavior, Padé expressions for the fluxes allow for computing these quantities along the whole trajectory of the test particle. The re-summed expressions for the radiation-reaction forces in Eq. (3.20) yield a smooth transition from the adiabatic inspiral regime through the quasi-geodesic plunge motion, for which $\epsilon \lesssim 1$, as shown in Ref. [10].

As we increase the PN order n of accuracy, we have more freedom to choose the Padé approximant. In Eq.(3.42) we have prescribed $m + k = n$, where m and k are the truncation orders of the Taylor expansions in the numerator and denominator functions, respectively. As n increases, different choices for the Padé approximant can be made. The general strategy is to use approximately *diagonal* Padé, such that $m \sim k$ with the additional requirement that the only poles are motivated by physical arguments, hence are not artifacts of the expansion procedure [133]. If this requirement is not sufficient, the Padé orders are fixed by comparing re-summed predictions against numerical evolutions [71]. For this reason, this method is often regarded as *semi-analytical*.

In Ref. [150] a new Padé procedure was introduced, denoted as *tuned Padé*. The idea is to fine-tune the location of the pole in the energy flux re-summed expression, to minimize the mismatch between the semi-analytical PN expansion and the numerical expression at the last stable orbit. Ref. [150] showed that this procedure allows to have better agreement with the numerical flux along the whole trajectory, in particular near the transition to plunge.

State-of-the-art re-summation procedures factor semi-analytical waveforms and fluxes into different components, each re-summed independently. The Newtonian limit is factored out, along with the leading tail terms (hereditary contributions) [74, 151]. In Ref. [74] it was argued that the motion during the plunge has non-quasi-circular features, regardless of the inspiral binary. It was proposed to introduce an additional factor in the waveform, accounting for non quasi-circular corrections. This factor is a superposition of terms activated by non-circular motion, such as $\propto p_{r_*}^n/(r\omega)^n$ with p_{r_*}, ω as defined in Eq. (3.20). Coefficients of each of these terms are fixed to improve the match between the semi-analytical waveform and a perturbative numerical evolution in the EMR limit.

3.4 Final remarks

In Chapters 5, 6 and 7 we are going to introduce the original results of this thesis. These investigations focus on the gravitational signal emitted by a test particle evolving on a SBH background, in generic planar orbits. These orbits are numerical, obtained by solving the Hamiltonian equations of motion in Eq. (3.20), with effective forces to drive the dynamics towards the merger. The forces that we are going to use were computed in Ref. [147]; here we briefly summarise later results and describe how these functions are built.

In Ref. [152], the radiation-reaction forces $\mathcal{F}_r$, $\mathcal{F}_\phi$ were computed for generic orbits and mass-ratios, in the context of the Effective One Body (EOB) approach [70]. These expressions were obtained through balance laws arguments, imposing that the energy $\dot{E}_{\rm orb}$ and angular momentum $\dot{L}_{\rm orb}$ losses of the orbit satisfy

$$\dot{E}_{\rm orb} + \dot{E}_{\rm Schott} + \dot{E}_\infty = 0 \ , \quad \dot{L}_{\rm orb} + \dot{L}_\infty = 0 \, , \tag{3.50}$$

where $\dot{E}_\infty$, $\dot{L}_\infty$ are the energy and angular momentum fluxes at infinity, carried by the gravitational waves. $\dot{E}_{\rm Schott}$ is the Schott energy change in the orbit [152] due to its interaction with the local gravitational field. A Schott term is not present in the angular momentum balance law: following Ref. [152], part of the

gauge freedom can be fixed so that this contribution vanishes. The orbital energy and angular momentum losses are directly related to the radiation-reaction forces, as

$$\dot{E}_{\rm orb} = \dot{r}\mathcal{F}_r + \dot{\varphi}\mathcal{F}_\varphi \ , \quad \dot{L}_{\rm orb} = \mathcal{F}_\varphi \, . \tag{3.51}$$

So that from Eq. (3.50), once the flux at infinity is known, it is possible to compute $\mathcal{F}_r$, $\mathcal{F}_\varphi$, $E_{\rm Schott}$. Ref. [152] computed these quantities *informed* at 2PN order, i.e. they contain corrections on the gravitational radiation up to 2PN after the Newtonian limit. We denote the results of Ref. [152] as $\mathcal{F}_r^{\rm 2PN}$, $\mathcal{F}_\varphi^{\rm 2PN}$, $E_{\rm Schott}^{\rm 2PN}$, to stress that these quantities are computed in a Taylor series, not re-summed. As a consequence, they are not suited to describe the whole dynamic, in particular the plunge regime.

Ref. [147] computed $\mathcal{F}_r$ valid along the full dynamical evolution from $\mathcal{F}_r^{\rm 2PN}$ of Ref. [152], as

$$\mathcal{F}_r = \frac{32\, p_{r_*}}{3r^4} P_2^0[\mathcal{F}_r^{\rm 2PN}] \, , \tag{3.52}$$

where with $P_2^0[\,\cdot\,]$ we denote the $m = 0$, $k = 2$ Padé approximant (see Eq. (3.42)). This is the radiation-reaction force we will use in the Hamiltonian equations of motion Eq. (3.20) for the results of Chapters 5, 6 and 7.

Ref. [147] computed the Schott energy from the 2PN informed expression in Ref. [152], $E_{\rm Schott}^{\rm 2PN}$, through the re-summation

$$E_{\rm Schott} = \frac{16\, p_{r_*}}{5r^3} P_2^0[E_{\rm Schott}^{\rm 2PN,c}]\, P_2^0[E_{\rm Schott}^{\rm 2PN,nc}] \, , \tag{3.53}$$

where $E_{\rm Schott}^{\rm 2PN,c}$ is the Schott energy informed at 2PN computed in the circular case, i.e. setting $p_{r_*} = \dot{p}_{r_*} = 0$ in the expression computed by Ref. [152]. The non-circular factor is then computed such that

$$E_{\rm Schott}^{\rm 2PN} = E_{\rm Schott}^{\rm 2PN,\,c}(r) \cdot E_{\rm Schott}^{\rm 2PN,\,nc}(r, p_{r_*}, p_\varphi) \, . \tag{3.54}$$

For $\mathcal{F}_\varphi$, two possible expressions for $\mathcal{F}_\varphi$ are compared in Ref. [147]. The first is obtained factoring the circular-motion limit of $\mathcal{F}_\varphi^{\rm 2PN}$ computed in Ref. [152], obtained imposing $p_{r_*} = \dot{p}_{r_*} = 0$, with the non-circular component, defined through

$$\mathcal{F}_\varphi^{\rm 2PN} = \mathcal{F}_\varphi^{\rm 2PN,\,c}(r) \cdot \mathcal{F}_\varphi^{\rm 2PN,\,nc}(r, p_{r_*}, p_\varphi) \, . \tag{3.55}$$

The circular component $\mathcal{F}_\varphi^{\rm 2PN,\,c}(r)$ is evaluated along $r_c = \omega_c^{-2/3}$, as valid for a circular motion (see Eq. (3.43)), with ω_c as instantaneous circular frequency [147]. Then, the 2PN informed $\mathcal{F}_\varphi^{\rm 2PN,\,c}(r_c)$ is replaced by the EOB re-summed expression present in the literature for a circular inspiral $\mathcal{F}_\varphi^{\rm EOB,\,c}(r_c)$ [151, 147]. The non-circular component is instead re-summed through a Padé, so that the first proposed expression for the radiation-reaction force $\mathcal{F}_\varphi$ is [147]

$$\mathcal{F}_\varphi^{\rm EOB,\,2PN\,nc} = \mathcal{F}_\varphi^{\rm EOB,\,c}(r_c) \cdot P_2^0[\mathcal{F}_\varphi^{\rm 2PN,\,nc}(r, p_{r_*}, p_\varphi)] \, . \tag{3.56}$$

This expression is compared with

$$\mathcal{F}_\varphi^{\rm EOB\,qc,\,nc} = -\frac{32\,\mu}{5\,M} r_c^4 \omega^5 \hat{f}(\omega) \cdot \hat{f}_\varphi^{\rm nc} \, , \tag{3.57}$$

which consists of the Newtonian order angular momentum flux computed in Ref. [152] for a quasi-circular motion (i.e. neglecting derivatives of r, ω), with the factor $\hat{f}_{\varphi}^{\mathrm{nc}}$ accounting for non-circular corrections. This factor is a combination of r, ω derivatives with coefficients of each term fine-tuned on numerical waveforms [147].

Ref. [147] computed the energy and angular momentum fluxes by solving numerically the evolution of a test particle plunging into a SBH. The perturbative numerical fluxes are compared with the predicted ones, computed with $\mathcal{F}_r$ in Eq. (3.52), E_{Schott} in Eq. (3.53) and $\mathcal{F}_{\varphi}^{\mathrm{EOB\,qc,\,nc}}$ in Eq. (3.57). The comparison is then repeated for the semi-analytical fluxes obtained through $\mathcal{F}_r$ in Eq. (3.52), E_{Schott} in Eq. (3.53) and $\mathcal{F}_{\varphi}^{\mathrm{EOB\,2PN\,nc}}$ in Eq. (3.56).

This comparison shows that Eq. (3.57) is better suited to describe the angular momentum loss of the orbit. Hence, we will use this $\mathcal{F}_{\varphi}$ for the original results presented in the thesis.

Chapter 4

Post-merger waveform: a phenomenological approach

In the previous chapter, we have focused on the orbital evolution of black-hole (BH) binaries (BBH) in the extreme mass-ratio (EMR) limit, discussing the equations of motion of these systems and introducing the effective forces driving the dynamics towards a merger. Now, we move the attention to gravitational waves generated by these binaries, but keeping the sources' mass ratios generic. These investigations have been enabled by the numerical relativity breakthrough of Refs. [153, 154, 155], numerically solving the (non-linear) Einstein's equations for a BBH merger from the inspiral up to and through the merger, until the final black hole has reached its stationary equilibrium configuration. Since these seminal works, the numerical relativity field has flourished: several independent codes have generated several catalogs, see e.g. [156, 157, 158, 159], of numerical waveforms relative to different types of progenitor's binary configurations: quasi-circular non-spinning/spin-aligned/spin-precessing progenitors, eccentric/hyperbolic orbits [160, 161, 162, 163], neutral (Kerr)/electrically charged (Kerr-Newman) [164, 165] BHs and finally, numerical waveforms in some modified theory of gravity [166, 167, 168, 169, 170, 171, 172, 173, 174, 175] are now available.

In Fig. 4.1, we show a non-linear numerical waveform obtained from the coalescence of two non-spinning BHs progenitors of comparable masses, generated with the SpeC code [176, 95, 96, 97, 98] and available in the public SXS catalog [156]. In particular, the signal has been decomposed in spin weight -2 spherical harmonics and we focus on the quadrupole $(\ell m) = (22)$, showing the radiation emitted close to the luminosity peak. As detailed in Chapter 1, the waveform is typically divided into three different components. It starts with the *inspiral* emitted while the two BHs are orbiting around each other, progressing towards the *merger signal*, emitted once a common horizon is formed ($\sim$ the quadrupole peak of luminosity). The relaxation towards a stationary equilibrium configuration can be described, at leading order, with vacuum perturbation theory results, as a superposition of quasi-normal modes (QNMs) [13, 177]. This stage is denoted as *ringdown* and is valid some time after the waveform peak $\sim 15M$ [11, 12]. As will be explored in this chapter, the QNMs complex frequencies are functions only of the final (product of the merger) BH mass M_f, spin J_f, electric Q_f or magnetic P_j charge [20, 21, 32, 31, 30, 29, 28, 27, 26,

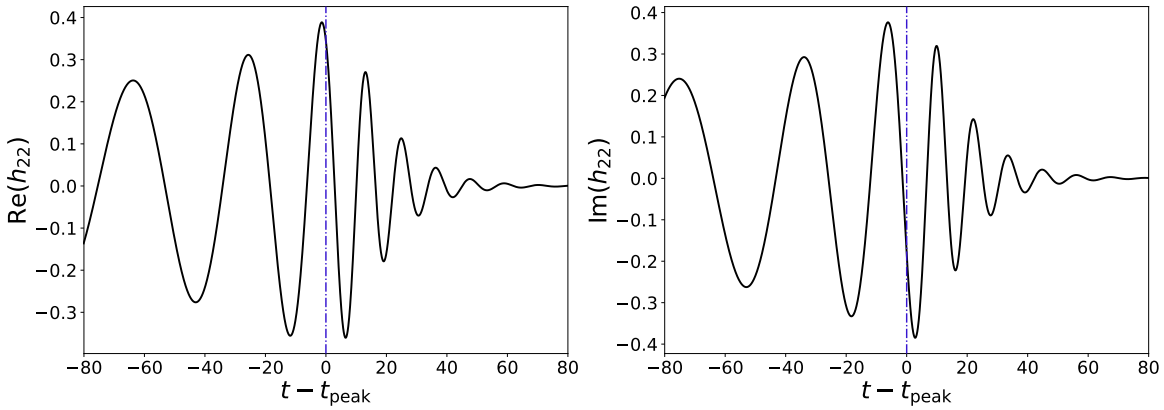

Figure 4.1: Real (left) and imaginary (right) component of the strain multipole h_{22} vs the time, translated with respect to the time $t_{\rm peak}$ of $|h_{22}|$ peak. Results are relative to the numerical waveform SXS:0305 of the SXS catalog [156], characterized by non-spinning progenitors in a circular orbit with mass ratio $q \simeq 1.2$.

25, 24, 23, 22], while their amplitudes encode information on the progenitor's orbit [76, 77, 11, 78, 12, 79, 49, 80, 69, 81, 82, 83].

Surprisingly, while non-linear effects are present in numerical waveforms [42, 43, 44, 45, 46, 51, 47, 48, 40, 49, 52, 53, 178, 54], these waveforms exhibit morphological features similar to those of perturbative evolutions computed for EMR systems, for what concerns the transient emitted between the waveform peak and the ringing regime. In fact, the functional expressions of the phenomenological models describing this signal are independent of the mass ratio [179, 73], as will be detailed later.

While there are analytical methods to compute the signal during the inspiral-plunge, e.g. the post-Newtonian (PN) scheme and (in the EMR and intermediate mass-ratio limits) the self-force approach, a similar first principles understanding of the post-merger signal is currently lacking. The goal of this chapter, is to provide an overview of past investigations on this portion of the waveform obtained through fits of numerical evolutions, both in the perturbative and in the fully non-linear case. The phenomenological picture arising from these studies introduces the intuition behind the original results presented in Chapter 7.

In the first section, Sec. 4.1, we review past efforts devoted to understanding the *modal content* of the ringdown, i.e. how many modes can be identified (which modes are the loudest), and how the QNMs amplitudes are related to the inspiral two-body problem. In Sec. 4.2, we discuss purely phenomenological models, able to reproduce the transient behavior connecting the waveform at its peak with the subsequent ringdown. These investigations are not only useful to build parametrized models, but can offer valuable insight into how to build a first-principles analytical model. In Sec. 4.3, we introduce an algorithm to perform Bayesian inference on numerical ringdown data. This algorithm is then applied to re-derive past results on Kerr BHs and to introduce new results for the ringdown of Kerr-Newman mergers. We conclude the chapter with some final remarks in Sec. 4.4, briefly summarizing the heuristic ringdown picture emerging from an a-posteriori analysis, and its limitations.

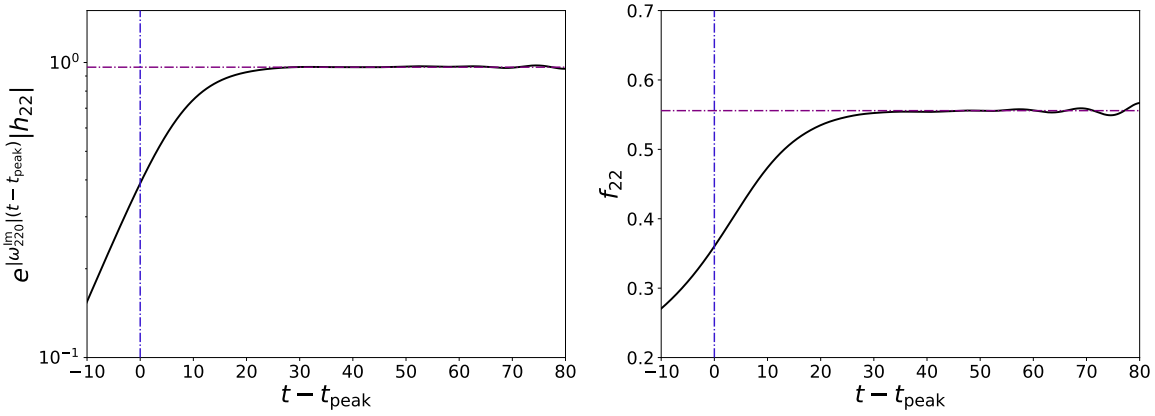

Figure 4.2: Rescaled amplitude (left) and instantaneous frequency, as defined in Eq. (4.5), (right) component of the strain multipole h_{22} vs the time, translated with respect to the time $t_{\rm peak}$ of $|h_{22}|$ peak. Results are relative to the numerical waveform SXS:0305 of the SXS catalog [156], characterized by non-spinning progenitors in a circular orbit with mass ratio $q \simeq 1.2$.

4.1 Stationary ringdown

In Chapter 2, we have discussed the response of a Schwarzschild BH to an external (small) perturbation, at linear order in this quantity. In particular, we have shown that this response can be divided into three different stages: an initial prompt response traveling on the light-cone, an intermediate ringing signal characterized by a superposition of exponentially damped vibrational modes, the QNMs, and an inverse power-law decay dominating the relaxation at late times.

It is interesting to investigate whether a similar structure can be found in fully non-linear numerical simulations, during the relaxation of a perturbed BH product of a comparable-mass BH binary merger. In this chapter, we focus on the ringdown and leave the tail to Chapter 6. We review past works which study the non-linear numerical signal some time after the waveform peak, fitting with the following template

$$h_+(t,r,\theta,\varphi) - i\,h_\times(t,r,\theta,\varphi) = \frac{1}{r}\sum_{\ell,|m|\leq\ell}\sum_{s=\pm,n} A_{\ell mns}\, e^{i\phi_{\ell mns}} \cdot e^{-i\omega_{\ell mns}t} \cdot {}_{-2}S_{\ell mns}(\theta,\varphi)\,, \tag{4.1}$$

where $h_{+,\times}$ are the polarization as observed at $\mathcal{I}^+$ in the TT-gauge and ${}_{-2}S_{\ell mns}$ are the spin weight -2 spheroidal harmonics [180], $\omega_{\ell mns}$ are the (complex) QNMs frequencies and $A_{\ell mns}$, $\phi_{\ell mns}$ are their amplitudes and phases, assumed to be constant quantities. The quantity s distinguishes between the *co-rotating* modes $\mathrm{Re}(\omega_{\ell mn+}) > 0$ and the *counter-rotating* modes $\mathrm{Re}(\omega_{\ell mn-}) < 0$, also denoted as *mirror modes*. We will neglect the counter-rotating modes in the discussion of the current chapter, since mirror modes are appreciably excited only for small remnant spins or very high mass ratios, neither of which will be considered. As discussed in Chapter 2, the QNFs are functions of the parameters describing the BH spacetime: according to the *no-hair conjecture* these quantities are the BH mass M, its angular momentum J and its electric Q or magnetic P charge [20, 21, 32, 31, 30, 29, 28, 27, 26, 25, 24, 23, 22]. In Eq. (4.1), the QNFs are relative to the final BH generated by the merger, so $\omega_{\ell mn} = \omega_{\ell mn}(M_f, J_f, Q_f, P_f)$. The QNMs amplitudes, on the other hand, depend both on the final spacetime configuration, i.e. on the

parameters (M_f, J_f, Q_f, P_f), but also on the perturbations triggering the ringdown response; we will come back to this point later.

In the template Eq. (4.1), we have considered an expansion in spin weight -2 spheroidal harmonics, instead of spherical, since the final BH producing the ringdown signal is, in general, a Kerr BH. Due to angular momentum conservation, even if initially the progenitors have vanishing spin, the final BH will have non-zero angular momentum. The final BH is Schwarzschild only for specific fine-tuned inspiral configurations.

Perturbations of a Kerr BH can be separated into radial part and angular part: at the QNFs, the former is solved by the QNMs radial profile, while the latter is solved by spin weight -2 spheroidal harmonics ${}_{-2}S_{\ell mn}$ [180]. However, as argued in Refs. [181, 182, 183, 11] , ${}_{-2}S_{\ell mn}$ are not orthonormal nor a complete set, hence numerical relativity waveforms are usually decomposed in the orthonormal basis of spin weight -2 spherical harmonics ${}_{-2}Y_{\ell m}$. In the limit $J\omega_{\ell mn} \to 0$, the spin -2 spheroidal harmonics reduce to spherical ones, and it is possible to perform a Taylor expansion in $J\omega_{\ell mn} \ll 1$ connecting these quantities [184]

$$ {}_{-2}S_{\ell mn}(\theta,\varphi) = {}_{-2}Y_{\ell m}(\theta,\varphi) + (J\omega_{\ell mn}) \sum_{\ell' \neq \ell} {}_{-2}Y_{\ell' m}(\theta,\varphi) c_{\ell' \ell m} + O\left[(J\omega_{\ell mn})^2\right] , \tag{4.2} $$

where the $c_{\ell' \ell m}$ can be found in Ref. [184]. For $J \in [0,1]$, it is possible to decompose the spheroidal harmonics into spherical ones as

$$ {}_{-2}S_{\ell mn}(\theta,\varphi) = \sum_{\ell'} A_{\ell \ell' mn} \cdot {}_{-2}Y_{\ell' m}(\theta,\varphi) \ , \quad A_{\ell \ell' mn}(J)\delta_{mm'} = \int d\Omega \, {}_{-2}S_{\ell mn}(\theta,\varphi) \cdot {}_{-2}Y_{\ell' m'}(\theta,\varphi) \ . \tag{4.3} $$

the coefficient $A_{\ell \ell' mn}$ were computed in Ref. [183]. Following Refs. [182, 11], inserting the expression above into the template in Eq. (4.1), it is possible to rewrite the ansatz used to analyze numerical waveforms in terms of spin weight -2 spherical harmonics. The template to describe each multipole (in ${}_{-2}Y_{\ell m}$) is then

$$ h_{\ell m}(t) = \sum_{\ell', n} A_{\ell \ell' mn} \, e^{i\phi_{\ell \ell' mn}} \cdot e^{-i\omega_{\ell' mn} t} , \tag{4.4} $$

with frequencies $\omega_{\ell' mn}$ computed solving the Teukolsky equation (i.e. in a Boyer-Lindquist coordinate system). Note that, from now on, we will simplify the notation as $A_{\ell \ell' mn} = A_{\ell' mn}$, $\phi_{\ell \ell' mn} = \phi_{\ell' mn}$. In Eq. (4.4), the spherical multipole (ℓm) receives contribution from modes with $\ell' \neq \ell$, this phenomenon is usually denoted as *mode-mixing* [182]. According to Eq. (4.2), the larger is the product between the final angular momentum and the QNF, $J_f \omega_{\ell' mn}$, the more excited are the mixed modes [182, 11].

In Fig. 4.2, we show the waveform emitted from a comparable-mass BH binary merger, for non-spinning progenitors. In particular, we focus on the merger and post-merger quadrupole $(\ell m) = (22)$ signal and plot its amplitude and instantaneous frequency. The amplitude has been rescaled with respect to the decay rate of the fundamental mode, i.e. with the factor $e^{-|\omega^{\rm Im}_{220}|(t-t_{\rm peak})}$, where ω_{220} is the QNF relative to the mode (220) of the final black hole. The frequency is defined as

$$ f_{\ell m} = -i \frac{d \log\left(h_{\ell m}/|h_{\ell m}|\right)}{d(t - t_{\rm peak})} \tag{4.5} $$

Some time after the peak of the quadrupole amplitude, more specifically $t \sim t_{\rm peak} + 20M$, the instantaneous frequency saturates to the fundamental mode one $\mathrm{Re}(\omega_{220})$, while the $|\omega^{\rm Im}_{220}|$-decay rescaled amplitude saturates to a constant. This indicates that the quadrupole amplitude leading behavior is $\propto e^{-i\omega_{220}(t-t_{\rm peak})}$, hinting that at least the fundamental QNM is present in the post-merger waveform. A similar behavior can be found for other (ℓm) multipoles, which are dominated by the least-damped QNM $(\ell m 0)$.

The amplitudes $A_{\ell mn}$ of the loudest QNMs in each multipole have been studied in several works [76, 77, 11, 78, 12, 79, 49, 80, 69, 81, 82, 83, 84] by fitting numerical waveforms with the template in Eq. (4.4), and it was found that these quantities carry information on the progenitors' binary. Ref. [76] was the first to investigate this dependence, focusing on the least damped mode for the multipoles (22), (21), (33), (44), considering different mass ratios and non-spinning progenitors. Ref. [76] found that the larger is the mass-ratio q, the more excited are the higher-multipoles, consistent with the analysis of Ref. [177]. This investigation was extended to progenitors with non-vanishing, aligned or anti-aligned spins (i.e. non precessing) in Ref. [77], where it was observed that the (210) mode is highly sensitive to the initial spins $\chi_{1,2}$ and its amplitude can be parametrized in terms of an effective spin parameter $\chi_{\rm eff}$ defined as

$$A_{21} = A_{21}(\chi_{\rm eff}) \ , \quad \chi_{\rm eff} = \frac{1}{2}\left(\chi_1 \sqrt{1-4\eta} + \chi_-\right) \ , \quad \chi_- = \frac{m_1\chi_1 - m_2\chi_2}{m_1+m_2} \, , \tag{4.6}$$

where η is the (M-rescaled) symmetric mass-ratio. Modes with $\ell = m$, e.g. (220), (330), (440), do not vary appreciably with the spin, showing a sub-leading dependence on this parameter [77]. These results can be heuristically explained considering that in a tensorial harmonic decomposition the $m = l - 1$ modes are magnetic terms, dominated by the leading order "magnetic" parameter, i.e. the spin [185]. During the inspiral, the PN expression for the $(\ell m) = (21)$ multipole is given by [186, 77]

$$h^{\rm PN,\,insp}_{21} \propto \frac{\nu(m_1+m_2)}{D} v^3 \left(\sqrt{1-4\nu} - \frac{3}{2} v \chi_-\right) , \tag{4.7}$$

with v typical velocity of the source. Comparing Eqs. (4.6) and (4.7) we see that the dependence on the symmetric mass-ratio ν and the spins $\chi_{1,2}$ of the (21) multipole, at leading order (since overtones are neglected), is carried from the inspiral through the ringdown [77]. Even multipoles, e.g. $(\ell m) = (22), (33)$, of the inspiral are less sensible to the spin than (21), since its contribution appears at higher PN orders: 1.5PN after the leading behavior, while for (21) the spin is present already at 0.5PN order after the leading one [77]. This result hints that also the ringdown multipoles (22), (33), (44) carry (at leading order, since we consider only the fundamental mode behavior) a similar structure as the inspiral ones [77]. To summarize, not only do the QNMs amplitudes bear imprints of the progenitors' binary, but these imprints reflect the same behavior as the respective multipoles in the inspiral phase. This is a very important consideration, which serves as a building block for the results that will be presented later on in the manuscript.

Refs. [11, 12, 79] extended these findings through a systematic investigation of PN-like ansatz for the QNMs amplitudes, in $\eta, \chi_{1,2}$ or quantities built from these parameters. In particular, Ref. [11] focused on non-spinning progenitors with different mass ratios, analyzing the behavior of additional modes and providing a closed form for their amplitudes, as expansions in the symmetric mass ratio η. The discussion was later extended to progenitors with aligned spins in Ref. [12] and new, more generic expressions for the

QNMs amplitudes were estimated, as functions of η and $\chi_{1,2}$. Ref. [79], focused both on non-spinning and aligned-spin progenitors with different mass ratios and tested templates to describe the multipoles near the merger characterized by the same behavior on $\eta, \chi_{1,2}$ as the inspiral multipoles at leading PN order computed in Ref. [187]. The comparison was performed not only during the plunge, but also $10M$ after the quadrupole peak. Interestingly, the PN-like templates well describe the (22), (21), (33), (44) multipoles after the merger has occurred, while they fail to capture the other odd $\ell + m$ multipoles. This result hints that only some multipoles retain in the ringdown the same structure they had during the inspiral, while others are more sensitive to the merger itself and get modified, for instance, due to mode-mixing.

Recent efforts have been dedicated to studying more complex binary configurations and the imprints left on the ringdown spectrum; for instance, Ref. [81] and Refs. [80, 83] discussed eccentric mergers and precessing systems, respectively.

As mentioned above, after the multipole peak, the numerical waveform saturates to the ringdown while emitting an *early-times transient* that lasts approximately $\sim 15M$ [11, 12]. Different proposals have been explored to describe this transient, ranging from the presence of high-overtones [13, 59] to non-modal non-linearities.

Overtones have a short lifetime, hence, if they are excited close to the merger, we can expect their most significant contribution to the total luminosity to be confined near this time. However, it was shown in Refs. [40, 84] that no more than $n \lesssim 2$ overtones can be confidently identified. In particular, higher overtones $n \gtrsim 2$ are *parametrically unstable*, meaning that the fitted amplitudes and phases are not smooth against small changes in the fit starting time or in the progenitors' binary parameters. We can identify two main factors preventing overtones $n \gtrsim 2$ extraction from numerical data: unknown noise sources or non-modal physics content not accounted for in the template Eq. (4.4). For instance, close to the peak non-linear effects might be relevant, as will be discussed shortly. The plunge source could yield non-modal effects that swamp high-overtones, see Chapter 7, and, at the same time, contribute to a time-dependence of the QNMs amplitudes and phases at early times. The tail contribution to the luminosity is larger close to the peak, compared to late times, and high overtones might decay below this signal early on after being excited, due to their short lifetime. To summarize, while a constant amplitude and phase QNMs template cannot be applied at early times when we expect overtones to be the loudest, at later times, once their amplitudes are constant, other effects competing in magnitude with the overtones are likely to be present. To extract higher overtones, a more detailed template, beyond Eq. (4.4), is needed. If other physical content is not explored nor accounted for, and the analysis is carried out with Eq. (4.4) and a large number of overtones, there is the risk of overfitting [40, 188].

The other proposal to describe the early times transient signal is based on non-linear effects. For instance, after a common horizon is formed, the BH spacetime described by (M_0, J_0) is perturbed and emits a signal composed of QNMs. However, part of this radiation is reabsorbed through the horizon, causing the BH's mass and spin to evolve $M_0 + \delta M$, $J_0 + \delta J$, exciting QNFs relative to these new parameters. This process is denoted as *absorption induced mode emission* (AIME) and has been extensively investigated in Refs. [51, 52, 53, 54]. Stationary ringdown templates, e.g. Eq. (4.4), are written in terms of the final mass and spin $M = M_f$, $J = J_f$, describing the BH spacetime once it has reached its equilibrium configuration;

for this reason, we expect that these templates might fail at early times. However, AIME effects are not sufficient to explain the transient behavior leading the waveform from its peak towards the stationary ringdown phase [54].

It is also important to mention non-linear effects of *modal* nature investigated by the literature. Pairwise coupling of QNMs in the second-order perturbation source yields a non-linear signal written as a superposition of exponentially damped sinusoids. The "parent" linear QNFs uniquely determine their complex frequencies, and these non-linear modes are denoted as quadratic QNMs [42, 43, 44, 45, 46, 178] (QQNMs). The coupling between linear order QNMs yields precise selection rules for the QQNMs; e.g. the coupling between two fundamental modes in the quadrupole leads to a QQNM in the $(\ell m) = (44)$ multipole. As a consequence, except in head-on collisions, QQNMs do not enter the quadrupole waveform but only affect higher multipoles. Quadratic QNMs in the $(\ell m) = (44), (55)$ and in the $(\ell m) = (20), (40)$ for head-on collisions, have been identified in numerical waveforms, through a posteriori fitting schemes [47, 48, 40, 49].

A detailed review of the topics and results discussed in this section can be found in Ref. [108].

4.2 Phenomenological models

In the previous section, we discussed efforts to understand the *modal* content of the post-merger signal. In the current, we focus on the literature devoted to constructing *phenomenological models* able to reproduce a numerical multipole from the time of its peak onwards, in a closed form through a parametrized template.

Initially, the same template introduced in Eq. (4.4) was used to describe numerical multipoles, from their peak to late times. Ref. [13] employed a superposition of $N = 3$ QNMs with complex amplitudes $A_{\ell mn} e^{i\phi_{\ell mn}}$ and final BH mass M_f and spin J_f as free parameters to be inferred from numerical data, while the complex frequencies were fixed to perturbation theory predictions $\omega_{\ell mn}(M_f, J_f)$. In Ref. [58] the same template was used, Eq. (4.4), but a new approach to compute the amplitudes was introduced: $A_{\ell mn}$, $\phi_{\ell mn}$ for each mode were fixed by requiring a smooth transition from the analytical inspiral-plunge waveform $h^{\rm insp-pl}_{\ell m}(t)$ to the post-merger one $h^{\rm QNMs}_{\ell m}$ at the time of the orbital frequency maximum $t_{\rm match}$. In particular, given N QNMs in the post-merger template, it was required a C^{N-1} differentiability of the waveform at the matching time, i.e.

$$\frac{d^k}{dt^k}\left[h^{\rm insp-pl}_{\ell m}(t) - h^{\rm QNMs}_{\ell m}(t)\right]_{t=t_{\rm match}} = 0 \ , \quad k = 0, ...N-1 \, . \tag{4.8}$$

In Ref. [189], another technique for the matching was proposed, requiring the analytical waveform to be C^0 on an extended *matching region* centered at the time of the orbital frequency peak $t_{\rm merge}$. In particular, given N QNMs, the following condition is required

$$h^{\rm insp-pl}_{\ell m}(t_{\rm match} + k\Delta_t) - h^{\rm QNMs}_{\ell m}(t_{\rm match} + k\Delta_t) = 0 \ , \quad k = -\frac{N-1}{2}, -\frac{N-1}{2}+1, ...\frac{N-1}{2} \, , \tag{4.9}$$

for a fixed Δ_t. Ref. [190] combined the two methods, by imposing continuity of the waveform and its first and second derivatives in a matching region, while later work of Ref. [191] impose continuity of

the waveform and its first derivative only. More importantly, Ref. [190] found that for non-precessing, spinning progenitors, the lowest real frequency among the QNFs is much higher than the orbital frequency at the time of the matching (i.e. near its peak). As result, the semi-analytical waveform frequency saturates much faster to the fundamental mode value, not reproducing the slow-growth observed in numerical data. This problem was solved in Ref. [190] by adding to the QNMs superposition a *pseudo*-QNM with complex frequency fine-tuned to reproduce the numerical waveform exactly. This result can be explained through the previous section discussion: a pure, constant amplitudes/phases QNMs description is only valid some time $\sim 15M$ after the peak of the multipole $t_{\rm peak} \sim t_{\rm match}$, while early times are dominated by a (yet unknown) transient.

Ref. [179] investigated the near-merger transient in numerical waveforms, with particular attention to the growth of the instantaneous frequency $f_{\ell m}$ of each multipole (ℓm), rescaled with respect to m, $f_{\ell m}/m$. It was observed that $f_{\ell m}/m$ evolves monotonically and is reminiscent of an activating function saturating to the multiple fundamental mode frequency. For this reason, Ref. [179] proposed the parametrized expression

$$\begin{aligned} m^{-1} f^{\rm fit}_{\ell m}(t) &= \Omega_i + (\Omega_f - \Omega_i) \cdot \left(\frac{1 + \tanh\left[\ln \sqrt{\kappa} + (t - t_0)/b\right]}{2} \right)^{\kappa} , \\ \Omega_i &= \Omega_f - \frac{b}{2} \dot{\Omega}_0 \left(1 + \frac{1}{\kappa}\right)^{\kappa+1} , \end{aligned} \tag{4.10}$$

with Ω_f, $\dot{\Omega}_0$, κ, b, t_0 free parameters to be fitted from numerical multipoles. The model in Eq. (4.10) was tested against numerical waveforms for different (ℓm) and different mass-ratios $q \sim [1, 6]$, showcasing excellent agreement from $t \approx t_{\rm peak} - 20M$ up to late times, with $t_{\rm peak}$ time at which the multipole amplitude is the largest.

State-of-the-art current EOB models employ a purely phenomenological model for the merger-ringdown portion of the waveform, suggested for the first time in Ref. [73], inspired by this "activating" behavior. The proposal of Ref. [73] is to factor out the fundamental mode $(\ell m 0)$ from the post-merger waveform and impose a specific time dependence for its amplitude and phase

$$h_{\ell m}(t) = A_{\ell m}(t) e^{i\phi_{\ell m}(t)} \cdot e^{-i\omega_{\ell m 0} t} . \tag{4.11}$$

At early times, we expect the amplitude of the multipole $A_{\ell m}(t)$ to be an increasing function of time t, since the matching time is close to the orbital frequency peak, preceding the multipole amplitude peak. The time-dependence of the amplitude and phase includes unmodeled non-linear and source-dependent content as well as overtones. These effects decay quickly and, at late times, we expect $h_{\ell m}(t)$ to be dominated by the constant amplitude and phase fundamental mode. It is reasonable to assume that the transition between these limits is smooth and that $A_{\ell m}$, $\phi_{\ell m}$ behave as *activating functions*. Ref. [73] tested this intuition against numerical evolutions finding that $A_{\ell m}(t)$, $\phi_{\ell m}(t)$ follow an *hyperbolic tangent*-like behavior, encapsulated in the following templates

$$\begin{aligned} A_{\ell m}(t) &= c_1^A \ \tanh\left(c_2^A t + c_3^A\right) + c_4^A , \\ \phi_{\ell m} &= -c_1^{\phi} \ \ln\left(\frac{1 + c_3^{\phi} e^{-c_2^{\phi} t} + c_4^{\phi} \, e^{-2c_2^{\phi} t}}{1 + c_3^{\phi} + c_4^{\phi}} \right) , \end{aligned} \tag{4.12}$$

where some parameters are fixed by imposing continuity constraints at the matching time, while others are fitted against a numerical waveform.

It is important to stress that the template in Eq. (4.12) describes both perturbative waveforms in the EMR limit and non-linear ones in the comparable masses case, showcasing yet again how non-linearities are suppressed in a black-hole binary merger. This result, then, provides a valuable insight into how to investigate the transient, since it hints that results found on the easier, perturbative EMR limit could later be generalized to the non-linear comparable masses case.

While it does not qualify as a phenomenological post-merger model, it is important to discuss the toy model introduced in Ref. [75] for the QNMs excitation, a useful starting point for the original results of this thesis. In Ref. [74], a heuristic picture for the QNMs excitation was proposed. This intuition is that the orbital frequency growth during the plunge quasi-resonantly excites the QNMs as it sweeps their real frequencies. Due to the QNFs' complex nature and since the maximum orbital frequency (reached at the light-ring crossing) is always below the fundamental QNF, a real resonance never occurs. However, in this picture, the fundamental mode and the first overtones' amplitudes can accumulate over a time interval close to the orbital frequency maximum. In Ref. [75], this intuition is used to create a toy model describing the QNMs excitation.

The QNMs response originated from a compact initial-data perturbation of a Schwarzschild BH can be written as a superposition of constant-amplitude, exponentially-damped sinusoids. The complex frequencies of these modes are identified through the multipole numbers (ℓm), the overtone number n and the sign of their real frequency. Hence, for fixed (ℓmn), the QNM solution $\psi_{\ell mn}$ to the homogeneous Regge-Wheeler/Zerilli problem, is

$$\psi_{\ell mn}(t) = C_{\ell mn+} e^{-i\omega_{\ell mn+} t} + C_{\ell mn-} e^{-i\omega_{\ell mn-} t}\,, \tag{4.13}$$

see Chapter 2 for more details. Following Ref. [75], this ansatz can be considered as the solution of a damped harmonic oscillator

$$\ddot{\psi}_{\ell mn} + 2\alpha_{\ell mn}\dot{\psi}_{\ell mn} + (\alpha^2_{\ell mn} + \sigma^2_{\ell mn})\psi_{\ell mn} = 0 \tag{4.14}$$

where we have used the $(\dot{\cdot})$ to denote differentiation with respect to the time coordinate t and we have defined $\alpha_{\ell mn} \equiv \mathrm{Im}(\omega_{\ell mn})$, $\sigma_{\ell mn\pm} \equiv \mathrm{Re}(\omega_{\ell mn\pm})$ as the imaginary and real component of each QNF $\omega_{\ell mn\pm}$, respectively.

Following Ref. [75], we introduce a driving force on the right-hand side of Eq. (4.14), e.g. $\tilde{f}_{\ell m}(t)$ defined in Eq. (A.4) of Appendix A for a test-particle source

$$\ddot{\psi}_{\ell mn} + 2\alpha_{\ell mn}\dot{\psi}_{\ell mn} + (\alpha^2_{\ell mn} + \sigma^2_{\ell mn})\psi_{\ell mn} = \tilde{f}_{\ell m}(t) \tag{4.15}$$

This new problem admits as a solution

$$\psi_{\ell mn}(t) = C_{\ell mn+}(t) e^{-i\omega_{\ell mn+} t} + C_{\ell mn-}(t) e^{-i\omega_{\ell mn-} t}\,. \tag{4.16}$$

Working under the assumptions of slow-varying amplitudes $C_{\ell mn\pm}(t)$ (with respect to the real frequency $\sigma_{\ell mn\pm}$), Ref. [75] computed the following solution

$$C_{\ell mn\pm}(t) = C_{\ell mn\pm}(t_0) + \frac{i}{2\sigma_{\ell mn\pm}} \int_{t_0}^{t} dt' \, \tilde{f}_{\ell m}(t') \cdot e^{i\omega_{\ell mn\pm} t'} \, . \tag{4.17}$$

This toy model describes the excitation of each QNM as the overlap integral between the driving force and the damped sinusoid representing the mode. The source function oscillates as $\tilde{f}_{\ell m}(t) \propto e^{-im\varphi(t)}$ where $\varphi(t)$ is the azimuthal coordinate of the test-particle, that can be approximated as $\varphi(t) \approx \Omega(t)t$, with $\Omega(t)$ (instantaneous) orbital frequency of the test-particle. Hence, the overlap integral is large when the orbital motion $m\Omega(t) \approx \sigma_{\ell mns}$ and suppressed otherwise: this model perfectly encapsulates the physical intuition of Ref. [74]. Ref. [75] computed numerically the activation functions for the fundamental mode and its mirror mode and some overtones $n \leq 3$; for higher overtones, non-physical features appear showing the toy model breakdown. The findings show that the fundamental mode is more excited with respect to its mirror mode, consistent with the quasi-resonant picture. As the overtone number n increases, the difference in excitation between the mode and its mirror one is less appreciable. This result can be explained by remarking that quasi-resonant effects are not present for large n due to the extremely short life-times of these modes [75].

4.3 Bayesian approach to ringdown modelling

In this section, we introduce an algorithm to analyze numerical waveforms data, based on Bayesian inference methods. We use this algorithm to re-derive some known results, in particular, to investigate the modal content of comparable-mass, non-spinning BBH waveforms, after the merger. Once we identify the (220), (221), (320) as the loudest modes in the quadrupole, we focus on the (220) and investigate its dependence on the mass ratio, to reproduce the analysis of Ref. [11]. Finally, we introduce some new results on the ringdown of Kerr-Newman non-linear mergers.

4.3.1 Bayesian inference

Suppose we have a dataset X_n of n-points, each corresponding to a time step, together with a model M predicting the data behavior, written in closed form in terms of N parameters a_i for $i = 1, ...N$, as $\mathrm{M}(a_i)$. We differentiate between two types of parameters: fixed and free; fixed parameters are assumed to be known quantities, while we want to *infer* the free parameters from the numerical data. Note that it is still possible to have some *a priori* information on the free parameters. Even if not sufficient to fix them, such information can still give valuable aid in the analysis. In particular, we construct a probability distribution, called *the prior* $P(a_i; M)$, containing all known information on the free parameters.

We wish to obtain the probability distribution $P(a_i; M, X_n)$ reflecting how well the model M and the parameters a_i can describe the dataset X_n. This distribution is called *posterior* and it can be computed by means of the *Bayes theorem* [192]:

$$P(a_i; M, X_n) = \frac{P(X_n; a_i, M) \cdot P(a_i; M)}{P(X_n; M)} \, . \tag{4.18}$$

In the above, we have introduced the *likelihood* $P(X_n; a_i, M)$ and the *evidence* $P(X_n; M)$, defined respectively as the probability distribution of the data given the model M and parameters a_i and its marginalization over the whole parameter space obtained weighting each $P(X_n; a_i, M)$ with the prior $P(a_i)$.

We consider datasets containing an unknown component ("noise") on top of the *true signal* we wish to investigate. For simplicity, we consider each data point X_n as drawn from a Gaussian distribution centered at the true value $\bar{X}_n$ and characterized by variance σ_n. Then, assuming that the true value is given by the model M, i.e. $\bar{X}_n = M(a_i)$, the likelihood can be written as follows

$$P(X_n; a_i, M) = \frac{1}{\sigma_n \sqrt{2\pi}} \exp\left[-\frac{1}{2}\left(\frac{X_n - M(a_i)}{\sigma_n}\right)^2\right] \tag{4.19}$$

This approach is an approximation leveraging a prediction for the physical content of the signal and a minimal understanding of the numerical noise. As discussed in the next section, if multiple waveform resolutions are available, the variance at each time step can be computed directly. If only a single resolution is available, the numerical noise can still be estimated heuristically at each time step. These assumptions amount to fixing the first two moments of the underlying distribution at each time step. Then, according to the *principle of maximum entropy* [192], the Gaussian distribution with the prescribed mean and variance is the best approximation to the "true" distribution that does not impose any assumptions beyond the specified information. This approximation introduces a limitation in our approach: to reliably extract subleading physical features, one would require both a more accurate signal model and a more detailed characterization of the noise.

In what follows, we agnostically focus on uniform prior distributions $P(a_i; M)$ (also denoted as *flat* prior). This implies that

$$P(a_i; M) = \theta(a_i - a_{\min}) \cdot \theta(a_{\max} - a_i)\,. \tag{4.20}$$

for some boundary values $[a_{\min}, a_{\max}]$.

With the above assumptions, in Eq. (4.18) the posterior distribution for the values a_i is proportional to the likelihood; hence, finding the parameters that best describe the data, assuming the model is correct, reduces to the problem of maximizing the exponential in Eq. (4.19) or, equivalently, minimizing the exponent therein. Error bars on the best parameters can be obtained as the interval of parameters containing 95% of the posterior; this is denoted as 95% confidence interval.

Note that the problem we wish to solve may not be restricted to determine the best parameters a_i to describe the data through a specific template: we might also want to test and compare different models. This can be done by comparing the evidence $P(X_n; M^k)$ for each M^k, the model with the largest evidence can be considered to best describe the data. Moreover, $P(X_n; M)$ is a useful tool to understand whether we are *overfitting* the data, or if adding more free parameters a_i is physically meaningful: if adding more a_i does not improve the evidence, we can disregard the additional information added to our model.

Model selection can also be performed by comparing the marginalized posterior probabilities of each model $P(M^k; X_n)$. The ratio of posteriors for two models M^1 and M^2 is related to the evidence ratio by

$$\frac{P(M_1; X_n)}{P(M_2; X_n)} = \frac{P(X_n; M_1)}{P(X_n; M_2)} \frac{P(M_1)}{P(M_2)}\,, \tag{4.21}$$

where $P(M^k)$ denotes the prior probability assigned to model M^k. Comparing posteriors incorporates more information than comparing evidences alone, as it includes prior assumptions about each model. In the following, to remain as agnostic as possible, we assign equal prior probabilities to different models, hence comparing posteriors or evidences becomes equivalent.

4.3.2 Software: `bayRing`

In the previous section, we presented a theoretical framework to estimate the parameters for which a given model best describes the data. Now, we are going to discuss a Python package which implements this algorithm and is targeted to analyze the ringdown in numerical simulations of compact objects' binary mergers.

The algorithm is called `bayRing` [193] and is based on the *nested sampling* algorithm as implemented in the CPNest package [194]. The general idea behind the algorithm is to explore the parameter space by evaluating the likelihood at various points (known as "live points", abbreviated in "nlive") drawn according to the prior distribution. Since we assume a uniform prior, compact in a certain domain, the sampler initially draws points uniformly within this domain. The term "nested" refers to the way the algorithm progressively explores nested shells of increasing likelihood. At each iteration, the point with the lowest likelihood is removed and replaced by a new point sampled from the prior, but constrained to have a likelihood greater than a given threshold. This threshold increases over time, allowing the algorithm to concentrate its exploration around the region of highest likelihood, while also computing the Bayesian evidence and producing posterior samples. To remove possible influences of the initial point at which the stochastic exploration starts, every posterior evaluation is repeated for four different random initial seeds and the posteriors of each evaluation are combined.

Finally, we set the error in our likelihood. We are going to work with waveforms contained within the SXS catalog [156]. For this dataset, two main sources of errors exist: finite numerical resolution, and approximate extrapolation of the waveform from a compact numerical domain to future null infinity. For each binary configuration, the catalog contains results at multiple resolutions and extrapolation orders. To account for this finite accuracy in our results, the variance σ is computed, at each time step, as

$$\sigma_n \equiv \sqrt{\left(X_n^{N,E}\right)^2 - \left(X_n^{N-1,E}\right)^2} + \sqrt{\left(X_n^{N,E}\right)^2 - \left(X_n^{N,E+1}\right)^2}\,. \tag{4.22}$$

where we have used the superscripts N, E to respectively denote the resolution level and extrapolation order of the numerical waveform analyzed. If only one waveform is available (as for the Kerr-Newman waveforms we will investigate), σ_n is fixed to a constant value for all n, set by the numerical floor of the evolution.

4.3.3 Ringdown of Kerr BHs: identifying the modes

In this section, we focus on non-spinning, uncharged BH binary mergers and investigate the *modal content* of the quadrupole $(\ell m) = (22)$ signal. We investigate how many modes can be extracted from

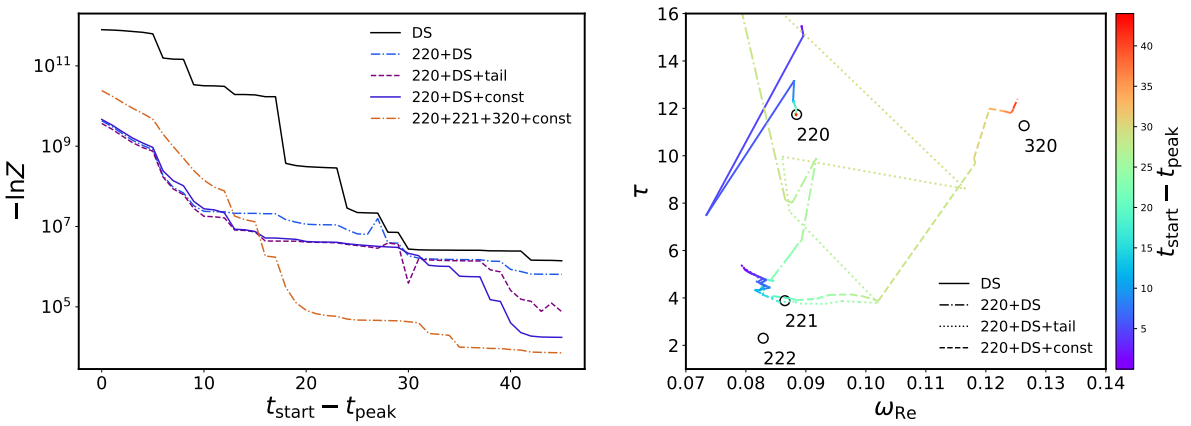

Figure 4.3: Parameter estimation results for the simulation SXS:0305 (mass-ratio $q \simeq 1.2$) with the algorithm `bayRing` [193], assuming the models in the labels. Left: Evidence Z of each model as a function of the starting time of the fit $t_{\rm start}$, quoted with respect to the time at which the waveform quadrupole reaches its maximum value $t_{\rm peak}$. Right: Real frequency $\omega_{\rm Re}$ and decay time τ recovered by the agnostic search. Each point represents the maximum posterior value obtained starting the inference at $t_{\rm start}$, shown on the color bar.

the numerical signal through the Bayesian inference algorithm `bayRing` [193], discussed in Sec. 4.3.2. We focus on the simulation labeled by SXS:0305, characterized by a mass-ratio $q \simeq 1.2$. We consider different models for our analysis:

- Exponentially damped sinusoids templates

$$h_{\ell m}(t) = \sum_{i=0}^{k} \bar{A}_i e^{i\phi_i} \cdot e^{-i\omega_i t - t/\tau_i}\,, \tag{4.23}$$

  with real amplitudes $\bar{A}_i$, phases ϕ_i, real frequencies ω_i and decay rates τ_i as free parameters to be inferred from the data. We will use the following notation for such models: kDS.

- QNMs superposition templates

$$h_{\ell m}(t) = \sum_{\ell' n} \bar{A}_{\ell' mn} e^{i\phi_{\ell' mn}} \cdot e^{-i\omega_{\ell' mn} t - t/\tau_{\ell' mn}}\,, \tag{4.24}$$

  where only real amplitudes $\bar{A}_{\ell' mn}$ and phases $\phi_{\ell' mn}$ are free parameters of the inference problem while real frequencies $\omega_{\ell' mn}$ and decay rates $\tau_{\ell' mn}$ are fixed to the perturbation theory values as functions of the final BH mass M_f and spin J_f extracted from the simulations. Mirror modes contributions are ignored, as they are negligible for the parameter space we will be considering. We will use the following notation for such models $(\ell' m0) + (\ell' m1) + ...(\ell' mn)$.

- QNMs superposition plus exponentially damped sinusoids templates

$$h_{\ell m}(t) = \sum_{i=0}^{k} \bar{A}_i e^{i\phi_i} \cdot e^{-i\omega_i t - t/\tau_i} + \sum_{\ell' n} \bar{A}_{\ell' mn} e^{i\phi_{\ell' mn}} \cdot e^{-i\omega_{\ell' mn} t - t/\tau_{\ell' mn}}\,, \tag{4.25}$$

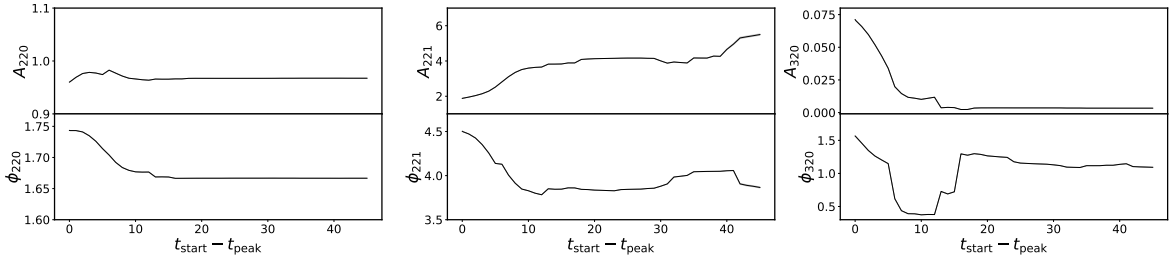

Figure 4.4: Parameter estimation results for the simulation SXS:0305 (mass-ratio $q \simeq 1.2$) with the algorithm `bayRing` [193], assuming as model (220) + (221) + (320) + const. On the top row, we show the amplitudes as rescaled with respect to the peak, $A_{\ell' mn} = \tilde{A}_{\ell' mn} e^{-i\omega_{\ell' mn} t_{\rm peak}}$ where $\tilde{A}_{\ell' mn}$ is the parameter inferred from the algorithm and $A_{\ell' mn}$ is the result we plot above. On the bottom row, we show the phases. On the left/center/right, results relative to the damped sinusoid with complex frequency fixed to that of the (220)/(221)/(320) mode, respectively. Note that phases have been unwrapped.

where the free parameters are the real amplitudes $\bar{A}_i$, $\bar{A}_{\ell' mn}$, phases $\phi_i, \phi_{\ell' mn}$, and, for the damped sinusoid part of the template, also the frequencies ω_i and decay rates τ_i. The quantities $\omega_{\ell' mn}$, $\tau_{\ell' mn}$ are instead fixed to the perturbation theory QNFs as functions of M_f and J_f. We will use the following nomenclature for these templates $(\ell' m0) + (\ell' m1) + ...(\ell' mn) + k$DS.

- Templates with a late-time dominating behavior, such as a constant

$$h_{\ell m}(t) = h_{\ell m}^{QNMs+DS}(t) + (C_{\rm Re} + iC_{\rm Im}) \,, \tag{4.26}$$

with $C_{\rm Re}$, $C_{\rm Im}$ fixed parameters a priori known, or a late-time tail

$$h_{\ell m}(t) = h_{\ell m}^{QNMs+DS}(t) + A_{\rm tail} e^{i\phi_{\rm tail}} t^{-p_{\rm tail}} \,, \tag{4.27}$$

with $A_{\rm tail}$, $\phi_{\rm tail}$, $p_{\rm tail}$ as free parameters. In the above equations, $h_{QNMs+DS}$ indicates one of the templates in Eqs. (4.23), (4.24) or (4.25). We will then use the following nomenclature for a template with a fixed constant $(\ell' m0) + ... + (\ell mn) + k$DS + const and $(\ell' m0) + ... + (\ell mn) + k$DS + tail for a template with a tail.

For all the analyses presented below, we will use uniform priors for the inference free parameters, with the following wide boundary values

$$\begin{aligned} &A_i \in [10, 150] \quad , \quad \phi_i \in [0, 2\pi] \quad , \quad \omega_i \in [-0.318, 0.318] \quad , \quad \tau_i \in [1, 50] \\ &A_{\ell' mn} \in [10, 150] \quad , \quad \phi_{\ell' mn} \in [0, 2\pi] \,, \end{aligned} \tag{4.28}$$

and we consider a sampler of size nlive = 64. For each template we consider, the inference procedure is repeated, varying the starting times in the range $t_{\rm start} - t_{\rm peak} \in [0, 45M]$, namely cropping an increasing fraction of the data, aiming to target the regions where our perturbative description does not apply. Since by definitions the parameters appearing in our template are considered to be constant, their value should not depend on the portion of data included (within error bars). Hence, the parameter estimation is

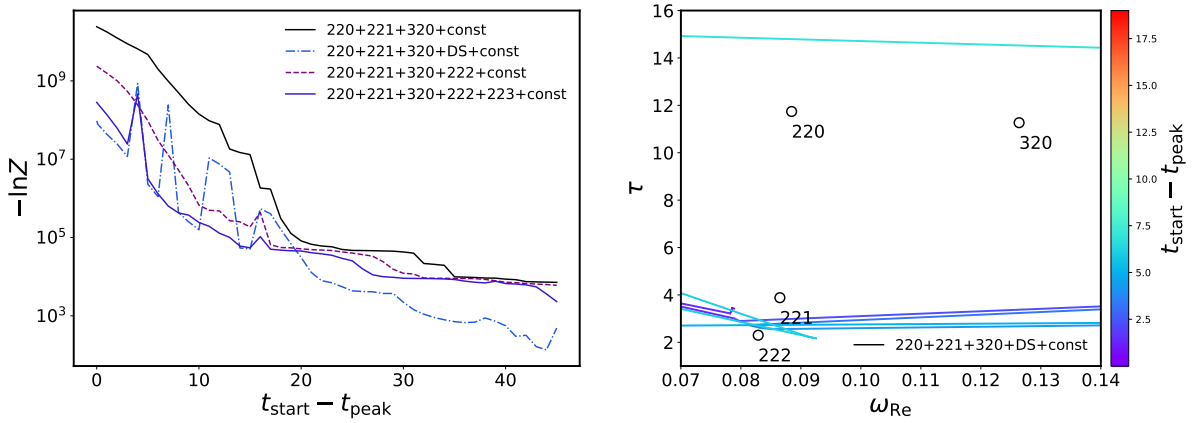

Figure 4.5: Parameter estimation results for the simulation SXS:0305 (mass-ratio $q \simeq 1.2$) with the algorithm `bayRing` [193], assuming different models, as reported in the labels. Left: Evidence Z of each model as a function of the starting time of the fit $t_{\rm start}$ quoted with respect to the time at which the waveform quadrupole reaches its maximum value $t_{\rm peak}$. Right: Real frequency $\omega_{\rm Re}$ and decay time τ recovered by the agnostic search. Each point represent the maximum posterior value obtained starting the inference at $t_{\rm start}$, shown on the color-bar.

considered successful only if the recovered parameters are approximately constant (within error bars) for a large enough time interval. Otherwise, the model might be failing, as a consequence of unmodeled physics or noise.

The first analysis that we will perform is denoted as *agnostic search*: the idea is to consider a template 1DS and identify the dominant mode ($\ell' mn$) in the numerical data, then to repeat the analysis for a template ($\ell' mn$) + 1DS to search for the next "loud" mode. The same algorithm is performed again, so that at each iteration the template contains all the QNFs previously identified plus a single damped sinusoid. The results of this procedure are shown on the right-panel in Fig. 4.3, where we show the evolution of the free parameters ω_i, τ_i as function of the starting time of the inference (identified by the color bar); note that we rescale the time with respect to the time $t_{\rm peak}$ at which the quadrupole amplitude reaches its maximum value. The agnostic search first iteration, with template 1DS, converges towards the fundamental mode (220) frequency. The second iteration, (220) + 1DS, identifies for earlier starting times $t_{\rm start} \lesssim t_{\rm peak} + 20M$ a mode with frequency close to the final BH (221) frequency, while at late times the parameters ω_i and τ_i evolve towards small and large values respectively. This result can be explained, at early times, by considering that overtones are generally short-lived, so we expect them to decay below other features of the signal at late times. Moreover, the small discrepancy between the recovered frequency and the (221) QNF of the final BH could be due to the fact that mass and spin of the BH are still evolving at early times and have not yet saturated to M_f, J_f. The late-time result hints that the template in Eq. (4.23) is not suited to describe the waveform for $t \gg t_{\rm peak}$ and we should instead investigate a non-oscillating template, e.g. a late-time tail. In Fig. 4.7, we show the late-time behavior of several simulations of the SXS catalog, including the SXS:0305: at late times the waveforms are dominated by a zero-frequency behavior. For this reason, we perform a new inference test with template (220) + 1DS + tail, yielding a minimal improvement

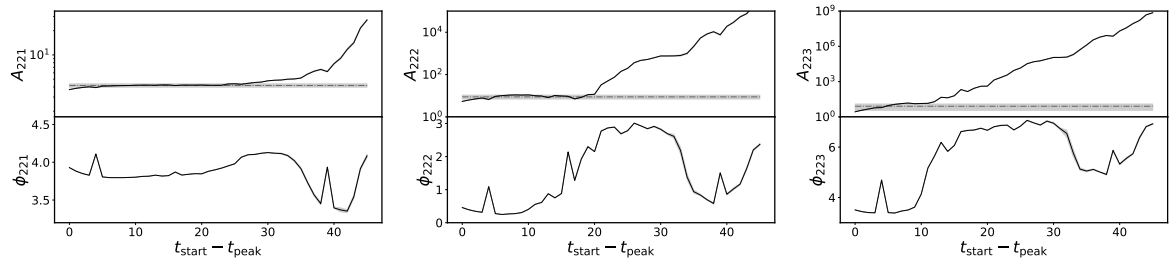

Figure 4.6: Parameter estimation results for the simulation SXS:0305 (mass-ratio $q \simeq 1.2$) with the algorithm `bayRing` [193], assuming as model (220) + (221) + (320) + (222) + (223) + const. On the top row, we show the amplitudes as rescaled with respect to the peak, $A_{\ell' mn} = \tilde{A}_{\ell' mn} e^{-i\omega_{\ell' mn} t_{\rm peak}}$ where $\tilde{A}_{\ell' mn}$ is the parameter inferred from the algorithm and $A_{\ell' mn}$ is the result we plot above. On the bottom row, we show the phases. On the left/center/right, results relative to the damped sinusoid with complex frequency fixed to that of the (221)/(222)/(223) mode, respectively. The horizontal lines correspond to the mean value of the amplitudes in the intervals $t_{\rm start} - t_{\rm peak} \in [0, 30M]/[0, 20M]/[0, 10M]$, respectively. The opaque regions represent the associated standard mean deviations. Note that phases have been unwrapped.

in the recovery of ω_i, τ_i at late times: the inferred frequency is close to the final BH (221) mode one for a longer time, but converges again towards a non-modal behavior for $t_{\rm start} \gtrsim 25M + t_{\rm peak}$.

From Fig. 4.7 we see that the simulation SXS:0305 seems to be dominated by a spurious numerical constant. For this reason, we perform a trial and error approach: we first assume the simplest possible template for the numerical error of SXS:0305, a constant, and infer this value by fitting the waveform at late times, yielding the following result

$$C_{\rm Re} + iC_{\rm Im} = 7.976 \cdot 10^{-6} - i\, 1.802 \cdot 10^{-5}\,. \tag{4.29}$$

Then, we reiterate the agnostic search with template (220) + 1DS + const, fixing the constant to the value above. The results for the free parameters ω_i, τ_i are shown in the right panel of Fig. 4.3; for early starting times, the inference procedure yields the same results as with other templates, identifying a mode with frequency close to the final BH (221) QNF. However, at intermediate times, the frequency recovered by the damped sinusoid evolves until it converges near the final BH (320) QNF. The presence of this mode is expected due to mode-mixing. This result can be interpreted as follows: the (221) is more excited than the mode-mixing (320), hence dominates the waveform close to its peak. However, the decay rate of the (221) is faster and, after a certain amount of time, this mode decays below the (long-lived) (320). The presence of spurious numerical constants was later confirmed by independent studies in the literature [49], and can be cured by transforming to the correct Bondi–Metzner–Sachs frame [84].

The above results are supported by the behavior of the evidence (denoted by Z), compared among all the different models we discussed, plotted on the left panel of Fig. 4.3. At early starting times $t_{\rm start} \lesssim 30M + t_{\rm peak}$, the model (220) + 1DS improves the evidence (i.e. lowers $-\ln Z$) by several orders of magnitude with respect to the (220) template, hinting further at the presence of the (221) at early times.

Adding a (free) tail or a (fixed) constant to the template (220)+1DS+tail or (220)+1DS+const significantly improves the evidence with respect to (220) + 1DS only for late starting times $t_{\rm start} \gtrsim 30M + t_{\rm peak}$. In particular, inserting the constant into the model yields higher evidence than adding a late-time tail.

The agnostic search discussed above hints at the presence of the (220), (221), (320) modes in the numerical quadrupole. We now move to the next step of the inference investigation, aimed at estimating the real amplitudes and phases of these QNMs. We repeat the parameter estimation test, for different starting times, considering the template (220) + (221) + (320) + const. We show in Fig. 4.4 the behavior of $A_{\ell' mn}$, $\phi_{\ell' mn}$ vs the time $t_{\rm start}$ at which the inference procedure is started, with rescaled amplitude $A_{\ell' mn}$ defined as $A_{\ell' mn} = \bar{A}_{\ell' mn} e^{-i\omega_{\ell' mn} t_{\rm peak}}$. If the variation of the recovered amplitudes and phases with respect to $t_{\rm start}$ is significant, it is an indication that the model we impose on the data is not appropriate, but the algorithm is still "trying" to reproduce other numerical features with our template. Hence, we need to identify the interval of $t_{\rm start}$ for which the inferred parameters are constant inside the error bars, estimated as the 95% *credible interval* of the posterior (i.e. given a parameter inside the error bar, there is 95% probability that it is the true parameter according to the posterior). We can then average values of $A_{\ell' mn}$, $\phi_{\ell' mn}$ inside these intervals, and assume these values as final, numerical estimates of the QNMs complex amplitudes.

From the results in Fig. 4.4, we see that the inferred parameters of the (220) are (approximately) constant inside the error bars, for times $t_{\rm start} \gtrsim 10M + t_{\rm peak}$, this time interval changes to $t_{\rm start} - t_{\rm peak} \in [\sim 10M, \sim 40M]$ for the overtone (221) and to $t_{\rm start} \gtrsim 20M + t_{\rm peak}$ for the (320) mode coming from the mixing. In the next section, we will repeat this procedure for several systems, characterized by different mass-ratios q in order to investigate the dependence of A_{220} on q.

We now extend the search to higher overtones by repeating the agnostic search with a template (220) + (221) + (320) + 1DS + const. The results for the inferred ω_i, τ_i are shown on the right panel of Fig. 4.5; the recovered values of τ_i are close to the final BH (222) damping time. However, the real frequency ω_i cannot be resolved by the algorithm, and oscillates over its prior interval. This result implies that overtones with $n > 2$ have magnitude comparable to numerical noise or other un-modelled physical signals, e.g. non-linear contribution. Hence, it is not possible to agnostically recover these modes without first handling these other subtleties, which are beyond the scope of our investigations. This result is compatible with past literature, e.g., with Ref. [40].

We perform a final analysis to investigate higher overtones, fixing the free frequencies to their QNFs; in particular, we consider the templates (220) + (221) + (320) + (222) + const and (220) + (221) + (320) + (222) + (223) + const. In the left panel of Fig. 4.5, we compare the evidence of these models with the ones of (220) + (221) + (320) + 1DS + const and (220) + (221) + (320) + const. For late starting times, the evidence significantly improves for the template with the free-damped sinusoid, however, by these times, the damped sinusoid in the model is not recovering any modal content, but rather a zero-frequency signal. Hence this result is only stressing the necessity of a better modelization of the noise or other physical features. Adding overtones with $n > 1$ to the template greatly improves the evidence at early times, however, the recovered amplitudes are constant, inside the error bars, for progressively shorter time

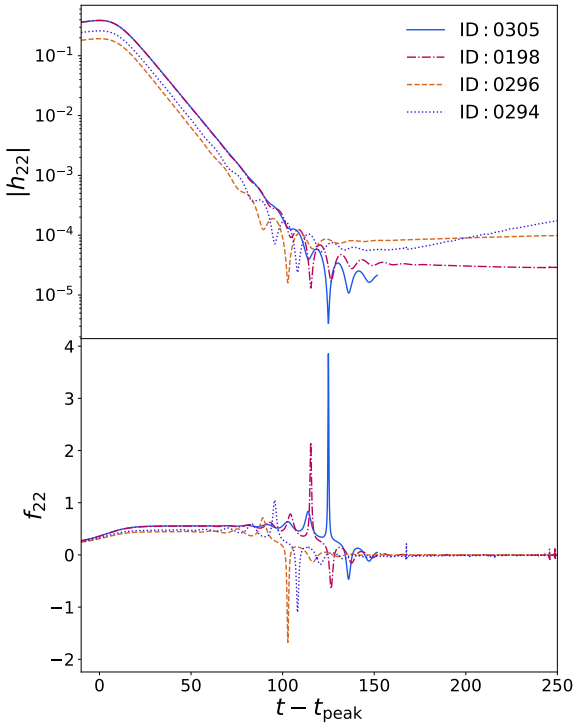

Figure 4.7: Amplitude (top) and instantaneous frequency (bottom) of the mode $(\ell m) = (22)$ vs the time, translated with respect to the amplitude peak. Different colors correspond to different numerical waveforms as shown in the labels, listed in Table 4.1.

SXS : ID	q	η
0305	1.221	0.247
0198	1.202	0.248
0259	2.499	0.204
0200	3.272	0.179
0294	3.499	0.172
0295	4.499	0.149
0296	5.499	0.130
0192	6.579	0.115
0195	7.761	0.101
0199	8.729	0.0922
0196	9.663	0.0849

Table 4.1: On the left, ID of the SXS waveform, mass-ratio q on the center column and symmetric mass-ratio η on the right.

intervals $t_{\text{start}} - t_{\text{peak}} \lesssim 30M, 20M, 10M$ respectively for the modes (221), (222), (223). Hence, we cannot confidently conclude if overtones with $n > 1$ are present in the waveform, and further analysis with a more detailed noise characterization or a different template accounting for other physical features is needed.

These results show that our framework is appropriate to extract QNM information from numerical simulations, yielding results compatible with the linearized theory. However, they also underline the limitations of a purely phenomenological approach: other than noise, the signal could contain (even at linear perturbative order) un-modelled physics beyond constant-amplitude QNM superpositions. These contributions require a first-principles approach to be appropriately characterized, the subject of Chapter 7. Moreover, an analytical model for the QNMs amplitudes could provide more stringent priors, aiding the parameter estimation.

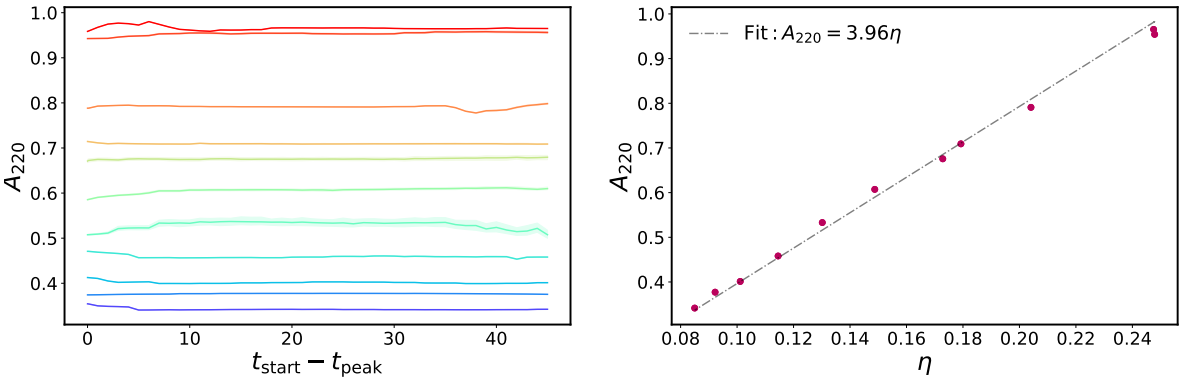

Figure 4.8: Left: Rescaled-to-peak amplitudes of the (220) mode vs the starting time of the inference analyses translated with respect to the time of the peak. Different colors are relative to the different numerical waveforms in Tab. 4.1. The analyses are performed with the algorithm `bayRing` [193], assuming as model (220) + (221) + (320). Right: Purple points are the average (220) mode amplitude A_{220} for the different simulations in Tab. 4.1, vs the symmetric mass ratio of the simulation η. The dot-dashed grey line is the result of a linear fit of the data, Eq. (4.31).

4.3.4 Ringdown of Kerr BHs: impact of the mass-ratio

After having characterized in detail a single binary configuration, we now extend our investigation to a set of binary mergers with varying parameters. We start by investigating the dependence of the (220)-mode rescaled amplitude A_{220} on the progenitors' mass ratio. In particular, we will focus on the symmetric mass-ratio, defined as

$$\eta = \frac{m_1 m_2}{M^2}\,, \tag{4.30}$$

with $m_{1,2}$ as progenitors initial masses. To extract A_{220} from numerical data, we use the Bayesian inference algorithm `bayRing` [193] and assume a template (220) + (221) + (320). The analysis is repeated, varying the starting time of the inference analysis $t_{\rm start} - t_{\rm peak} \in [0, 45M]$, for all the simulations in Table 4.1.

Note that we do not include any constant in the templates, unlike in the previous section: some waveforms are characterized by a zero-frequency noise with a clear time-dependence, as shown in Fig. 4.7. In principle, a detailed characterization of the noise for each waveform could be performed, but since we now focus only on the loudest mode, well-above the noise floor for a prolonged time interval, this is not needed,

We identify the values of $t_{\rm start}$ at which the rescaled quantity $A_{220} = \bar{A}_{220} e^{-i\omega_{220} t_{\rm peak}}$ is approximately constant as the interval $t_{\rm start} - t_{\rm peak} \in [5M, 40M]$ and we compute mean value $A^{\rm av}_{220}$ and standard deviation of A_{220} inside this region, for each η. The results are shown in Fig. 4.8: on the left-panel, we show the rescaled amplitude A_{220} vs the starting time of the inference procedure, for all the different simulations considered, while on the right-panel we show the behavior of the inferred $A^{\rm av}_{220}$ along with error bars given by the standard deviation. We fit the data with a linear template $A^{\rm av}_{220} = a \cdot \eta$, motivated by the behavior of the (22) PN multipole in the inspiral [187]. We determine a by minimizing the chi-squared χ^2 value; the

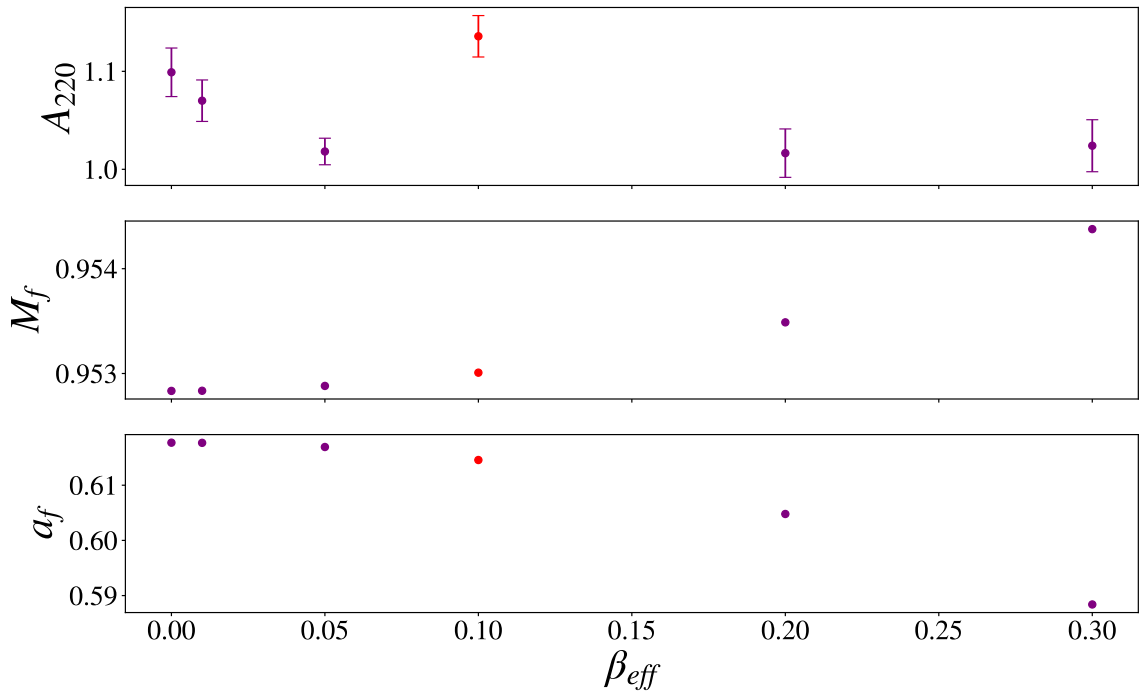

Figure 4.9: Inferred amplitude of the (220) mode rescaled with respect to $t_{\rm peak}$ (top), final BH mass M_f (center) and final BH spin a_f (bottom) as function of the effective charge parameter $\beta_{\rm eff}$ as defined in Eq. (4.32). Values are relative to different numerical evolutions of initially non-spinning charged BHs with the same charge-to-mass ratio $\beta_i = q_i/m_i$ and mass-ratio $q = 1.241$. The red dot highlights the only data point which does not follow the trend for the amplitude A_{220}.

result yields

$$A_{220}^{\rm av} = a \cdot \eta \ , \quad a = 3.964 \pm 0.001 \ . \tag{4.31}$$

The above result is consistent with the value found in Ref. [11, 12]. The important remark, however, is the agreement with the leading order PN-expression of the inspiral (22) multipole: it hints at the possibility of analytically computing QNMs amplitudes through the inspiral source multipoles. We will come back to this point in Chapter 7.

4.3.5 Ringdown of Kerr-Newman BHs: effective charge imprints

Previous works focused on the impact of different orbital configurations [80, 81, 83], mass-ratios [76, 11, 49, 69, 82] and progenitors' spins [77, 12, 49, 69, 82] on the QNMs amplitudes in the ringdown. It is interesting to investigate then how the picture changes if we consider progenitors described by a solution more generic than Kerr. We will focus on Kerr-Newman BHs and add an electric charge Q to the BHs in the inspiral binary. Non-linear solutions of these systems were computed for the first time numerically in Refs. [164, 165], focusing on non-spinning progenitors in quasi-circular orbits, through the EinsteinToolkit [195].

We have analyzed six numerical waveforms of this (private) charged-BH catalog, characterized by mass-

ratio $q = 1.241$ and different progenitors charges; in particular, we focus on BHs with charges of the same sign and such that the charge-to-mass ratios $\beta_i \equiv q_i/m_i$ of the progenitors coincide $\beta_1 = \beta_2$. In the same fashion as Refs. [77, 11, 12], we build a PN-inspired *effective charge* parameter, as follows

$$\beta_{\rm eff} = \frac{m_1\beta_1 + m_2\beta_2}{m_1 + m_2} \quad , \quad \beta_i = \frac{q_i}{m_i} \,, \tag{4.32}$$

where $m_{1,2}$ and $q_{1,2}$ are the progenitors masses and charges respectively. As shown in Fig. 4.9, the final BH mass M_f and spin $a_f = J_f/M_f$ are clear functions of $\beta_{\rm eff}$, with a non-linear trend. We are then motivated to try to use this quantity to parametrize the QNMs amplitudes, in particular, focusing on the (220) mode.

We have performed an inference analysis with the algorithm `bayRing` [193] on the numerical data, assuming as template (220) and imposing as QNFs the values computed in Ref. [196] as functions of the final BH parameters (M_f, J_f, Q_f), varying the starting times in $t_{\rm start} - t_{\rm start} \in [0, 45M]$. In the region $t_{\rm start} - t_{\rm start} \in [5M, 40M]$, the rescaled amplitudes A_{220} are (approximately) constant inside the error bars. We compute, for each simulation, mean and standard deviation of this quantity. The values we obtain are shown on the top panel of Fig. 4.9: except for one simulation, the values appear to follow a clean dependence on the charge parameter. We leave the exact nature of this dependency to future work. However, we note that a PN model for the inspiral BHs orbit and the emitted waveform monopoles could provide an ansatz in terms of $\beta_{\rm eff}$ or even provide a better quantity to parametrize the amplitude. An interesting avenue of future investigation will be to extend to this non-linear regime the EMR results found in [197], where the $\ell = 1$ electromagnetic modes were found to contribute to the gravitational multipoles for high-enough charges.

4.4 Concluding remarks

The above discussion highlights that the post-merger waveform, once a stationary ringdown is reached, shows clear imprints of the progenitors' inspiral. However, the analytical computation of such dependence has not yet been achieved. At the same time, an understanding of the early stages of the post-merger waveform is still lacking, and (known) non-linear effects fail to capture the dominating transient behavior for $t \lesssim 15 + t_{\rm peak}$.

An analytical computation of the amplitudes' dependence on the binary configuration would naturally start in the EMR limit. What would be the extent of the validity of such a result to the comparable-mass regime discussed here? A hint of the fact that the comparable-mass regime could be well described (at least in a first approximation) by a perturbative calculation comes from the phenomenological models described in Eq. (4.12). These can describe the post-peak transient and smoothly connect it to late times, when the slowest decaying mode dominates the ringdown. An interesting result is that the same time-dependence of Eq. (4.12) was found to accurately describe the transient for both the EMR limit and the comparable masses case. Albeit mass-ratio corrections and background changes will necessarily need to be included in the free coefficients entering such templates, this is a powerful hint that the same underlying physical mechanism is likely active in the transient for both EMR and comparable-mass regimes. These results suggest we go back to perturbation theory and model the transient and the QNMs response as excited by

a *two-body problem* rather than in vacuum, from a first-principles, purely-analytical approach. A clear insight into the EMR perturbative limit could then point towards new results in the comparable-masses fully non-linear case. This investigation is the subject of Chapter 7.

Chapter 5

Late-time tails: extreme mass ratio mergers

In Chapter 2, we investigated the response of a black hole (BH) in vacuum to an initial-data perturbation, at linear order. We showed that the late-time response of the BH is governed by an inverse power-law behavior denoted as Price's law [121, 17, 14, 15]. This effect originates from the back-scattering of small frequency components of the perturbation, from the long-range curvature of the background. If the observer is at finite distance, then the late-time signal behaves as $t^{-2\ell-3-a}$, with $a = 0$ for initial data with $\partial_t\psi(t = 0, r) \neq 0$ and $a = 1$ for $\psi(t = 0, r) \neq 0,\ \partial_t\psi(t = 0, r) = 0$ [121, 17, 122, 123, 126]. If the observer is at future null infinity $\mathcal{I}^+$, then the late times are dominated by an inverse power law decay in the retarded time $\tau \equiv t - r_*$, as $\tau^{-\ell-2-a}$, with $a = 0,\ 1$ as above [14, 124, 126].

In the presence of matter, e.g. for a BH perturbed by an infalling test particle , this back-scattering problem was studied analytically by Blanchet and Damour [198, 199, 200] in the context of Multipolar Post-Minkowskian (MPM) theory and by Poisson et al. [201, 138]. In particular, the former investigations showed that the tail is a *hereditary* effect carrying information on the entire history of the system. These works focused on the inspiral stage, while little attention has been paid to hereditary effects in the post-merger phase of a binary merger.

Ref. [75] performed numerical evolutions of BH binary mergers in generic orbits within a perturbative setting, incorporating radiation-reaction effects through an analytical expression based on post-Newtonian (PN) results, and resummed according to Effective One Body (EOB) techniques [147]. This study unexpectedly found an enhancement of several orders of magnitude of the tail amplitude when increasing the progenitors' binary eccentricity, resulting in an earlier transition from a quasi-normal modes (QNMs) to a tail-dominated regime. The mechanism behind this enhancement was initially unknown, since no first-principles investigation of the late-time tail excitation was available. This result was later explained in Ref. [1], where an explicit modelization of hereditary contributions to the post-ringdown signal of binary mergers was put forward. In this chapter, we discuss this original result.

Another set of investigations was initially attempted to explain the late-time phenomenology of Ref. [75]. Ref. [55] showed that a source behaving as $\sim \delta(r_* - v_s t) r^{-\beta}$, with v_s constant velocity and $\beta \geq 0$, propagated through the prompt response Green's function in Eq. (2.93), can originate a new late-time inverse power-law decay, different from Price's law. However, through a series of numerical experiments, Ref. [55]

found that this new effect is only present for unbound systems: if the system ends in a merger, the late times are dominated by Price's tail. The reason behind this finding is that the "new tail" introduced in Ref. [55] is not hereditary (as Price's law is), rather instantaneous: once the source emitting this signal has vanished, the effect disappears from the full waveform. As a consequence, the "instantaneous tail" of Ref. [55] cannot explain the late-time phenomenology observed in Ref. [75]. However, an interesting by-product of the analysis in Ref. [55] is the prediction of a new non-linear term at late times. In fact, a persistent source at late times, after the merger has occurred, and with the correct fall-off in r, is present at higher perturbative orders. Through a series of numerical experiments, Ref. [55] found that the second order source of the multipole $\ell = m = 4$ (decaying as $S \propto r^{-2}$ at large distances) does indeed generate at late times a new *instantaneous second order tail effect*, behaving as an inverse power-law with a slower fall off than Price's law. We will come back to this result and its implications in Sec. 6.4 and Chapter 8.

In this chapter, we discuss the derivation of an explicit integral formula capable of predicting the late-time tail enhancement, connecting tail terms to properties of the test-particle non-circular motion in the inspiral, and matching the eccentricity dependence found within previous numerical evolutions. The expressions introduced for the *source-driven* tail are relevant to any kind of non-spinning binary merger, as showcased by applying them not only to eccentric binaries, but also to dynamical captures and radial infalls. We find a much more complex behavior compared to the predictions of source-free perturbation theory, with a non-monotonic variation in the tail exponent at intermediate times, due to a superposition of a large number of exact power-laws. In the asymptotic $\tau \to \infty$ limit, homogeneous perturbation theory results are instead recovered. In particular, asymptotic perturbations of systems that become bounded and eventually merge behave as Price's law ($\tau^{-\ell-2}$). Finally, to single out the reason behind the enhancement of tail terms with eccentricity, we carry out two additional sets of investigations. First, we study changes in the tail when integrating over different portions of the inspiral motion, isolating the dominant contribution to the tail excitation, and characterizing the key role of the motion around the last apastron. Second, through an expansion in large r and small tangential velocities, we show how an eccentric binary, which spends a larger fraction of time at large distances just before merger, can emit tail signals that are both enhanced and constructively interfere with each other.

The chapter is structured as follows. First, in Sec. 5.1, we introduce our perturbative framework and discuss the RWZHyp code [93, 94], used to evolve the binary system and numerically solve for the emitted gravitational strain. Then, in Sec. 5.2, we present the analytical model of the source-driven tail. Sec. 5.3 is dedicated to test the model predictions against numerical evolutions of eccentric binaries, dynamical captures, radial infalls and scattering configurations. In Sec. 5.4, we identify the mechanism behind the tail enhancement with binary eccentricity, and highlight the key contribution of motion around the last apastron. In Sec. 5.5 we discuss a parametrization of the signal amplitude at the time the tail starts dominating over the QNMs, in terms of different progenitor's binary parameters: the eccentricity at the separatrix and the impact parameter, Eq. (5.21), at the light-ring crossing. In Sec. 5.6, we characterize the tail term as a superposition of a large number of inverse power-laws. While the main focus of the chapter

is the radiative tail observed at $\mathcal{I}^+$, in Sec. 5.7 we briefly discuss the tail observed at finite distances. In Sec. 5.8 we summarise the results presented.

Unless explicitly stated, we work in geometric units $c = G = 1$ and assume all quantities are rescaled with respect to the central black hole mass M.

5.1 Perturbative and numerical framework

Our analysis focuses on small mass ratios, thus we linearize Einstein's equations and discard higher-order corrections. We impose both the BH and infalling test particle to be initially non-spinning. Since we are working at linear perturbative order, the remnant (post-merger) BH is also consequently non-spinning. The background metric is thus the Schwarzschild metric:

$$ds^2 = -A(r)dt^2 + \frac{dr^2}{A(r)} + r^2 d\Omega^2 \,, \tag{5.1}$$

with $A(r) = 1 - 2/r$. We expand the strain observed at large distances $r \gg 1$ in spin-weighted -2 spherical harmonics modes ${}_{-2}Y_{\ell m}(\Theta, \Phi)$:

$$h_+ - \mathrm{i} h_\times = \sum_\ell \sum_{m=-\ell}^{\ell} h_{\ell m}(t) {}_{-2}Y_{\ell m}(\Theta, \Phi) \,. \tag{5.2}$$

As discussed in Chapter 2, it is possible to build to gauge invariant quantities that transform under parity as $(-1)^\ell$ and $(-1)^{\ell+1}$ denoted $\Psi^{(\mathrm{e})}_{\ell m}$ and $\Psi^{(\mathrm{o})}_{\ell m}$ respectively. These quantities are directly related to the strain multipoles in Eq. (5.2) through

$$h_{\ell m} = \frac{1}{r}\sqrt{\frac{(\ell+2)!}{(\ell-2)!}}\left(\Psi^{(e)}_{\ell m} + i\Psi^{(o)}_{\ell m}\right) + O\left(\frac{1}{r^2}\right) , \tag{5.3}$$

where, depending on the parity of $\ell + m$, only one of the two terms on the right-hand side vanishes. As discussed in Chapter 2, the functions $\Psi^{(e/o)}$ satisfy two (decoupled) inhomogeneous Schrödinger-like equations, the Regge-Wheeler/Zerilli (RWZ) equations Eqs. (2.20), (2.25), that we rewrite here as

$$O^{(e/o)}\Psi^{(e/o)}_{\ell m}(t, r_*) = S^{(e/o)}_{\ell m}(t, r), \tag{5.4}$$

where we have introduced the Regge-Wheeler/Zerilli operators $O^{(e/o)}$ as

$$O^{(e/o)} \equiv \left[\partial_t^2 - \partial_{r_*}^2 + V^{(e/o)}_{\ell m}(r_*)\right], \tag{5.5}$$

In the following, when it is not necessary to distinguish the two cases, we will drop the superscripts (e/o).

The potentials in the equation above are the RWZ ones [202, 92], Eqs. (2.21), (2.26), and the driving source is built from the in-falling particle stress-energy tensor [92]. As a consequence, it is localized along the particle trajectory $r(t)$ at all times. This feature can be made explicit by writing

$$S^{(e/o)}_{\ell m} = f^{(e/o)}_{\ell m}\delta(r - r(t)) + g^{(e/o)}_{\ell m}\partial_r\delta(r - r(t)) \,. \tag{5.6}$$

In Appendix A we report the full expressions of the functions $f_{\ell m}^{(e/o)}, g_{\ell m}^{(e/o)}$ for a point-particle, as found in Ref. [92].

In the present work, we will compute analytical and numerical solutions of the Cauchy problem given by Eq. (5.4), always using as initial conditions:

$$\Psi_{\ell m}(t=0,r) = \partial_t \Psi_{\ell m}(t=0,r) = 0\,. \tag{5.7}$$

These initial conditions are not physical. In fact, realistic systems emit gravitational waves from the moment they are created. Effectively, Eq. (5.7) means neglecting all the history of the system before a certain time and thus imposing a formally incorrect solution. This implies a partial loss in information, but also an initial transient in which the emitted radiation does not correspond to a real, physical solution of the linearised Einstein equations and, for this reason, is commonly denoted as "junk radiation". In Appendix B, we motivate the negligible influence of junk radiation on our results, determining the approximate initial conditions of Eq. (5.7) as appropriate for our purposes.

Unless specified, the trajectory of the particle will always be computed numerically, solving the system of Hamiltonian equations [100] introduced in Chapter 3

$$\begin{aligned}
\dot{r} &= \frac{A}{\hat{H}} p_{r_*}\,, \\
\dot{\varphi} &= \frac{A}{r^2 \hat{H}} p_\varphi, \\
\dot{p}_{r_*} &= A\hat{\mathcal{F}}_r - \frac{A}{r^2\hat{H}}\left(p_\varphi^2 \frac{3-r}{r^2} + 1\right), \\
\dot{p}_\varphi &= \hat{\mathcal{F}}_\varphi\,,
\end{aligned} \tag{5.8}$$

where (p_{r_*}, p_φ) are the μ-rescaled momenta conjugate to the variables (r_*, φ), and $\hat{H}$ is the μ-rescaled Hamiltonian of a test particle in Schwarzschild background of Eq. (3.9), that we rewrite as

$$\hat{H} = \sqrt{A\left(1 + \frac{p_\varphi^2}{r^2}\right) + p_{r_*}^2}\,. \tag{5.9}$$

Finally, $\hat{\mathcal{F}}_r$ and $\hat{\mathcal{F}}_\varphi$ are the components of the dissipative force that drives the dynamics, whose general expression can be found in [147, 101]. These quantities are analytical, built from a PN-based, EOB-resummed analytical expansion for the fluxes of energy and angular momentum observed at infinity, as computed in [101, 147]. Such fluxes have been shown to be consistent with the corresponding numerical expressions in Ref. [75], hence consistent with emission of gravitational waves (GWs) computed from the evolution. More details on these radiation-reaction forces are discussed in Sec. 3.4. It is important to note that at the operational level, the GW expressions obtained as numerical output of the evolution will *not* directly enter the particle trajectory within our implementation. Hence, the trajectory is not informed by the numerical waveform. This approach will be a key point when feeding the particle trajectory as input to our semi-analytical computations used to derive a prediction for the GW strain, ensuring that numerical errors in the numerically-computed GWs (against which we will compare the prediction obtained) cannot contaminate the semi-analytical predictions.

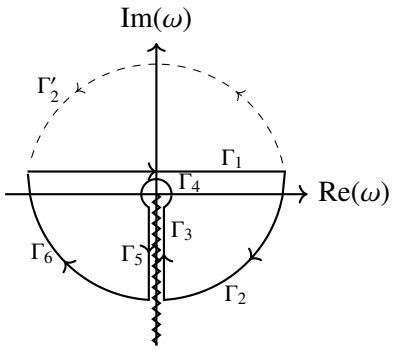

Figure 5.1: Schematic representation of the complex-frequencies plane relative to the integrand in Eq. (2.81). The zig-zagged line is the branch cut in the integrand. Thick and dashed lines represent two possible closed contours: $\Gamma_1 + \Gamma_2'$ and $\Gamma_1 + \Gamma_2 + \Gamma_3 + \Gamma_4 + \Gamma_5 + \Gamma_6$.

To solve the problem in Eq. (5.4)-(5.7)-(5.8) numerically, we employ the time-domain code RWZHyp[1] [93, 94]. The software uses a homogeneous grid in tortoise coordinate r_* and, at large distances, a hyperboloidal layer (over which r_* is compactified [126]) is attached to the standard computation domain, where the trajectory evolves. We define ρ to be the compactified coordinate and τ the retarded time in the layer. The coordinates of the layer (τ, ρ) are connected to those of the standard computational domain (t, r_*) as follows:

$$\tau - \rho = t - r_* \,. \tag{5.10}$$

The hyperboloidal layer allows for the extraction of the GW strain at future null infinity $\mathcal{I}^+$ at a finite location ρ_+. The grid in r_* ends, for negative values, at a finite quantity, in order to keep the horizon outside of the computational domain. The code uses double precision, hence our computations will have a precision of at most $\sim 10^{-16}$. Numerical strain values close to this threshold will be considered dominated by numerical error. In Appendix B, we also show that the numerical resolution used in all the results discussed below is adequate for our purposes and does not affect any of the results obtained below.

Due to the inclusion of radiation reaction, the trajectory is non-linear. By feeding this trajectory into the source for the linearized perturbations, we obtain a treatment that is not formally consistent with first-order perturbation theory. In Chapter 1, we provide arguments supporting the validity of this approach. In Chapter 8, we discuss which of the results in this chapter remain valid within a first-order perturbation theory framework. For the results that rely on the inclusion of dissipative effects in the dynamics, we also outline a future direction to render them formally consistent with first-order perturbation theory.

5.2 Long-range propagation in curved backgrounds with a source

5.2.1 General solution

The general solution of Eqs. (5.4)-(5.7), in terms of the Schwarzschild coordinates (t, r), can be written as the convolution

$$\Psi_{\ell m}(t, r) = \int_{-\infty}^{t} dt' \int_{-\infty}^{\infty} dr' \, S_{\ell m}(t', r') \, G_{\ell}(t, t'; r, r') \, . \tag{5.11}$$

Where $G_\ell(t, t'; r, r')$ is the Green's function, defined as solution to the impulsive problem

$$\hat{O}|_{t,r_*} \, G_{\ell}(t, t'; r, r') = \delta(t - t') \, \delta(r - r') \, . \tag{5.12}$$

Note that we assume homogeneous boundary conditions on the Green's function, for all times, at $r'_* \to \pm\infty$. In Sec. 2.2.2, we have reviewed the derivation of the propagator controlling the tail, which can be obtained in the limit of large r', r and small frequencies[2] $\omega M \ll 1$, following Refs. [14, 106]. The former approximation is connected to the tail being due to the corrections to the flat light-cone propagator, arising from the long-range spacetime curvature [14, 198, 15]. The latter approximation encodes the fact that small frequency waves are the ones interacting the most with the curved geometry on large scales [16, 14, 15], and implies that the propagator we derive is the retarded Green's function only in the limit of large retarded times τ compared with the source retarded time, $\tau \gg t' + \rho_+$.

We introduce an additional factor to the time domain radiative tail propagator in Eq. (2.85), by adding a causality condition that follows from the choice of the *retarded* GF, instead of the *advanced* one. As discussed in Sec. 2.2.2, in Fourier domain the GF, $\tilde{G}_{\rm Tail}(\omega; r, r')$ in Eq. (2.81), is singular at $\omega = 0$. To perform the anti-transform and compute the GF in time domain, $G_{\rm Tail}(t - t'; r, r')$, we analytically continue ω into the complex plane. The singularity $\omega = 0$ corresponds to a branch-point, due to the multi-valued nature of the complex logarithm $\ln \omega$ appearing in $\tilde{G}_{\rm Tail}(\omega; r, r')$ expression. While the branch point is fixed, the location of the branch-cut is not predetermined; we have fixed the branch-cut on the negative imaginary axis following Ref. [14, 15]. In doing so, we have selected the retarded GF, while fixing the branch-cut on the positive imaginary axis would have selected the advanced one. In fact, with the branch cut in the lower-half plane, we close the complex contour either with two quarters of circumference of radius $|\omega| \to \infty$ on the lower half plane, or with a semi-circle of radius $|\omega| \to \infty$ in the upper half plane, as shown in Fig. 5.1. The choice is made by requiring that the exponential in the anti-transform integrand Eq. (2.82) is well behaved inside the whole complex contour. We rewrite this exponential in the code coordinates Eq. (5.10) as

$$e^{-i\omega(t-t'-r_*)} = e^{-i\omega(\tau-t'-\rho_+)} \, . \tag{5.13}$$

For $\tau - t' - \rho_+ > 0$, Eq. (5.13) is regular if we close the contour on the lower half plane. Then, when $\tau - t' - \rho_+ > 0$ we close the contour along the thick line in Fig. 5.1, $\Gamma_1 + \Gamma_2 + \Gamma_3 + \Gamma_4 + \Gamma_5 + \Gamma_6$, in the region where we fixed the branch-cut. For $\tau - t' - \rho_+ < 0$, instead, Eq. (5.13) is regular on the upper half plane; for these times we close the contour along the dashed line in Fig. 5.1, $\Gamma_1 + \Gamma'_2$, in a region where

[1] The version of the RWZHyp code bears the tag `tails`, on the `rwzhyp_eccentric` branch.

[2] In this section exclusively, we use explicit units of M to highlight the relevant scales.

there is no branch-cut. As a consequence, fixing the branch-cut at $\mathrm{Re}(\omega) = 0$, $\mathrm{Im}(\omega) < 0$, implies that the tail response is present only for $\tau - t' - \rho_+ > 0$.

Fixing the branch cut at $\mathrm{Re}(\omega) = 0$, $\mathrm{Im}(\omega) > 0$, would have yielded the tail response only at times $\tau - t' - \rho_+ < 0$.

Following the above reasoning, the retarded propagator of the late-time signal, assuming that the observer is located at $\mathcal{I}^+$, is

$$G_\ell(\tau, t'; \rho_+, r') = \theta(\tau - t' - \rho_+) \cdot \frac{(-1)^\ell 2^{\ell+1} \ell!(\ell+1)!}{(2\ell+1)!} \frac{(r')^{\ell+1}}{(\tau - t' - \rho_+)^{\ell+2}}\,, \tag{5.14}$$

with the Heaviside function to reinforce causality. Plugging in the result above in the general expression for the tail strain Eq. (5.11), together with the point-particle source expression Eq. (5.6), and considering an observer located at (τ, ρ_+), yields

$$\Psi_{\ell m}(\tau, \rho_+) = c_\ell \int_{-\infty}^{\tau-\rho_+} dt' \frac{r^\ell(t') \left\{ r \left[f_{\ell m}(t', r) - \partial_r g_{\ell m}(t', r) \right] - (\ell+1)\, g_{\ell m}(t', r) \right\}_{r=r(t')}}{(\tau - t' - \rho_+)^{\ell+2}}\,, \tag{5.15}$$

where we have denoted as $r(t')$ the value of r along the point-particle trajectory and we have defined the factor c_ℓ as

$$c_\ell = \frac{(-1)^\ell 2^{\ell+1} \ell!(\ell+1)!}{(2\ell+1)!}\,. \tag{5.16}$$

Note that $f_{\ell m}$ and $g_{\ell m}$ in the above are computed along the trajectory as well. In Appendix A, we show the full expressions of the functions $f_{\ell m}, g_{\ell m}$ for a point-particle, as computed in [92, 100]. The failure of our model for $\tau - \rho_+ \approx t'$ is made manifest by the upper limit of integration in Eq. (5.15), since the integrand is singular at this point. We can interpret this by stating that our model can describe signals travelling well inside the light-cone, but fails to describe signals marginally close to it. In the present work, we will focus our attention on systems that become bounded after a certain timescale, and we will limit our analysis to the post-merger signal. Since the source contribution to Eq. (5.15) dies exponentially after the light-ring crossing, we expect our results not to be influenced by the singularity in $t' \approx \tau - \rho_+$.

We briefly discuss systems that are unbounded at all times, e.g. scattering scenarios, in Sec. 5.3.5.

5.2.2 Intermediate vs asymptotic behavior

The analytic model for the tail, Eq. (5.15), is an integral over the entire past history of the source. For this reason, we expect the tail to show a more complicated phenomenology compared to what is predicted by source-free perturbation theory [16, 15, 126], reviewed in Sec. 2.3.2. In general, since the source is an oscillating function, the real and imaginary parts of the late-time waveform Eq. (5.15) are non-monotonic functions. Moreover, we cannot sort out from the integral a single power-law behavior in the observer retarded time τ, since the integral is rather a superposition of power-laws in τ with location of the asymptote (corresponding to the zero in the denominator) depending on the integration variable t'. Since the source decays exponentially after the light-ring crossing [75], there exists a certain timescale after which the source information will not affect the signal anymore, leaving place to a single pure power-law in τ dictating the asymptotic decay of the perturbation.

Two questions arise from the above intuition. The first concerns the timescale that an observer at $\mathcal{I}^+$ has to wait in order for the tail to be a single power-law, the second is relative to the value of the power-law exponent in this asymptotic limit. To answer the above questions, we start considering initially unbounded systems originating at a time $T_{\rm in}$, that become bounded after a certain timescale $T_{\rm bound}$ due to radiation reaction. For the moment, we assume that the observer is located at very late times $\tau \gg T_{\rm bound}$, after the merger has occurred. Then we can separate the integration domain in Eq. (5.15) accordingly, in an interval during which the system is unbounded, $(T_{\rm in}, T_{\rm bound})$, and one over which the system is bounded $(T_{\rm bound}, \tau - \rho_+)$. We focus first on the contribution to the late-time signal of the dynamics in the interval $(T_{\rm in}, T_{\rm bound})$, during which we assume the test particle to be in the far-away region $r' \gg M$, moving slowly. As a consequence, the spacetime curvature can be neglected and the test-particle trajectory can be approximated as $x_i(t) \simeq v_i t$ with v_i constant velocity, i.e. we expand the source Eq. (5.6) neglecting all terms $O(G)$ or higher, and work at lowest PN order. The source for the $(\ell, m) = (2, 2)$ mode can be written in terms of the (tt)-component of the particle stress energy tensor $T_{tt} = \mu\delta^3(x_i - v_i t)$, as

$$S_{22}^{(e)} \propto r T_{tt}^{(2,2)} = \mu \frac{\delta(r - |v|t)}{r} \,. \tag{5.17}$$

Plugging this expression in Eq. (5.15), yields

$$\psi_{\rm unbound}(\tau, \rho_+) \propto \int_{T_{\rm in}}^{T_{\rm bound}} dt' \frac{\mu |v|^2 t'^2}{(\tau - t' - \rho_+)^4} \,. \tag{5.18}$$

The integral above can be carried out analytically, and it reads

$$\psi_{\rm unbound} \propto \frac{(\rho_+ - \tau)^2 + 3\,(-\rho_+ + \tau)\,T_{\rm in} + 3{T_{\rm in}}^2}{3\,(\rho_+ - \tau - T_{\rm in})^3} - \frac{(\rho_+ - \tau)^2 + 3\,(-\rho_+ + \tau)\,T_{\rm bound} + 3{T_{\rm bound}}^2}{3\,(\rho_+ - \tau - T_{\rm bound})^3} \,. \tag{5.19}$$

When considering the limit $\tau \gg T_{\rm in}, T_{\rm bound}$, each of the terms in Eq. (5.19) gives a leading power-law contribution $\propto \tau^{-1}$, equal in modulo but opposite in sign. A similar cancellation can be found for the $\propto \tau^{-2}, \tau^{-3}$ contributions, leaving a dominant power-law $\propto \tau^{-4}$.

We now analyze the contribution to the late-time signal of the bounded dynamics. As mentioned above, after the light-ring crossing, the source decays exponentially [75], hence does the integrand in Eq. (5.15). If we let $T_{\rm f}$ be the time at which the source can be considered zero (up to a given precision), when performing an observation at times $\tau > \rho_+ + T_{\rm f}$, we can replace the upper limit of integration with $T_{\rm f}$. Then, we Taylor expand the integrand, assuming $\tau \gg T_{\rm f} + \rho_+$

$$\psi_{\rm bound}(\tau, \rho_+) = \frac{c_\ell}{\tau^{\ell+2}} \cdot \int_{T_{\rm bound}}^{T_{\rm f}} dt' S_\ell(t') \left[1 + \sum_{n=1}^{\infty} \frac{(\ell + 1 + n)!}{n!\,(\ell + 1)!} \left(\frac{t' + \rho_+}{\tau}\right)^n\right] , \tag{5.20}$$

where we denoted as $\psi_{\rm bound}(\tau, \rho_+)$ the contribution to the late-time signal of the bounded dynamics. The result in Eq. (5.20) is a superposition of power-law decays [3], with the smallest decay being $\propto \tau^{-\ell-2}$. We expect the importance of faster decaying terms to depend on the pre-merger dynamics, apart from the observer retarded time τ. As we move τ to progressively late times, the faster decaying contributions will

[3] Note that this result is fundamentally different from the one obtained in Ref. [15]. In the latter, power-laws corrections to the propagator giving rise to Price's law were computed. Instead, the propagator we consider is the same as the one through which Price's law can be derived.

e_0	$\hat{H}_0$	$p_{\varphi,0}$	r_0	b_{LR}	$e_{\rm sep}$	t_{LR}	$n_{\rm api}$
0.9	0.9890	3.9170	83.000	3.9315	0.869	14555	9
0.8	0.9791	3.8313	40.000	3.8881	0.778	5386	7
0.7	0.9713	3.7671	26.667	3.8429	0.670	6921	13
0.6	0.9649	3.7139	20.000	3.7998	0.563	8955	21
0.5	0.9587	3.6502	15.400	3.7699	0.483	5654	15
0.4	0.9538	3.6001	12.500	3.7400	0.393	4856	14
0.3	0.9525	3.6103	11.429	3.7075	0.276	14895	47
0.2	0.9484	3.5514	9.375	3.6909	0.201	7996	25
0.1	0.9453	3.5044	7.778	3.6766	0.114	3773	11
0.0	0.9449	3.5000	7.000	3.6693	0.000	4308	40*

Table 5.1: From left to right: initial eccentricity, initial energy and angular momentum, initial radius, impact parameter at the light-ring crossing, eccentricity at the separatrix crossing, time of the light-ring crossing and number of apastri. The results are relative to the eccentric and quasi-circular simulations. For eccentric orbits, we initialize the trajectory at an apastron, hence r_0 is the coordinate of the first apastron. For the quasi-circular case, we do not show the number of apastra, but show instead the number of orbits before the plunge. Note that the eccentricity decreases during the inspiral, but because of its definition in terms of radial turning points, it can increase close to the separatrix, as exemplified in Fig. 1 of [75].

eventually die off, leaving Price's law as the dominant component. The transient regime characteristic timescale depends on the *excitation coefficients* of each power-law contribution: the more enhanced these coefficients are, the longer the intermediate regime will be. From Eq. (5.20), these coefficients depend on an integral of the source $S(t')$ multiplied by a factor $(t'+\rho_+)^n$. Hence, the excitation coefficient of each power-law correction to Price's law depends both on the specific orbital dynamics under consideration and on the amount of inspiral history included in the evolution, for timescales at which the source is still appreciably excited. Instead, at very early past times, the source suppression will cut off the contribution of higher-order terms. We refer the reader to Sec. 5.6 for a quantitative discussion on the latter point.

To summarize, the above results show that, even if the system is initially in an unbounded configuration, the asymptotic relaxation is dominated by a $\tau^{-2-\ell}$ power-law, while the τ^{-1}, τ^{-2}, τ^{-3} contributions cancel out. This result is in agreement with the homogeneous perturbation theory literature [16, 14, 15]. The intermediate behavior of the tail in the post-merger phase can instead be approximated by a superposition of exact power-laws in τ, with expansion coefficients depending on the source history. In the following, we will apply this expansion from $T_{\rm in}$, for both initially and dynamically bounded systems. We briefly discuss in Sec. 5.3.5 the analytical prediction for the tail signal emitted in a scattering scenario.

$n_{\rm enc}$	$\hat{H}_0$	$p_{\varphi,0}$	r_0	b_{LR}	$e_{\rm sep}$	t_{LR}
1	1.000001	3.9980	300.0	3.9687	...	2650
2	1.000001	4.0065	300.0	3.9457	0.955	8059
3	1.000001	4.0150	300.0	3.9327	0.927	15947
4	1.000001	4.0235	300.0	3.9232	0.907	23827
5	1.000001	4.0320	300.0	3.9155	0.892	31878
6	1.000001	4.0405	300.0	3.9075	0.876	40228
7	1.000001	4.0447	300.0	3.8968	0.851	45037
8	1.000001	4.0490	300.0	3.8737	0.819	49786

Table 5.2: From left to right: number of encounters, initial energy and angular momentum, initial radius impact parameter at the light-ring crossing, eccentricity at the separatrix and time of the light-ring crossing. The results are relative to the dynamical capture simulations. The case $n_{\rm enc} = 1$ corresponds to a direct capture. In this case, there are no eccentric orbits before the merger, hence we do not report $e_{\rm sep}$.

5.3 Comparison with numerical results

We now analyze the (ℓm) multipolar components of the waveform produced by a particle orbiting around a Schwarzschild BH. The main focus will be on the (22) mode, as it is the loudest mode emitted by BBH mergers, while we briefly discuss results for the (32) and (44) modes in Subsec.5.3.4. The investigation of the (32) mode is interesting since it allows us to test our analytical prediction in Eq.(5.15) for perturbations in the odd sector. Moreover, this mode might become relevant for spinning BHs and hence could be of interest for future investigations on late-time tails. The (44) mode is the first in which quadratic QNMs appear. These modes are long-lived and may be comparable in magnitude to the tail at intermediate times. Thus, a correct characterization of tail signals in the (44) multipole could aid in the extraction of quadratic modes in non-linear numerical investigations.

We focus our attention on bounded orbits with varying eccentricities, on dynamical captures (i.e. initially unbounded orbits becoming bounded after some time due to radiation reaction), and finally on radial infalls from different distances. In Subsec. 5.3.5, we briefly discuss a scattering scenario (i.e., the particle arrives from infinity, has a close encounter with the BH, and then escapes to infinity again). In Fig. 5.2, we report examples of these different dynamics. In Table 5.1 and 5.2 we show the relevant parameters for each configuration considered. Note that we always impose the initial polar and azimuthal angles to be $\theta = \pi/2$ and $\varphi = 0$, respectively. For bounded orbits, we report the initial eccentricity and the number of apastri before merger. For dynamical captures, we show the number of encounters. For simulations ending in an eccentric merger, we report the eccentricity at the separatrix crossing time [4]. For all simulations, we show the initial energy and angular momentum, the initial distance from the BH in terms of the coordinate

[4]During the inspiral, the test particle can be assumed to move along eccentric stable orbits identified through the eccentricity e and the semi-latus rectum ι, as long as $\iota - 2e \geq 6$ is satisfied. Values of e and ι such that $\iota_{\rm sep} = 6 + 2e_{\rm sep}$ identify the last stable orbit, denoted as separatrix. We refer to Chapter 3 for a more thorough discussion of this topic.

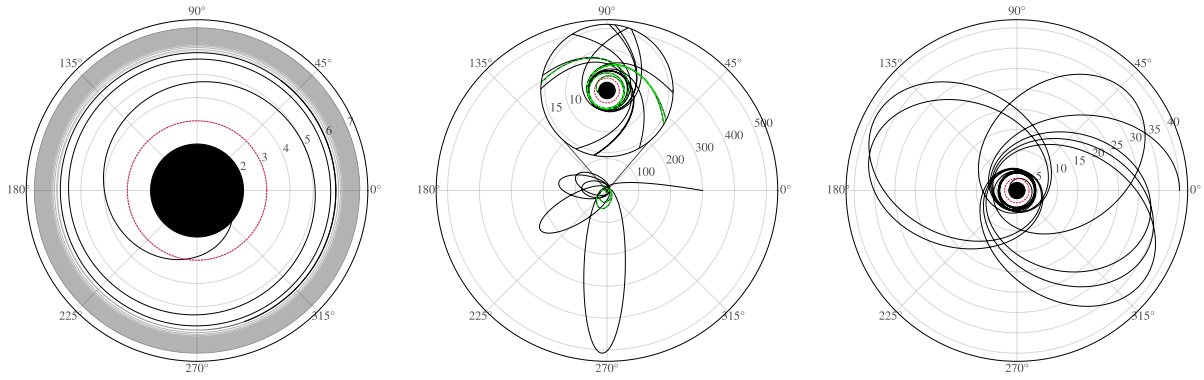

Figure 5.2: Left: quasi-circular inspiral and plunge, with test particle initialized at a distance $r_0 = 7.0$. Center: Dynamical capture configuration, with initial angular momentum $p_{\varphi,0} = 4.0405$. A zoomed-in view of the dynamics at smaller radii is shown in the inset. Right: trajectory of a test particle moving in an orbit with initial eccentricity $e_0 = 0.8$. The red line marks the light ring. The green line highlights the portion of the trajectory used in Fig. 5.15.

r_0, the time of the light-ring crossing and the impact parameter computed at the light-ring crossing b_{LR}, where we define b as the ratio [75, 203]

$$b = p_\varphi / \hat{H} \,. \tag{5.21}$$

The eccentricity is defined (for bounded systems) through its relation with the apastron and the periastron coordinates $r_{\rm apo,peri}$ of the orbit [147, 101, 75], as in Eq. (3.15). Note that the initial eccentricity alone is not enough to predict the dynamical evolution of a binary. Another parameter is necessary, e.g. the initial semilatus rectum, which can be computed from initial energy and angular momentum as in Eq. (3.17). For bounded orbits, we select a test-particle mass $\mu = 10^{-3}$, while, for simplicity, when simulating dynamical captures we set the test-particle mass to be $\mu = 10^{-2}$. This choice is because given certain initial conditions $(E_0, p_{\varphi,0})$, the test particle can either be directly captured by the central BH, have multiple close encounters before the merger, or scatter away. As discussed in Refs. [204, 163], the region within the parameter space $(E_0, p_{\varphi,0})$ for which captures involving multiple encounters are possible, decreases with the increase of the mass ratio. Hence, the larger is the mass of the test particle, the easier it is to obtain different multiple encounters simulations. Below, we will always show mass-rescaled quantities so that this choice will not affect our results. Finally, we analyze five different radial infalls, with the test particle of mass $\mu = 10^{-2}$, initial energy $E_0 = 1.00$ and angular momentum $p_{\varphi,0} = 0.0$, from different initial distances $r_0 = \{100, 200, 300, 400, 500\}$. The time of the light-ring crossing in these configurations is $t_{LR} = \{496, 1370, 2495, 3825, 5331\}$ respectively. The trajectory of the test particle in the aforementioned settings is computed numerically by means of the RWZHyp code, as detailed in Sec. 5.1. We use the same code to obtain the numerical (linear) waveform produced by the motion of said systems, as observed at $\mathcal{I}^+$, to test the model introduced in the previous section. In particular, we plug the numerical trajectory solved

by RWZHyp in the integral form Eq. (5.15) and use a trapezoidal method [5] built in the `scipy` [6] [205] library to compute the integration. Since we are interested in the tail part of the signal, we focus on two quantities of interest that can be extracted from $h_{\ell m}$, the amplitude $A_{\ell m}(\tau) = |h_{\ell m}|$ and the tail exponent

$$p \equiv \frac{d \ln A_{\ell m}(\tau)}{d \ln \tau} \,. \tag{5.22}$$

Note that we do not assign ℓm indices to p in order to keep the notation simple. In the present section, we always shift the axis of the retarded time τ to have a zero at the time of the light-ring crossing [7]. We have checked that this is close to the peak of $A_{\ell m}$ for all the configurations considered, so that it is possible, from our results, to estimate correctly the order of magnitude of the tail amplitude when it starts to dominate over the ringdown, with respect to the peak amplitude of the whole signal. We refer to Table I of Ref. [75] for an estimate of the delay between the peak of the orbital frequency and the quadrupolar amplitude for eccentric and quasi-circular orbits.

5.3.1 Initially bounded case: eccentric and quasi-circular binaries

We now focus on systems initialized as bounded. We start by considering initial data for the particle trajectory on a quasi-circular binary, and then we increase the eccentricity. In Table 5.1 we report the initial conditions and eccentricities of all the systems we have considered. To compute the numerical evolutions with the RWZHyp code, we have multiplied the source in Eq. (5.4) by a factor μ^{-1}. This does not change the results in the waveform except for an overall multiplicative factor, allowing us to circumvent the threshold given by double precision. In Fig. 5.3 we show the results of our numerical experiments, together with the analytical prediction for the late-time signal in Eq. (5.15). In particular, we show the amplitude of the $(2, 2)$ mode, rescaled with respect to the test-particle mass $\mu = 10^{-3}$, and the tail exponent p as defined in Eq. (5.22). Below each plot, for simulations with $e_0 > 0.3$, we report the residuals, defined as $100 * (X_{\rm numerical} - X_{\rm analytical})/X_{\rm numerical}$, quantifying the agreement level between numerical and analytical results, $X_{\rm numerical}$ and $X_{\rm analytical}$ respectively.

As already noted in [101, 206], the time at which the tail starts to dominate on the ringdown strongly depends on the eccentricity of the progenitors' binary, and is due to a different amplitude of the tail at these intermediate times. In particular, the higher the eccentricity, the more the tail is excited, and the sooner it starts to dominate. The first test of our model is to reproduce this scaling in the amplitudes. From the left panel of Fig. 5.3, it can be seen how for eccentricities larger than $e_0 \sim 0.3$ the model reproduces the amplitude of the tail, from the moment it starts to dominate over the ringdown, to asymptotically late times. In particular, the agreement is good for $e_0 \geq 0.8$, for which the residuals are $\leq 10\%$. As the eccentricity decreases, the residuals increase approximately by an overall constant factor, but remain $\leq 17\%$. For small eccentricities, our model can only infer the order of magnitude of the amplitude at the transition. In

[5] Note that we also tested the built-in function implementing Simpson's rule, yielding the same results.

[6] Specifically, we use `integrate.trapz`$[f(t), dx = dt']$ (or `integrate.simps`$[f(t), dx = dt']$), where $f(t)$ is the integrand in Eq. (5.15) computed along the numerical trajectory, while dt' is the spacing between the time steps of the latter.

[7] The reference retarded time enters the definition of p: choosing a different value implies assuming a different functional form for the tail, since it moves its asymptote. This does not affect the asymptotic value of p, but only its intermediate behavior.

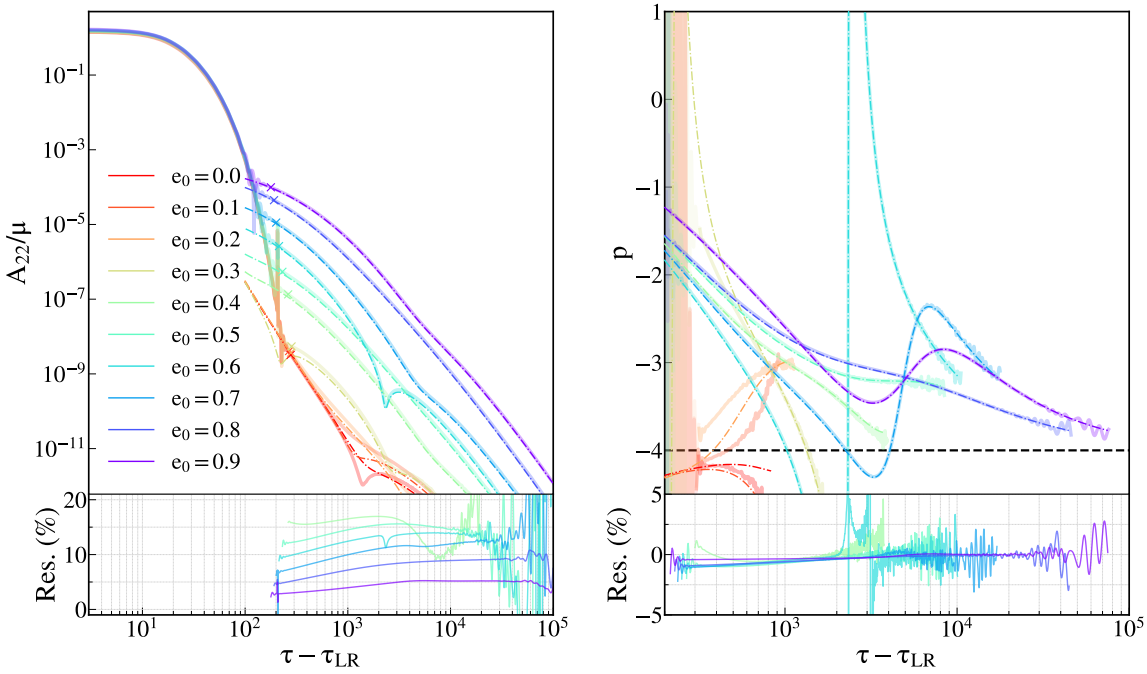

Figure 5.3: Left: Mass-rescaled amplitude of the $(2, 2)$ waveform multipole vs the observer retarded time, translated with respect to the time τ_{LR} at which the test particle crosses the light-ring. Right: value of the tail exponent, Eq. (5.22). The thick solid lines are the numerical experiments, computed by integrating Eq. (5.4) with the RWZHyp code. The thin dot-dashed lines are the analytical prediction for the late-time behavior Eq. (5.15). The dashed black horizontal line on the right, is Price's law. These results are relative to the eccentric and quasi-circular simulations of Table 5.1, each labeled by the initial eccentricity e_0. We cut the simulations for values of the amplitude $A_{22}/\mu = 10^{-12}$, four orders of magnitude before the numerical precision threshold dictated by double precision and when numerical noise becomes noticeable (high frequency oscillations in the plot on the right). Below each plot, for simulations with $e_0 > 0.3$, the residuals between numerical results and analytical predictions are shown, in %, to quantify the agreement/mismatch.

the right panel of Fig. 5.3, we report the tail exponent p extracted from numerical experiments and from our model. The model reproduces with very high accuracy the numerical experiments for $e_0 > 0.3$, but not for lower eccentricities. For $e_0 > 0.3$, the residuals are in the interval $[-2.5, 2.5]$%, when not taking into account the high-frequency oscillations at late times in the numerical waveforms (due to numerical noise). Also, note that for the simulation $e_0 = 0.6$, the residuals diverge at $\tau \simeq \tau_{LR} + 3 \cdot 10^3$, due to the numerical value of p crossing zero. These residuals do not show any clear trend in the eccentricity. The high accuracy in the prediction of the exponent p is consistent with the mismatch between analytical predictions and numerical results for A_{22} being well approximated by a constant factor through the evolution, since by definition p is not sensitive to an overall rescaling of A_{22}. The mismatch for low eccentricities is expected and consistent with the fact that Eq. (5.15) was derived always assuming a source localized at large r with respect to the BH. Hence, the longer the test particle spends far away from the BH during the inspiral, the better agreement we can expect. In a medium/high eccentric binary, this condition is satisfied up to times

close to the merger, while, for low eccentricities, the test-particle trajectory receives support at small r for a longer time during the last stage of the inspiral, as can be seen in Fig. 5.10 of Sec. 5.4. Instead, we do not have a clear understanding as to why the residuals seem to be approximately constant along the tail evolution. We leave the investigation of this behavior and related model improvements to future work.

Note that we cut the results in Fig. 5.3 for values of the amplitude $A_{22}/\mu = 10^{-12}$, four orders of magnitude above the numerical double precision threshold. Right before the simulations are cut, high-frequency oscillations are already present in the numerical results. For low eccentricity configurations, the tail starts to dominate when the signal is close to this strain value. Hence, we could partially impute the mismatch between our model and the experiments to limitations in numerical precision.

As mentioned in the previous section, our model predicts the tail to be a hereditary effect that depends on the entire inspiral history. In particular, it is an integral over the source that, for generic orbits, is an oscillating function. We thus expect a more complex behavior than a monotonic relaxation to a single power-law as in e.g. Ref. [126]. For instance, destructive interference among various components of the back-scattered signal can result in the amplitude A_{22} nearly going to zero before increasing again (as dictated by the very late-time behavior), implying a quasi-divergence in the tail exponent, which depends on the amplitude derivative.

This is confirmed by the numerical evolutions, as shown in the right panel of Fig. 5.3, where for $e_0 = 0.6$ the cusp in the amplitude is reflected in an almost singular behavior [8] of the tail exponent p.

5.3.2 Dynamically bounded case

We now analyze systems which are initially unbounded and, after a certain time, become bounded due to radiation reaction, eventually merging. In Table 5.2 we show the initial conditions used for all of the simulations and, for each one of them, the number of close encounters between the test particle and the BH. Some of these configurations have also been studied in Ref. [163]. In Fig. 5.4, the results of the numerical evolutions computed by integrating Eq. (5.4), (5.7) with the RWZHyp code are compared with the analytical model Eq. (5.15). Below each plot, we show the behavior of the absolute value of the residuals. From this comparison, we see a good agreement for all of the simulations considered, from intermediate to late times. In particular, the absolute value of the residuals is $\leq 10\%$ for the amplitude A_{22} and $\leq 1\%$ for the tail exponent, for all simulations in Table 5.2. This implies that our model is able to reproduce both the amplitude of the tail, as well as the non-trivial evolution of the exponent p, from the time it starts to dominate over the QNMs, up to very late times. We note that the amplitude of the tail at the transition time increases as the number of encounters decreases. We elaborate this point in further detail in Sec. 5.4, where we discuss which inspiral trajectory feature is able to enhance or suppress the tail. Here, we just point out that this scaling in the amplitude is consistent with what is found in Fig. 5.3. In fact, GWs are mainly emitted at turning points along the trajectory, hence a larger number of encounters during the inspiral phase implies that the test-particle orbit loses more energy and angular momentum

[8] We do not fully include its evolution in the plot for visualization reasons. Since it spans a wide range, capturing it completely would make the visualization of other results significantly harder.

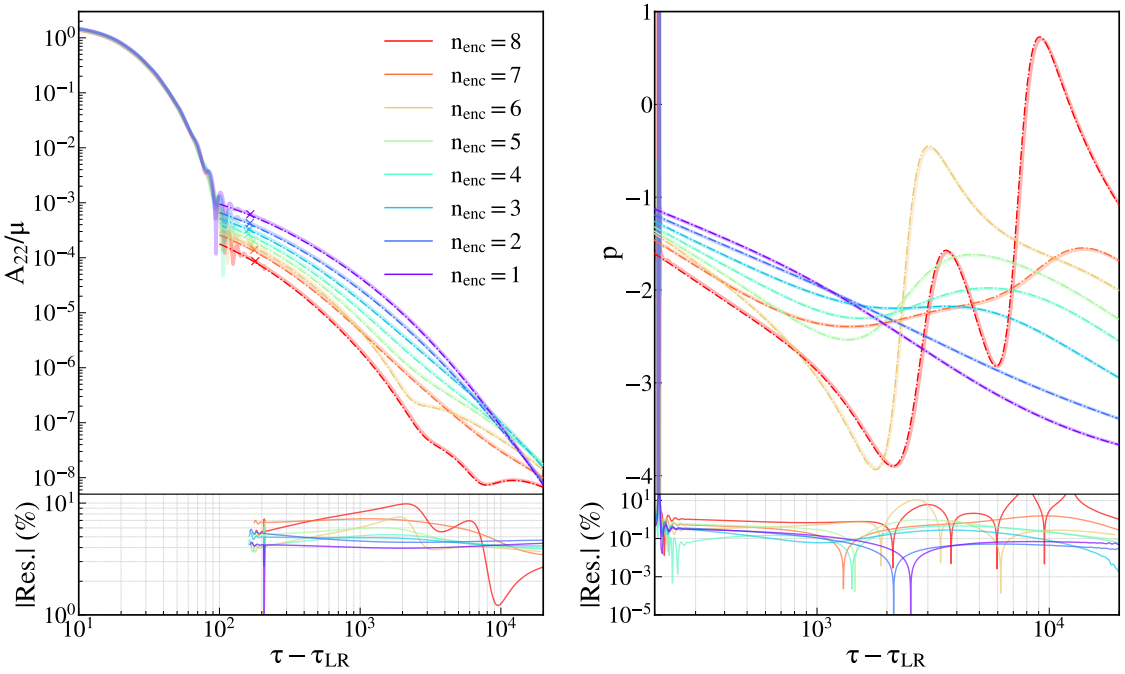

Figure 5.4: Left: Mass-rescaled amplitude of the $(2,2)$ waveform multipole vs the observer retarded time translated with respect to the time of light-ring crossing τ_{LR}. Right: value of the tail exponent, Eq. (5.22). The thin dot-dashed lines are the analytical predictions for the late-time behavior, Eq. (5.15), while the thick solid lines are numerical experiments obtained by integrating the Zerilli equation with the RWZHyp code. The results are relative to the dynamical captures in Table 5.2, each simulation is labeled by the number of encounters $n_{\rm enc}$ between the test particle and the BH. Below each plot, the absolute value of the residuals between numerical results and analytical predictions is shown to quantify the agreement.

before the merger, resulting in a progressive circularization of the orbit, Fig. 5.12. Quantitatively, for the dynamical capture configurations with $n_{\rm enc} > 2$ under consideration, it holds $e > 0.95$ after the first encounter. The larger the initial angular momentum, the higher the eccentricity after the first encounter, since less radiation is emitted. However, systems with large angular momenta will undergo multiple close encounters before plunging, so that the final eccentricity at the separatrix-crossing will be lower. Indeed, the configuration with $n_{\rm enc} = 8$ results in the lowest eccentricity at separatrix-crossing, having $e_{\rm sep} = 0.797$.

From the discussion in Sec 5.2.2, we expect that the tail exponent p will relax towards a $-\ell - 2$ value at asymptotically late times. In fact, we show that the slower decaying terms, led by $\sim \tau^{-1}$, vanish at asymptotically late times, for systems ending in a merger, at first order in perturbation theory. The results depicted in Fig. 5.4 seem to confirm these predictions: for simulations with $n_{\rm enc} = 1, 2$ number of encounters, the exponent p is relaxing towards $p = -4$. Simulations with larger $n_{\rm enc}$ take a longer time to merge, and as a result of a more prolonged history, there is a longer intermediate behavior in the post-merger tail (see Sec. 5.6 for more details). In particular, the relaxation of p towards its asymptotic limit is not monotonic for $n_{\rm enc} > 2$. As already discussed in the previous section, this happens because the

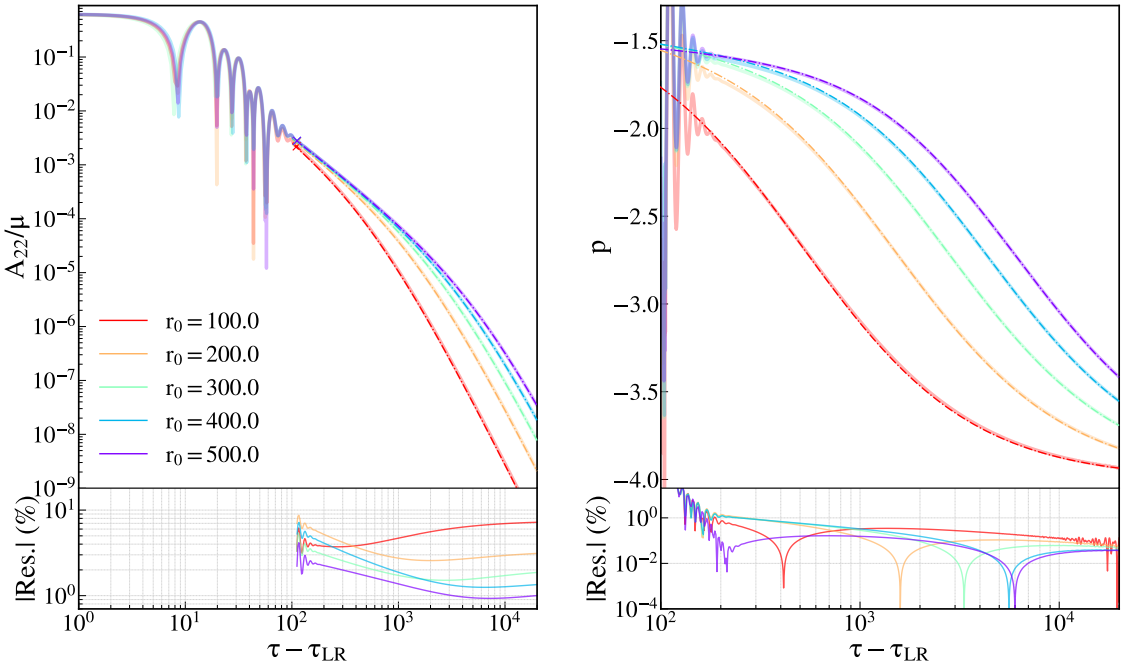

Figure 5.5: Left: Mass-rescaled amplitude of the $(2, 2)$ waveform multipole vs the observer retarded time translated with respect to the time of light-ring crossing τ_{LR}. Right: value of the tail exponent, Eq. (5.22). The thin dot-dashed lines are the analytical predictions for the late-time behavior, Eq. (5.15), while the thick solid lines are numerical experiments obtained by integrating with the RWZHYP code. The results are relative to radial infalls starting from the distances r_0 in the labels, with initial energy $E_0 = 1.00$. Note that the particle is infalling in the xy-plane, along the x axis. Below each plot, the absolute value of the residuals between numerical results and analytical predictions is shown to quantify the agreement.

source is oscillating, hence destructive interference between tail signals generated at different times can give rise to such non-monotonic behavior. In Sec. 5.6 we will study in more detail the case with $n_{\rm enc} = 8$, by means of a numerical evolution long enough to recover Price's law, and indeed will characterize the non-monotonic intermediate behavior of p as a superposition of a large number of power-laws in τ, with different decay rates.

5.3.3 Radial infall

In Fig. 5.5 we compare numerical experiments against the analytical prediction Eq. (5.15) for radial infalls from different initial distances $r_0 = \{100, 200, 300, 400, 500\}$. In the plots, we show the absolute value of the residuals to quantify the agreement. The analytical prediction matches very accurately all the numerical evolutions, with the absolute value of the residuals being $\lesssim 10\%$ ($\lesssim 1\%$) for the amplitude (tail exponent). It should also be noted how the amplitude at the transition from a QNMs to a tail-dominated behavior is larger than all of the configurations previously analyzed; we will explain this phenomenon in Sec. 5.4. As concerns the intermediate behavior, defined as the relaxation to the asymptotic limit, i.e. Price's law, there are two important considerations to be made. The further from the BH is the initial

location of the test particle, the longer is the intermediate behavior of the tail, before approaching $\sim \tau^{-4}$. Moreover, this relaxation is monotonic. This is a consequence of the source being non-oscillating, since φ is fixed along the entire trajectory. As mentioned above, this removes the destructive interference among tail signals emitted close to each other, yielding a monotonic relaxation.

Ref. [207] shows the post-merger tail generated by a geodesic radial infall from $r_0 = 7$, when observed at $\mathcal{I}^+$. As in our case, the relaxation of p therein depicted is monotonic. However, in Ref. [207] the tail exponent p reaches the asymptotic value from below, i.e. from smaller values. In our case, the value $p \to -4$ is reached from above. We have verified that this apparent discrepancy stems from the different definitions adopted in Eq. (5.22), in particular in the choice of a reference time. As mentioned above, in the present work, unless explicitly stated, we report all results with τ translated with respect to τ_{LR}, the time at which an observer at $\mathcal{I}^+$ sees the test particle crossing the light-ring. In Ref. [207], the time is instead translated with respect to the radial infall starting time. This choice can change the intermediate behavior of p and yield the observed inversion of the tail exponent relaxation towards a constant value.

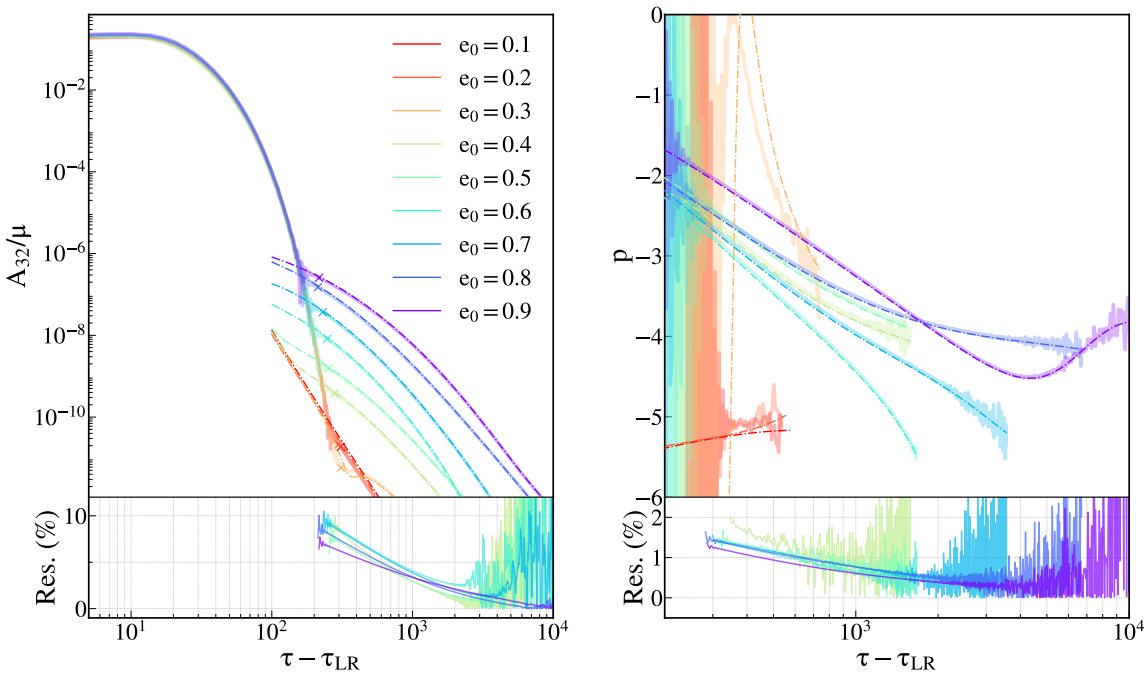

Figure 5.6: Left: Mass-rescaled amplitude of the $(3, 2)$ waveform multipole against the observer retarded time, translated with respect to the time τ_{LR} at which the test particle crosses the light-ring. Right: value of the tail exponent, Eq. (5.22). The thick solid lines are the numerical evolutions, computed by integrating Eq. (5.4) with the RWZHYP code. The thin dot-dashed lines are the analytical prediction for the late-time behavior, Eq. (5.15). These results are relative to the eccentric simulations of Table 5.1, each labeled by the initial eccentricity e_0. We cut the simulations for values of the amplitude $A_{32} = 10^{-16}$, corresponding to the double precision numerical threshold. Below each plot, for simulations with $e_0 > 0.3$, the absolute value of the residuals between numerical results and analytical predictions is shown, in %, to quantify the agreement/mismatch.

5.3.4 Eccentric and quasi-circular binaries: higher modes

We investigate the late-time decay of the waveform multipoles $(\ell m) = (32)$ and (44).

The results of the comparison between model Eq. (5.15) and the numerical evolutions, focusing on eccentric binaries of Table 5.1, is reported in Fig. 5.6 and Fig. 5.7 for the $(3, 2)$ and $(4, 4)$ mode respectively. Note that we cut both numerical evolutions and analytic results for values of the (non-rescaled) amplitude smaller than the double precision threshold 10^{-16}. This implies that, for the (44) mode, we can only study the late-time tail in configurations with initial eccentricity $e_0 \geq 0.5$ of Table 5.1.

We find a scaling in the amplitude of the tail with eccentricity, similar to what is found for the (22) mode, Fig. 5.3. The model is in good agreement with the numerical experiments for high eccentricities, while it performs worst for $e_0 \leq 0.3$, for the (32) mode. We attribute these discrepancies to the fact that the tail starts to dominate the signal very close to the double precision threshold. Moreover, as already stated, we expect the analytical model to fail for small eccentricities, since in these systems the test particle

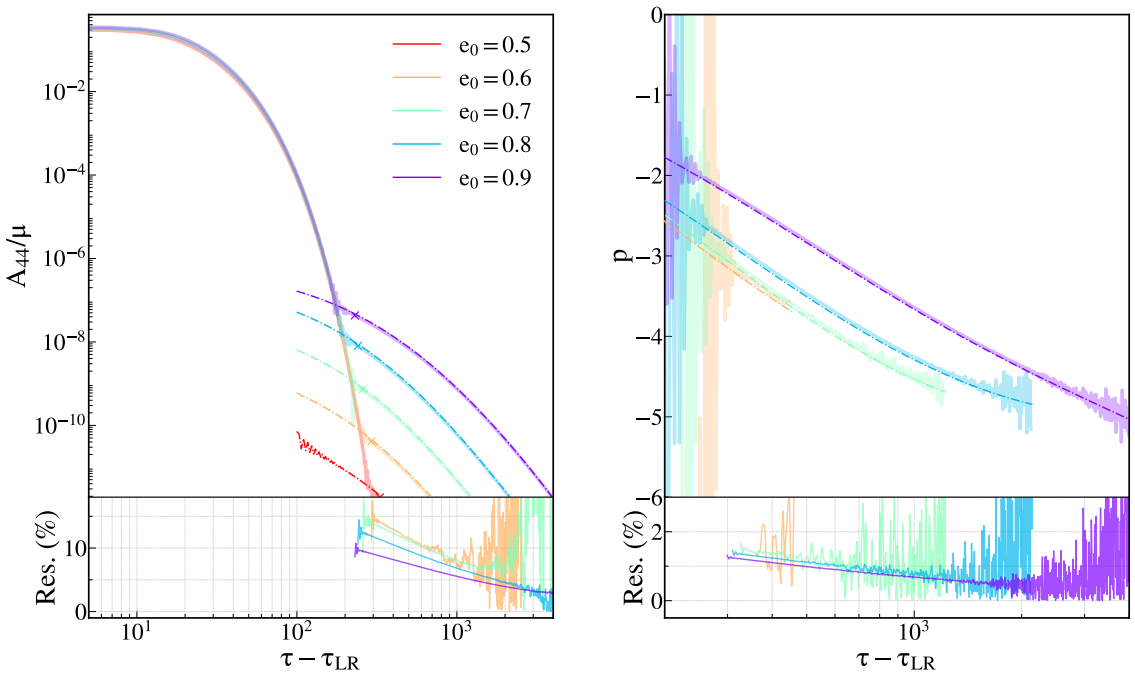

Figure 5.7: Left: Mass-rescaled amplitude of the $(4, 4)$ waveform multipole against the observer retarded time, translated with respect to the time τ_{LR} at which the test particle crosses the light-ring. Right: value of the tail exponent, Eq. (5.22). The thick solid lines are the numerical experiments, computed by integrating Eq. (5.4) with the RWZHyp code. The thin dot-dashed lines are the analytical prediction for the late-time behavior Eq. (5.15). These results are relative to the eccentric simulations of Table 5.1, each labeled by the initial eccentricity e_0. We cut the simulations for values of the (non-rescaled) amplitude $A_{44} = 10^{-16}$, corresponding to the double precision numerical threshold. Below each plot, the absolute value of the residuals between numerical results and analytical predictions is shown, in %, to quantify the agreement/mismatch.

spends a greater amount of time at small distances from the BH, close to the merger, where our model is not formally valid. To quantify the agreement/mismatch between the numerical evolutions $X_{\text{numerical}}$ and the analytical results $X_{\text{analytical}}$ we have shown in Figs. 5.6, 5.7, for $e_0 \geq 0.4$, the residuals, defined as $100 * (X_{\text{numerical}} - X_{\text{analytical}})/X_{\text{numerical}}$. For both modes considered, the residuals of the tail exponent are in the interval $(0, 2)\%$, while for the amplitudes the residuals are in the interval $(0, 10)\%$, $(0, 15)\%$ for the (32) and the (44) mode respectively.

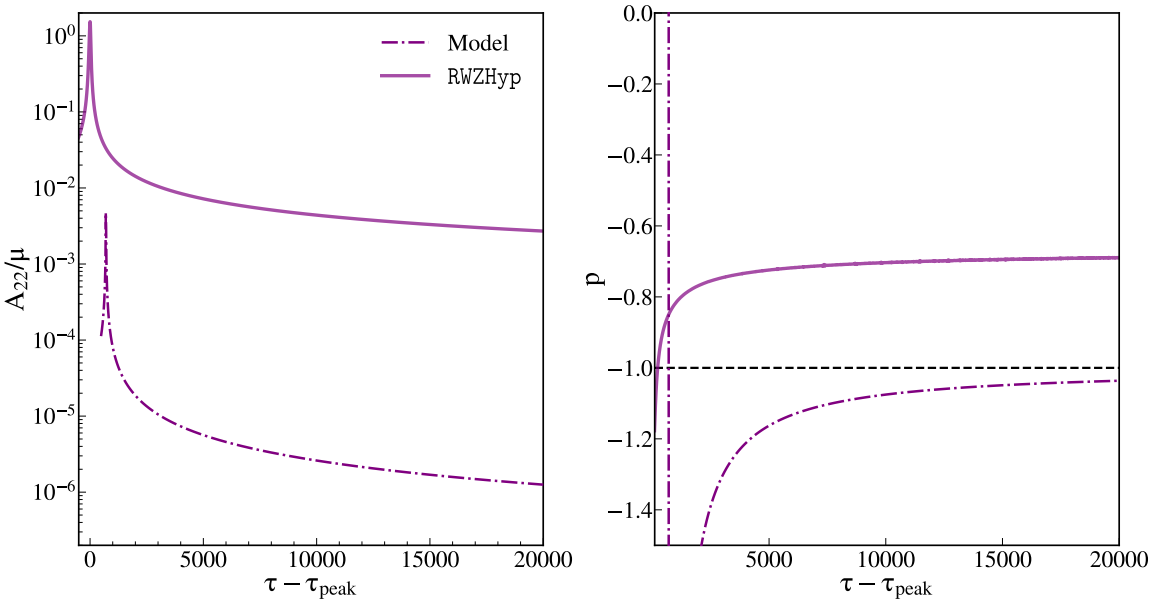

Figure 5.8: Left: Mass-rescaled amplitude of the $(2,2)$ waveform multipole against the observer retarded time, translated with respect to the time of the A_{22} peak. Right: value of the tail exponent, Eq. (5.22). Thick lines are results of numerical evolutions, computed by integrating Eq. (5.4) with the RWZHyp code. Dot-dashed lines are the leading order tail in Eq. (5.24), normalized to remove the factor in Λ. These results are relative to a scattering simulation from $r_0 = 300$, with initial energy and angular momentum $E_0 = 1.000001$, $p_{\varphi,0} = 4.070195$, evolved considering geodesics motion.

5.3.5 Scattering configurations

Signals that travel well inside the flat light-cone are correctly described by Eq. (5.15), which instead fails to describe signals propagating on or marginally close to it. This is manifest in the singular behavior of the integrand, when computed at the upper bound of integration $t' + \rho_+ \simeq \tau$. If we consider systems that eventually merge, and focus on the signal emitted at asymptotically late times, we never encounter this singularity. For these systems, the source (hence the integrand) decays exponentially after the light-ring crossing. It is interesting to investigate what happens to our model if we try to apply it to systems that do not merge. An example is a scattering situation; in this setting, the test particle is unbounded from the BH, and the source never vanishes. Then, we introduce a dimensionless timescale Λ in the upper limit of integration in Eq. (5.15) $\tau - \rho_+ \to (1-\Lambda)(\tau - \rho_+)$, that effectively select only signals travelling with velocities $\leq \Lambda$. We consider a test particle travelling far away from the BH, $r' \gg M$ with a small constant velocity, such that the source contribution in the integral form Eq. (5.15) is proportional to $\propto \mu |v|^2 t'^2$. The signal observed at $\mathcal{I}^+$ as predicted by Eq. (5.15) is

$$\psi \propto \mu v^2 \int_{T_{in}}^{(1-\Lambda)(\tau-\rho_+)} dt' \frac{t'^2}{(\tau - \rho_+ - t')^4}. \tag{5.23}$$

The expression above can be solved analytically. We assume the observer at $\tau - \rho_+ \gg T_{\rm in}$ and keep corrections up to $O\left[\left(\frac{T_{\rm in}}{\tau-\rho_+}\right)^4\right]$. Then Eq. (5.23) becomes

$$\psi \simeq -8\pi Y^*_{\ell m} c_\ell \frac{1+2\ell}{\ell(\ell+1)-2}|v|^2\mu \cdot \left[\frac{(-1+\Lambda)^3}{3\Lambda^3}\frac{1}{\tau-\rho_+} + \frac{T_{\rm in}^3}{3\,(\tau-\rho_+)^4}\right]. \tag{5.24}$$

There is a clear issue: as we consider signals propagating marginally close to the flat light-cone $\Lambda \to 0$, the amplitude of the $(\tau-\rho_+)^{-1}$ tail in the above expression diverges. In the context of the classical soft graviton theorem, logarithmic corrections to the scattering amplitude give rise to a τ^{-1} tail [208, 209]. Our model appears to be in agreement with this prediction. However, we regard this result as incomplete, due to the presence of the arbitrary cutoff Λ. We leave to future work either the physical interpretation of the scale factor Λ, or a "renormalization" procedure to get rid of this cutoff.

For completeness, we compare the leading $(\tau-\rho_+)^{-1}$ term of Eq. (5.24) with a numerical scattering evolution. For this simulation, we do not include radiation reaction in the Hamiltonian equations of motion Eq. (5.8), thus the trajectory is geodesic. The results are shown in Fig. 5.8, where we have normalized the predicted behavior in order to remove the cutoff Λ. As expected, the analytical model fails completely to reproduce the correct amplitude of the signal. The numerical evolution seems to converge towards a slower decay than $(\tau-\rho_+)^{-1}$. We leave a more in-depth investigation of the scattering scenario, both numerical and analytical, to future work.

5.4 Tail amplitude: last apastron contributions

In Fig. 5.3, it is shown that the time of transition from a QNM to a tail-dominated behavior depends on the eccentricity of the progenitors' binary. Similarly, Figs. 5.4, 5.5 show a similar behavior for other classes of non-circular orbits. In the present section, we investigate which specific features of the non-circular orbits are causing the tail enhancement, focusing on the $(\ell m) = (22)$ multipole.

First, we isolate the portion of the point-particle inspiral trajectory which contributes the most to the tail amplitude. To do so, we compare the tail amplitude obtained from the numerical evolution and our model, and study how this comparison evolves as we change the initial time of the integration in our semi-analytical computation, to include progressively less inspiral history. Beyond understanding which portion of the trajectory is determining the tail, an additional byproduct of this analysis is learning "how much history" needs to be included in order to obtain a reasonable estimate of the tail amplitude, within some accuracy threshold. This information is useful, e.g. when aiming to extract tail terms from simulations of comparable-mass mergers, in which only a limited number of cycles is available. Then, based on the intuition drawn from the above investigation, we derive an expansion that allows us to deduce which specific orbital features are determining the tail behavior.

Throughout the present section, we refer to $A_{\rm tail} \equiv A_{22}(\tau_{\rm trans})$ as "tail amplitude", where $\tau_{\rm trans} = \bar{\tau} + 5\tau_{220}$, and $\bar{\tau}$ is the time of the flex in the frequency ω_{22} of the (22) multipole, when transitioning from the fundamental mode frequency ω_{220} to a zero value, i.e. the one corresponding to the tail regime. The factor $5\tau_{220}$ serves to exclude the QNMs portion, and we found it to be a reasonable approximation for the time

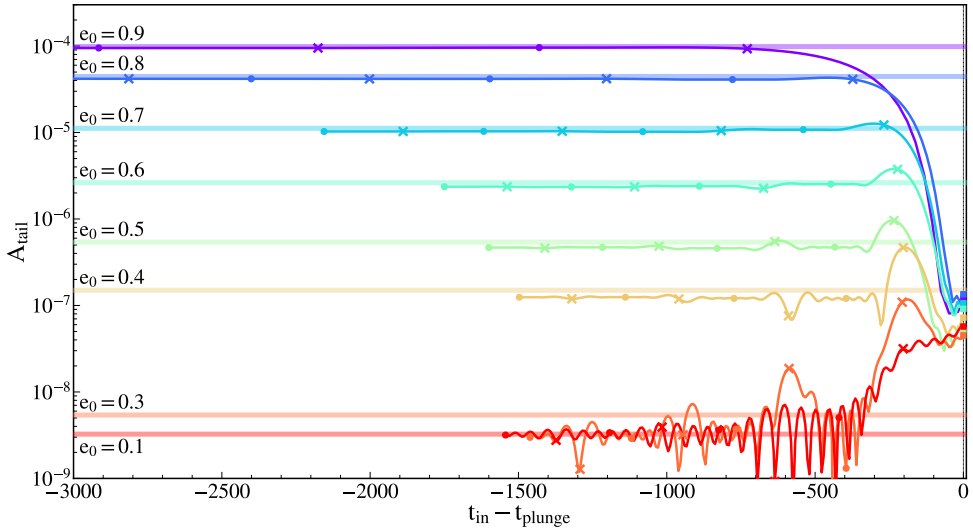

Figure 5.9: Horizontal opaque lines: amplitude of the $(2, 2)$ multipole, A_{22} at the transition between QNM and tail-dominated regime, obtained by integrating the full problem in Eq. (5.4), (5.7) with the RWZHYP code. Each color corresponds to one of the simulations in Table 5.1, labeled by the value of the initial eccentricity e_0. For readability of the plot, we do not display the results relative to $e_0 = 0.2$, characterized by the same oscillatory behavior as $e_0 = 0.1$. The thick lines represent the values of A_{22} at $\tau_{\rm trans}$ computed with the model Eq. (5.15), by changing the initial time $t_{\rm in}$ of integration on the x-axis. The x-axis is also translated by subtracting the plunge time, i.e. the last time at which $\ddot{r} \equiv 0$ before the merger. Crosses (dots) indicate the time of apastra (periastra).

at which the tail starts to dominate, see also Ref. [206].

5.4.1 Eccentric binaries

The results of the analysis described above are depicted in Fig. 5.9, for the simulations in Table 5.1. Note that, for all the eccentricities available, we start the integration in the analytical model Eq. (5.15) from the fourth periastron before the merger. Numerical evolutions include more orbits; however, we did not consider it relevant to include additional past history in the analysis, due to the converging behavior of $A_{\rm tail}$ vs $t_{\rm in}$.

For intermediate to high eccentricities, the motion around the last apastron is the part of the trajectory that mostly determines $A_{\rm tail}$. In particular, for high eccentricities, one could consider only the motion from the last apastron, and still correctly determine $A_{\rm tail}$. Instead, when considering intermediate eccentricities, an oscillatory behavior arises. We interpret these oscillations as due to ingoing and outgoing motion near the last apastron, generating tail terms that are comparable in modulo but opposite in sign, leading to cancellations. From this picture, we get the heuristic intuition that the tail is enhanced by a motion happening near an apastron, at large distances from the BH, $r \gg 2$. As can be seen in Fig. 5.10, this regime corresponds to small radial and angular velocities $\dot{r}, p_\varphi/r \ll 1$. To verify such intuition, we expand

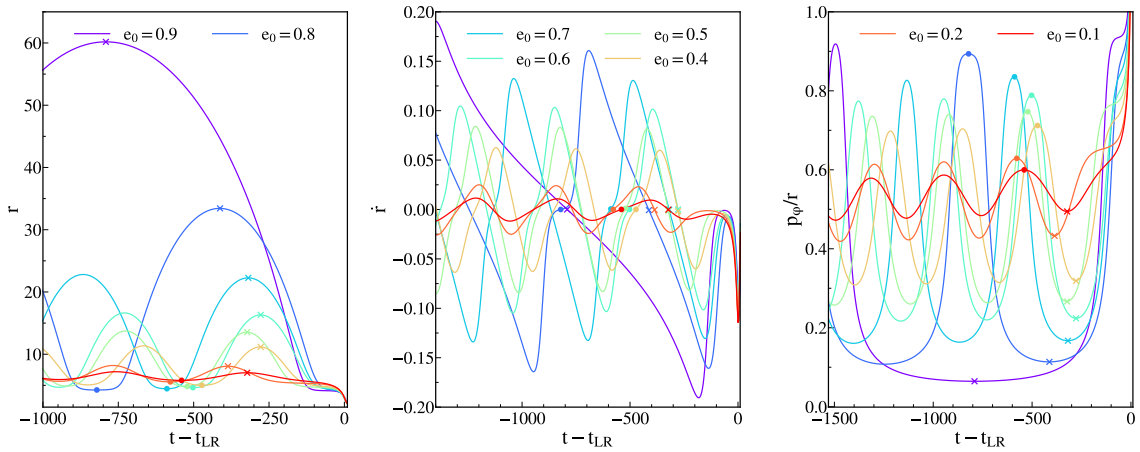

Figure 5.10: Radius (left), radial velocity (center) and angular momentum per unit r (right) vs the time translated with respect to the time of the light ring crossing. Different colours identify the different eccentric simulations of Table 5.1, labeled by the initial eccentricity e_0. The crosses (dots) indicate the last apastron (periastron).

Eq. (5.15) according to these conditions, starting from the large distance ($r \gg 2$) approximation, yielding

$$\Psi_{\ell m}(\tau,\rho_+) = \int_{T_{in}}^{T_f} dt' \frac{r^\ell(t') e^{-im\varphi(t')} P_{\ell m}(\cos\theta_0)}{(\tau - t' - \rho_+)^{\ell+2}} \cdot \hat{H}\left[a_1\sqrt{1-\dot{r}^2} + a_2 \dot{r}\frac{p_\varphi}{r\hat{H}} + a_3 \frac{p_\varphi^2}{r^2\hat{H}^2}\right], \tag{5.25}$$

where the coefficients $a_{1,2,3}$ are given by

$$\begin{aligned} a_1 &= a_0\,(\ell+1)\,(\ell+2)\,, \\ a_2 &= a_0 4im\,, \\ a_3 &= a_0\left(\lambda - 2m^2 - 2\right), \\ a_0 &= c_\ell \frac{8\pi\mu}{\lambda\,(\lambda-2)}\,. \end{aligned} \tag{5.26}$$

We now expand in small $\dot{r}, p_\varphi/r \ll 1$. Considering the expression for the energy per unit mass Eq. (5.9) in these limits, we obtain

$$\Psi_{\ell m}(\tau,\rho_+) = \int_{T_{in}}^{T_f} dt' \frac{r^\ell(t') e^{-im\varphi(t')} P_{\ell m}(\cos\theta_0)}{(\tau - t' - \rho_+)^{\ell+2}} \cdot \left[a_1 - \frac{a_1}{2}\dot{r}^2 + a_2\dot{r}\frac{p_\varphi}{r} + \left(a_3 + \frac{a_1}{2}\right)\frac{p_\varphi^2}{r^2}\right]. \tag{5.27}$$

This integral form confirms our previous intuition. The overlap between the propagator and the source is enhanced for large distances r, since low-frequencies signals (the ones contributing to the tails) not only are scattered the most by the background, but are also emitted by a motion on large scales. It is important to note the oscillatory term in the integrand of Eq. (5.27) for $m \neq 0$ modes. This term implies that the faster φ varies, the more destructive the interference between tail signals emitted close to each other will be. For each eccentric orbit, the test particle is the furthest away from the BH at the apastron $r_{\rm apo}$. The further the location of the apastron, $r_{\rm apo}$, the smaller is the angular velocity $\dot{\varphi}$ at this location, as prescribed by Kepler's second law, promoting the emission of an enhanced tail signal. Both these features are related

to the eccentricity; systems with higher eccentricity have larger $r_{\rm apo}$ and smaller $\dot{\varphi}_{\rm apo}$, indicating that the expansion in small p_φ/r in Eq. (5.27) is an expansion in the eccentricity [9], as implied by Fig. 5.10.

Hence, in an eccentric merger, the late-time signal in the post-ringdown waveform is the tail generated at the last apastron before merger. The larger the eccentricity of the last orbit before merger, the further the last apastron, and the smaller the test-particle angular velocity at this location. While the test particle is moving near the last apastron, at each time step it generates a tail signal that is more enhanced the larger the distance from the BH. Destructive interference among these subsequent tail signals is more suppressed the smaller the source angular velocity, in favor of constructive interference. This results in an enhanced tail, dominating the late-time strain.

Note that the oscillatory term suppressing the tail signal, $e^{-im\varphi(t')} = 1$ for $m = 0$, regardless of the binary configuration. This implies that the late-time tails in the $(\ell 0)$ multipoles are enhanced even for quasi-circular mergers, as observed in numerical simulations in Ref. [211].

If for very high eccentricities, near the apastra, we can neglect the last two terms in the square parentheses, these become relevant for intermediate eccentricities. In particular, the third term depends on the sign of $\dot{r}$, and is the one responsable for the cancellations among tails emitted close to the apastron during outgoing and ingoing motion, observed in Fig 5.9. The second term in Eq. (5.27) depends as well on $\dot{r}$, but not on its sign. It does not imply cancellation among ingoing and outgoing motion, but is part of the expansion around the apastron. In particular, as we move away from it, this factor, opposite in sign to the leading order, suppresses the tail.

The approximation in Eq. (5.27) does not hold for low-eccentricities since, in these cases, the test particle is located near the BH during the whole last stage of the inspiral, see Fig. 5.10.

5.4.2 Dynamical captures and radial infalls

We analyze the trajectory of the test particle in the dynamical captures listed in Table 5.2. These systems are initialized as unbounded, and, during the first encounter, become bounded due to emission of gravitational radiation, resulting in highly eccentric orbits that eventually merge. As shown by the results in Fig 5.12, if the number of encounters $n_{\rm enc} > 1$, near the last apastron the particle is far away from the BH with small tangential velocity p_φ/r. As the number of encounters $n_{\rm enc}$ increases, the distance from the BH at the last apastron decreases, while the tangential velocity increases, resulting in less time spent around this location. This is due to the fact that the GWs are emitted mainly at the turning points, thus the more encounters are present, the more the orbit loses energy and evolves towards a more "circularized" setting. Thus, we expect a reasoning similar to the one in the previous section to hold, considering that a higher $n_{\rm enc}$ implies a smaller eccentricity of the last stable orbit, as discussed in Sec. 5.3.2.

We repeat the experiment of the previous section, i.e. we compare $A_{\rm tail}$ from the numerical evolutions with the one computed from the model Eq. (5.15), varying the starting time of integration, $t_{\rm in}$. The part of history relevant to determining $A_{\rm tail}$ is the motion from the last apastron, in agreement with what was

[9] This intuition is in agreement with the Newtonian limit, in which $\left(p_\varphi^2/r - 1\right) \sim e$, see for instance the discussion in [210].

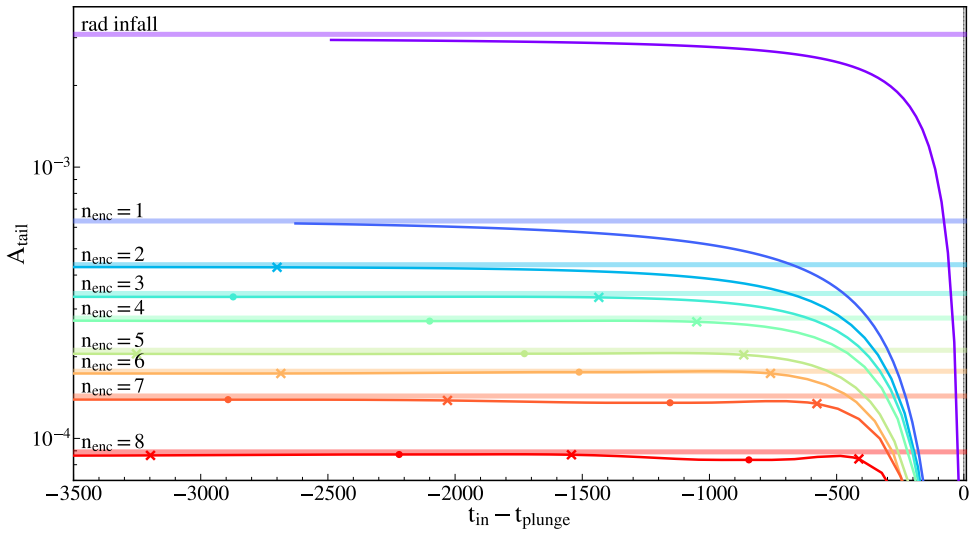

Figure 5.11: Horizontal opaque lines: amplitude of the $(2,2)$ multipole A_{22} at the transition between QNM and tail-dominated regime, obtained by integrating the full RWZ problem in Eq. (5.4), (5.7) with the RWZHyp code. Each color corresponds to one of the captures in Table 5.2, labeled by the value of the number of encounters $n_{\rm enc}$, plus a radial infall from the same distance $r_0 = 300$. The solid lines represent the values of A_{22} at $\tau_{\rm trans}$ computed with the model Eq. (5.15), by changing the initial time t_{in} of integration that is on the x-axis, translated with respect to the plunge time, i.e. the last time at which $\ddot{r} \equiv 0$ before the merger. Crosses (dots) indicate that the starting time of integration is a turning point far from (close to) the BH.

found in the previous section for bounded orbits. In fact, from the comparision of the trajectories in Fig. 5.10 and Fig. 5.12, we see that, even for the larger value of $n_{\rm enc}$ considered in Table 5.2, the last orbit has features compatible with an eccentricity close to the two most eccentric simulations in Table 5.1 (see also discussion in Sec. 5.3). In such a setting, as mentioned above, the last two terms in Eq. (5.27) can be neglected and the influence of in/out-going motion near the last apastron on $A_{\rm tail}$ is negligible.

An interesting limiting case is $n_{\rm enc} = 1$, for which the orbit does not have a turning point. Consistent with the intuition developed above, we find that contributions from all times are relevant in this case, as depicted in Fig. 5.11. Similar considerations also hold for a radial infall starting from the same initial distance of $r_0 = 300$. A curious feature to note is that in the $n_{\rm enc} = 1$ case, the amplitude is suppressed with respect to a radial infall from the same distance. This is puzzling at first since, as depicted in Fig. 5.12, the $n_{\rm enc} = 1$ simulation dynamics is close to the radial infall one, except in the plunge phase that, however, does not seem to influence $A_{\rm tail}$, as shown in Fig. 5.11. The reason of this can be traced back to p_φ/r, that remains small for the whole orbit, allowing us to consider the expansion of Eq. (5.27). The third term in the expansion, proportional to $\dot{r}$ and p_φ/r, acts as a small negative contribution with respect to the leading one in the $n_{\rm enc} = 1$ case, due to the ingoing nature of the motion. At the same time, the oscillating factor $\sim e^{-im\varphi}$ will induce interference among subsequent tail terms. These terms are not present for a radial infall (the latter being a constant), explaining the amplitude suppression in the $n_{\rm enc} = 1$ case, compared to

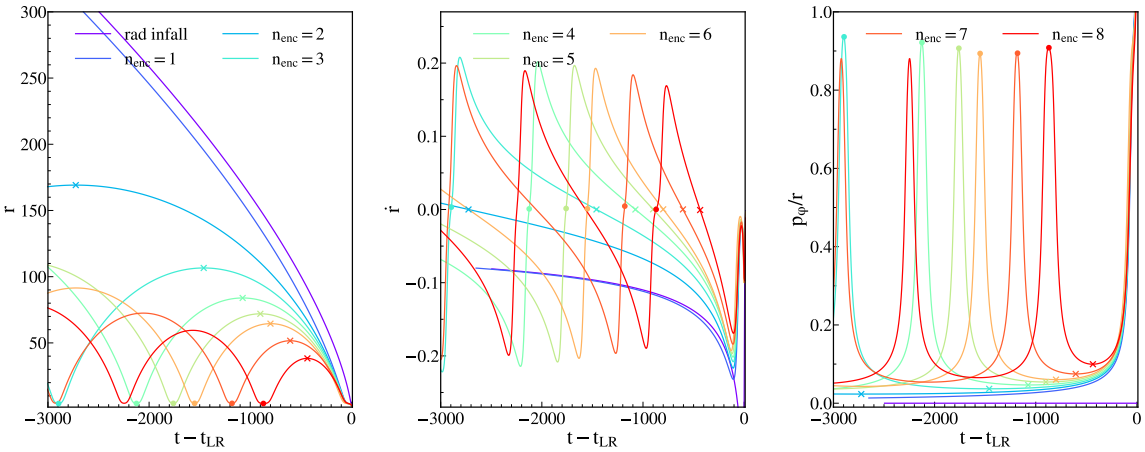

Figure 5.12: Radius (left), radial velocity (center) and angular momentum per unit r (right) vs the time translated with respect to the time of the light ring crossing. Different colours identify the different simulations of dynamical captures listed in Table 5.2, labeled by the number of encounters $n_{\rm enc}$, plus a radial infall from the same distance $r_0 = 300$. The crosses (dots) indicate the last turning points, further (closer) to the BH.

a radial infall from the same distance.

5.5 Tail amplitude parametrization

From the analysis in Sec. 5.4, it emerged that it is not practical to describe $A_{\rm tail}$ in terms of the initial eccentricity e_0, since $A_{\rm tail}$ rather depends on the eccentricity of the last orbit before the merger. In fact, as already discussed at the beginning of Sec. 5.3, the eccentricity evolves during the inspiral in a non-trivial way. Hence, the initial eccentricity, taken alone, is not sufficient to determine e at late stages of an orbit. The two parameters that have been previously used in the literature to parametrize the merger/ringdown waveform, able to quantify the eccentricity of the last inspiral stages, are the eccentricity at the separatrix $e_{\rm sep}$, [101], and the impact parameter at the light-ring crossing/merger [75, 203, 81]. In Fig. 5.13, we show the amplitude of the (22) mode at the time in which the tail starts to dominate over the QNMs, $A_{\rm tail}$, as a function of the eccentricity at the separatrix $e_{\rm sep}$ and as a function of the impact parameter Eq. (5.21) at the light-ring crossing b_{LR} translated with respect to its value for a quasi-circular plunge. These plots suggests $e_{\rm sep}$ to be more suited to parametrize $A_{\rm tail}$, while there is a double-valued behavior of $A_{\rm tail}$ in b_{LR}, exhibiting two branches, one for bounded orbits and one for dynamical captures.

It is not straightforward to connect $e_{\rm sep}$, b_{LR} to the motion near the last apastron, and we leave a more detailed study on the parametrization of $A_{\rm tail}$ to future work. However, the results in Fig. 5.13 hint that the eccentricity at the separatrix is a good quantity to capture the features of the last orbit and to describe the late-time tail enhancement.

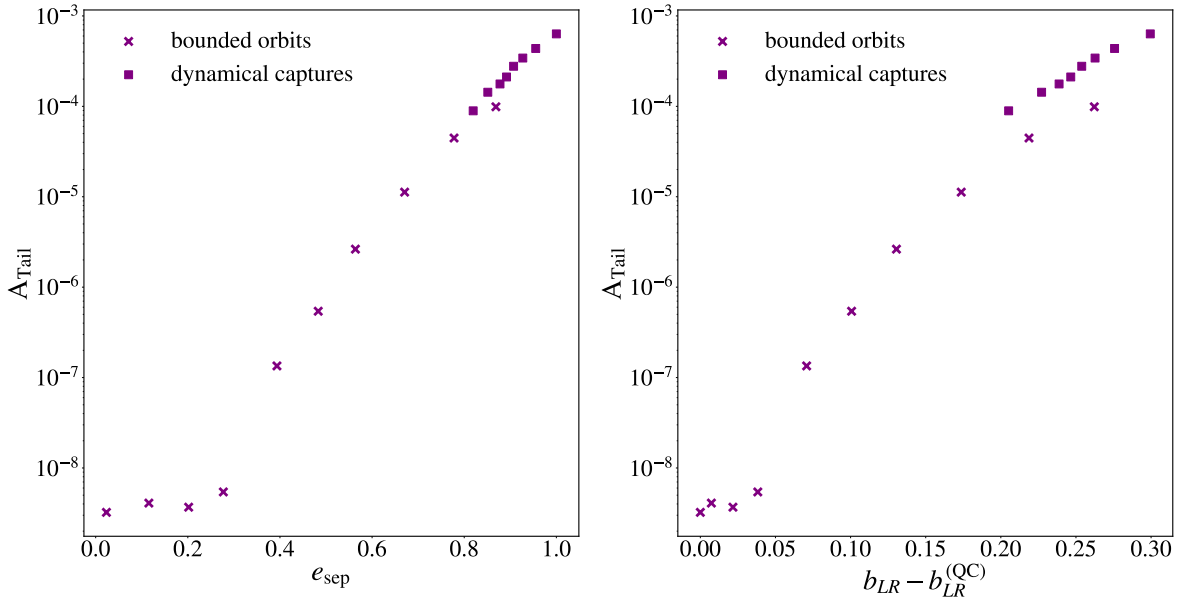

Figure 5.13: Amplitude of the (22) mode at the time at which the tail starts to dominate over the QNMs, $A_{\rm tail}$, vs the eccentricity at the separatrix $e_{\rm sep}$ (left) and the impact parameter in Eq. (5.21) at the light-ring crossing (right). The results are relative to the bounded orbit simulations of Table 5.1 and the dynamical captures in Table 5.2.

5.6 Power-laws superposition

In the previous sections, we discussed the amplitude of the tail around the time at which it starts to dominate over the QNMs-driven regime. Now, we focus on the phenomenology of the tail after this time. As derived in Secs. 5.2 and 5.3, the tail is initially dominated by an intermediate transient, leaving place after some time to Price's law. Here, we characterize the decaying behavior of the transient regime and present a very long-lived selected simulation to explicitly show that Price's law is recovered both numerically and analytically, as expected. In particular, we analyze the dynamical capture of Table 5.2 with $n_{\rm enc} = 8$. At the end of the section, we report the same analysis for a radial infall from $r_0 = 300$ and for the inspiral with initial eccentricity $e_0 = 0.9$ of Table 5.1.

Our model predicts that the intermediate behavior can be described by a superposition of power-laws in observer retarded time τ, Eq. (5.20). The lowest order of this expansion corresponds to Price's law, and thus will dominate at asymptotically late times. This prediction is in agreement with the aforementioned numerical evolutions, as shown by the results in Fig. 5.14 and Fig. 5.16. Note that, in deriving Eq. (5.20), we considered as the upper limit of integration in the analytical model a time T_f large enough so that the source has vanished. In all of the configurations analyzed in the present section, we study the tail from the time at which it starts dominating the strain. By this time, in the limits of double precision, the test particle has effectively already crossed the horizon, and the source has long vanished. Hence, we do not set an upper limit for the integral in Eq. (5.20), but we integrate over all $t' < \tau - \rho_+$. However, as explained above, the integrand has vanished before the earliest time τ at which we compute the analytical

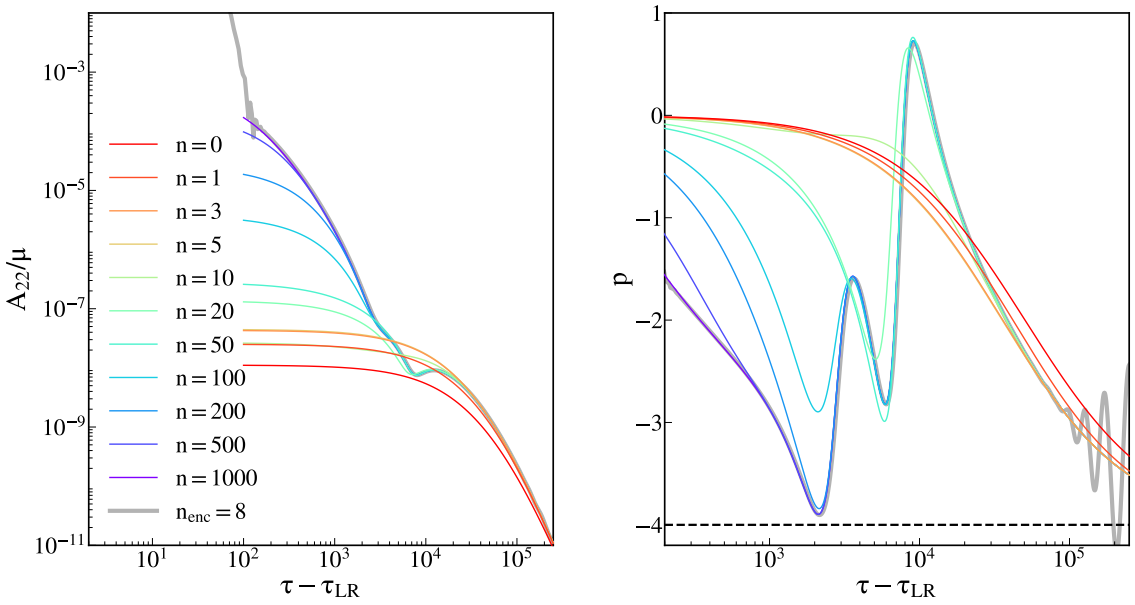

Figure 5.14: Left: Mass-rescaled amplitude of the $(2,2)$ waveform multipole against the observer retarded time, translated with respect to the time τ_{LR} at which the test particle crosses the light-ring. Right: value of the tail exponent, Eq. (5.22). The system under study is the dynamical capture with $n_{\rm enc} = 8$ in Table 5.2. The time between initializing the test particle and the light-ring crossing is $\sim 5 \cdot 10^4$. The gray thick line corresponds to the numerical experiment obtained by integrating Eqs. (5.4),(5.7) with the RWZHYP code. High-frequency oscillations in the plot on the right for very late times ($\gtrsim 10^5$) are due to numerical noise. The coloured lines are computed through the expansion in power-laws in the retarded time τ, Eq. (5.20). The label n specifies how many power-laws have been added to Price's law (horizontal line in the right panel).

tail as an expansion in power-laws superposition. For instance, for the radial infall analyzed in Fig. 5.16, the source has vanished and $r = 2$ at a time ~ 54 after the light-ring crossing.

The intermediate regime relevance can be quantified by how many power-laws are necessary to reach convergence, which in Fig. 5.14 corresponds to $n \sim 1000$. The excitation coefficient of each Price's law correction term $\sim \tau^{-n-\ell-2}$ is given by an integral over the source $S_{\ell m}(t')$, multiplied by a factor $(t'+\rho_+)^n$. The term $(t'+\rho_+)^n$ seems to imply that the longer the inspiral's past history, the more enhanced the excitation coefficient of $\tau^{-n-\ell-2}$ is. However, moving $T_{\rm in}$ further and further in the past will yield a convergent behavior of the waveform, due to the presence of the weight $S(t')$ which is suppressed in this limit. In fact, as discussed in Sec. 5.2.2, $S(t')$ can either vanish in the asymptotic past, or give rise to a suppressed $1/\tau$ tail that does not propagate at asymptotically late times (see also the discussion in Sec. 5.3.5).

To test these predictions, we turn to the dynamical capture analyzed in Fig. 5.14. At the beginning of this simulation, the system is unbounded. Going earlier in time with respect to the history considered would result in a suppressed source, hence a suppressed tail contribution. Instead, the source is not suppressed once the system becomes bounded, during subsequent encounters. Hence, "excluding" some

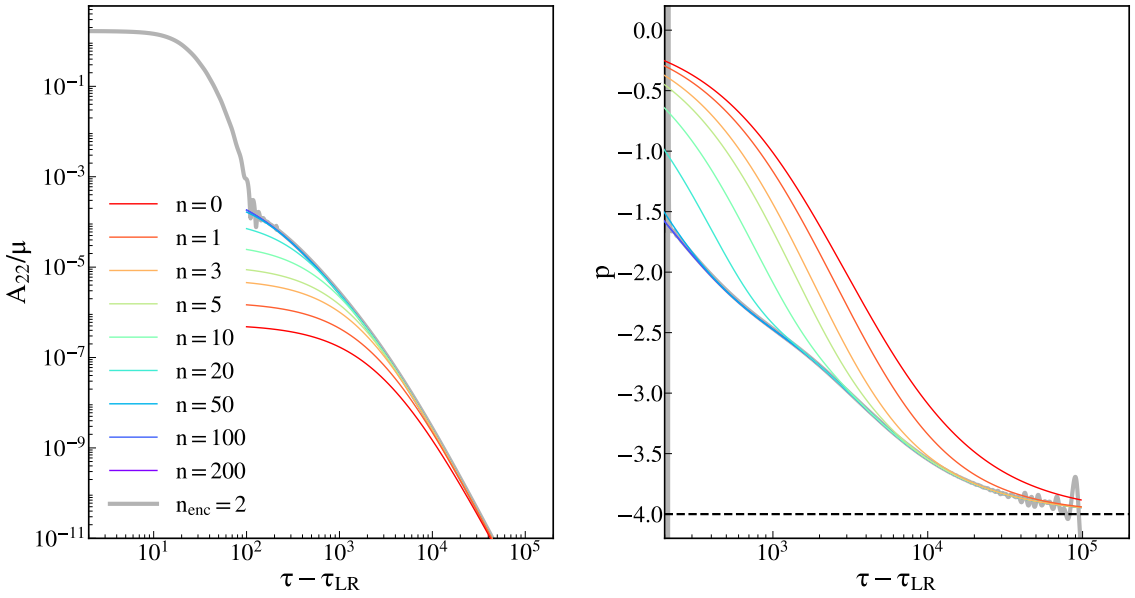

Figure 5.15: Left: Mass-rescaled amplitude of the (22) waveform multipole against the observer retarded time, translated with respect to the time τ_{LR} at which the test particle crosses the light-ring. Right: value of the tail exponent, Eq. (5.22). The system under study follows the same trajectory of the dynamical capture with $n_{\rm enc} = 8$ in Table 5.2. However, the integration included only the last $n_{\rm enc} = 2$ encounters of the same evolution. The time between initializing the test particle and the light-ring crossing is $\sim 2 \cdot 10^3$. The gray thick line corresponds to the numerical experiment obtained by integrating Eq. (5.4),(5.7) with the RWZHyp code. High-frequency oscillations in the plot on the right for very late times ($\gtrsim 3 \cdot 10^4$) are due to numerical noise. The coloured lines are computed through the expansion in power-laws in the retarded time τ, Eq. (5.20). The label n specifies how many power-laws have been added to Price's law.

past encounters from the integral in Eq. (5.20), would significantly change the excitation coefficients of the power-laws therein, giving rise to a different intermediate regime of p. We show this point explicitly by running the same analysis as in Fig. 5.14, but changing the initial time of integration in Eq. (5.20), $T_{\rm in}$. We compare these results with a numerical evolution obtained initializing the test particle (hence starting the integration) along a different point of the same inspiral trajectory. The initial conditions on the emitted radiation are still imposed as in Eq. (5.7), while the initial conditions of the test particle are such that the trajectory remains unchanged. The starting time for the numerical integration is fixed to match the initial time of the analytical one. The section of the trajectory considered is highlighted (green) in Fig. 5.2, in particular, we now consider a motion including only the last two encounters. In the original simulation the test particle orbited around the BH for a time $\sim 5 \cdot 10^4$ before the light-ring crossing while we have now reduced this time to $\sim 2 \cdot 10^3$. The results of the analysis, shown in Fig. 5.15, confirm the model's prediction: faster decaying power-laws are less excited when considering a reduced amount of history. As a consequence, the system reaches Price's law on a shorter timescale. In particular, when considering a longer fraction of the inspiral, as in Fig. 5.14, Price's law is approached well further than a time $\sim 2 \cdot 10^5$ after the light-ring crossing (estimate based on the amplitude). Instead, when considering a

trajectory including only the last two encounters, Price's law is recovered at $\sim 10^4$. In agreement with the model, the number of power-law terms required to recover the numerical result has now significantly decreased to $n \sim 200$. These analyses further stress the impact of initial conditions on the extraction of the tail exponent, in stark contrast to the amplitude at transition, which is far less dependent on the trajectory integration, as shown in the previous section.

Note that all the simulations considered are consistent with Price's law at asymptotically late times, and slower decaying terms led by the τ^{-1} tail, discussed in Sec. 5.2.2, are not present. Such a result holds for systems that are originally unbounded, as in Fig. 5.14, as well as for systems directly initialized as bounded, Figs. 5.15, 5.16. This is consistent with the picture of Sec. 5.2 and linear perturbation theory [16, 14, 15].

To conclude, we test the expansion of the analytical model Eq. (5.15) in n exact power-laws Eq. (5.20) valid at large retarded times τ, against numerical evolutions of the radial infall from $r_0 = 300$ and the orbit with initial eccentricity $e_0 = 0.9$ of Table 5.1. The results are shown in Fig. 5.16, top and bottom row respectively.

The results are in perfect agreement with what was already discussed at the beginning of the current section. In particular, the history considered for the radial infall has approximately the same length ($\sim 2 \cdot 10^3$) as the simulation in Fig. 5.15. As a result, the number of faster-decaying terms necessary to reach convergence ($n \sim 200$) in the post-merger tail is also of the same order as in Fig. 5.15, as is the timescale after which Price's law (i.e. agreement with the $n = 0$ term) is recovered in the amplitude ($\sim 10^4$). The eccentric simulation in Fig. 5.16 (bottom row) has a longer inspiral before the merger, $\sim 1.5 \cdot 10^4$. As a consequence, a larger number of faster-decaying terms are necessary compared to the radial plunge simulation to reach Price's law, which happens on a longer timescale ($\sim 10^5$) consistently with the case of Fig. 5.14, as expected.

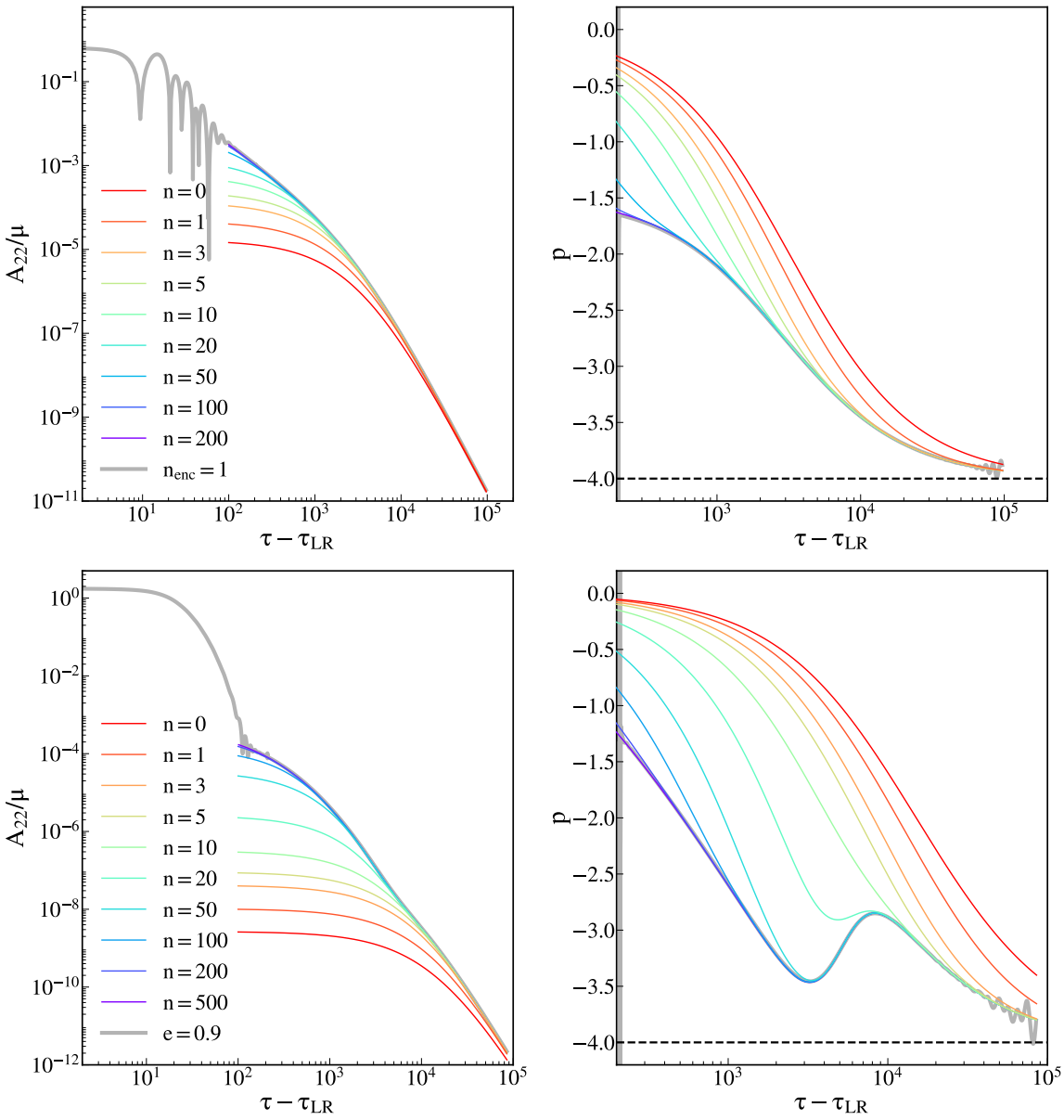

Figure 5.16: Left: Mass-rescaled amplitude of the $(2, 2)$ waveform multipole against the observer retarded time, translated with respect to the time τ_{LR} at which the test particle crosses the light-ring. Right: value of the tail exponent, Eq. (5.22). Top row: the system under study is the radial infall from $r_0 = 300$ with $E_0 = 1.00$. The time between initializing the test particle and the light-ring crossing is $\sim 2 \cdot 10^3$. Bottom row: the system under study is the orbit with initial eccentricity $e_0 = 0.9$ in Table 5.1. The time between initializing the test particle and the light-ring crossing is $\sim 1.5 \cdot 10^4$. The gray thick line corresponds to the numerical experiment obtained by integrating Eq. (5.4),(5.7) with the RWZHyp code. High-frequency oscillations in the plots on the right for very late times ($\sim 10^5$) are due to numerical noise. The coloured lines are computed through the expansion in power-laws in the retarded time τ, Eq. (5.20). The label n specifies how many power-laws have been added to Price's law (horizontal line in the right panel).

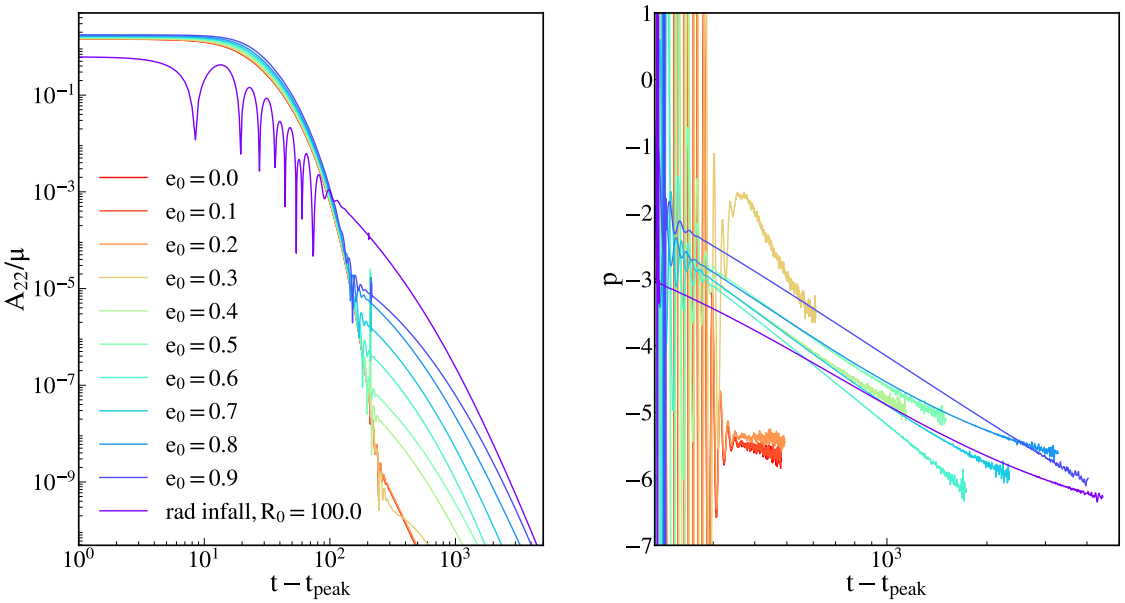

Figure 5.17: Left: Mass-rescaled amplitude of the $(2, 2)$ waveform multipole extracted at finite distance, against the observer retarded time translated with respect to the time of the A_{22} peak. Right: value of the tail exponent, Eq. (5.22). Numerical experiments, computed by integrating Eq. (5.4) with the RWZHYP code. These results are relative to the eccentric and quasi-circular simulations of Table 5.1, each labeled by the initial eccentricity e_0, and a radial infall from $r_0 = 300$ with $E_0 = 1.00$. The observer is located at $r_{obs} = 200$. We cut the simulations for values of the amplitude $A_{44} = 10^{-14}$, two orders of magnitude before the numerical precision threshold dictated by double precision.

5.7 Tail observed at finite distances

All the results reported in the chapter so far were extracted at $\mathcal{I}^+$, in terms of the retarded time τ. Concerning real observations, we can consider our detectors to be at $\mathcal{I}^+$ with very good approximation [212]. However, often numerical waveforms of comparable mass mergers are extracted at finite distances. Hence, in this section we analyze the tail produced in the numerical evolutions of Tabs. 5.1 and for a radial infall from $r_0 = 300$ with initial energy $E_0 = 1.00$, as observed at finite distance. The results are shown in Fig. 5.17, considering an observer placed at $r_{\rm obs} \sim 200$ from the BH. We observe the same scaling of the tail amplitude with the binary eccentricity as the one appearing at $\mathcal{I}^+$, Fig. 5.3. For each configuration, the tail is suppressed in amplitude by approximately one order of magnitude when observed at a finite distance compared to $\mathcal{I}^+$. The tail exponent p, Eq. (5.22), is relaxing towards a smaller value than in Fig. 5.3. It is not possible to determine this quantity exactly, due to the waveforms hitting the numerical double precision threshold before reaching the asymptotic relaxation regime. However, these results are compatible with vacuum perturbation theory, i.e. a relaxation with leading behavior $\sim t^{-2\ell-3}$ at finite distance [16, 14, 15], compared to $u^{-\ell-2}$ ($u^{-\ell-3}$) for stationary (static) initial conditions at $\mathcal{I}^+$.

5.8 Summary

In this chapter, we have investigated the late-time relaxation of a Schwarzschild BH perturbed by an infalling test particle. We worked in non-homogeneous perturbation theory, with a source representing the matter content of the test particle, and an orbit driven by a highly accurate EOB-resummed analytical radiation reaction. Analyzing the late-time propagation of low-frequency signals, we derived an analytical formula for the late-time perturbations, Eq. (5.15). This model is an integral over the entire past history of the system, revealing that the late-time relaxation of a BH carries imprints of the system's information in the far past. We tested this model against numerical evolutions obtained by solving the full Regge-Wheeler/Zerilli equations for different inspiral configurations. Our model is in good agreement with these non-circular results, as shown in Fig. 5.3, Fig. 5.4 and Fig. 5.5, respectively for bounded elliptical binaries, dynamical captures and radial infalls.

The results discussed in this chapter shed light on the nature of tails in the presence of a source, somehow hidden in homogeneous perturbation theory [16, 14, 15], in which the integral over the "history" of the system is reduced to a local expression computed on a Cauchy hypersurface, see the discussion in Chapter 2. In the non-homogeneous case, the tail is in fact due to the interaction of a time-varying quadrupole source with the long-range structure of the background. Low-frequency signals emitted by the source will interact the most with the background, resulting in their scattering; as a consequence, an observer at large distances from the BH will not see the signal as travelling on the light-cone, but with all the velocities inside it. This is the heuristical intuition behind the formal result in Eq. (5.15), that explains how the late-time relaxation of a BH is, in fact, an effect analogous to the hereditary tail of multipolar-post-Minkowskian theory [198] (see Eq. (3.40) and the discussion in Sec. 3.2).

We have found that $A_{\rm tail}$, the amplitude of the tail at the transition between the QNM and tail dominance $\tau_{\rm trans}$, depends mainly on the motion near the last apastron for eccentric binaries or dynamical captures Figs. 5.9, 5.11. In particular, we have shown that the tail is enhanced by motion at large distances with small tangential velocity; the first condition guarantees that the overlap between the source and the tail-propagator is large, while the second is necessary to minimize destructive interference among tail signals emitted close to each other. For this reason, $A_{\rm tail}$ is maximized for a radial infall vs a capture initialized at the same distance. For a radial infall from small distances $r_0 \lesssim 200$, $A_{\rm tail}$ is larger the further the infall starts, while it saturates to a maximum value for $r_0 \sim 200$, Fig. 5.5. These results are able to explain the scaling of the tail amplitude with the progenitors' binary eccentricity observed in Ref. [75] in the test-mass case and discussed in Ref. [206] for comparable masses.

We have also proposed an expansion of the tail expression Eq. (5.15), valid at late retarded times $\tau \gg \rho_+ + t'$, as superpositions of power-laws in τ. This approximation allows us to sort out the complicated behavior of the tail in a contribution that scales as the leading homogeneous perturbation theory tail (the slowest power-law that dominates the asymptotic limit), with faster decaying terms whose excitation coefficients depend on the nature of the source, that eventually die out of the signal. In particular, for the systems that eventually become bounded and merge, we recover the asymptotic decay $\sim \tau^{-\ell-2}$ of Refs. [16, 14, 15]. Slower decaying contributions, led by $\sim \tau^{-1}$, emitted during the initial unbounded stage (in the

case of a dynamical capture) cancel out at asymptotically late times. We have tested the expansion Eq. (5.20) against numerical experiments, to understand the relevance of the fast decaying contributions. The results of Figs. 5.14, 5.16 show that a large number of fast-decaying power-laws is necessary to correctly reproduce the numerical experiments, starting from the time $\tau_{\rm trans}$ at which the tail starts to dominate over the QNMs. We leave for future work the exploration of alternative closed-form expressions for late-time tails that may be more compact and require fewer terms, potentially making them better suited for parameter inference.

For completeness, we have also analyzed the behavior of higher multipoles of the waveform: an odd mode, the (32), and the (44), in Sec. 5.3.4. We observe for both modes a similar enhancement of the tail amplitude with the initial eccentricity, Fig. 5.6, 5.7, and a similar level of agreement with the numerical evolutions. These results are particularly relevant for the (44) mode, since this is the lowest mode in which quadratic QNMs significantly appear for a binary merger. A complete description of the ringdown in a non-linear setting would, in fact, benefit from the inclusion of the tail, when considering a generic planar orbit.

In Sec. 5.3.5 we have studied a scattering case. In this setting, the source is present at all times, hence it will continue to emit signals at asymptotically late times. Our model fails to describe such a system; however, when appropriately regularised, it still predicts a τ^{-1} tail signal travelling marginally close to the flat light-cone, in agreement with the classical soft graviton theorem [208, 209].

In Sec. 5.5 we show the behavior of the tail amplitude by the time it starts to dominate the strain, $A_{\rm tail}$, as a function of the eccentricity at the separatrix $e_{\rm sep}$ and the impact parameter in Eq. (5.21) at the light-ring crossing b_{LR}. From our results, it emerges that $e_{\rm sep}$ is more suited to describe $A_{\rm tail}$ than b_{LR}. In particular, $A_{\rm tail}$ is not a function of b_{LR}, since it exhibits a double-valued behavior with respect to this parameter.

All our results are expressed in terms of the radiative coordinate τ, as observed at $\mathcal{I}^+$, acting as a very good approximation to what would be observed in a real detection on Earth. However, when performing numerical simulations in a fully non-linear setting, the signal is often extracted at a finite distance in terms of the time coordinate t. Hence, to connect with these latter studies, we have studied a configuration extracted at finite distance in Sec. 5.7; as shown in Fig. 5.17, such settings preserve the scaling of the tail with the progenitors' binary eccentricity, however the amplitude of the tail is suppressed of at least one order of magnitude, also for a radial infall. In Chapter 6, we will discuss in more detail how to extract the radiative tail from numerical simulations (both perturbative and non-linear) in which the signal is computed at finite distances only.

The analytical model and numerical evolutions presented in this chapter, are in complete agreement with the independent study in Ref. [213]. In particular, with a focus limited to numerical experiments, Ref. [213] identified the apastron of an eccentric orbit as the location where tails are excited the most. Unlike the current chapter, Ref. [213] compared geodesic motion with orbital evolutions employing different prescriptions for radiation reaction, showing that the latter has a negligible impact on the tail signal. Ref. [213] extends the current study to a test particle infalling in a Kerr background, showcasing how the mechanism of tail enhancement due to the inspiral eccentricity also holds in the presence of spin.

However, future work is necessary to fully understand the impact of spin on this late-time signal.

Chapter 6

Late-time tails: comparable masses mergers

In the present chapter, we discuss the results of Ref. [2] and present the first robust extraction of late-time tails from fully non-linear numerical relativity (NR) simulations of comparable-mass black-hole (BH) binaries.

Characterizing tail effects in numerical simulations is challenging, because excitations of quasinormal-modes (QNM) can take a long time to decay [214]. Hence, to identify tail contributions, we must look for them in a regime where QNMs are short-lived, and the tail amplitude is large. The first is easy to achieve by targeting remnant BHs with small angular momentum (shorter relaxation time). The second condition is harder to obtain if we do not know a priori the dependence of the tail amplitude on the binary's initial conditions. In Chapter 5, we discussed how late-time tails are excited and explained how certain binary configurations can lead to an enhancement of their amplitude. This was done by introducing a first-principles analytical model that, for a given bounded trajectory, accurately describes the source-driven tail behavior in generic orbital configurations. The model shows how the simple picture of a single "Price tail" needs to be replaced by a superposition of a large number of inverse power-law components giving rise to a long, slowly-decaying transient. A key prediction of the model is that the tail amplitude reaches its maximum for radial infalls; hence, in this chapter, we restrict to head-on collisions. These analytical predictions, together with considerations presented in [215, 216], equip us with the necessary understanding of initial-data (ID) and boundary effects to extract a tail signal in non-linear mergers, and constitute the required semi-analytical tool to verify the robustness of numerical evolutions.

Exploiting the very high accuracy of the SpEC code [99], we demonstrate the extraction of tail effects in fully non-linear 3+1 evolutions, displayed in Fig. 6.1. The figure shows the amplitude of the gravitational wave (GW) news quadrupolar mode extrapolated to $\mathcal{I}^+$, for several head-on binary simulations with mass ratios close to unity. Around $140M$ after the peak, the amplitude transitions from an exponentially damped quasinormal-driven regime to a slowly-decaying non-oscillatory behaviour. The result aligns remarkably well with perturbative linear evolutions of an infalling test particle with compatible ID, further validating the numerical computation and pointing towards a suppression of non-linear tails contributions [55].

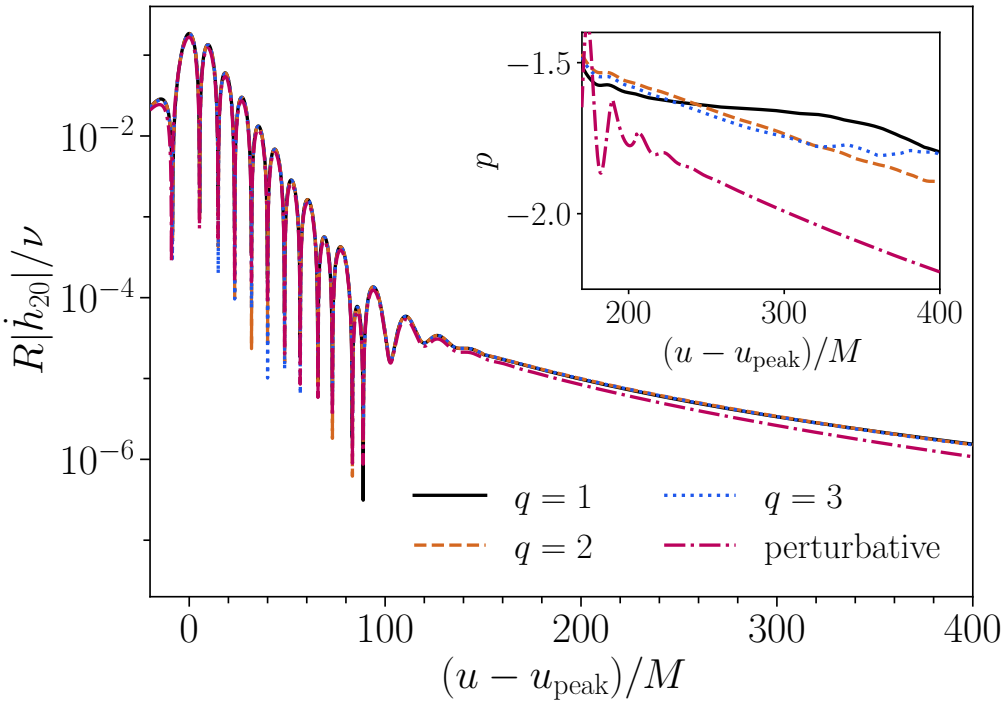

Figure 6.1: Mass-rescaled quadrupolar news amplitude, as a function of retarded time from the peak. The inset shows the behaviour of the tail exponent, as defined in Eq. (6.1). Thick lines represent non-linear evolution of head-on comparable-mass collisions, while the dot-dashed line represents a perturbative evolution of a radial infall with compatible initial data.

The chapter is structured as follows. In Sec. 6.1 we introduce the conventions that will be adopted. In Sec. 6.2 we report on the numerical methods employed both in the non-linear and perturbative cases. In Sec. 6.3, we discuss in more detail the results obtained, their interpretation, and possible non-linear effects behind the subtle differences between linear and non-linear evolutions. We conclude summarising open questions and future avenues for tail signals in Sec. 6.4.

6.1 Conventions

We use geometric units $c = G = 1$ and denote the retarded time as u. The GW strain is decomposed in spin-weight -2 spherical harmonics modes, $h_{\ell m}(t)$. To avoid memory contributions or gauge effects that could spoil tail extraction, entering as a constant offset, we focus on the GW news function $\dot{h}_{\ell m}$. Modes beyond the quadrupolar are subdominant, hence we are going to focus on $\ell = 2$. Exploiting the cylindrical symmetry of the problem, we present all results in a frame [217] in which the two BHs collide along the z-axis and hence the $m = 0$ is the only non-zero $\ell = 2$ waveform multipole. At asymptotically late times, it holds: $h_{\ell m} \propto u^{\bar{p}}$, $\dot{h}_{\ell m} \propto u^{\bar{p}-1}$, with $\bar{p} = -(\ell + 2)$ for Schwarzschild BHs. Hence, it is convenient to define a "strain tail exponent" as

$$p(t) = 1 + \frac{d \ln |\dot{h}_{\ell m}|}{d \ln u} \,. \tag{6.1}$$

so that $p(t) = \bar{p}$ at asymptotically late times. With $m_{1,2}$ we indicate the Christodoulou masses [218] of the individual black holes at the relaxation time of the simulation (i. e., when the high-frequency oscillations in the Christodoulou masses have settled down), $M = m_1 + m_2$ is the total Christodoulou mass of the system, $\nu = m_1 m_2/M^2$ the symmetric mass ratio, and $q = m_1/m_2 \geq 1$ the binary mass ratio. The time axis is constructed by setting $t = 0$ at the peak of $|\dot{h}_{20}(t)|$, and is quoted in units of M. The tortoise coordinate in perturbative evolutions is $r_* = r + 2M \log(\frac{r}{2M} - 1)$, with r the standard Schwarzschild coordinate. We indicate the distance between the binary and the observer with R.

6.2 Numerical methods

We generate non-linear evolutions of head-on collisions with the SpEC code [95, 96, 97, 98, 99], whose methods are summarised in [219, 220]. The initial data (ID) [221, 222, 223, 224] are constructed using the extended conformal thin sandwich equations [225] and the evolution is carried out with the generalized harmonic formulation [226, 227]. Standard SpEC runs stop at a retarded time of $100M$ after merger, which is typically enough to only resolve the quasinormal ringdown. In order to capture the waveform behavior on longer time scales, here we carry out simulations with much longer post-merger components, stopping at retarded time $400M$ after merger.

We compare these NR waveforms with linear perturbative waveforms of radial infalls into a Schwarzschild BH, numerically computed using the RWZHyp[1] code [93, 94]. We solve for the Regge-Wheeler/Zerilli equations, governing the evolution in time of the gauge-invariant quantities $\Psi^{(e/o)}_{\ell m}$

$$\left[\partial_t^2 - \partial_{r_*}^2 + V^{(e/o)}_{\ell m}(r_*)\right] \Psi^{(e/o)}_{\ell m}(t, r_*) = S^{(e/o)}_{\ell m}(t, r)\,. \tag{6.2}$$

These master variables encode the odd/even metric degrees of freedom at the linear level [100], as discussed in Chapter 2. In the linear evolutions, we set null ID $\Psi^{(e/o)}_{\ell m}(t = 0, r) = \partial_t \Psi^{(e/o)}_{\ell m}(t = 0, r) = 0$, as the perturbations are driven by the presence of the source $S^{(e/o)}_{\ell m}$. The latter is evaluated on the infalling test-particle trajectory. We refer to Sec. 5.1 for additional details and to Appendix A for the source explicit expression. For radial infalls with null ID, the odd sector is identically zero; hence, in what follows, we drop the superscript. Following an effective one body (EOB)-inspired approach, we compute the particle's trajectory solving the associated Hamiltonian equations of motion, Eq. (3.20), where dissipative effects linked to the GW emission are taken into account by including a radiation-reaction force [100, 74]. Such a force was computed for generic orbits by means of a PN-based, EOB-resummed analytical expansion [152, 147] for the fluxes of energy and angular momentum observed at infinity, and shown to be consistent with the corresponding numerical quantities in [101]. In Sec. 3.4, more details on the radiation-reaction we use are provided. Note that, due to the short time-scale of the dynamics in the configurations we consider, the inclusion of the radiation reaction force has a small impact on the evolution. In particular, the impact of radiation reaction on the waveform amplitude is below $\lesssim 10^{-7}$ along the whole post-merger evolution

[1] The version of the RWZHyp code used bears the tag `tails`, on the `rwzhyp_eccentric` branch.

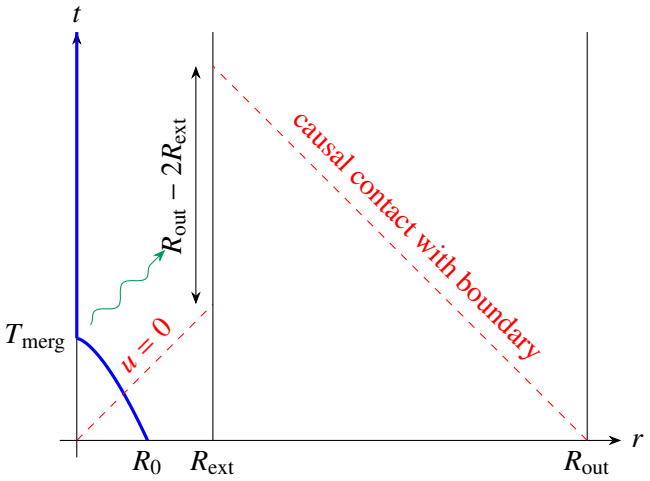

Figure 6.2: Schematic spacetime diagram demonstrating the geometry of the head-on merger and remnant, retarded time u, extraction spheres, and outer boundary.

until late times, while its impact on the trajectory is at most at the level of $\lesssim 10^{-6}$. Hence, the motion can be effectively considered as a geodesic.

At large distances, the master function $\Psi_{\ell m}$ is related to the linearized strain's spin weight -2 spherical harmonic modes $h_{\ell m}$ through [92]

$$h_{\ell m} = \frac{1}{r}\sqrt{\frac{(\ell+2)!}{(\ell-2)!}}\,\Psi_{\ell m} + O\left(\frac{1}{r^2}\right). \tag{6.3}$$

Moreover, the source term $S_{\ell m}(t,r)$ is linearly proportional to the mass ratio, which in the test-particle limit is equivalent to the symmetric mass ratio, so $\Psi_{\ell m} \propto \nu$. To compare perturbative waveforms with NR comparable-mass results, we will thus always rescale the perturbative results $\Psi_{\ell m}$ by ν. The NR waveforms are also rescaled with their symmetric mass ratio.

To compare full NR results against perturbative test-mass limit ones, we initialize the two systems with compatible ID. We only consider non-spinning black holes. The SXS simulation ID are given by setting the angular momentum to zero and imposing that the Arnowitt-Deser-Misner (ADM) energy $E_{\rm ADM}$ is equal to the total rest mass of the system M within relative accuracy of 10^{-4}, so that the two black holes are at rest at infinite separation, and the initial binding energy is close to zero. We generate equivalent test-mass data by imposing that the test particle is at rest at infinity, i. e. by setting its initial energy equal to its mass.

6.2.1 Outer boundary

The SpEC code imposes data on the outer boundary, located on a sphere with radius $R_{\rm out}$, such that constraints are preserved [226], and the physical degrees of freedom are chosen assuming that there is no gravitational radiation entering the numerical domain [228, 229]. In curved spacetimes, however, a

certain amount of radiation is always scattered back. Back-scattering, giving rise to wave propagation well within the light-cone, is precisely the mechanism responsible for tails generation [198, 199, 201, 138, 1] (see discussion in Chapters 2, 5), and a small $R_{\rm out}$ would imply missing a significant fraction of such contribution. Hence, to capture the vast majority of the back-scattered radiation, we place the outer boundary exceptionally far away from the binary location (see Tab. 6.1).

Moreover, due to imperfect boundary conditions, when radiation reaches the boundary, a non-physical numerical artifact is generated, contaminating the signal with numerical noise. As pointed out in Refs. [215, 216], this contamination can alter the structure of tails. Therefore, to study the long-range and late-time tails contribution, it is important that our simulations remain causally disconnected from the boundary. To avoid such contamination, we chose $R_{\rm out}$ to be large enough such that the boundary is never in causal contact with the extraction spheres for the entire evolution (see Table 6.1). This causal structure, our evolution domain, and the locations of finite-radius observers are visualized in Fig. 6.2.

6.2.2 GW extraction

The RWZHyp software uses a numerical domain that is decomposed into two regions, a compact inner region and an outer hyperboloidal layer [230, 126, 231]. The inner region contains the particle trajectories and has a uniform grid in r_*, ranging from $r_* = -100M$ to a large positive r_* value. The hyperboloidal

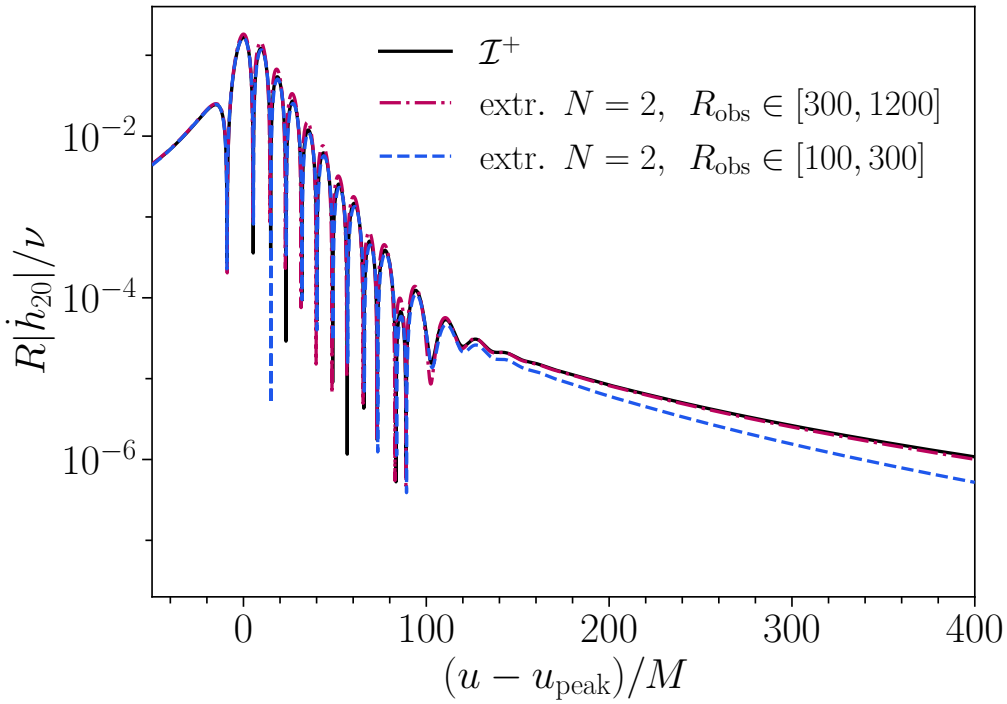

Figure 6.3: Mass-rescaled quadrupolar news amplitude. Comparison of the waveform directly extracted at $\mathcal{I}^+$ (black solid) using RWZHyp, while the dashed and dot-dashed lines correspond to waveforms extrapolated to $\mathcal{I}^+$ using a polynomial extrapolation built from finite-distance observer locations $R_{\rm obs} \in [300M, 1200M]$ (purple) and $R_{\rm obs} \in [100M, 300M]$ (blue).

layer, compactified over r_*, is attached to the positive end of the inner region in order to bring $\mathcal{I}^+$ into the computational domain. As a result, perturbative waveforms can be computed both at finite distances, in terms of the coordinate time t, as well as at $\mathcal{I}^+$ in terms of the retarded time u.

In SpEC the GW information is extracted on spheres, whose radii $R_{\rm ext}$ are distributed in the interval $[300M, 1200M]$ and are held fixed across all simulations in this work, as opposed to standard SpEC runs in which their radii scale with $R_{\rm out}$. The extracted finite radius waveform data are extrapolated to $\mathcal{I}^+$ by a standard polynomial fit using the method of [232] as implemented in the scri package [233, 234, 235, 236, 237].

The idea behind this extrapolation technique is the following. First, we introduce a quantity u that, in the limit of large distances, is a null coordinate [232]

$$u \equiv t_{\rm corr} - \left[R + 2E_{\rm ADM} \log\left(\frac{R}{2E_{\rm ADM}} - 1\right)\right], \tag{6.4}$$

with

$$R \equiv \left[\frac{1}{4\pi}\int d\Omega \sqrt{\det(g_{\mu\nu})}\right]^{1/2} \quad , \quad t_{\rm corr} \equiv \int_0^t dt' \frac{\langle N\rangle}{\sqrt{1-2E_{\rm ADM}/R}}, \tag{6.5}$$

where $g_{\mu\nu}$ is the spacetime metric and $\langle N\rangle$ is the lapse average value on the extraction 2-sphere [232]. The strain multipoles $h_{\ell m}$ are computed at different $R_{\rm ext}$ as a function of the coordinate u. Then, for each "retarded time-step" u_i of the evolution, the quantities $R \cdot h_{\ell m}(u_i, R)$ are fitted across the extrapolation radii with a polynomial in R determined by the strain peeling properties towards $\mathcal{I}^+$, truncated at order $N-1$ [232]

$$R \cdot h_{\ell m}(u_i, R) = h^{(0)} + h^{(1)}R^{-1} + ... + h^{(N-1)}R^{N-1}, \tag{6.6}$$

N is defined as the *extrapolation order*. The strain at $\mathcal{I}^+$ is recovered in the limit $R \to \infty$ as [232]

$$\lim_{R\to\infty} R \cdot h_{\ell m}(u_i, R) = h^{(0)} \tag{6.7}$$

To understand whether this extrapolation technique can actually recover the tail signal observed at $\mathcal{I}^+$ without introducing numerical artifacts, we first discuss it in the perturbative limit, where the generation and propagation of the tail signal are understood. Then, we run a series of numerical (perturbative) experiments to test the method's robustness, leveraging the availability of perturbative numerical waveforms computed both at finite distances and at $\mathcal{I}^+$.

The tail in the strain observed at finite distances in terms of the coordinate time t has an asymptotic behaviour $\propto t^{-3\ell-m}$ [16, 14]. Hence, it is suppressed with respect to the signal observed at $\mathcal{I}^+$ as a function of the retarded time u, which is instead characterized by a decay $\propto u^{-\ell-2}$. However, even when observed at finite distance, the asymptotically late-time decay is characterized by a transient radiative tail $\propto u^{-\ell-2}$, behaving as the one observed at $\mathcal{I}^+$ [14]. This transient eventually leaves place to the $\propto t^{-3\ell-m}$ term. In [125], ID-driven perturbative numerical simulations confirmed this picture, showing that a progressively longer transient appears as the observer is moved away from the source. The physical interpretation is the following: tail terms are generated by the interaction of small frequency signals with the long-range, slow decay of the background. Smaller frequencies can probe larger scales and get back-scattered more

SXS identifier	q	D_0/M	$R_{\rm out}/M$	u_{con}/M
SXS:BBH:3991 [238]	1	100	4000	1600
SXS:BBH:3997 [239]	2	100	4000	1600
SXS:BBH:3998 [240]	3	100	4000	1600
SXS:BBH:3994 [241]	1	100	8000	5600
SXS:BBH:3995 [242]	1	200	8000	5600
SXS:BBH:3996 [243]	1	400	8000	5600

Table 6.1: List of simulations and relevant parameters: D_0 is the initial separation, $R_{\rm out}$ is the radius of the outer boundary and $u_{con} = R_{\rm out} - 2R_{\rm ext}$ denotes the approximate retarded time at which the outermost extraction radius (located at $1200M$) would enter in causal contact with the outer boundary. The first column states the identifier in the SXS waveform catalog [220, 156]. Numerical data are available from Caltech Data [244, 245, 246, 247, 248, 249, 238, 250, 251, 241, 242, 243, 239, 240] and can also be accessed through the sxs python package [252, 156].

efficiently. If the observer is located close to the BH, smaller frequencies cannot reach it and, as a consequence, the observed tail is quenched.

With this phenomenology in mind, we extrapolate the numerical waveforms obtained from non-linear evolutions at finite distance to $\mathcal{I}^+$, using the SXS standard polynomial extrapolation procedure of [232] as implemented in the scri package [233, 234, 235, 236, 237], with polynomial order $N = 2$. In Fig. 6.6, we also compare to the results obtained with $N = 3$, showing that the extrapolation order does not alter our conclusions. We choose extraction radii at large distances in the interval $[300M, 1200M]$. To gain intuition about whether our procedure leads to a correct extraction of tails, we perform a test on the perturbative waveforms computed with the RWZHyp code, where we can compare finite distance results to waveforms directly computed at $\mathcal{I}^+$, see Fig. 6.3. In particular, we compare two different extrapolations, computed considering $R_{\rm obs} \in [100M, 300M]$ and $R_{\rm obs} \in [300M, 1200M]$ respectively. For the extrapolation technique, we employ the same algorithm used for the non-linear waveforms: the procedure of Ref. [232] previously described as implemented in the scri package [233, 234, 235, 236, 237]. Since we are considering linear perturbations on top of a Schwarzschild BH, we consider $u = t - r_*$ as a null coordinate and $R = r$. As expected from our argument above, the extrapolation performed with $R_{\rm obs}$ closer to the BH yields a large mismatch with respect to the one computed at $\mathcal{I}^+$. On the other hand, extrapolating with $R_{\rm obs}$ far enough from the BH, yields an extrapolation in excellent agreement with the tail computed at $\mathcal{I}^+$ by means of the hyperboloidal layer. The agreement slowly decreases in time; as expected, the extrapolated waveform undergoes a faster decay after the initial evolution.

6.3 Results

In Table 6.1 we report the parameters of the simulations carried out with the above methods. Fig. 6.1 shows the resulting news function, normalized by the symmetric mass ratio, with respect to the retarded time u. A first striking result from Fig. 6.1 concerns the dependence on the mass ratio. In fact, after mass-rescaling the waveforms, the comparable-mass waveforms with different mass ratios are very similar (differences around the percent level), suggesting that finite mass-ratio corrections do not play a significant role in the waveform generation, including the tail part.

We also compute the tail exponent $p(t)$ (Eq. (6.1)), reported in the inset of Fig. 6.1. Its magnitude is much smaller than the asymptotic Price-law value ($\bar{p} = -4$, for this multipole), towards which we expect it to slowly converge [1], as discussed in Chapter 5. Such a decrease in exponent magnitude significantly boosts the tail amplitude at intermediate times. This result agrees with the analytical perturbative picture of [1] discussed in Chapter 5, according to which tail emission is maximized for motion at large distances from the central BH, with small angular velocity. The additional numerical time derivative required for the exponent computation, combined with finite resolution, tends to introduce high-frequency noise. To compute the tail exponent at late times we therefore apply a Savitzky-Golay filter [253] on the waveform to suppress high-frequency oscillations. In the next section, we compare the unfiltered tail exponent with the one computed after applying the filter, showcasing that our conclusions are not impacted by the filtering.

Even the test-mass perturbative case (similarly rescaled, and aligned minimizing the post-peak mismatch) shows a remarkable agreement with the non-linear evolutions, displaying the same slowly-decaying behaviour and an identical overall morphology. Such results confirm that the tail is primarily generated by the source term. This aligns with previous findings, which showcased how test-particle perturbative evolutions proved to be a remarkably accurate tool for the modelling of inspiral-merger-ringdown waveforms [100, 74, 254]. Somewhat surprisingly, though, this framework provides *quantitatively accurate* predictions even for comparable mass systems [255, 256], as we confirm here. This is true even in the (a priori strong-field) merger stage, as notably depicted also in Fig. 2 of [103].

However, in Fig. 6.1 above, there is a visibly growing mismatch as the tail evolves, with the non-linear evolution displaying a slower decay with respect to the perturbative result. This may be due to a variety of effects, including the presence of non-linear tail components (computed in [55] for $\ell = 4$ modes within second order perturbation theory, see also [50]), together with corrections due to the finite mass ratio or the time-dependent background in the non-linear case [51, 52, 257, 54, 53]. Although the good agreement in the quasinormal-driven regime suggests the last two effects are likely small, the hereditary nature of tails implies that small differences in the evolution can accumulate and impart a larger effect.

In the remainder of this section, we will investigate the robustness of our results. We begin by discussing the filtering technique applied to the late-time portion of the non-linear signal to remove high-frequency oscillations that could otherwise spoil the investigation of the tail exponent p. Next, we present a series of tests obtained by changing the initial binary configuration, particularly the initial separation R_0, or the

numerical setup of the non-linear simulations. As we will show, the late-time signal is not appreciably affected by these variations. Finally, we briefly discuss results obtained through Cauchy Characteristic Evolution (CCE) and compare them with the extrapolation method introduced in Sec. 6.2.2 that is used for all the results of the current chapter.

6.3.1 Waveform filtering

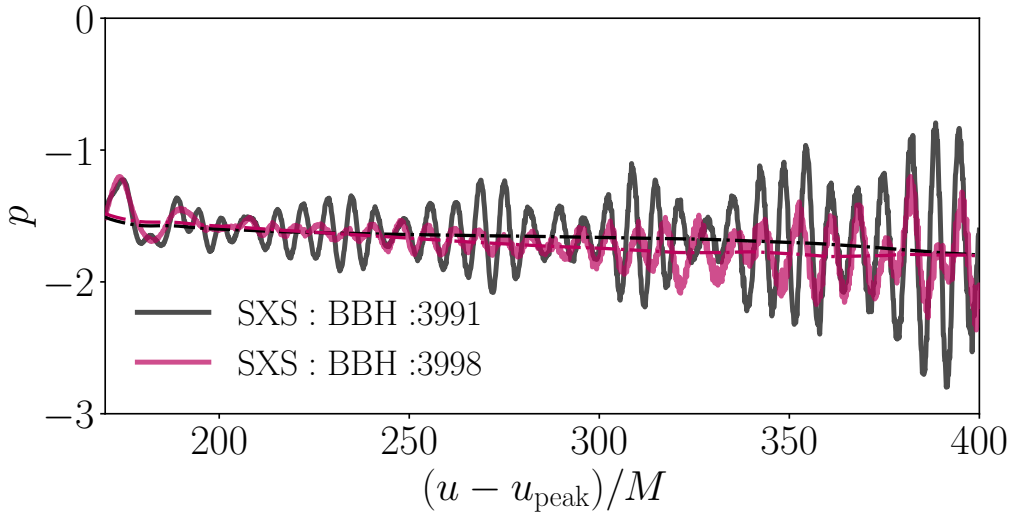

Figure 6.4: Tail exponent of Eq. (6.1) as a function of retarded time from the peak, extracted from both unfiltered (solid thick) and filtered (dashed thin) numerical data. Results relative to two representative comparable-mass SpEC simulations of Tab. 6.1.

To reduce high-frequency numerical noise in the NR waveforms, we applied a Savitzky-Golay filter. The filter, acting on a sliding time window, is applied on the news amplitude in the interval $u - u_{\rm peak} \in [150M, 400M]$. The two dominant noise frequency components are suppressed by applying the filter with a window length of $20M$ and then $6M$, respectively, suppressing the modulations and high-frequency oscillations contaminating the news. The tail exponent is instead filtered with a $20M$-long window. The filter fits the data with a polynomial function in the specified time window, then sets the fit prediction at the center of the interval as the value of the filtered function. We select a linear fitting function, using `scipy.signal.savgol_filter(data, window_length=window_length, polyorder=1)`.

In Fig. 6.4 we compare the filtered and unfiltered tail exponents, for two exemplary SpEC simulations analyzed in this work. We report the simulations SXS:BBH:3991 and SXS:BBH:3998, which are evolved under the same R_{out} but different binary ID, to showcase how the result obtained is robust with respect to different binary ID. Albeit contaminated by high-frequency noise, a clear decaying trend for the exponent is distinguishable.

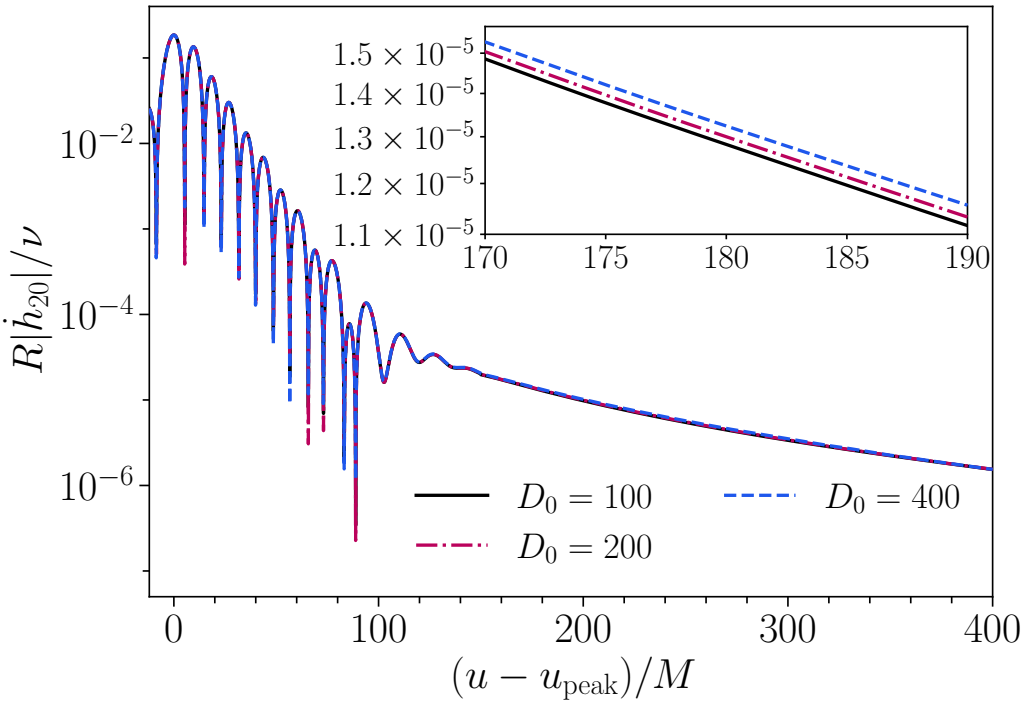

Figure 6.5: Mass-rescaled quadrupolar news amplitude for equal-mass runs with different initial separation D_0.

6.3.2 Impact of initial separation

We investigate a sequence of NR simulations with $q = 1$ and varying initial separation (with identifiers SXS:BBH:3994, SXS:BBH:3995 and SXS:BBH:3996 in Table 6.1). If ID are set up consistently, the three evolutions should give close to indistinguishable results. This is what Fig. 6.5 shows, with very small differences even when increasing the initial separation by a factor of four. This confirms the robustness of our numerical evolutions. However, in practice, our ID at different separations will not be perfect (i. e. will not correctly capture the entire past binary history). In this case, the tail amplitude is expected to *increase* with larger initial separation, since this enhances the overlap between the source and the tail propagator [1], consistently with tails hereditary nature [198, 199, 201, 138], as discussed in Chapter 5. Such an increase is expected to be small for large enough separations, so that most binary history is already captured. This is confirmed by Fig. 6.5, showing a small increase in the tail amplitude when increasing the separation, another validation of our results' robustness.

6.3.3 Resolution tests

In Fig. 6.6 we compare three different resolution levels (see [219, 220]), for the SXS:BBH:3991 case (see Tab. 6.1). We report the residuals relative to the highest resolution available, Lev3, with smaller

extrapolation order, $N = 2$, defined as

$$\text{Res.(X)} = 100\frac{|\dot{h}_{20}^{(\text{X})}| - |\dot{h}_{20}^{(\text{Lev3,N=2})}|}{|\dot{h}_{20}^{(\text{Lev3,N=2})}|}\,. \tag{6.8}$$

The tail properties are unchanged with increasing resolution, and differences between different resolution levels are too small to affect any of the considerations previously discussed, including comparisons with perturbative waveforms.

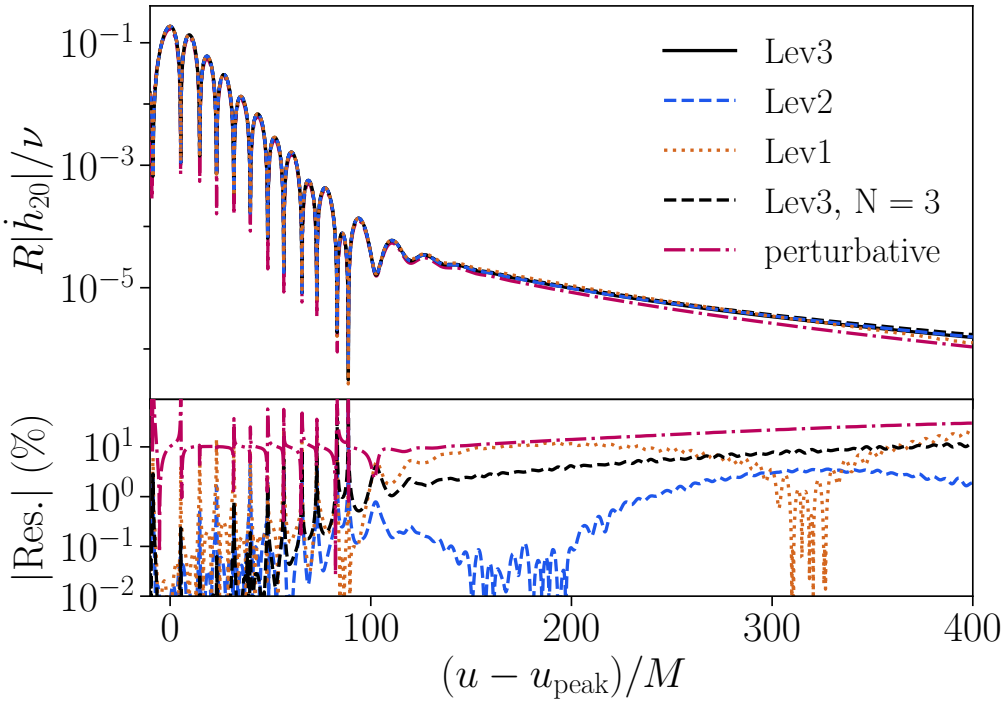

Figure 6.6: Top: Mass-rescaled quadrupolar news amplitude for different resolution levels (solid) for the SXS:BBH:3991 case. A higher extrapolation order is shown in dashed black (other lines refer to $N = 2$), while the purple dot-dashed line reports the perturbative result. Bottom: residuals with respect to the highest resolution (Lev3).

6.3.4 Cauchy-characteristic evolution

We investigate the waveforms obtained through CCE and compare the late-time portion of the signal with the extrapolated to $\mathcal{I}^+$ one. A CCE evolution consists of two steps. The initial step is the standard Cauchy evolution: the spacetime is evolved and the signal is extracted on a 2-sphere at a finite distance, far from the GWs source. In the second step, the spacetime computed at different times on the extraction sphere is used to start a characteristics integration extended to $\mathcal{I}^+$.

We run SpECTRE code's CCE module [176, 258, 259] on worldtubes with radii $[300, 600, 900, 1200]M$. Initial data for the first null hypersurface for each simulation was created using SpECTRE's default

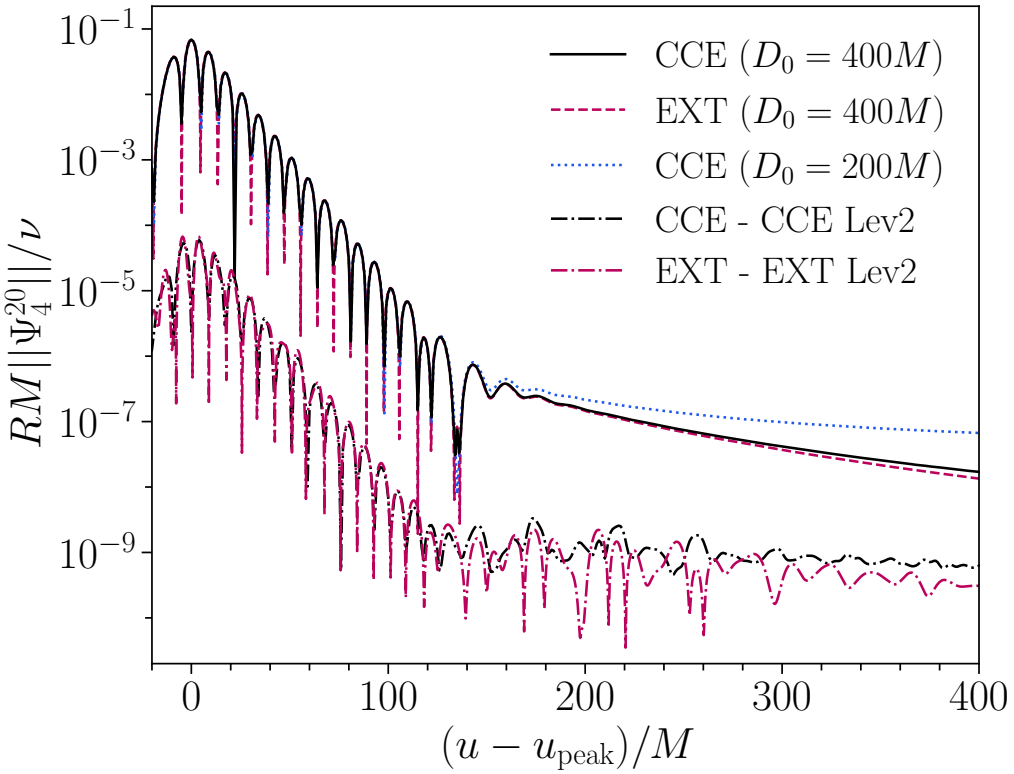

Figure 6.7: Mass-rescaled quadrupolar Ψ_4 amplitude, as a function of retarded time from the peak. The CCE ($R_{\rm ext} = 600M$) and extrapolated ($N = 2$) waveforms of SXS:BBH:3996 with $D_0 = 400M$ are shown in black and purple. The CCE waveform SXS:BBH:3995 with $D_0 = 200M$ is shown in blue. Differences between the two highest Cauchy-evolution resolutions for SXS:BBH:3996 are shown with dot-dashed lines.

CONFORMALFACTOR method. After running CCE, we mapped each system to the superrest frame of its remnant black hole 50M before the end of the simulation [260, 261, 262, 212].

In Fig. 6.7 we show the Newman-Penrose scalar Ψ_4 extracted using CCE (with $R_{\rm ext} = 600M$)[2] and extrapolation, for the cases SXS:BBH:3995 and SXS:BBH:3996. We also show the residual between the highest and next-highest resolutions for both the CCE and extrapolated waveforms. As can be seen, while the CCE and extrapolated waveforms for $D_0 = 400M$ seem to agree fairly well, for $D_0 = 200M$ the CCE waveform has a much slower falloff than the extrapolated waveform. We suspect that this inconsistency is likely due to the initial data in CCE. In particular, with a shorter simulation, like SXS:BBH:3995 with $D_0 = 200M$, there is less time for the radiation due to unphysical initial data to propagate out of the system. Consequently, the late-time tail behavior between the two simulations can take on fairly different structures. We choose to work with extrapolated waveforms for the main results presented in this chapter, to mitigate this effect. Understanding the impact of initial data on the tails of CCE waveforms will be the subject of future studies.

[2]We use $R_{\rm ext} = 600M$ since this worldtube radius shows marginally better agreement with the extrapolated waveform. Larger worldtube radii tend to yield a slightly slower falloff. The reason behind this behaviour will be investigated in future work.

6.4 Summary and future avenues

We have investigated and uncovered late-time gravitational-wave tails in 3+1 non-linear simulations of black holes collisions through the highly accurate SpEC code, robustly validating this result through a number of numerical tests. The waveforms display a remarkable agreement with perturbative results, a fact that deserves further scrutiny in future works.

Our results raise several interesting questions. On the modeling side, these include: What is the non-linear content of late-time tails? Can second-order tails explain the observed differences between linear and non-linear evolutions? Or can these instead be accounted for by higher-order (self-force type) corrections to the trajectory or the dynamical background? A one-power slower decay is predicted by mathematical relativity results of Ref. [263] when accounting for non-linearities. Could this be the cause of our deviations from perturbation theory? Precision studies on this subject will benefit from longer simulations and the development of Cauchy Characteristic Matching (CCM) techniques [264, 265, 266] or non-linear codes in hyperboloidal coordinates [267, 268, 269, 270], to uncover the subtle role of non-linearities.

At the same time of the work that we discussed in this chapter, based on Ref. [2], another investigation of late-time tails in fully non-linear numerical evolutions of head-on collisions appeared, Ref. [271], using CCM to compute the waveform at $\mathcal{I}^+$. Notably, the two studies yield consistent results for the equal-mass case, the only overlapping dataset. The CCM method of Ref. [271] could be employed in the future to study late-time tails emitted by comparable masses eccentric mergers, to further test Chapter 5 predictions in a fully non-linear setting.

Chapter 7

Dynamical excitation of quasi-normal modes

In Chapter 2, we have reviewed known results for linear perturbations of a Schwarzschild black hole (BH). We showed that the Green's function (GF) of this geometry has a series of infinite simple poles in the complex Fourier domain, denoted as quasi-normal frequencies (QNFs). The GF depends only on the background and, as a consequence of the no-hair conjecture, the QNFs are functions only of the (Schwarzschild) BH mass M [24, 26, 272, 27]. If the perturbations originate from Gaussian-like initial data, the QNFs generate a *ringing* signal: a superposition of exponentially damped sinusoids called quasi-normal modes (QNMs), whose amplitudes depend on the initial data.

A ringdown signal is also emitted by more complex initial data, e.g. the ones generated by a BH binary merger right after a common horizon has formed. A posteriori fits of numerical waveforms emitted by BH binary mergers show that the QNMs amplitudes are highly sensitive to the inspiral configurations [76, 77, 11, 78, 12, 79, 49, 80, 69, 81, 82, 83, 84], as detailed in Sec. 4.1. For certain modes, the amplitude can be parametrized as a function of progenitors' binary quantities, such as the mass ratio and the spins, to closely resemble the dependence of the respective post-Newtonian multipole during the inspiral [76, 77, 11, 79]. This suggests that the inspiral post-Newtonian and the post-merger ringdown modes share the same "source". Therefore, computing accurate predictions of the QNMs amplitudes requires understanding how the plunge-merger dynamics couples to the ringdown. Several works derived a heuristic intuition for this process, based either on phenomenological [179, 73] or toy models [74, 273, 75], as discussed in Sec. 4.2. However, to the best of our knowledge, a first-principles understanding of the ringdown dynamical excitation is missing.

Two broad strategies have been explored in the past to analytically predict the QNMs amplitudes. The first, valid for generic mass ratios, entails modeling the post-merger initial data (e.g., the close-limit approximation [274, 275]). In this chapter, we focus on a second approach valid in the extreme mass-ratio limit, which consists of treating the binary companion as an external source within perturbation theory. This approach has the advantage that it can be systematically extended to higher mass ratios, through higher orders in BH perturbation theory or through the effective one body (EOB) framework. Past

literature within this framework, Ref. [276], is limited to a specific binary configuration (radial infalls) and provides results valid only at late times (when the constant-amplitude ringdown template well describes the waveform). The difficulty in extending analytical computations at earlier times lies in not knowing how the QNMs signal propagates with respect to the light-cone. Being interested in physical signals, the retarded GF is the appropriate GF component to be selected, propagating signals either on or inside the light-cone. We refer to the prescription selecting over which portion of the light-cone the QNMs signal travels as the *"QNMs causality condition"*. As discussed in Sec. 2.3.1, an exact QNMs causality condition was computed for a toy-model geometry [41], while, for a Schwarzschild BH background, only a heuristic prescription was proposed [14, 118, 15, 119], valid if the source of the perturbations is localized far away from the light-ring.

In the present chapter, we focus on the ringdown driven by a point particle infalling into a Schwarzschild BH through generic planar orbits. We compute a first-principles (i.e. obtained by solving perturbatively Einsteins' equations) model for the full signal propagated by the QNMs GF, for a given trajectory. We do not limit the analysis to the late-time, constant-amplitude regime; instead, we provide a prediction for the dynamical QNMs excitation during the inspiral-plunge. To achieve this result, we derive an accurate QNMs causality condition and show that it automatically resolves a common obstacle in the analytic calculation of the QNMs amplitudes: the GF divergence for a source extended towards the horizon. We find that the signal can be divided into two components that we denote as excitation and impulsive contributions. The impulsive contribution is "local": it only depends on the source configuration at the time it is emitted. The excitation contribution is an "history" term which accumulates past information and that, at late times, yields the constant-amplitude QNMs response. In Chapters 5, 6, we have discussed another contribution depending on the history of the source, hereditary tails. Tails propagator decays much slower than the QNMs ones, as a consequence, this signal can accumulate "more efficiently" past history. Instead, the constant-amplitude ringdown in the post-merger signal is mainly influenced by the last stages of the plunge. Hereditary tails are characterized by a zero-frequency propagator; as a consequence, the effect of an oscillating source translates in destructive interference between subsequent tail signals (see Sec. 5.4). The QNMs propagator is a superposition of terms oscillating with different frequencies. Each of these QNFs is quasi-resonantly excited by the oscillating source during the inspiral-plunge. During this stage of the dynamics, the instantaneous frequency of the full QNMs response is effectively driven by the test-particle source, and the modes' amplitudes behave as activation functions in time. After the particle crosses the light-ring, the source gradually stops contributing to the QNMs amplitudes, which saturate to constant values. The signal emitted by the source while it approaches the horizon is quenched by its infinite redshift, escaping towards an observer at $\mathcal{I}^+$ as a superposition of an infinite tower of exponentially-damped, zero-frequency contributions, that we denote *redshift terms*. The existence of these redshift terms is in agreement with past literature [16, 277, 278, 279]. As a by-product of the analysis, we also explicitly compute for the first time the amplitude of the fundamental mode in the quadrupole, for generic planar orbits.

The plan of the chapter is as follows. In Sec. 7.1, we introduce the methods and conventions used in this chapter, or refer to the other section of this thesis where they are detailed. In Sec. 7.2, we derive the QNMs

causality condition, then study the QNMs GF convolution with the test-particle source. We also employ near-horizon expansions to assess the regularity and temporal structure of the QNMs signal, and study the role of the source redshift. In Sec. 7.3 we detail our predictions for a quasi-circular plunge and show that the qualitative picture is unchanged for intermediate to high eccentricities. We then discuss a radial infall. We construct the portion of the waveform propagated by the QNMs GF and evaluate its agreement with a complete numerical solution of the perturbative equation. In Sec. 7.4 we provide an analytical prediction of the ringdown quadrupolar total amplitude, phase and leading redshift term as a function of the eccentricity at the separatrix and the impact parameter, Eq. (7.70), at the light-ring crossing. We summarise our findings and briefly discuss future directions in Sec. 7.5.

7.1 Conventions and methods

We work in geometric units $c = G = 1$. Our analysis focuses on non-spinning BH binaries with small mass ratios, thus we linearize Einstein's equations and discard higher order corrections. The background metric is thus Schwarzshild Eq. (5.1). We rescale $r \to r/\mathrm{M}$. We will use this convention throughout the chapter. Since at first perturbative order the mass and spin of the BHs are unchanged, the final BH will not be spinning. For this reason, we can expand the strain in spin-weighted spherical harmonics modes ${}_{-2}Y_{\ell m}(\theta, \varphi)$, retaining consistency with the spacetime symmetries both in the inspiral and the ringdown phase (i.e. no mode-mixing [183] arises):

$$h(t, r, \theta, \varphi) = \sum_{\ell \geq 2, |m| \leq \ell} h_{\ell m}(t, r) {}_{-2}Y_{\ell m}(\theta, \varphi) \tag{7.1}$$

The even (odd) components of the strain are obtained by solving the Zerilli (Regge-Wheeler) equation

$$\left[\partial_t^2 - \partial_{r_*}^2 + V_{\ell m}(r_*)\right] \Psi_{\ell m}(t, r_*) = \mathcal{S}_{\ell m}(t, r_*)\,, \tag{7.2}$$

where we have introduced the tortoise coordinate with the convention $r_* = r + 2\,\log(r/2 - 1)$. The strain multipoles $h_{\ell m}$ can be computed from the Regge-Wheeler/Zerilli eigenfunctions $\Psi_{\ell m}$ through

$$\Psi_{\ell m} = \frac{h_{\ell m}}{\sqrt{(\ell + 2)\,(\ell + 2)\,\ell\,(\ell - 1)}} \tag{7.3}$$

We divide the source function on the right-hand side into two different components

$$\mathcal{S}_{\ell m}(t, r_*) = S_{\ell m}(t, r_*) + S^{\mathrm{ID}}_{\ell m}(t, r_*)\,. \tag{7.4}$$

$S^{\mathrm{ID}}_{\ell m}$ is the initial-data source, i.e.

$$S^{\mathrm{ID}}_{\ell m}(t, r_*) = \Psi_{\ell m}(t_0, r_*)\partial_t \delta(t - t_0) + \partial_t \Psi_{\ell m}(t_0, r_*)\delta(t - t_0)\,. \tag{7.5}$$

While the source function $S_{\ell m}(t, r_*)$ of Eq. (7.4) has a generic time dependence.

We focus on perturbations of a Schwarzschild BH driven by a test particle infalling into it. Since we initialize the test particle far away from the BH, we can assume null data of the perturbation field on the initial Cauchy hypersurface $t = t_0$, i.e.

$$\Psi_{\ell m}(t = t_0, r_*) = \partial_t \Psi_{\ell m}(t = t_0, r_*) = 0\,. \tag{7.6}$$

This condition implies $S^{\rm ID}_{\ell m} \equiv 0$, hence Eq. (7.4) depends only on the source function $S_{\ell m}$. The latter is localized on the test-particle trajectory and can be decomposed into two pieces

$$S_{\ell m}(t, r_*) = \tilde{f}_{\ell m}(t, r_*)\, \delta(r_* - r_*(t)) + \tilde{g}_{\ell m}(t, r_*)\, \partial_{r_*} \delta(r_* - r_*(t)) \,. \tag{7.7}$$

Explicit expression for the source functions $\tilde{f}_{\ell m}$, $\tilde{g}_{\ell m}$ can be found in Appendix A.

The test-particle trajectory $(r(t), \varphi(t), \theta(t) = \pi/2)$, with $\varphi(t)$, $\theta(t)$ azimuthal and polar angle respectively, is computed solving the Hamiltonian equations of motion in Eq. (5.8) driven by radiation-reaction effective forces discussed in Sec. 3.4. These equations are solved numerically with the RWZHyp code [93, 94]. The code also solves for the gravitational perturbation $\Psi_{\ell m}$ at future null infinity $\mathcal{I}^+$, which we will use to test our analytical predictions. The analytical results presented in this Chapter are informed only on the numerical trajectory, which is completely independent from the numerical waveform. More details on the RWZHyp code can be found in Sec. 5.1.

Due to the inclusion of radiation reaction, the trajectory is non linear. By feeding this trajectory into the source for the linearized perturbations, we obtain a treatment that is not formally consistent with first-order perturbation theory. We refer to Chapter 1 for a discussion of the validity of this approach. In Chapter 8, we argue that, due to the quasi-geodesic nature of the motion during the final stages of the plunge, we expect the results presented in this chapter to be valid within a first-order perturbation theory framework.

7.2 Analytical predictions

7.2.1 QNMs propagation and regularity

The general solution of Eq. (7.2) can be computed by means of the Green's function (GF) method as

$$\Psi(t, r_*) = \int_{-\infty}^{\infty} dt' \int_{-\infty}^{\infty} dr'_* G(t - t'; r_*, r'_*) \mathcal{S}(t', r'_*) \,, \tag{7.8}$$

In Chapter 2, we reviewed this method and investigated the GF of a Schwarzschild BH background. Following Ref. [14], we showed that this GF can be separated into three different components: an initial "prompt" response, a late-time "tail" and, at intermediate times, a "ringing" signal. The latter is a superposition of exponentially decaying oscillatory modes, the quasi-normal modes (QNMs). In this chapter, we will focus on the portion of the signal (7.8) propagated by the QNMs GF.

In Eq. (7.8), the integral is not actually performed in the entire domain $t' \in (-\infty, \infty)$; the choice of GF will self-consistently impose a causality condition describing how the signal propagates with respect to the light-cone. In particular, to describe a physical signal we select the retarded GF, which enforces the condition of propagation inside/on the light-cone. As detailed in Sec. 2.3.1, in the past the QNMs response was considered as a *scattering* off the peak of the potential barrier describing the curved background geometry [14, 118, 15, 119]. Following this heuristic argument, given initial data localized at $(t', r'_* \gg 0)$ and an observer located at $r_* \gg r'_*$, the QNMs response was expected to dominate the signal only for $t - r_* \geq t' + r'_*$.

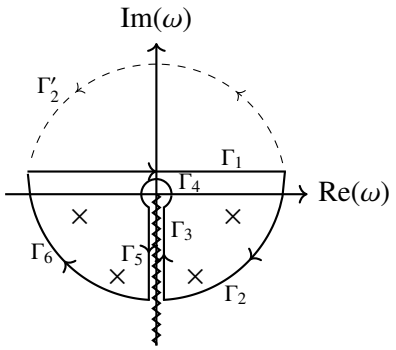

Figure 7.1: Schematic representation of the complex-frequencies plane relative to the integrand in Eq. (7.14). The zig-zagged line is the branch cut, crosses are the simple poles of the integrand. Thick and dashed lines represent two possible closed contours: $\Gamma_1 + \Gamma_2'$ and $\Gamma_1 + \Gamma_2 + \Gamma_3 + \Gamma_4 + \Gamma_5 + \Gamma_6$. Figure taken from Ref. [1].

In this section, we derive a first-principle prescription identifying over which portion of the light-cone the QNMs GF propagates a generic perturbation source.

We do not impose any prescription on the source coordinate r_*', but we assume an observer placed far away $r_* \gg r_*'$ and $\omega r_* \gg 1$. The GF in the Fourier domain can be written as follows

$$\tilde{G}(\omega; r_*, r_*') = \frac{i\, e^{i\omega r_*}}{2\omega A_{\rm in}(\omega)} \tilde{u}^{\rm in}(\omega, r_*')\,, \tag{7.9}$$

obtained substituting the asymptotic expression for $\tilde{u}^{\rm out}$, Eq. (2.52), and the Wronskian expression in Eq. (2.66) into the definition Eq. (2.49). In Eq. (7.9), $\tilde{u}^{\rm in}(\omega, r_*')$ is a solution of the homogeneous RWZ equation in frequency domain, Eq. (2.50), which reduces to a *unitary ingoing* plane wave $e^{-i\omega r_*}$ in the limit $r_* \to -\infty$, as in Eq. (2.51). In particular, as detailed in Sec. 2.2.1, the solution $\tilde{u}^{\rm in}$ can be written as

$$\tilde{u}^{\rm in}(\omega, r_*) = A_{\rm in}(\omega)\tilde{u}_{\infty-}(\omega, r_*) + A_{\rm out}(\omega)\tilde{u}^{\rm out}(\omega, r_*)\,, \tag{7.10}$$

with $\tilde{u}_{\infty-}$ satisfying $\tilde{u}_{\infty-} \to e^{-i\omega r_*}$ in the limit $r_* \to \infty$. The quasi-normal frequencies (QNFs) are values $\omega = \omega_n$ for which $A_{\rm in}(\omega_n) = 0$. At these frequencies, $\tilde{u}^{\rm in}$ reduces to a solution behaving as a purely ingoing (outgoing) plane wave at the horizon (infinity), i.e. $\propto e^{\pm i\omega r_*}$ for $r_* \to \pm\infty$.

Substituting Eq. (7.10) into Eq.(7.9), the Fourier domain GF can be divided in two contributions

$$\tilde{G}(\omega; r_*, r_*') = \tilde{G}^{(1)}(\omega; r_*, r_*') + \tilde{G}^{(2)}(\omega; r_*, r_*')\,, \tag{7.11}$$

with

$$\tilde{G}^{(1)}(\omega; r_*, r_*') = \frac{i}{2\omega}\, e^{i\omega r_*} \tilde{u}_{\infty-}(\omega, r_*')\,, \tag{7.12}$$

$$\tilde{G}^{(2)}(\omega; r_*, r_*') = \frac{i\, A_{\rm out}(\omega)}{2\omega A_{\rm in}(\omega)} e^{i\omega r_*} \tilde{u}^{\rm out}(\omega, r_*')\,. \tag{7.13}$$

The term $\tilde{G}^{(2)}$ has isolated poles at the QNFs, yielding the time-domain QNMs response, while $\tilde{G}^{(1)}$ is regular at the QNFs. As a consequence, only $\tilde{G}^{(2)}$ propagates the QNMs: in this chapter we focus on this component and discard $\tilde{G}^{(1)}$.

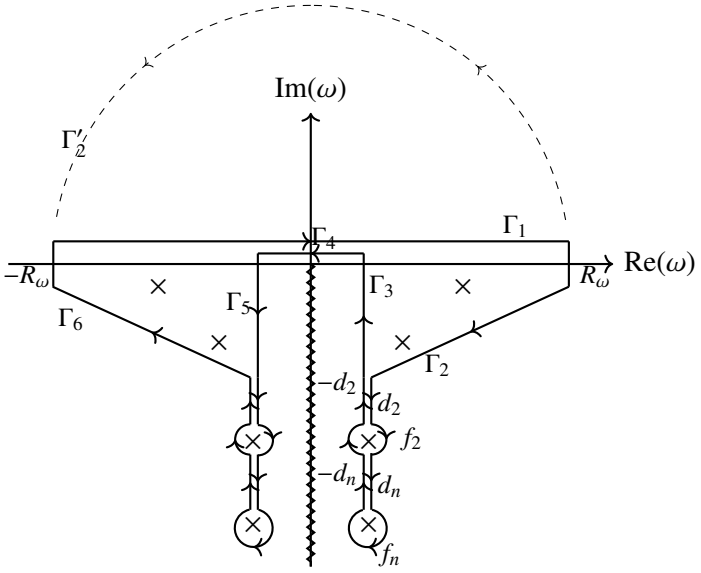

Figure 7.2: Smooth deformation of the closed contour in Fig. 7.1, shown as a thick line. The deformation is performed without crossing any singularity, hence integration along the two closed contours yields the same result. The contour in Fig. 7.1 is computed for a radius $R \to \infty$ of the two quarters of circumference in the lower-half plane. The current contour is computed for $R_\omega \to \infty$ and overtone number $n \to \infty$. Only in this limit is it possible to close the semi-circles enclosing the QNFs, as schematically represented in the figure.

The time-domain retarded GF responsible for the QNMs signal is given by the following anti-Fourier transform

$$G^{(2)}(t-t';r_*,r'_*) \equiv \int_{-\infty}^{\infty} d\omega \frac{e^{-i\omega(t-t')}}{2\pi} \tilde{G}^{(2)}(\omega;r_*,r'_*) \equiv \int_{-\infty}^{\infty} d\omega\, I(\omega;t,t',r_*,r'_*)\,. \tag{7.14}$$

The integrand is singular in $\omega = 0$ since, for small ω, $\tilde{u}^{\rm out} = \tilde{u}_{\infty+}$ has the explicit expression in Eq. (2.62) and contains a contribution $\propto \ln\omega$. To compute the integral along the real ω axis, we analytically continue ω to the complex plane. The general structure of the integrand in the complex plane is well known [14] and shown in Fig. 7.1. The function $I(\omega;t,t',r_*,r'_*)$ has a branch cut originating from the branch point $\omega = 0$, which we fix on the negative imaginary axis in order to select the *retarded* GF (see the discussion in Sec. 5.2). The integration in Eq. (7.14) is then performed on an axis parallel to the real line shifted at $\mathrm{Im}(\omega) = \epsilon > 0$ with $\epsilon \ll 1$. In the lower half-plane $\mathrm{Im}(\omega) < 0$, there is an infinite number of isolated simple poles which, in the limit $\mathrm{Im}(\omega) \to -\infty$ share the same real component $\mathrm{Re}(\omega_n) \ll 1$ [104]. From now on, we will use the following notation for the real and imaginary components of the frequency $\mathrm{Re}(\omega) \equiv \omega^{\rm Re}$ and $\mathrm{Im}(\omega) \equiv \omega^{\rm Im}$.

The integral along the (shifted) real axis in Eq. (7.14) can be computed by means of the residue theorem, once we choose a prescription to close the complex contour. We distinguish between two contours, shown in Fig. 7.1. Both share the line parallel to the real axis and extending to infinity. One contour is closed on the upper half-plane and the other on the lower half. In the upper half-plane the integrand in Eq. (7.14) has no poles nor branch cuts, while in the lower half-plane the contour is closed to avoid the branch cut, as

in Fig. 7.1. The closed contour is selected so that the residue theorem can be applied: the integrand needs to be regular except for isolated poles. In particular, it needs to be regular for $\mathrm{Im}(\omega) \to +\infty$ if we integrate along $\Gamma_1 + \Gamma_2'$, and for $\mathrm{Im}(\omega) \to -\infty$ if we integrate along $\Gamma_1 + \Gamma_2 + ...\Gamma_6$. Since we are interested in the QNMs, i.e. the contribution coming from the poles in the lower half plane, we investigate the values of (t, r_*, t', r_*') for which the integration can be carried over $\Gamma_1 + \Gamma_2 + ...\Gamma_6$.

We can deform the contour in Fig.7.1 without changing the value of the integral, provided that no singularity is excluded from the enclosed region. In the limit $\omega^{\mathrm{Im}} \to -\infty$ the QNFs have a small real part and are close to the branch cut. In this limit, we deform the contour to encircle the QNFs, as shown in Fig. 7.2. Integrating along the thick line in Fig. 7.1 yields the same result as integrating over the thick contour shown in Fig. 7.2, since the new contour can be "stretched" into the old one without crossing any singularity. From the schematic representation of Fig. 7.2 for $\omega^{\mathrm{Im}} \to -\infty$, in the lower half-plane the contour can be deformed to encircle each QNF. The lines connecting each QNFs (d_i in Fig. 7.2) give vanishing contribution, since integration along $-d_i$ and d_i cancels out. Then, for $\omega^{\mathrm{Im}} \to -\infty$ we can approximate the homogeneous mode u^{out} in Eq. (7.13) with the solution at the QNFs

$$\tilde{u}^{\mathrm{out}}(\omega; r_*') \simeq \tilde{u}_h(\omega; r_*') \equiv e^{i\omega\left[r_*' - 4\log\left(\frac{r'-2}{r'}\right)\right]}\, \hat{a}(\omega, r')\,. \tag{7.15}$$

with $\tilde{u}_h(\omega; r_*')$ defined in Eq. (2.56) and where we have introduced $\hat{a}(\omega, r')$ as

$$\hat{a}(\omega, r') \equiv \frac{\sum_{k=0}^{\infty} a_k(\omega)\left(1 - \frac{2}{r'}\right)^k}{\sum_{k=0}^{\infty} a_k(\omega)}\,. \tag{7.16}$$

Substituting Eq. (7.15) into the integrand of Eq. (7.14), we can write the expression of $I(\omega)$ near the QNFs, valid for $|\omega^{\mathrm{Im}}| \gg 1$

$$I(\omega \approx \omega_n; t, t', r_*, r_*') \simeq \left[\frac{i\, A_{\mathrm{out}}(\omega)}{4\pi\omega A_{\mathrm{in}}(\omega)} \cdot \hat{a}(\omega, r')\right] \cdot e^{-i\omega[t - r_* - C(t', r_*')]}\,, \tag{7.17}$$

with $C(t', r_*')$ defined as

$$C(t', r_*') \equiv t' + r_*' - 4\log\left(\frac{r'-2}{r'}\right)\,. \tag{7.18}$$

and $\hat{a}(\omega, r')$ defined in Eq. (7.16).

We will assume that the following limits are satisfied

$$\lim_{\omega^{\mathrm{Im}} \to -\infty} \frac{1}{\mathrm{Im}(\omega)} \log\left|\frac{A_{\mathrm{out}}(\omega)}{A_{\mathrm{in}}(\omega)}\right| = 0 \quad , \quad \lim_{\omega^{\mathrm{Im}} \to -\infty} \frac{\log|\hat{a}(\omega, r')|}{\mathrm{Im}(\omega)} = 0 \quad \forall\, r'\,. \tag{7.19}$$

The first limit can be motivated by the results of Andersson [280, 15] obtained in the limit of large ω. In particular Andersson [15] explicitly computed the ratio $A_{\mathrm{out}}/A_{\mathrm{in}}$ in the limit $\omega \gg 1$, as

$$\frac{A_{\mathrm{out}}(\omega)}{A_{\mathrm{in}}(\omega)} = \frac{(4i\omega)^{4i\omega} e^{-4i\omega}\Gamma(1/2 - 4i\omega)}{\sqrt{\pi} e^{i\pi/2}}\,. \tag{7.20}$$

We expand the expression above in the limit $\omega^{\mathrm{Im}} \to -\infty$ and approximate $\omega^{\mathrm{Re}} \approx 0$

$$\lim_{\omega^{\mathrm{Im}} \to -\infty} \left|\frac{A_{\mathrm{out}}(i\omega^{\mathrm{Im}})}{A_{\mathrm{in}}(i\omega^{\mathrm{Im}})}\right| = \frac{1}{\sqrt{2}} |\sec\left(4\pi|\omega^{\mathrm{Im}}|\right)| = \frac{\sqrt{2}}{|e^{4i\pi|\omega^{\mathrm{Im}}|} + e^{-4i\pi|\omega^{\mathrm{Im}}|}|}\,. \tag{7.21}$$

We substitute this expression in the first limit in Eq. (7.19), and find

$$\lim_{|\omega^{\rm Im}|\to\infty} -\frac{1}{2|\omega^{\rm Im}|}\log\left[\frac{1}{2}e^{-8i\pi|\omega^{\rm Im}|}\left(1+e^{8i\pi|\omega^{\rm Im}|}\right)^2\right]=0 \tag{7.22}$$

The second limit in Eq. (7.19) can be shown to be valid for $r'\gg 1$, since $\hat{a}(\omega, r'\gg 1)\to 1$ regardless of ω. The term $\hat{a}(\omega)\to 1$ does not contain contributions $\sim e^{i\omega r'}$, hence we expect the second limit in Eq. (7.19) to be valid everywhere.

Then, the behavior of the integrand in Eq. (7.14) for $|\omega^{\rm Im}|\gg 1$ is determined by the exponential term in Eq. (7.17)

$$\lim_{\omega^{\rm Im}\to-\infty} I(\omega;t,t',r_*,r'_*)=\begin{cases} <\infty\ , & t-r_*\geq C(t',r'_*)\,,\\ \to\infty\ , & t-r_*<C(t',r'_*)\,.\end{cases} \tag{7.23}$$

We conclude that for $t-r_*\geq C(t',r'_*)$ the integral in Eq. (7.14) should be computed through a closed contour in the lower half complex ω plane ($\Gamma_1+...\Gamma_6$ in Fig. 7.1), where it picks up the QNM contributions. Instead, for $t-r_*<C(t',r'_*)$ the contour should be closed on the upper half plane ($\Gamma_1+\Gamma'_2$ in Fig. 7.1), where $\tilde{u}^{\rm in,out}$ are analytical: this integration does not contribute to the QNMs response. The integration of Eq. (7.14) can proceed as detailed in Sec. 2.2.1, with the addition of an Heaviside function resulting from the above discussion

$$G^{\rm QNMs}_{\ell m}(t-t';r_*,r'_*)=\theta\left[t-r_*-C(t',r'_*)\right]\sum_{n=0}^{\infty}\sum_{s=\pm}B_{\ell mns}\,e^{-i\omega_{\ell mns}[t-r_*-C(t',r'_*)]}\hat{a}(\omega_{\ell mns},r')\,. \tag{7.24}$$

The *geometrical excitation factors* $B_{\ell mns}$ were introduced in Eq. (2.74), as functions of the coefficients $\alpha_{n,s}$ defined therein. The results presented in this chapter make use of the $\alpha_{n,s}$ computed by Leaver [14]. Note that Leaver [14] works with a variable s related to our frequency as $s=-2i\omega$. As a consequence, our definition of the coefficients $\alpha_{n,s}$ differs from Leaver's one by $\alpha_{n,s}=-2i\alpha^{\rm Leaver}_{n,s}$.

In Eq. (7.24), the Heaviside function crucially determines how the QNMs response is propagated on the curved BH spacetime, i.e. on which section of the light-cone interior $t-r_*\geq t'-r'_*$ the QNMs travel,

$$t-r_*\geq C(t',r'_*)\,. \tag{7.25}$$

Given its role, we thus refer to $C(t',r'_*)$ as the *causality condition function*.

In Fig. 7.3 we show the light-cone portion selected by the condition (7.25) assuming $t'=0$ for different radii r'_* of the initial pulse in Eq. (2.45). We compare this condition with the "scattering" condition usually considered in the literature [14, 118, 15, 119] when discussing the propagation of QNMs, i.e. $t-r_*>t'+r'_*$.

Our condition (7.18) has the following asymptotic behavior

$$\begin{aligned} C(t',r'_*)&\simeq t'-r'_* \quad r'_*\to 2\,,\\ C(t',r'_*)&\simeq t'+r'_* \quad r'_*\gg 2\,.\end{aligned} \tag{7.26}$$

Substituting the above limits into Eq. (7.25), yields

$$\begin{aligned} t-r_*&\geq t'-r'_* \quad r'_*\to 2\,,\\ t-r_*&\geq t'+r'_* \quad r'_*\gg 2\,.\end{aligned} \tag{7.27}$$

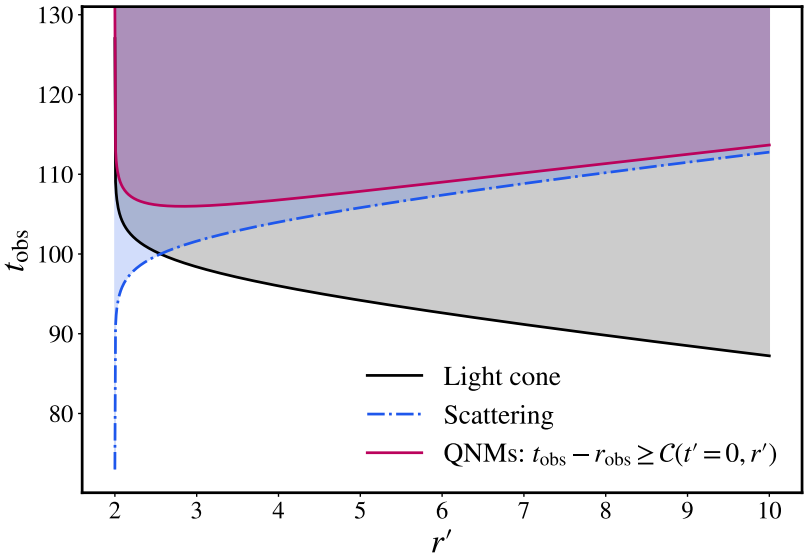

Figure 7.3: Time $t = t_{\rm obs}$ at which an observer located at $r_{*,\rm obs} = 100$M sees an impulsive signal emitted at r'_* and $t' = 0$. In black, a signal traveling on the light cone $t_{\rm obs} - r_{*,\rm obs} = t' - r'_*$. In blue, a perturbation scattering at $r_* = 0$, i.e. $t_{\rm obs} - r_{*,\rm obs} = t' + r'_*$. In purple, the propagation of QNMs, i.e. $t_{\rm obs} - r_{*,\rm obs} = C(t', r'_*)$ with $C(t', r'_*)$ defined in Eq. (7.18).

Both limits are captured in Fig. 7.3. For initial data far from the BH, the "scattering" causality condition well approximates Eq. (7.18). However, when approaching the light-ring, the "scattering" prescription becomes ill-defined: for $r'_* < 0$ it prescribes a signal traveling outside the light cone (going below the black line in Fig. 7.3). For data well inside the light-ring, we find that QNMs propagate along the light-cone, and are thus affected by the horizon redshift, as we are going to explicitly show below. Interestingly, Eq. (7.18) corresponds to the hyperboloidal time coordinate in the minimal gauge [281, 282, 283]. This yields the first prediction of our computation: the QNMs GF propagates perturbations on hyperboloidal slices in the minimal gauge.

Note that the causality condition in Eq. (7.24) guarantees that the GF is regular for all (t', r'_*). If we consider an initial pulse approaching the horizon, it holds $C(t', r'_* \to -\infty) \to \infty$. As a consequence, the exponential piece in Eq. (7.24) diverges as $e^{|\omega^{\rm Im}_{\ell mn}| C(t', r'_*)}$. However, the amplitude observed at $\mathcal{I}^+$ stays finite: the causality condition in Eq. (7.24) shifts the time at which an observer at $\mathcal{I}^+$ can see the perturbations towards infinity, exactly at $t - r_* = C(t', r'_*) \to \infty$, canceling the divergence. The physical interpretation is that a signal emitted at the horizon undergoes an infinite redshift, reaching the observer only at $t - r_* \to \infty$. Hence, the divergent piece $e^{|\omega^{\rm Im}_{\ell mn}| C(t', r'_*)}$ in Eq. (7.24) does not require any regularization procedure: one should simply compute the full observable. We will discuss this point in more detail and compare our results with regularization techniques proposed in the literature in Sec. 7.2.3.

The QNMs GF in Eq. (7.24) is only a portion of the full GF, given by the contribution of the simple poles (the QNFs) of $\tilde{G}^{(2)}$ to the Fourier transform in Eq. (7.14). The full Fourier transform of $\tilde{G}^{(2)}$ receives contributions also from the branch cut and from the $\omega^{\rm Re} \gg 1$ contour in Fig. 7.2. Since the branch

cut is present only in the lower-half ω-plane, and we close the contour in this portion of the plane for $t - r_* \geq C(t', r'_*)$, the branch cut contribution coming from $\tilde{G}^{(2)}$ will also carry a factor $\theta\left[t - r_* - C(t', r'_*)\right]$ in time domain. The response propagated (in time domain) by the Fourier anti-transform of $\tilde{G}^{(1)}$ is, instead, unaffected by this causality condition, since $\tilde{G}^{(1)}$ is analytical at the QNFs. We argue that this piece originates the prompt response, propagating signals on the curved light-cone $t - r_* \geq t' - r'_*$. Here, we focus on the QNM component and leave the treatment of the other two contributions to future studies.

7.2.2 QNMs signal

We now compute the QNM response to a test particle falling into a Schwarzschild BH on a generic trajectory, by solving Eq. (7.2) with null initial data

$$\Psi_{\ell m}(t = 0, r_*) = \partial_t \Psi_{\ell m}(t = 0, r_*) = 0\,. \tag{7.28}$$

i.e. $S^{\rm ID}_{\ell m} \equiv 0$ in Eq. (7.4) and $\mathcal{S}_{\ell m} = S_{\ell m}$ from Eq. (7.7). This is a good approximation when the evolution starts with the particle far away from the BH, much before the merger occurs. The explicit expression for $S_{\ell m}$ is given in Appendix A.

Substituting the source $S_{\ell m}$ and the QNMs GF in Eq. (7.24) into the general solution Eq. (7.8), yields

$$\Psi_{\ell m}(t, r_*) = \sum_{n,s} B_{\ell mns} e^{-i\omega_{\ell mns}(t - r_*)} \left[c_{\ell mns}(t - r_*) + i_{\ell mns}(t - r_*)\right]\,. \tag{7.29}$$

with

$$\begin{aligned} c_{\ell mns}(t - r_*) = \int_{-\infty}^{\infty} dt' \int_{-\infty}^{\infty} dr'_* \delta(r'_* - r_*(t'))\theta\left[t - r_* - C(t', r'_*)\right] \times \\ \left[u_{\ell mns}(t', r'_*)\tilde{f}_{\ell m}(t', r'_*) - \partial_{r'_*}\left(u_{\ell mns}(t', r'_*)\tilde{g}_{\ell m}(t', r'_*)\right)\right] \end{aligned}\,, \tag{7.30}$$

$$i_{\ell mns}(t - r_*) = \int_{-\infty}^{\infty} dt' \int_{-\infty}^{\infty} dr'_* \delta(r'_* - r_*(t'))\delta\left[t - r_* - C(t', r'_*)\right] \frac{\partial C(t', r'_*)}{\partial r'_*} \cdot u_{\ell mns}(t', r'_*)\tilde{g}_{\ell m}(t', r'_*)\,. \tag{7.31}$$

We compute Regge-Wheeler modes ($\ell + m$ odd) through a Mathematica notebook implementing Leaver's algorithm [104]. The Zerilli modes ($\ell + m$ even) are computed from the Regge-Wheeler ones through Chandrasekhar transformations (see Chapter 4 of Ref. [113]), as we review in Appendix C. In order to track the role of the causality condition, we write $u_{\ell mns}$ in Eqs. (7.30), (7.31) as

$$u^{\rm odd}_{\ell mns}(t', r'_*) = e^{i\omega_{\ell mns} C(t', r'_*)} \cdot \hat{a}(\omega_{\ell mns}, r')\,, \tag{7.32}$$

with $\hat{a}(\omega_{\ell mns}, r')$ as in Eq. (7.16) for Regge-Wheeler modes and

$$u^{\rm even}_{\ell mns}(t', r'_*) = e^{i\omega_{\ell mns} C(t', r'_*)} \cdot \hat{z}(\omega_{\ell mns}, r')\,, \tag{7.33}$$

for Zerilli modes. The expression of $\hat{z}(\omega, r)$ is lengthy, and shown in Appendix C.

The two terms in Eqs. (7.30), (7.31) are labeled "excitation" $c_{\ell mns}$ and "impulsive" $i_{\ell mns}$ coefficients, respectively. The excitation coefficients originate from the $\delta(r'_* - r_*(t'))$ piece in the source, and yield

the constant QNMs amplitudes at late times. These coefficients are an integral over the past history of the source, hence they accumulate in time more or less efficiently depending on the overtone number (i.e. on the decay rate of the eigenmode). The coefficients $i_{\ell mns}$ come from the $\partial_{r_*}\delta(r'_* - r_*(t'))$ portion of the source in Eq. (7.7), after integrating by parts in dr'_*. This integration is justified since the function convoluted with the Dirac delta vanishes at the boundaries (as discussed in Sec. 7.2.1, the causality condition regularize the diverging QNMs eigenmodes at $\mathcal{H}^+$). Contrary to the $c_{\ell mns}$, the $i_{\ell mns}$ are not integrals over the past history of the source (hence cannot accumulate), but are strictly local terms (see Eq. (7.36)). The $i_{\ell mns}$ terms do not appear in the absence of a persistent source (e.g., in the response to initial data confined to one slice). For this reason, we have denoted the $i_{\ell mns}$ as impulsive coefficients. More details are given in Sections 7.2.3, 7.3.

The double integral in the definition of $i_{\ell mns}$ can be solved using the properties of the Dirac delta. We first use $\delta(r'_* - r_*(t'))$ to solve the integral in r'_* and evaluate the integrand in dt' on the trajectory $r_*(t')$. Then, we use the following Dirac delta property to compute the integral on t'

$$\delta\left[t - r_* - C(t', r_*(t'))\right] = \frac{r^2(\bar{t})\delta(t' - \bar{t})}{\dot{r}_*(\bar{t})\left[8 - r^2(\bar{t})\right] - r^2(\bar{t})}\,, \tag{7.34}$$

where we have introduced $\bar{t} = \bar{t}(t - r_*)$ solution of

$$t - r_* - C(\bar{t}, r_*(\bar{t})) = 0\,. \tag{7.35}$$

Substituting Eq. (7.34) into Eq. (7.31), and after performing the integration in t', we find the expression for the impulsive coefficients

$$i_{\ell mns}(t - r_*) = \frac{\left[r^2(\bar{t}) - 8\right] u_{\ell mns}(\bar{t}, r_*(\bar{t}))\tilde{g}_{\ell m}(\bar{t}, r_*(\bar{t}))}{\dot{r}_*(\bar{t})\left[8 - r^2(\bar{t})\right] - r^2(\bar{t})}\,. \tag{7.36}$$

To compute the excitation coefficients $c_{\ell mn}$, we use the Dirac delta to solve the integral in t' through the property

$$\delta(r'_* - r_*(t')) = -\frac{\delta(t' - t(r'_*))}{\dot{r}_*(t(r'_*))} \tag{7.37}$$

We are then left with an integral in r'_*, with integrand computed on the trajectory $t(r'_*)$

$$c_{\ell mns}(t - r_*) = -\int_{\bar{r}_*}^{\infty} dr'_* \frac{1}{\dot{r}_*(t(r'_*))}\left[u_{\ell mns}\tilde{f}_{\ell m} - \partial_{r'_*}\left(u_{\ell mns}\tilde{g}_{\ell m}\right)\right]_{(t(r'_*), r'_*)}\,, \tag{7.38}$$

where we define $\bar{r}_* = \bar{r}_*(t - r_*)$ solution of

$$t - r_* - C(t(\bar{r}_*), \bar{r}_*) = 0\,. \tag{7.39}$$

We will solve the integral Eq. (7.38) numerically in Section 7.3.

It is useful to introduce two new functions $\psi_{\ell mns}$, $\zeta_{\ell mns}$ denoted respectively as *excitation and impulsive contributions* to the full QNMs signal in Eq. (7.29), as

$$\psi_{\ell mns}(t - r_*) \equiv B_{\ell mns}c_{\ell mns}(t - r_*)\, e^{-i\omega_{\ell mns}(t - r_*)}\,, \tag{7.40}$$

and

$$\zeta_{\ell mns}(t-r_*) \equiv B_{\ell mns} i_{\ell mns}(t-r_*)\, e^{-i\omega_{\ell mns}(t-r_*)}\,. \tag{7.41}$$

So that we can rewrite Eq. (7.29) as

$$\Psi_{\ell m}(t,r_*) = \sum_{n,s}\left[\psi_{\ell mns}(t-r_*) + \zeta_{\ell mns}(t-r_*)\right]\,. \tag{7.42}$$

7.2.3 QNM signal after light-ring crossing

We now analyze the behavior of the integral appearing in the excitation coefficients expressions, Eq. (7.38), after the particle apparent location ($\bar{r}$ in Eq. (7.39)) has crossed the light ring ($r_{\rm LR}=3$ for a Schwarzschild background) and is falling towards the horizon $\mathcal{H}^+$, i.e. for values of the integrand variable in the interval $r'\in(2,r_{\rm LR}]$.

Near $\mathcal{H}^+$, at leading order, the source functions and QNMs have the following behavior

$$\tilde{f}_{\ell m}(t(r'_*),r'_*), \tilde{g}_{\ell m}(t(r'_*),r'_*) \propto (r'-2)+O[(r'-2)^2]\,, \tag{7.43}$$

$$u_{\ell mns}(t(r'_*),r'_*) \propto e^{i\omega_{\ell mns}t(r')}(r'-2)^{-2i\omega_{\ell mns}}\left[1+O(r'-2)\right]\,. \tag{7.44}$$

Inside the light ring, the motion of a test particle is quasi-geodesic [10, 9], and it holds, in the limit $r\to 2$

$$t(r') \propto -2\log(r'-2)+O(r'-2)\,, \tag{7.45}$$

i.e.,

$$e^{i\omega_{\ell mns}t(r')} \propto (r'-2)^{-2i\omega_{\ell mns}}\left[1+O(r'-2)\right]\,. \tag{7.46}$$

This follows from an expansion around $r=2$ of the orbit, using e.g. Eq. (10.27) of [4].

Since we focus on retarded times $t-r_*$ such that $\bar{r}(t-r_*)<r_{\rm LR}$, we can split the integral in Eq. (7.38), in an integral over $r'\in[r_{\rm LR},\infty)$ and one over $r'_*\in[\bar{r},r_{\rm LR}]$

$$c^{\bar{r}<r_{\rm LR}}_{\ell mnp} = c_{\ell mnp}(\bar{r}=r_{\rm LR}) - \int_{\bar{r}}^{r_{\rm LR}} dr' \frac{A^{-1}(r')}{\dot{r}_*(t(r'_*))}\left[u_{\ell mnp}\tilde{f}_{\ell m} - \partial_{r'_*}\left(u_{\ell mnp}\tilde{g}_{\ell m}\right)\right]_{(t(r'_*),r'_*)}\,. \tag{7.47}$$

We consistently expand the source functions $\tilde{f}_{\ell m}(t(r'_*),r'_*)$, $\tilde{g}_{\ell m}(t(r'_*),r'_*)$ and the QN eigenmodes $u_{\ell mns}(t(r'_*),r'_*)$ near $\mathcal{H}^+$ at $r=2$, fixing the test-particle energy and angular momentum $\hat{H}$, p_φ to their values at the light ring. We then substitute these Taylor-expanded expressions in the second term on the right-hand side of Eq. (7.47) and expand its integrand in the same limit. Considering the leading order behavior in Eqs. (7.43), (7.44) and (7.46), the near-horizon contribution to $c_{\ell mns}$ can be approximated as

$$c^{\bar{r}<3}_{\ell mns}(t-r_*) - c_{\ell mns}(\bar{r}=3) \simeq \sum_{k=0}^{\infty}\gamma_{k,\ell mns}\left[1-(\bar{r}-2)^{k+1-4i\omega_{\ell mns}}\right]\,, \tag{7.48}$$

where we have defined

$$\gamma_{k,\ell mns} \equiv \frac{\xi_{k,\ell mns}}{k+1-4i\omega_{\ell mns}}\,, \tag{7.49}$$

with $\xi_{k,\ell mns}$ constant coefficients of the integrand expansion, which depend on the geodesic parameters.

In this sum, terms for which $4|\omega^{\rm Im}_{\ell mn}| - k > 1$ diverge for $\bar{r} = 2$. For a Schwarzschild BH, $4|\omega^{\rm Im}_{22n}| > 1$ for $n > 0$, hence at least one term in the k sum is divergent for the overtones. Only the excitation coefficients of the fundamental mode and its mirror mode, $c_{220\pm}$, are regular as $\bar{r} \to 2$. However, this divergence does not appear in the observable waveform. In fact, $\bar{r}$ is an *apparent* trajectory, function of the observer's retarded time $t - r_*$. It corresponds to the point of the test-particle trajectory at which the signal that reaches $\mathcal{I}^+$ at the retarded time $t - r_*$ is emitted, traveling on the light-cone portion selected by our QNM causality condition (7.18). An observer can never "see" an object fall through the event horizon of a BH, since the signals emitted by the object are infinitely redshifted in this limit. This translates in $t - r_* \to \infty$ as $\bar{r} \to 2$, which contributes a redshift factor that automatically regularizes the coefficients $c_{\ell mns}$, $i_{\ell mns}$.

This can be seen explicitly as follows. By definition of $C(t, r)$ in Eq. (7.18), along a geodesic trajectory inside the light-ring as in Eq. (7.45), we can approximate

$$C(t(\bar{r}), \bar{r}_*) \simeq -4 \log\left(1 - \frac{2}{\bar{r}}\right) \ , \ \ \bar{r} \to 2 \, . \tag{7.50}$$

Substituting into Eq. (7.39) yields

$$\bar{r} - 2 = \bar{r} \cdot e^{-(t - r_*)/4} \, . \tag{7.51}$$

Note that we have recovered the well-known redshift factor for a Schwarzschild black hole, given by its horizon surface gravity $\kappa_{\mathcal{H}^+}$ (see Eq.(12.5.4) of [284])

$$\kappa_{\mathcal{H}^+} = \frac{1}{4} \, . \tag{7.52}$$

When we insert the near-horizon apparent trajectory (7.51) into the expansion of the excitation coefficient (7.48), we find

$$c^{\bar{r}<3}_{\ell mns}(t - r_*) - c_{\ell mns}(\bar{r} = 3) \simeq \sum_{k=0}^{\infty} \gamma_{k,\ell mns} \left[1 - \bar{r}^{k+1-4i\omega_{\ell mns}} e^{-\frac{k+1}{4}(t-r_*)} e^{i\omega_{\ell mns}(t-r_*)}\right] . \tag{7.53}$$

The divergence is now isolated in the factor $e^{i\omega_{\ell mns}(t-r_*)}$, for $t - r_* \to \infty$. Once we reconstruct the signal, this divergent term cancels with the $e^{-i\omega_{\ell mns}(t-r_*)}$ factor in Eq. (7.29). In particular, the excitation contribution of each QNM $\psi_{\ell mns}$, defined in Eq. (7.40), is regular at all times and, for the apparent trajectory portion $\bar{r} < 3$, it holds

$$\psi^{\bar{r}<3}_{\ell mns}(t - r_*) \simeq \chi_{\ell mns} e^{-i\omega_{\ell mns}(t-r_*)} + e^{-(t-r_*)/4} \sum_{k=0}^{\infty} \alpha_{k,\ell mns}(t - r_*) e^{-\frac{k}{4}(t-r_*)} \, , \tag{7.54}$$

where we have defined

$$\begin{aligned} \chi_{\ell mns} &= B_{\ell mns} \left[c_{\ell mns}(\bar{r} = 3) + \sum_{k=0}^{\infty} \gamma_{k,\ell mns}\right] , \\ \alpha_{k,\ell mns}(t - r_*) &= B_{\ell mns} \, \gamma_{k,\ell mns} \, \bar{r}^{k+1-4i\omega_{\ell mns}} \, . \end{aligned} \tag{7.55}$$

Since $\bar{r}$ is a function of $(t - r_*)$ such that in the limit $t - r_* \to \infty$ it holds $\bar{r} \to 2$, then in the same limit $\alpha_{k,\ell mns} \to B_{\ell mns} \, \gamma_{k,\ell mns} \, 2^{k+1-4i\omega_{\ell mns}}$.

The first line of Eq. (7.54) is, as one might have expected, a complex exponential with a QN frequency $\omega_{\ell mns}$ and constant coefficient $\chi_{\ell mns}$, which is regular for all n. The second line arises from the divergent component in the excitation coefficient and is also regular for all n. This term, however, does not decay in time as a QNM. To leading order in the $k-$expansion, the new term decays as $e^{-(t-r_*)/4}$, i.e., it is a pure redshift contribution that we will denote as *leading redshift term*. Each redshift term has a coefficient $\alpha_{k,\ell mns}$ that saturates to a constant at late times.

The late-time constant QNM amplitudes $\chi_{\ell mns}$ receive two contributions: the first term on the right-hand side of Eq. (7.55) accumulates during the inspiral and is a history term; the second is a local contribution of the near-horizon quasi-geodesic behavior. Each mode's contribution to the redshift terms amplitudes $\alpha_{k,\ell mns}$, instead, is purely local and is activated by the near-horizon motion. These properties can be interpreted as follows. The test-particle orbital frequency grows during the initial stages of the plunge, until it reaches a maximum at the light-ring crossing; at later times, this frequency quickly decays to zero. The test-particle source on the right-hand side of Eq. (7.2) oscillates with the test particle orbital frequency as $e^{-im\varphi(t)}$. As a result, each QNM excitation is driven by the oscillating source until the light-ring crossing, while it resembles a free oscillator for later times (see also discussion related to Fig. 7.8), when the driving force has zero frequency. This is reflected in the late-time QNM amplitudes expression: each QNF is quasi-resonantly excited before the light-ring crossing, and the history term in the definition of $\chi_{\ell mns}$ is dominated by the portion of the trajectory where the test-particle orbital frequency is closest to the QNF. After the light-ring crossing, the driving force is non-oscillating. Hence, each QNM is excited as a free oscillator, and the contribution of the post light-ring crossing motion is constant along this portion of the trajectory (the term which depends on $\gamma_{k,\ell mns}$ in Eq. (7.55)). However, the QNM propagated response is not a free oscillator: there is still a forcing term on the right-hand side of Eq. (7.2) with zero frequency. The particular solution associated with this non-oscillating driving force is the redshift.

For the quadrupole modes, it holds $|\omega^{\rm Im}_{22n>0}| > 1/4$. As a consequence, the redshift term will eventually dominate the QNM decay of all overtones. The time of transition to a redshift-led decay depends on the relative amplitudes of the QNM with respect to the redshift terms. We investigate this for different orbital configurations in Sec. 7.3.

In the mathematical relativity literature, it was already known that perturbations at the horizon measured by an observer at $\mathcal{I}^+$ must be exponentially redshifted, as discussed by Rodnianski and Dafermos [277] and noted already by Price [16] in the context of a spherical collapse. Refs. [278, 279] found, respectively, the leading and sub-sub-leading redshift terms for a test particle plunging into a Kerr BH. In particular, Refs. [278, 279] focused only on the near-horizon limit, computing the convolution of the source and the GF in the frequency domain, later switching to the time domain. Instead, in the present chapter, we compute the convolution of the source and the (full) QNMs GF as already defined in the time domain. The near-horizon expansion is a byproduct of our analysis and will be tested against the full result in Sec. 7.3.

We repeat the same calculation for the impulsive coefficients $i_{\ell mns}$ in Eq. (7.36) and their contribution to the QNM signal $\zeta_{\ell mns}$, as defined in Eq. (7.41). Expanding both source functions and the QN eigenmodes

in the limit $r' \to 2$, given the leading order behaviors in Eqs. (7.43), (7.44) and (7.45), we find

$$i^{\bar{r}<3}_{\ell mns}(t - r_*) \simeq (\bar{r} - 2)^{1-4i\omega_{\ell mns}} \sum_{k=0}^{\infty} \beta_{k,\ell mns} (\bar{r} - 2)^k \ . \tag{7.56}$$

For the quadrupole overtones, $1 - 4|\omega^{\rm Im}_{22n>0}| < 0$. Hence, there is at least one term in the k-sum above that is divergent at the horizon. Exploiting the causality condition through Eq. (7.51), we can write the impulsive contribution $\zeta_{\ell mns}$ to the full waveform as

$$\zeta^{\bar{r}<3}_{\ell mns}(t - r_*) \simeq e^{-\frac{(t-r_*)}{4}} \sum_{k=0}^{\infty} \delta_{k,\ell mns}(t - r_*) \cdot e^{-\frac{k}{4}(t-r_*)} \ . \tag{7.57}$$

where we have introduced

$$\delta_{k,\ell mns} \equiv B_{\ell mns}\, \beta_{k,\ell mns} \bar{r}^{k+1-4i\omega_{\ell mns}} \ , \tag{7.58}$$

so that at late times $t - r_* \to \infty$, we have $\delta_{k,\ell mns} \to B_{\ell mns}\, \beta_{k,\ell mns} 2^{k+1-4i\omega_{\ell mns}}$. Again, the divergence is exactly canceled by the factor $e^{-i\omega_{\ell mns}(t-r_*)}$ in the full signal, so that all terms in Eq. (7.57) are finite.

Past literature on QNMs excitation coefficients, to the best of our knowledge, did not account for causality; hence, the radial integral in Eq. (7.38) is always extended to the horizon, $\bar{r} = 2$, (see e.g. [276] in the case of a test-particle source) resulting in a divergence if the source of the perturbation is not compact towards $\mathcal{H}^+$. Refs. [14, 118] proposed an analytical continuation on a deformed contour in the complex r-plane to regularize the integral. This is equivalent to adding a regularizing counter term [51, 285], exactly removing the divergent piece in Eq. (7.48) as detailed in Appendix D. We will refer to this approach as "standard regularization".

Instead, here we find that causality implies that the excitation coefficients are time-dependent: this dependence is encoded in the lower limit of the radial integral in Eq. (7.38), $\bar{r}$. Indeed, these coefficients depend explicitly on $\bar{r}$ as defined in Eq. (7.39), the apparent location of the test particle for the observer at $\mathcal{I}^+$, as a consequence, they are a function of $t - r_*$. Due to the horizon infinite redshift, the excitation coefficients are only evaluated at $\bar{r} \to 2$ in the limit $t - r_* \to \infty$. By substituting this time dependence into Eq. (7.48), it is possible to see that the divergence term, removed by the standard regularization, yields a regular *observable* decaying with the BH redshift. However, the two methods are not inconsistent with each other: the standard regularization technique is only valid in the limit $t - r_* \to \infty$. At this time, all the information emitted by the source while falling towards the horizon has escaped to $\mathcal{I}^+$, and the redshift term, canceled by the standard regularization, has effectively vanished.

7.3 Time-dependent ringdown

In this section, we investigate the excitation $c_{\ell mns}$ and impulsive $i_{\ell mns}$ coefficients and their contribution to the waveform multipole $\Psi_{\ell m}$, defined as $\psi_{\ell mns}$ in Eq. (7.40) and $\zeta_{\ell mns}$ in Eq. (7.41) respectively. Then, we use these contributions to construct the predicted signal propagated by the QNMs GF, Eq. (7.42), and compare this result against numerical perturbative simulations. We focus on the quadrupole $(\ell m) = (22)$, and consider as trajectories the quasi-circular inspiral $e_0 = 0.0$ in Table 5.1 and a radial infall from $r_0 = 50$

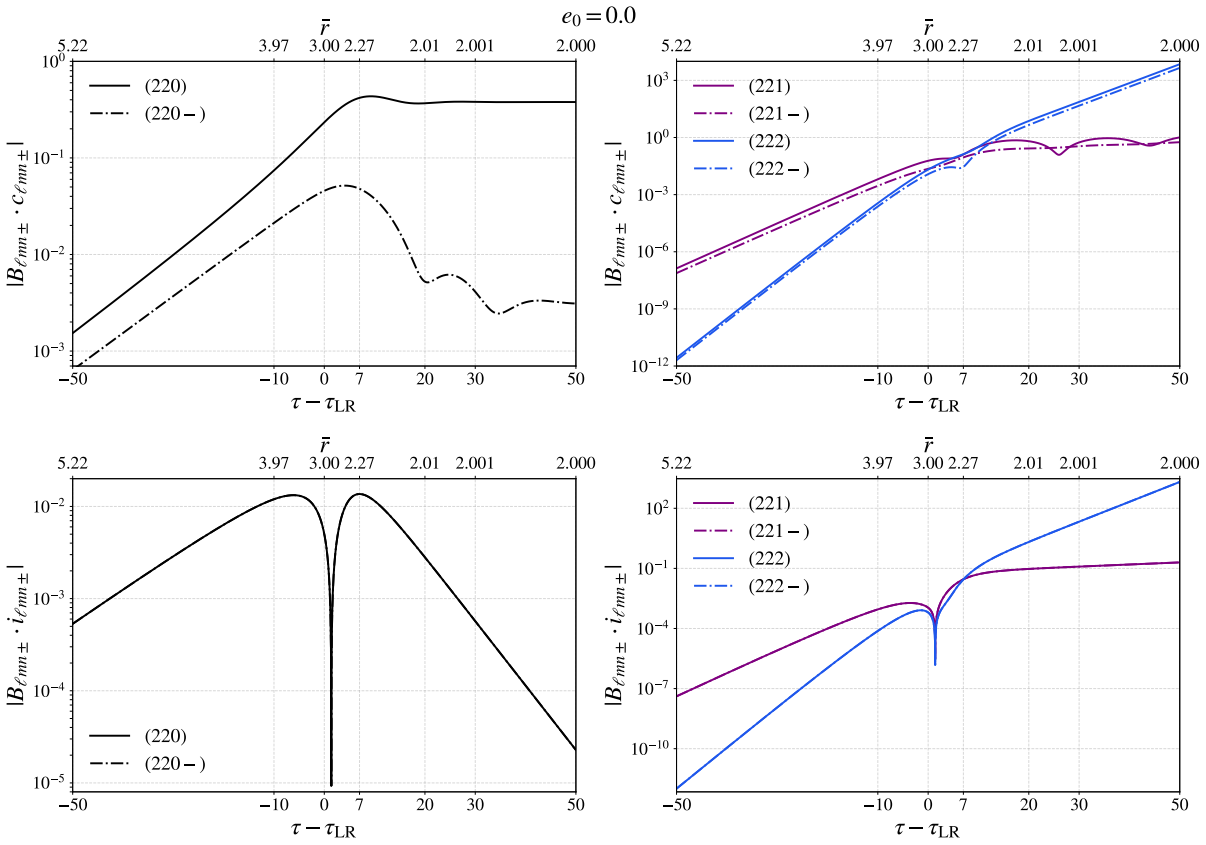

Figure 7.4: Top: Absolute value of the QNM excitation coefficients $c_{22n\pm}$ (top) and impulsive ones $i_{22n\pm}$ (bottom) (weighted with the geometric excitation factors $B_{22n\pm}$) of the modes (220±) (left) and (221±), (222±) (right), vs the retarded time of the observer τ with respect to $\tau_{\rm LR}$, as defined in Eq. (7.59). On the top horizontal axes, we show the apparent location $\bar{r}$ of the test particle emitting the signal observed at τ, as defined in Eq. (7.39). Results relative to a quasi-circular orbit, $e_0 = 0.0$ in Table 5.1.

with test-particle initial energy $E_0 = 1.00$. A brief comment on additional configurations, the eccentric inspirals $e_0 = 0.5,\ 0.9$ in Table 5.1, can be found at the end of the section, in Sec. 7.3.5.

We solve numerically for the trajectory by means of the RWZHyp code, as detailed in Sec. 7.1. This quantity is then fed into the integral in Eq. (7.38) for $c_{\ell mns}$ and into expression Eq. (7.36) for $i_{\ell mns}$. We perform the integral in Eq. (7.38) to compute the excitation coefficients, after the change of variables $dr = A(r)dr'_*$, through the Python function `numpy.integrate.sims`.

We use $\tau = t - r_* + \rho_+$, as in Eq. (5.10), to denote the observer's retarded time. We also rescale all times by

$$\tau_{\rm LR} \equiv C(t(r = 3), r = 3)\,. \tag{7.59}$$

This is the retarded time at which the signal that is emitted when the test particle crosses the light ring, traveling on the QNM light-cone section Eq. (7.25), reaches the observer at $\mathcal{I}^+$.

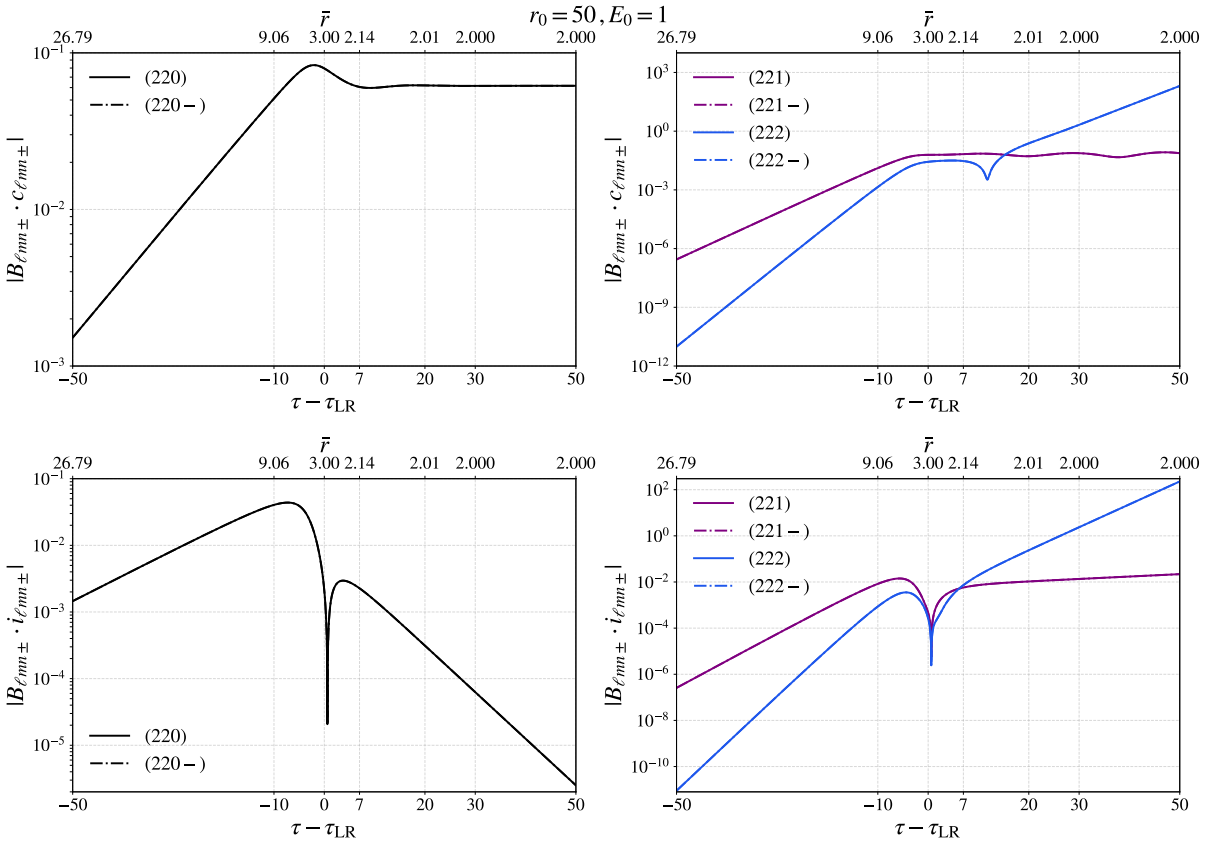

Figure 7.5: Same as Fig. 7.4, for radial infall from $r_0 = 50$ with test-particle initial energy $E_0 = 1.00$.

7.3.1 Excitation $c_{22n\pm}$ and impulsive $i_{22n\pm}$ coefficients

In Fig. 7.4 we show the excitation and impulsive coefficient of the (220±) and the first two overtones (221±), (222±), for the quasi-circular inspiral $e_0 = 0.0$ in Tab. 5.1.

The c_{220+} coefficient behaves approximately as an activation function: it grows until it reaches a maximum value around $\tau \approx \tau_{\rm LR} + 7$, and it saturates to a constant at late times. Interestingly, c_{220+} grows even once the test particle has crossed the light ring. In particular, its maximum is emitted when the test particle is at $\bar{r} \approx 2.27$. The mirror mode c_{220-} appears to be more sensitive to the near horizon motion: this quantity has a maximum around the same $\tau\,, \bar{r}$ as c_{220+}, but it saturates to a constant value at much later times, for $\tau \approx \tau_{\rm LR} + 40$, $\bar{r} \to 2$.

In the bottom panel of Fig. 7.4, we show the impulsive coefficients for the modes (220±), $i_{220\pm}$. Contrary to the coefficients $c_{220\pm}$, which grow and eventually saturate to a constant, the $i_{220\pm}$ contribute only close to the light-ring crossing, and vanish at both early and late times. These results are in agreement, at late times, with the expansions in Eqs. (7.48), (7.56). In fact, since we are considering $n = 0$, then $4|\omega^{\rm Im}_{220}| \simeq 0.356 < 1$ and all terms in the expansions in Eqs. (7.48), (7.56) are regular. Equation (7.48) is dominated by a constant in the limit $\bar{r} \to 2$, with all the other terms vanishing, yielding the constant amplitude of the (220±). The expansion for the impulsive coefficients in Eq. (7.56), instead, vanishes for $\bar{r} \to 2$ as $(\bar{r} - 2)^{1-4|\omega^{\rm Im}_{220}|}$.

In Fig. 7.4, we also show the excitation and impulsive coefficients for the first two overtones and their mirror modes (221±), (222±). We find that both $c_{221\pm}$ and $i_{221\pm}$ grow (although slowly) in τ, $\bar{r}$ and do not saturate to a constant value nor vanish in the limit $\tau \gg \tau_{\rm LR}$, $\bar{r} \to 2$. This can be explained through the near horizon expansions in Eqs. (7.48), (7.56), considering that $4\omega^{\rm Im}_{221} \simeq 1.096 \gtrsim 1$: the leading order behavior in these expressions is given by $(\bar{r}-2)^{1-4|\omega^{\rm Im}_{221}|}$, which diverges (slowly). Even if this divergent contribution has a smaller amplitude than the constant $O[(\bar{r}-2)^0]$ term present in $c_{221\pm}$, it will eventually dominate the excitation coefficient.

For the (222±) modes, $4|\omega^{\rm Im}_{222}| \simeq 1.91$. In this case, the post light-ring crossing behavior of $c_{222\pm}$, $i_{222\pm}$ displays a faster growth compared to the first overtone coefficients. In $c_{222\pm}$, the divergent behavior $(\bar{r}-2)^{1-4|\omega^{\rm Im}_{222}|}$, completely swamps the constant contribution in Eq. (7.48). The retrograde mode c_{222-} shows a very short time interval $\approx 5M$ in which it is approximately constant. For higher overtones, our results are similar to what is already shown in Fig. 7.4 for $n > 0$: $c_{22n>0\pm}$, $i_{22n>0\pm}$ diverge at late times, with higher overtones displaying a faster growth.

In Fig. 7.5, we repeat the same analysis for a radial infall from $r_0 = 50$ with initial energy $E_0 = 1.00$. Note that the (+), (−) modes are degenerate, as expected from the perturbation symmetry. The $c_{220\pm}$ behavior is qualitatively similar to the quasi-circular plunge. However, now $c_{220\pm}$ reach their maximum at $\tau \lesssim \tau_{\rm LR}$, or $\bar{r} \lesssim 3$, earlier than in the quasi-circular case.

The overtone behavior is more interesting. As shown in the top right panel of Fig. 7.5, the $c_{221\pm}$ are increasing functions at early times (as in the quasi-circular case) but saturate to an approximate constant value just before the particle reaches the light ring. In the quasi-circular case, the $c_{221\pm}$ exhibit a growing trend at all times, also after the light-ring crossing, albeit slow. The excitation coefficient of the $n = 2$ overtone and its mirror mode exhibit a similar behavior: $c_{222\pm}$ grow until a time $\tau \lesssim \tau_{\rm LR}$, then there is a transient during which $c_{222\pm}$ is approximately constant lasting until $\tau \approx 10 + \tau_{\rm LR}$. Only after this time, $c_{222\pm}$ starts growing. In the quasi-circular case, instead, the $c_{222\pm}$ grow at all times.

We interpret these results as follows: in the radial infall, the amplitude of the term giving rise to the late time divergence in the overtones, $O[(\bar{r}-2)^{1-4|\omega^{\rm Im}_{22n}|}]$ in Eq. (7.48), is suppressed with respect to the amplitude of the constant term $O[(\bar{r}-2)^0]$.

Finally, in the bottom panel of Fig. 7.5, we investigate the impulsive coefficients $i_{22n\pm}$, $n = 0, 1, 2$ excited in the radial infall. For $\tau \gtrsim \tau_{\rm LR}$ the $i_{22n\pm}$ are smaller than in the quasi-circular case, showcasing a suppression of the divergent factor $O[(\bar{r}-2)^{1-4|\omega^{\rm Im}_{22n}|}]$ also in the impulsive terms.

Overall, in the full signal propagated by the QNMs GF, Eq. (7.29) all terms behaving as $\propto O[(\bar{r}-2)^{1-4|\omega^{\rm Im}_{22n}|}]$ are suppressed for radial infalls.

As shown in the bottom row of Figs. 7.4 and 7.5, the impulsive coefficients $i_{\ell mn\pm}$ of the fundamental mode and the first two overtones have a zero near the apparent light-ring crossing. This feature signals a change in the behavior of the coefficients, marking the time after which the near-horizon expansion in Eq. (7.56) becomes valid. Such a sharp change in behavior is not visible in the excitation coefficients $c_{\ell mns}$; the reason is that, at late times, there is an additional component in their definition (the constant in Eq. (7.48))

which interferes with the time-dependent one.

7.3.2 Excitation $|\psi_{22n\pm}|$ and impulsive $|\zeta_{22n\pm}|$ contributions to the waveform

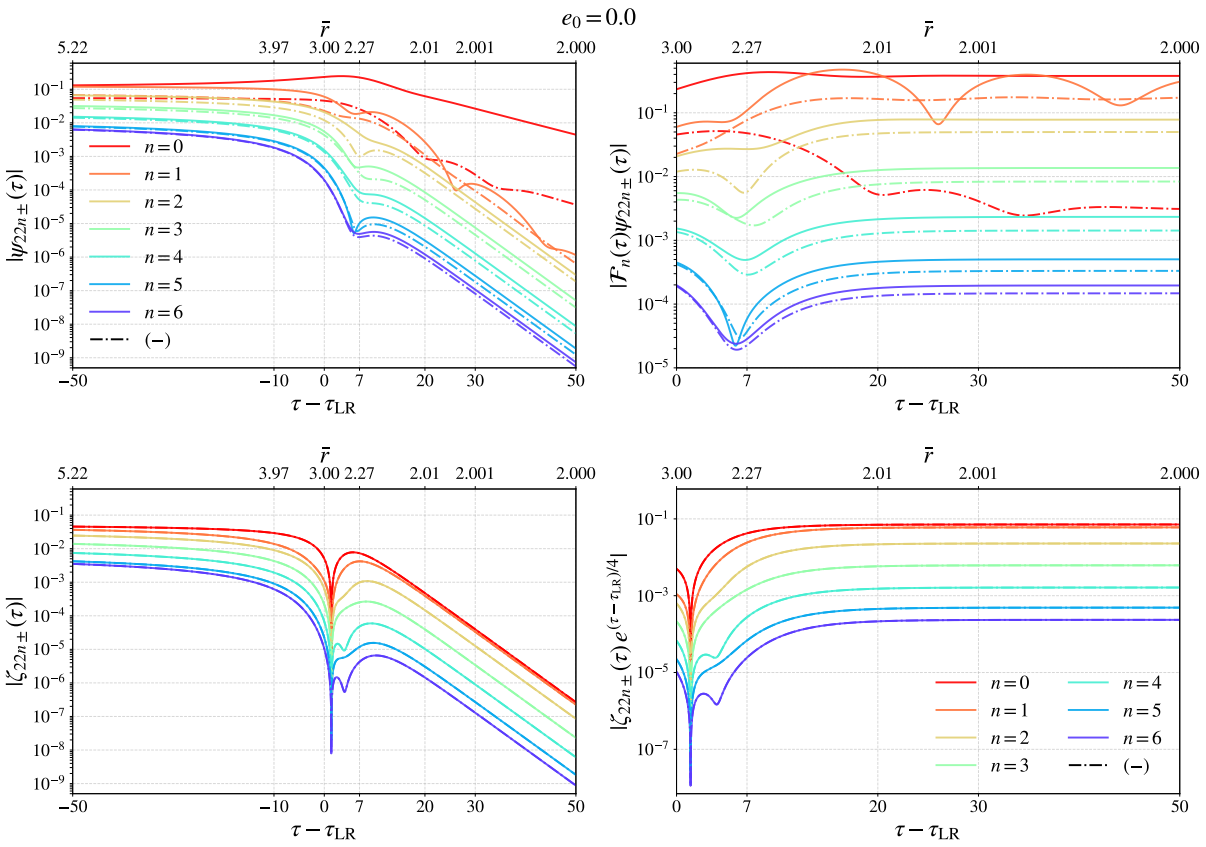

Figure 7.6: Left: Contribution to the full signal of the excitation coefficients $\psi_{22n\pm}$ in Eq. (7.40) (top row) and impulsive ones $\zeta_{22n\pm}$ in Eq. (7.41) (bottom row) vs the retarded time of the observer at $\mathcal{I}^+$. Right: Contribution of excitation and impulsive coefficients to the full signal rescaled by their late-time asymptotics, with $\mathcal{F}_n(\tau)$ as defined in Eq. (7.60). Thick lines are results relative to the $(22n+)$ modes, n (different colors) denotes the overtone number. In dot-dashed, the mirror modes $(22n-)$ results. The retarded time of the observer is translated with respect to $\tau_{\rm LR}$, retarded time at which a signal emitted at the light-ring crossing and traveling along the QNMs portion of the light cone in Eq. (7.39) reaches $\mathcal{I}^+$, as defined in Eq. (7.59). On the top horizontal axes, the apparent location $\bar{r}$ of the test particle emitting the signal observed at τ, as defined in Eq. (7.39). Results relative to a quasi-circular inspiral-plunge, $e_0 = 0.0$ in Table 5.1.

In the previous section, we analyzed the excitation and impulsive coefficients of the modes $(22n\pm)$ with $n = 0, 1, 2$, and we have shown that for the overtones $n > 0$, the coefficients diverge as $\tau \gg \tau_{\rm LR}$, $\bar{r} \to 2$. We motivated this behavior with the near-horizon expansions in Eq. (7.48), identifying the origin of this divergence. As argued in Sec. 7.2.3, this divergence leads to an observable and should not be regularized: even if the QN eigenfunctions are not regular at the horizon, a signal emitted at this location reaches $\mathcal{I}^+$ in

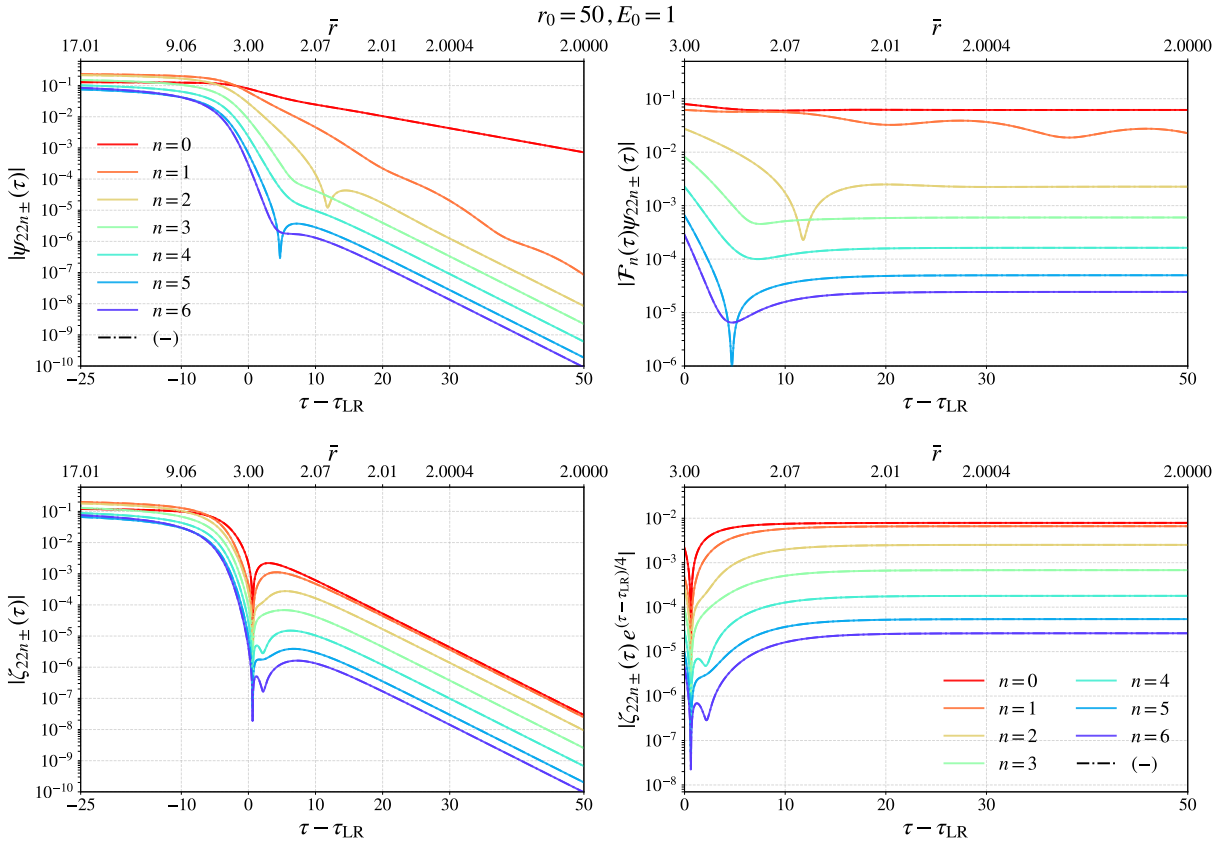

Figure 7.7: Same as Fig. 7.6, but for a radial infall from initial separation $r_0 = 50$ with initial energy $E_0 = 1.00$.

an infinite amount of time, exactly canceling the divergence.

In this section, we instead analyze the excitation $\psi_{\ell mn\pm}$ and impulsive $\zeta_{\ell mn\pm}$ contributions to the waveform for several QNMs. Interestingly, our calculations predict a new component of the signal at times $\tau > \tau_{\rm LR}$: a pure *redshift term*. This signal coexists with the standard constant-amplitude QNMs in $\psi_{\ell mn\pm}$, and completely dominates $\zeta_{\ell mn\pm}$.

In Fig. 7.6, we show the absolute value of $|\psi_{22n\pm}|$, $|\zeta_{22n\pm}|$ for $n \leq 6$ in a quasi-circular orbit, as function of $\tau - \tau_{\rm LR}$ and of the apparent position of the source $\bar{r}$, defined in Eq. (7.39).

The fundamental mode excitation contribution (top left) grows until $\tau \approx 7 + \tau_{\rm LR}$, $\bar{r} \approx 2.27$, then displays an exponential decay. The behavior of $|\psi_{22n>1\pm}|$, $|\psi_{220-}|$ is different: these quantities do not have a peak near the light ring, but are decreasing functions of τ starting from early times $\lesssim \tau_{\rm LR} - 50$. Interestingly, for the modes (220−), (221), the excitation contribution is influenced by the source even for $\bar{r} - 2 \ll 1$, carrying information of the near-horizon region at late times, in agreement with the behavior of their excitation coefficients shown in Fig. 7.4.

For $n > 0$ there is a transition near $\tau \approx 7 + \tau_{\rm LR}$, $\bar{r} \approx 2.27$: before, each $|\psi_{22n>0\pm}|$ decays in $\tau - \tau_{\rm LR}$ at a different rate, while for $\tau \gtrsim 7 + \tau_{\rm LR}$ all $|\psi_{22n>0\pm}|$ decay with the same rate. These results are consistent with those of Sec. 7.3.1 and consistent with the near-horizon expansion of Eq. (7.48), giving rise to the

redshift term $\propto e^{-\tau/4}$ in Eq. (7.54). To better interpret this result, in the top right of Fig. 7.6 we show the behavior of the rescaled quantity $|\mathcal{F}_n(\tau)\cdot\psi_{22n\pm}(\tau)|$, where

$$\begin{aligned}\mathcal{F}_{n=0}(\tau) &\equiv e^{|\omega^{\rm Im}_{220}|(\tau-\tau_{\rm LR})}\,,\\ \mathcal{F}_{n>0}(\tau) &\equiv e^{(\tau-\tau_{\rm LR})/4}\,.\end{aligned} \tag{7.60}$$

For $\tau \gtrsim 7+\tau_{\rm LR}$, $|\mathcal{F}_n(\tau)\psi_{22n\pm}(\tau)|$ saturate to a constant value. Hence Eq. (7.60) correctly identifies the asymptotic behavior of (the inverse of) $|\psi_{22n\pm}|$ at late times.

This experiment confirms the picture depicted by Eq. (7.54): at late times, in each $\psi_{22n>0\pm}$, the overtone's characteristic rapid decay is *swamped* by the leading redshift term. In particular, in a quasi-circular plunge, the ratios between each QNM amplitude, $\chi_{\ell mn\pm}$, and each QNM contribution to the leading redshift term, $\alpha_{0,\ell mn\pm}$ in Eq. (7.55), are such that the transition takes place close to the light-ring crossing, as shown in Fig. 7.6. Note that the first overtone (221±) has imaginary frequency $\omega^{\rm Im}_{221}\sim 0.274$ close to the redshift decay factor $\kappa_{\mathcal{H}^+}=0.25$. This explains the oscillations around a constant value for the rescaled quantity $|\mathcal{F}_n\psi_{221+}|$ shown in Fig. 7.6, as an interference between the leading redshift term in ψ_{221+} and its QNM decay. These oscillations are not present for ψ_{221-}: we then argue that the mirror mode (221−) is less excited with respect to (221+) and the leading redshift term in $n=1$.

In Sec. 7.3.5 we show these results for two eccentric configurations, $e_0=0.5,\,0.9$ in Table 5.1, finding the same overall picture.

In Fig. 7.7, we investigate the excitation contributions $\psi_{22n\pm}$ for a radial infall from $r_0=50$ with test-particle initial energy $E_0=1.00$. To investigate the relative QNM and redshift term excitation $\alpha_{0,\ell mn\pm}/\chi_{\ell mn\pm}$, we study again $|\mathcal{F}_n\cdot\psi_{22n\pm}|$, top right of Fig. 7.7. The rescaled overtones contributions saturate at late times towards a constant value for $n\geq 2$, while $|\mathcal{F}_1\cdot\psi_{221\pm}|$ is a decaying function at late times $\tau\sim 50+\tau_{\rm LR}$. This implies that $\psi_{221\pm}$ decays with its QNF behavior $\sim e^{-|\omega^{\rm Im}_{221}|\tau}$ even for $\tau\sim 50+\tau_{\rm LR}$. Moreover, the transition from a QNM to a redshift term decay for the $n=2,3,4$ happens at later times compared to the quasi-circular and eccentric cases, which are shown in Figs. 7.6, 7.11 and 7.12. Consistently with results in Sec. 7.3.1, the redshift term (originating from the divergent piece in $c_{22n\pm}$) is less excited in a radial infall compared to quasi-circular or eccentric plunges (even for large eccentricities). We argue that this is due to the faster timescale of radial infall, which allows less information emitted near the horizon to escape to infinity.

Similarly, on the bottom row of Figs. 7.6, 7.7, we show the contribution of the impulsive coefficients $|\zeta_{22n\pm}|$ for a quasi-circular plunge and a radial infall. In Section 7.3.5 we discuss the results obtained for $e_0=0.5,0.9$, Figs. 7.11, 7.12, similar to those for $e_0=0.0$. The $|\zeta_{22n\pm}|$ are slowly decreasing functions of τ, $\bar{r}$ with different trends, up until $\tau\sim 0,\bar{r}\sim 3$. From this time/apparent source location (corresponding to the light-ring crossing) there is a change in the behavior, and the $|\zeta_{22n\pm}|$ follow an exponential decay, which is the same regardless of n. To investigate this behavior, we study

$$|\zeta_{22n\pm}\,e^{(\tau-\tau_{\rm LR})/4}|\,, \tag{7.61}$$

shown on the right bottom panels of Figs. 7.6, 7.7 (see also Figs. 7.11, 7.12 in Sec. 7.3.5). At $\tau\gtrsim\tau_{\rm LR}$ or $\bar{r}\gtrsim 3$, this rescaled function saturates towards a constant, from which we infer the leading order coefficient of the expansion in Eq. (7.57).

Comparing the behavior of $|\zeta_{22n\pm}|$ in a quasi-circular or eccentric plunge, Figs. 7.6, 7.11 and 7.12, versus a radial infall, Fig. 7.7, we see that the impulsive contributions are more excited (suppressed) for $\tau \lesssim \tau_{\rm LR}$ ($\tau \gtrsim \tau_{\rm LR}$) in the radial infall. We conclude that the redshift decay present in the post light-ring crossing signal is suppressed for radial infalls also in the impulsive contributions $|\zeta_{22n\pm}|$. This is consistent with the results discussed in the previous section, where we observed a suppression of the leading divergent term in the near horizon expansion for $i_{\ell mn\pm}$, Eq. (7.56), originating the redshift contribution in the $\bar{r} \to 2$ expansion of $\zeta_{\ell mn\pm}$, Eq. (7.57).

7.3.3 Predicted QNMs waveform vs numerical waveform

We can now use the excitation and impulsive contributions investigated in the previous section to construct the QNMs portion of the signal, Eq. (7.42).

In Fig. 7.8, we compare the analytical results obtained by adding up to n overtones and their mirror modes with the full (perturbative) numerical waveform obtained through the RWZHyp code, for the quasi-circular inspiral-plunge. We show the strain polarizations, its amplitude and instantaneous frequency as observed at $\mathcal{I}^+$ as a function of the retarded time τ, translated with respect to $\tau_{\rm LR}$ defined in Eq. (7.59). In particular, we show the rescaled amplitude $A_{22}e^{-\omega^{\rm Im}_{220}(\tau-\tau_{\rm LR})}$: since the fundamental mode dominates over other contributions at late times, as shown in Fig. 7.6, we expect this rescaled variable to saturate to a constant.

We quantify the agreement between the analytical and the numerical waveforms through the residuals

$$\text{Res.}[\%] = 100 \cdot \frac{X_{\rm numerical} - X_{\rm analytical}}{X_{\rm numerical}} \tag{7.62}$$

The late-time signal for $\tau > \tau_{\rm LR} + 20$ is in good agreement with our prediction, with residuals $\sim 2\%$ in the amplitudes and $\sim 0.4\%$ in the frequencies. At earlier times, the residuals are much larger. In particular, Fig. 7.8 shows a burst in proximity of the light-ring crossing $\tau \lesssim 10 + \tau_{\rm LR}$, $\bar{r} \lesssim 2.13$. This result suggests that the signal propagated through the QNMs GF is not sufficient to reproduce the full signal around the time of light-ring crossing. Other contributions must be taken into account, coming from the prompt response and the branch-cut portion of the GF.

At late times $\tau \gtrsim 20 + \tau_{\rm LR}$, the signal is dominated by the fundamental mode. As we move to earlier times, the overtones become progressively more relevant. For $0 \lesssim \tau - \tau_{\rm LR} \lesssim 20$, the first two overtones must be included in the sum in Eq. (7.42). For times $\tau \lesssim \tau_{\rm LR}$, instead, $n \approx 5$ overtones are necessary to reach convergence in the analytical prediction.

The instantaneous frequency of the predicted signal in Fig. 7.8, grows in time until it saturates to a constant value, corresponding to the fundamental mode, with beatings due to its mirror mode. For times $\tau \lesssim \tau_{\rm LR}$, the growth in frequency is similar, albeit shifted, to the numerical waveform. However, while the latter smoothly connects to the fundamental mode real frequency, our analytical prediction showcases a more intricate behavior. In particular, the frequency of the QNMs portion of the signal grows until it has a (local) peak at the light ring crossing, then saturates to a constant value with a faster growth. Indeed, before the light-ring crossing, the source oscillates with $m\dot{\varphi}$, and $\dot{\varphi}$ grows in time until it reaches a maximum

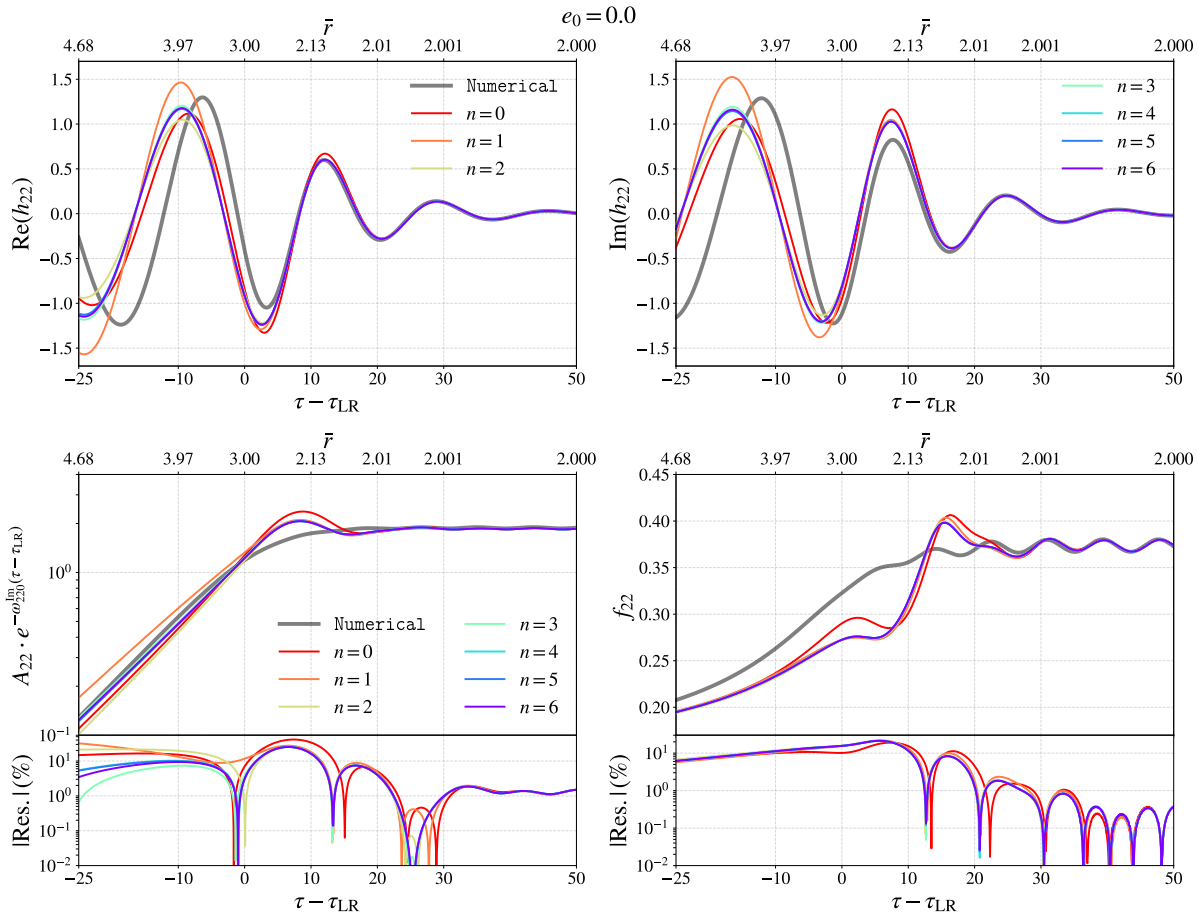

Figure 7.8: Top: polarizations of the strain quadrupole vs the retarded time τ of the observer at $\mathcal{I}^+$. Bottom: quadrupole amplitude A_{22} rescaled with the factor $e^{-\omega_{220}^{\mathrm{Im}}(\tau-\tau_{LR})}$ (left) and instantaneous frequency (right) vs τ. The retarded time τ is translated with respect to τ_{LR}, the time at which the signal emitted by the test particle at the light-ring crossing, traveling on the QNMs portion of the light-cone in Fig. 7.3 reaches $\mathcal{I}^+$, defined in Eq. (7.59). On the top horizontal axes, the apparent location $\bar{r}$ of the test particle emitting the signal observed at τ, as defined in Eq. (7.39). In gray, the numerical results obtained through the RWZHYP code. Coloured lines represent the analytical prediction Eq. (7.29) obtained summing over a different number n of overtones (different colors) and their respective counter-rotating modes. Results relative to a quasi-circular inspiral-plunge, $e_0 = 0.0$ in Table 5.1. In the bottom left panel, we also show the residuals between numerical and analytical predictions for different values of n, as defined in Eq. (7.62).

exactly at the light-ring crossing. Afterwards, both the source and the orbital frequency rapidly die down. Hence, the analytical predictions in Fig. 7.8 validate the quasi-resonant picture of Refs. [74, 75] for the QNMs excitation during the plunge: until the source is still active, its typical oscillation drives the QNMs response, afterwards the system behaves as a free-oscillator.

In Fig. 7.9, we repeat the analysis for the radial infall. We show the time derivative of the only non vanishing polarization (+), rescaled by its late-time asymptotics, $|\dot{h}_{22}\, e^{-\omega_{220}^{\mathrm{Im}}(\tau-\tau_{\mathrm{LR}})}|$. The time derivative serves to obtain a cleaner comparison by suppressing the tail part of the signal, prominent in radial infalls.

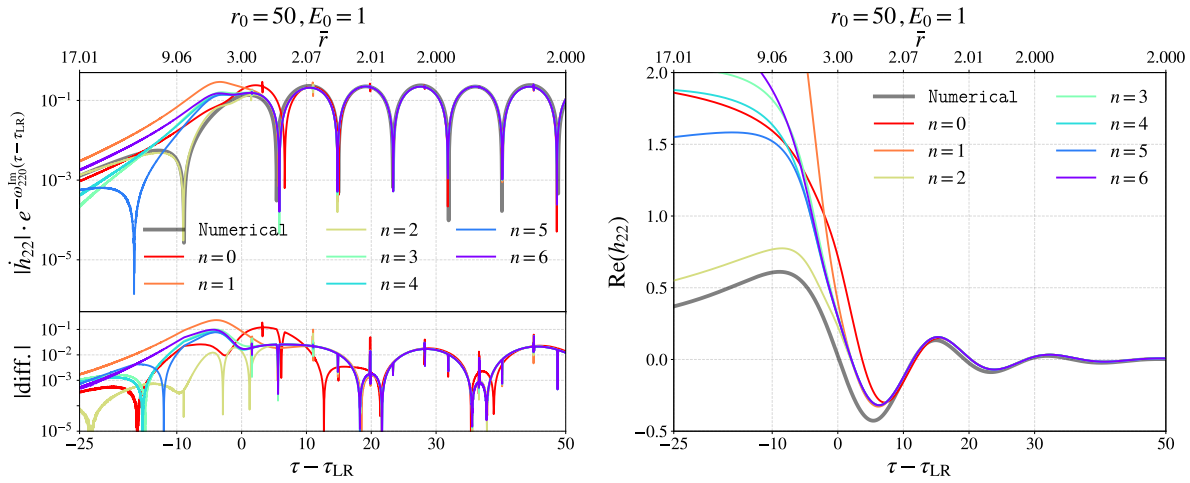

Figure 7.9: Left: Quadrupolar news amplitude rescaled with the factor $e^{-\omega_{220}^{\rm Im}(\tau-\tau_{LR})}$ (top) vs the retarded time τ of the observer at $\mathcal{I}^+$ and absolute value of the difference between numerical and analytical results (bottom). Right: + polarization of the strain (22) mode (right) vs τ. The retarded time τ is translated with respect to τ_{LR}, defined in Eq. (7.59). On the top horizontal axes, the position of the source (test particle) when it emitted the signal observed at τ, defined in Eq. (7.39). In gray, the numerical results obtained through the RWZHYP code. Coloured lines represent the analytical prediction Eq. (7.29) obtained summing over a different number n of overtones (different colors) and their respective counter-rotating modes. Results relative to a radial infall from $r_0 = 50$ with initial energy $E_0 = 1.0$. Numerical and analytical waveforms have been aligned in phase. Spikes on the left panel are numerical noise product of the alignment procedure.

Interestingly, for this binary configuration, more overtones are needed at early times $\tau \lesssim \tau_{\rm LR}$ in order to achieve convergence in the QNMs signal.

Even though we are not able to reproduce the initial transient leading to the ringdown, our analytical prediction can be smoothly extended to earlier times, yielding a fundamental piece in the analytical description of the plunge transient. In fact, we predict that at $\tau \approx \tau_{\rm LR} - 25$ the QNMs portion of the signal cannot be neglected, since it is comparable in magnitude with the perturbative numerical waveform. The usual constant-amplitude ringdown picture [276], cannot be extended to the plunge since it diverges for times earlier than the *ringdown starting time* $t_{\rm start}$.

7.3.4 Leading redshift term

We now investigate the contribution of the redshift term to the post-light-ring-crossing signal. As shown in Eq. (7.54), for $\bar{r} \ll 3$ the excitation contribution $\psi_{\ell mn\pm}$ consists of two different terms: a constant amplitude QNM and an infinite number of redshift terms, the leading one behaving as $\sim e^{-\tau/4}$. The impulsive contribution $\zeta_{\ell mn\pm}$ does not contribute to the QNMs constant amplitudes, but only to the tower of redshift terms as can be seen from the near horizon expansion in Eq. (7.57). Then, substituting Eqs. (7.54) and (7.57) into Eq. (7.42), we can write the full signal propagated by the QNMs GF after the light-ring

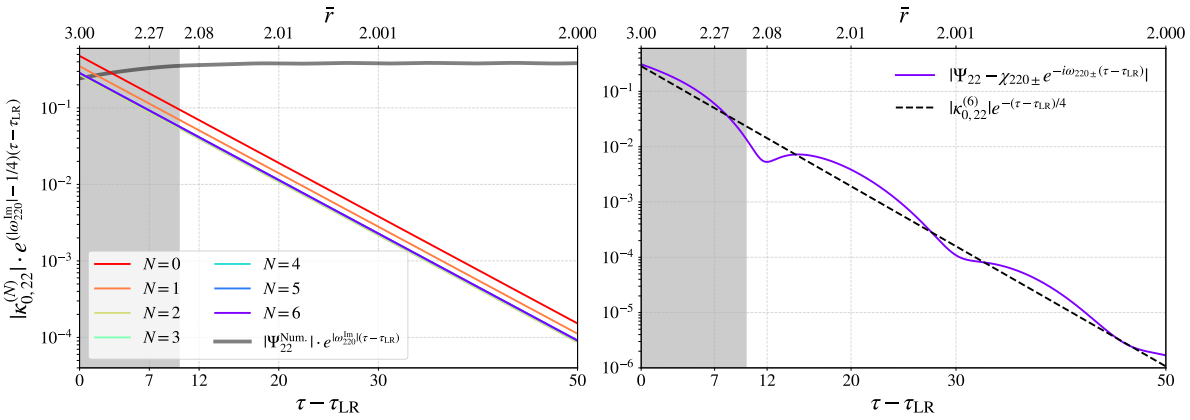

Figure 7.10: Left: Leading redshift term amplitude in Eq. (7.65) computed summing the excitation/impulsive contributions of regular/mirror modes up to N overtones, rescaled with the factor $e^{(|\omega^{\rm Im}_{220}|-1/4)(\tau-\tau_{\rm LR})}$, vs the retarded time τ of the observer at $\mathcal{I}^+$. In gray, the numerical quadrupole function Ψ_{22} rescaled with the fundamental mode decay $e^{|\omega^{\rm Im}_{220}|(\tau-\tau_{\rm LR})}$, computed through the RWZHYP code. Right: In black dashed, the total leading redshift term computed summing contributions up to $N = 6$ in Eq. (7.65) vs the retarded time τ. In violet, the analytical prediction for the quadrupole function Ψ_{22}, minus the fundamental and its mirror mode excitation contributions. Quantities are plotted in absolute value. The retarded time τ has been translated with $\tau_{\rm LR}$ defined in Eq. (7.59). On the top axis, the apparent location of the test particle, defined through Eq. (7.39). Results relative to the quasi-circular inspiral $e_0 = 0.0$ in Table. 5.1.

crossing, as

$$\Psi^{\bar{r}\ll 3}_{\ell m}(t - r_*) = \sum_{n,\,s} \chi_{\ell mns} e^{-i\omega_{\ell mn}(t-r_*)} + \kappa_{0,\ell m} e^{-\frac{t-r_*}{4}} + \sum_{k=1}^{\infty} \kappa_{k,\ell m} e^{-\frac{j+1}{4}(t-r*)}\,, \tag{7.63}$$

where we have introduced the *redshift amplitudes* $\kappa_{j,\ell m}$ as

$$\kappa_{k,\ell m} \equiv \sum_{n=0}^{\infty} \sum_{s=\pm} (\alpha_{k,\ell mns} + \delta_{k,\ell mns})\,, \tag{7.64}$$

with $\alpha_{k,\ell mn\pm}$, $\delta_{k,\ell mn\pm}$ defined in Eqs. (7.55) and (7.58) respectively, in the limit $\bar{r} \to 2$.

The individual excitation and impulsive contribution of each overtone n to the leading redshift term $k = 0$, has already been investigated in Figs. 7.6, 7.7. Now, we are interested in the superposition of all these contributions, and in particular in the dominant redshift amplitude, Eq. (7.64) with $k = 0$. To investigate how many overtones contribute to the total redshift amplitude, we introduce the following quantity

$$\kappa^{(N)}_{k=0,\ell m} \equiv \sum_{n=0}^{N} \sum_{s=\pm} (\alpha_{0,\ell mns} + \delta_{0,\ell mns}) \tag{7.65}$$

and study its convergence in N. The results are shown in the left panel of Fig. 7.10 for the quasi-circular trajectory. In particular, we show the amplitude of the perturbative numerical quadrupole Ψ_{22}, rescaled with the factor $e^{|\omega^{\rm Im}_{220}|(\tau-\tau_{\rm LR})}$, compared with the asymptotic redshift contribution rescaled by the same factor

$$|\kappa^{(N)}_{0,22}| \cdot e^{(|\omega^{\rm Im}_{220}|-1/4)\,\cdot\,(\tau-\tau_{\rm LR})}\,. \tag{7.66}$$

The quantities $\alpha_{0,22n\pm}$, $\delta_{0,22n\pm}$, necessary to compute $\kappa^{(N)}_{0,22}$, have been extracted from the right panels of Fig. 7.6. To compute $\alpha_{0,22n>0\pm}$, $\delta_{0,22n\pm}$, we average over $\tau - \tau_{\rm LR} \in [40, 70]$ the rescaled quantities shown in this plot. For $\alpha_{0,220\pm}$, we first compute the amplitudes $\chi_{220\pm}$, using the same averaging procedure. The values of $\alpha_{0,220\pm}$ are extracted averaging over $\tau - \tau_{\rm LR} \in [40, 70]$ the quantity

$$e^{(\tau-\tau_{\rm LR})/4}\left[\psi_{22n\pm}(\tau) - \chi_{220\pm}e^{-i\omega_{220\pm}(\tau-\tau_{\rm LR})}\right] . \tag{7.67}$$

From the right panels of Fig. 7.6, we learned that the near horizon expansions Eqs. (7.54), (7.57) with constant coefficients are valid for $\tau \gtrsim 10 + \tau_{\rm LR}$. Hence, the estimate of the redshift contribution in Eqs. (7.63), (7.64) should be accurate after this time only and not before. In the left panel of Fig. 7.10, results in the time interval $\tau < 10 + \tau_{\rm LR}$ are shaded and will be excluded from the following discussion.

The left panel of Fig. 7.10 suggests that only the overtones $n < 3$ contribute significantly to the leading redshift term. Moreover, note that for $10 \lesssim \tau - \tau_{\rm LR} \lesssim 25$, the redshift contribution is relatively loud, at most two orders of magnitude smaller than the leading (220+) mode behavior.

When discussing Fig. 7.6, we argued that the contribution of each $\psi_{22n>0\pm}$ to the redshift swamps the respective overtone decay for $\tau \gtrsim 10 + \tau_{\rm LR}$. However, this is not yet a definitive result: after combining the excitation contributions $\psi_{22n\pm}$ with the impulsive ones $\zeta_{22n\pm}$ and summing over all $n, \pm$, the total redshift amplitude could, in principle, be suppressed with respect to the overtones. In the left panel of Fig. 7.10, however, we see no evidence for this cancellation: the amplitude only decreases by a factor of ~ 2 when adding together all the contributions (impulsive/excitation) of the overtones and regular/mirror modes to the redshift. To investigate this in more detail, we have plotted the difference between the total predicted QNMs response and the asymptotic fundamental mode

$$\Psi_{22}(\tau) - \sum_{s=\pm}\chi_{220\pm}e^{-i\omega_{220}(\tau-\tau_{\rm LR})} , \tag{7.68}$$

where Ψ_{22}, see Eq. (7.42), is computed as

$$\Psi_{22}(\tau) = \sum_{n=0}^{6}\sum_{s=\pm}\left[\psi_{22ns}(\tau) + \zeta_{22ns}(\tau)\right] . \tag{7.69}$$

The absolute value quantity is shown on the right panel of Fig. 7.10, compared with the leading redshift behavior $|\kappa_{0,22}|e^{-(\tau-\tau_{\rm LR})/4}$. For $\tau \gtrsim 15 + \tau_{\rm LR}$, the decay of Eq. (7.68) is consistent with the leading redshift term one, $\sim e^{-(\tau-\tau_{\rm LR})/4}$, hinting that after this time the overtones in the full signal are swamped by the leading redshift term.

7.3.5 Additional eccentric configurations

The qualitative behavior between the redshift factor and QNMs decay does not seem to be affected by the initial eccentricity. Figs. 7.11 and 7.12 analyze the eccentric plunges of Tab. 5.1 with respectively $e_0 = 0.5$ and $e_0 = 0.9$. In both cases, the redshift factor starts dominating over the QNMs decay for $n > 0$ at a retarded time $\tau - \tau_{\rm LR} \approx 7$, in agreement with the quasi-circular case in Fig. 7.6.

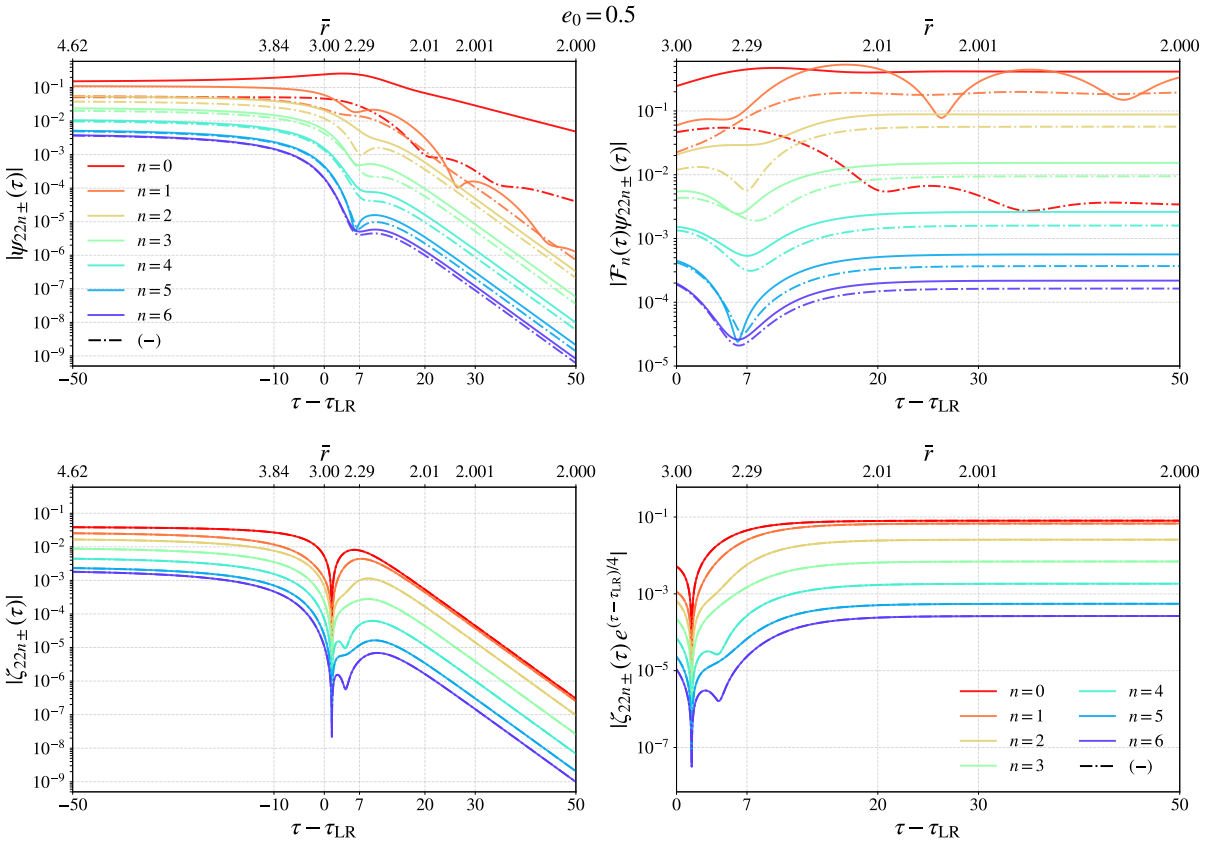

Figure 7.11: Same as Fig. 7.6, but for $e_0 = 0.5$.

7.4 Dependence on the inspiral configuration

In this section, we investigate the dependence of the late-time behavior of the leading $(\ell m) = (22)$ mode on the eccentricity of the test-particle orbit. Specifically, we fix the observer at $\tau = 40 + \tau_{\rm LR}$, when the transient has long decayed out of the strain and the signal is well described by the near-horizon expansion Eq. (7.63).

We define two parameters to assess the eccentricity of the inspiral: the eccentricity at the separatrix $e_{\rm sep}$ and the impact parameter evaluated at the light-ring crossing

$$b_{\rm LR} = \left.\frac{E}{p_\varphi}\right|_{r_{\rm LR}}, \tag{7.70}$$

a gauge-invariant quantity [203].

In Fig. 7.13 we show the amplitude A_{22} and phase ϕ_{22} of the quadrupole at $\tau = 40 + \tau_{\rm LR}$ vs $b_{\rm LR}$ and $e_{\rm sep}$. We compare the results directly extracted from the numerical simulations (simply quoting the numerical values, without fitting) with the analytical values computed through Eq. (7.42). Our prediction is in excellent agreement with the perturbative numerical waveform, and it shows a clear dependence of the post-merger quadrupole amplitude on the inspiral's eccentricity. In particular, we show that the eccentricity can increase A_{22} more than $\sim 25\%$.

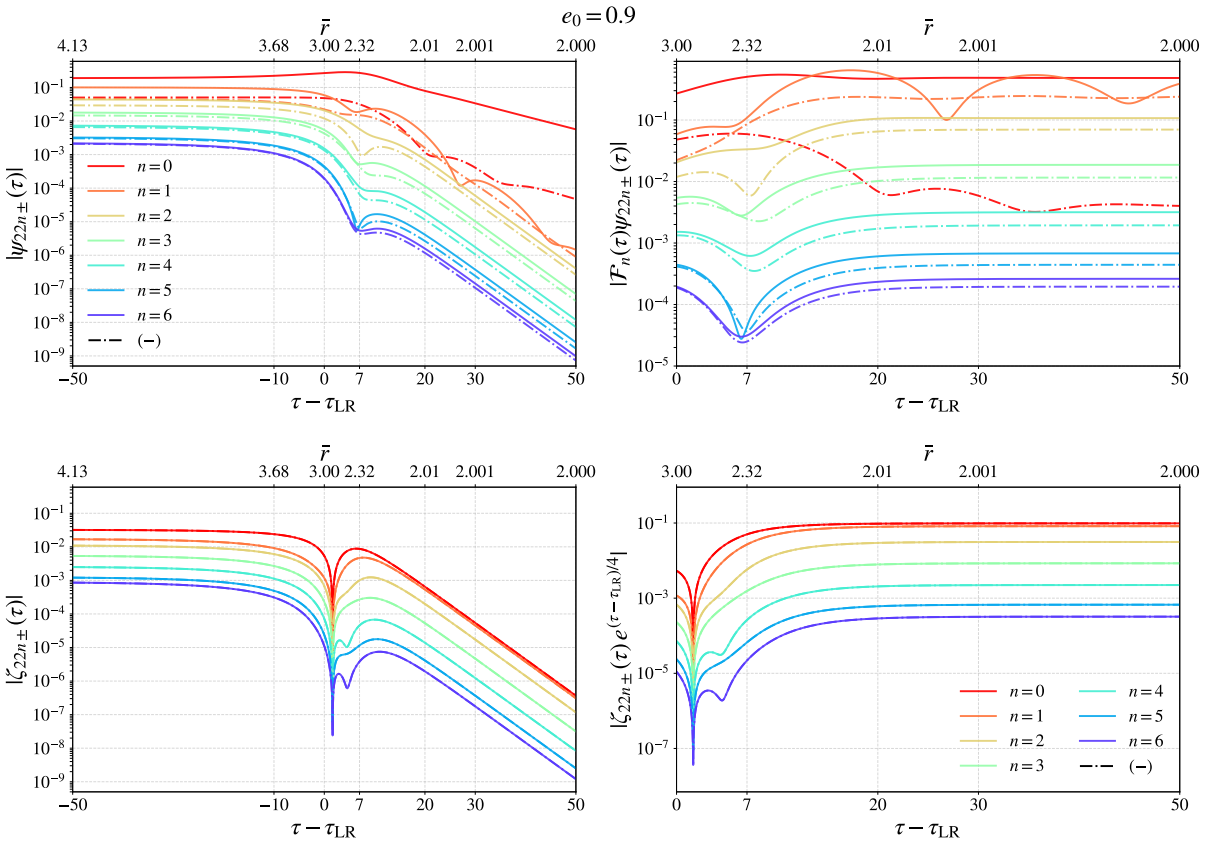

Figure 7.12: Same as Fig. 7.6, but for $e_0 = 0.9$.

In the right panel of Fig. 7.10, we show the dependence of the leading redshift term amplitude in the quadrupole, $|\kappa_{0,22}|$, on the quantities $b_{\rm LR}$, $e_{\rm sep}$. Similarly to ϕ_{22}, we find an oscillatory $|\kappa_{0,22}|$ as function of the eccentricity.

7.5 Summary and future directions

In this chapter, we have investigated the dynamical excitation of QNMs, driven by a test particle falling into a Schwarzschild BH on generic planar orbits. In particular, we have investigated the full signal propagated by the QNMs GF. For the first time, we have derived by first principles a causality condition prescribing the propagation of QNMs within the light-cone, from a generic source location (t', r'_*). For a source localized far from the BH, this condition, shown in Eq. (7.25), reduces to the usual heuristic prescription found in the literature as a scattering from the potential peak [14, 118, 15, 119]. Inside the light ring, the prescription in Eq. (7.25) approaches the light-cone. The "first time" at which the QNMs response reaches the observer Eq. (7.18) corresponds to the retarded time in the minimal gauge, and the exact portion of the light-cone selected by the causality condition is shown in Fig. 7.3.

Thanks to this prescription, we can compute the convolution of the QNMs GF with the source, along the whole inspiral-plunge-merger up to late times. We adopted null initial data since we assume a

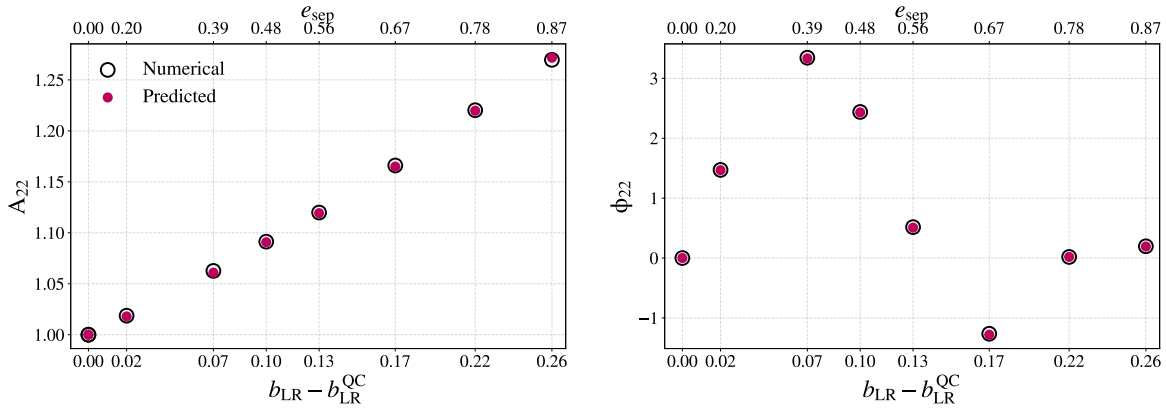

Figure 7.13: Amplitude (left) and phase (right) of the quadrupole at $\tau = 40 + \tau_{\rm LR}$ for the eccentric orbits in Table 5.1. We show on the bottom x-axis the orbit's impact parameter at light-ring crossing, Eq. (7.70), on the top axis the eccentricity at the separatrix. In black circles, numerical results computed with the RWZHyp code. In purple dots, analytical predictions computed as in Eq. (7.42). Numerical/analytical quantities have been rescaled with the quasi-circular numerical/analytical values.

test particle initialized far away from the BH, much before the merger has occurred. The general expression of the source can be found in Eq. (7.7): it is localized along the particle trajectory and is a superposition of a term proportional to a Dirac delta, and a term proportional to its derivative. These different source terms originate two distinct responses, that we have denoted as excitation $\psi_{\ell mns}$ and impulsive contributions $\zeta_{\ell mns}$, see Eqs. (7.40) and (7.41) respectively. These contributions can be written as retarded time-dependent coefficients, denoted respectively as excitation $c_{\ell mns}(t - r_*)$ and impulsive $i_{\ell mns}(t - r_*)$ coefficients, weighted with the standard geometrical excitation coefficients $B_{\ell mns}$ and with the factor $e^{-i\omega_{\ell mns}(t-r_*)}$. The $c_{\ell mns}(t - r_*)$ accumulate in time, i.e. are integrals over the past history, see Eq. (7.30), while the $i_{\ell mns}(t - r_*)$ are purely local, see Eq. (7.31).

For the modes (220±), the excitation coefficients behave similarly to activating functions: they grow during the inspiral, have a maximum near the light-ring crossing and eventually saturate to a constant amplitude at late times, once the (stationary) ringdown dominates the signal. The impulsive coefficients of the (220±) modes, instead, grow in amplitude until the light-ring crossing and then decay at later times.

We have found that the excitation and impulsive coefficients of the overtones $n > 0$ all diverge at late retarded times. This is due to the fact that, even if the test-particle source vanishes at the horizon $r \to 2$, the QNMs eigenfunctions diverge faster in this limit. However, this divergence never impacts actual observables. In fact, we do not observe the coefficients $c_{\ell mns}$, $i_{\ell mns}$ but rather their contribution to the waveform $\psi_{\ell mns}$, $\zeta_{\ell mns}$, and these quantities are regular at all times. The divergence of the QNMs eigenfunction is exactly at the horizon, but a signal emitted at this location escapes at $\mathcal{I}^+$ in an infinite amount of time. Reinforcing the requirement that inside the light ring the QNMs are propagated along the light-cone, naturally arising from our causality condition Eq. (7.25), we push the divergence in the excitation and impulsive coefficients at $t - r_* \to \infty$, yielding a regular signal.

Be $\bar{r}$ the position of the test particle emitting a signal at $\bar{t}$, which travels on the light-cone section selected

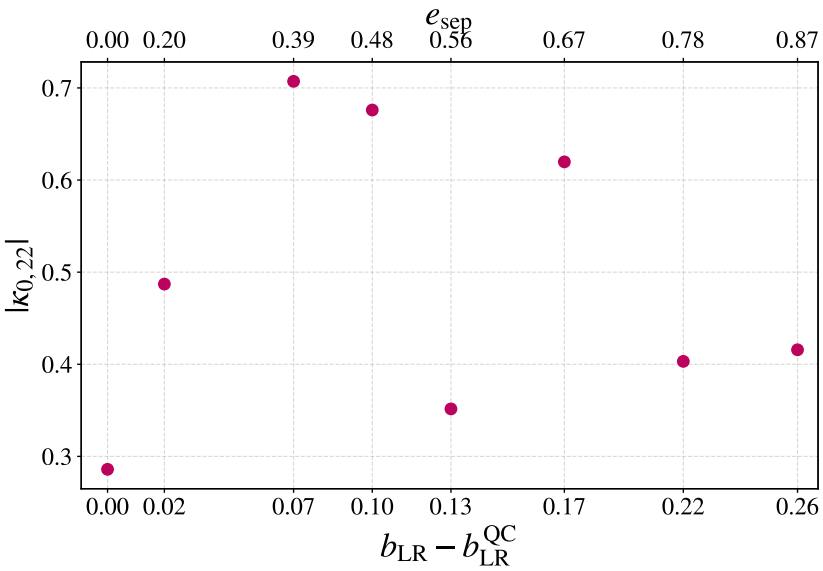

Figure 7.14: Amplitude of the leading redshift term in the quadrupole $\kappa_{0,22}$ defined in Eq. (7.64), for the simulations of Table 5.1. The quantity is computed summing over $N = 6$ overtones contribution, through the procedure described in Sec. 7.3.4 to obtain the results of Fig. 7.10. On the bottom x-axis we show the impact parameter at light-ring crossing, Eq. (7.70), of each configurations; on the top axis we show the eccentricity at separatrix crossing.

by Eq. (7.25) and reaches $\mathcal{I}^+$ at $t - r_*$. We have expanded the post light-ring crossing signal in the limit ($\bar{t} \to -\bar{r}_*, \bar{r} \to 2$). We have then shown that each excitation contribution can be rewritten as a constant amplitude QNM, plus a new behavior. This additional term is a superposition of an infinite number of zero real frequency terms exponentially decaying in the retarded time, with multiples of the BH surface gravity $\kappa_{\mathcal{H}^+}$ as decay rates. We have denoted these new pieces as *redshift terms*. The slowest decaying term in this sum is denoted as *leading redshift term* and has decay rate $\kappa_{\mathcal{H}^+} = 1/4$. The impulsive contribution only yields redshift terms at late times. After combining the excitation and impulsive contributions, we have the following prediction for the post light-ring crossing signal

$$\Psi_{\ell m}^{\bar{r}\ll 3}(t - r_*) = \sum_{n,\pm} \chi_{\ell m n \pm} e^{-i\omega_{\ell m n}(t-r_*)} + \kappa_{0,\ell m} e^{-\frac{t-r_*}{4}} + \sum_{j=1}^{\infty} \kappa_{j,\ell m} e^{-\frac{j+1}{4}(t-r_*)}\,, \tag{7.71}$$

The leading redshift term decays slower than the overtones $n > 0$, hence, depending on the amplitude $\kappa_{0,\ell m}$, there exists a certain retarded time $\tilde{\tau}$ at which the overtones' contribution to the signal is smaller than the redshift one. In particular, we have found that in quasi-circular and eccentric inspiral-plunges the overtones are swamped by the redshift for $\tilde{\tau} \approx 15 + \tau_{\rm LR}$. Radial infalls represent a special case in which the redshift excitation is highly suppressed. As a consequence, the first overtone decay dominates over the leading redshift up to late times $\approx 50 + \tau_{\rm LR}$. We stress that the redshift terms are not uniquely a feature of the background geometry, like the quasi-normal frequencies. These terms arise from the presence of a source approaching the horizon. The specific functional form of the redshift contribution stems from the particular near-horizon behavior of the QN eigenmodes and of the test-particle source.

We have compared the analytical prediction for the signal propagated by the QNMs GF against perturbative numerical simulations. The QNMs signal alone cannot reproduce the initial transient dominating the plunge-merger stage signaling that prompt and tail contributions must be taken into account. However, it constitutes a fundamental piece: the QNM response is comparable with the numerical waveform one even at times $\tau \approx \tau_{\rm LR} - 25$.

The analytical prediction presented in this chapter partially solves the problem of the *"ringdown starting time"*. Usual templates for the (stationary) ringdown include only a superposition of constant-amplitudes QNMs, since these models are built with no information on how the QNM response is activated. As a consequence, it is necessary to introduce the heuristic parameter $\tau_{\rm LR}$ denoted as ringdown starting time

$$h^{\rm ring}_{\ell m}(\tau) = \theta(\tau - \tau_{\rm start}) \sum_{n,\pm} A_{\ell m n \pm}\, e^{-i\omega_{\ell m n \pm}(\tau - \tau_{\rm start})}\,, \tag{7.72}$$

At times $< \tau_{\rm LR}$, the above template cannot be used to describe the waveform, since it would yield a divergent prediction. In this work, we have removed the necessity to introduce $\tau_{\rm start}$ since we have a smooth analytical prediction for how the QNM response is activated in time.

It might still be useful to gauge the time $\tau_{\rm start}$ at which a numerical waveform is expected to enter the stationary ringdown regime. Our model can only provide a partial solution: we can predict when the QNMs amplitudes become constant. However, we cannot predict when the prompt response and the tail contributions can be safely neglected. In this sense, the start time problem is still present and future work will be needed to address it properly.

In Refs. [278, 279], the redshift terms were investigated in the context of a test particle plunging into a Kerr BH. The convolution of the QNMs GF with the test-particle source is computed in frequency domain (i.e. not taking into account causality) through a near horizon expansion. The results are then switched to the time domain. In this framework, Ref. [278] computed the leading redshift term; however, Ref. [279] argued that this mode vanishes due to a cancellation, leaving only the sub-sub-leading one. In the current chapter, we obtain the full tower of redshift terms from a more generic framework: we first compute the signal propagated by the (full) QNMs GF in time domain and only afterwards a near-horizon expansion is performed. Our results point towards the presence of the leading redshift mode in the signal, in disagreement with Ref. [279]. We leave for future work a more detailed comparison with the results of Ref. [279], to understand the origin of this discrepancy.

Finally, we provided the first analytical prediction for the imprint of the inspiral eccentricity on the ringdown quadrupolar waveform. We have quantified the inspiral eccentricity through the eccentricity at the separatrix and the impact parameter at the light ring crossing, defined in Eq. (7.70). We have shown that these parameters can modify the quadrupolar amplitude in the ringdown by up to 25%, with analytical predictions in excellent agreement with numerical results.

The results of this chapter have several applications in gravitational-wave physics: in the context of ringdown modelling for GW observations, in the interpretation and fitting of NR simulations and, poten-

tially, for tests of general relativity and horizon physics with GW observations. We will discuss in detail these implications in Chapter 8. Here, we sketch a first exploration of the causality condition for QNMs propagation on a Kerr background.

7.5.1 Kerr quasi-normal modes propagation

Following Leaver [104], the ingoing solution Eq. (7.10) at the QNFs can be expanded as follows in a Kerr geometry

$$\begin{aligned}\tilde{u}^{\rm in}(\omega, r_*) = &\left[(r-r_-)^3\left(\frac{r-r_+}{r-r_-}\right)^{2+i\frac{2r_+a}{r_+-r_-}m}\hat{d}(\omega,r)\right]\times \\ &\exp\left\{i\omega\left[r_* - \frac{4r_+}{r_+-r_-}\log\left(\frac{r-r_+}{2}\right) + 4\log\left(\frac{r-r_-}{2}\right)\right]\right\}\,,\end{aligned} \tag{7.73}$$

where a is the BH adimensional spin and we have defined

$$\hat{d}(\omega, r) \equiv \sum_{k=0}^{\infty} d_k(\omega)\left(\frac{r-r_+}{r-r_-}\right)^k\,. \tag{7.74}$$

Note that r_* is now the Kerr tortoise coordinate

$$r_* \equiv r + \frac{2r_+}{r_+-r_-}\log\left(\frac{r-r_+}{2}\right) - \frac{2r_-}{r_+-r_-}\log\left(\frac{r-r_-}{2}\right). \tag{7.75}$$

Following the same reasoning discussed in Sec. 7.2.1, assuming an observer at $\mathcal{I}^+$, we can rewrite the causality condition as

$$t - r_* \geq C^{\rm Kerr}(t', r'_*) \equiv t' + r'_* - \frac{4r_+}{r_+-r_-}\log\left(\frac{r-r_+}{2}\right) + 4\log\left(\frac{r-r_-}{2}\right)\,. \tag{7.76}$$

It is straightforward to prove that $C^{\rm Kerr} \to C$ as in Eq. (7.18) in the limit $a \to 0$.

The horizon redshift $\kappa_{\mathcal{H}^+}$ of a Kerr BH is equal to

$$\kappa^{\rm Kerr}_{\mathcal{H}^+} \equiv \frac{r_+ - r_-}{4r_+}\,. \tag{7.77}$$

Then, the near horizon behavior of the causality condition in Eq. (7.76) is

$$C^{\rm Kerr}(t(\bar{r}), \bar{r}_*) \simeq -\frac{1}{\kappa^{\rm Kerr}_{\mathcal{H}^+}}\log\left(\frac{\bar{r}-r_+}{2}\right)\,, \quad \bar{r} \to r_+\,. \tag{7.78}$$

Future investigations are needed to assess the presence and relevance of redshift terms for a test particle infalling in a Kerr geometry.

Chapter 8

Conclusions and future directions

The main focus of this thesis has been to investigate the relaxation of a Schwarzschild black hole (SBH) following an external perturbation, at linear order in the perturbation.

In the past, this problem has been extensively investigated under different conditions. The majority of efforts in the literature have been devoted to evolving some small amplitude initial data on top of the SBH, focusing in particular on Gaussian-like initial data. In this thesis, we have focused on a different, more complex problem: the relaxation of a BH following a binary black hole merger. Consequently, the aim has been to predict the impact of the inspiral two-body problem on post-merger waveforms.

A posteriori investigations of numerical relativity waveforms yield a heuristic picture of the post-peak transient leading to the ringdown response. According to this intuition, the transient can be understood as an "activation" process, during which the quasi-normal frequencies (QNFs) are progressively excited in an almost-resonant manner by the two-body problem source [74, 75]. Interestingly, the transient shares similar features both in the extreme mass-ratio and in the comparable masses case [73], hinting at a common behavior leading this relaxation towards the ringdown, which can be applied to generic mass ratios.

Past results showcase the imprint of the inspiral two-body problem in the constant amplitudes of the QNMs excited in the ringdown [76, 77, 11, 78, 12, 79, 49, 80, 69, 81, 82, 83]. We reproduced previous work by analyzing non-spinning, quasi-circular BH binary numerical simulations from the SXS catalog [156] using the Bayesian inference algorithm bayRing [193]. The aim was to identify the modal content of the post-peak waveforms and to investigate the dependence of the loudest mode in the quadrupole on the progenitors' mass ratio. As a result, we have confidently recovered the fundamental mode, the first overtone and the lowest mode-mixing, while we could not identify higher overtones from the numerical data, in agreement with past literature [40, 84]. This result hints at the presence of non-modal signals in the numerical waveform, comparable in magnitude with higher overtones, hence spoiling their extraction. As argued in Ref. [40], this unmodeled feature could be due to numerical noise or have a (yet unknown) physical origin.

We find that the amplitude of the quadrupole fundamental mode A_{220} is linearly dependent on the

progenitors' mass ratio, consistent with results in Refs. [11, 12]. In particular, we recover $A_{220} \simeq 3.964\,\eta$, with η symmetric mass ratio and A_{220} rescaled with respect to its value at the time of the quadrupole amplitude peak. We have extended the analysis to quasi-circular mergers of non-spinning progenitors with electric charge, producing a Kerr-Newmann remnant. We have introduced an effective charge parameter in terms of the charge to mass ratio of each progenitor, then showed the non-linear dependence in this quantity of the fundamental mode amplitude and the remnant mass and spin at the quadrupole peak time.

This analysis hinted at the pivotal role of the inspiral-plunge two-body problem in the excitation of the ringdown response. Perturbative results of Ref. [75] showed a several orders of magnitude enhancement of the post-merger late-time tail, increasing with the progenitors' orbital eccentricity. This result found no explanation in past tails literature (mainly focused on initial data Gaussian-like perturbations), and was suggestive of the fact that also at late times the signal carries information on the inspiral two-body problem.

To address this problem, we have investigated the late-time tails emitted by a test particle infalling in a Schwarzschild BH through generic planar orbits. We presented an analytical model able to describe the late-time signal, built through the convolution of the radiative tail Green's function with the test-particle source. The model is an integral along the whole past history of the inspiral, making manifest the hereditary nature of late-time tails. Comparison with perturbative numerical waveforms shows good agreement with our predictions for intermediate to high eccentricities, from the time the tail starts dominating the strain up to very late times.

We used the model to explain the tail amplitude enhancement with the progenitors' binary eccentricity, as observed in perturbative numerical experiments. The overlap between the tail propagator and the source is larger for sources localized further away. Hence, our model predicts an enhanced tail emission for a motion happening at large distances from the BH. The integral over the trajectory receives contributions from a function oscillating as $e^{-im\varphi(t)}$, with m azimuthal number of the multipole under study and $\varphi(t)$ azimuthal coordinate of the test particle on the equatorial plane. When this phase oscillates fast, it induces destructive interference between subsequent tail signals. Instead, when the phase is approximately constant, the interaction is constructive. In an eccentric orbit, the conditions of large distances and small angular velocities are satisfied at the apastron. In particular, the larger the eccentricity, the further the apastron and, due to Kepler second law, the smaller the angular velocity at this location. As a consequence, our model predicts that the tail emission during an eccentric merger is enhanced at the last apastron before merger; the tail observed in the post-ringdown is emitted at this location, much before the light-ring crossing, far away from the potential barrier peak. This enhancement mechanism reinforces the close relation between late-time tails and the large-scale structure of the background, showing how tails yield complementary probes with respect to QNMs, which are instead sensitive to smaller scales.

The radiative tail generated by an initial-data perturbation of a Schwarzschild BH is a single inverse power-law $\propto (t - r_*)^{-\ell-2-a}$, with ℓ multipole of the strain [14] and $a = 0, 1$ depending on the initial-data nature. By employing the same propagator, we proved that the late-time tail excited by a two-body problem has a much richer content. In particular, we computed the post-merger tail as a superposition of an infinite number of inverse power-laws. The slowest decaying term is the radiative tail $\propto (t - r_*)^{-\ell-2}$, while higher

order corrections are sensitive to the trajectory features and, in particular, to its time duration. These corrections give rise to a long-lived transient, e.g. for a radial infall of duration $\approx 2 \cdot 10^3 M$, the transient dominates the strain for $\approx 5 \cdot 10^4 M$. We concluded that for observational purposes, many fast-decaying power-law terms dominate the detected signal over Price's law.

Once the mechanism behind tails generation and propagation in the perturbative extreme mass-ratio limit was identified, we successfully applied this insight to study tails in non-linear comparable masses mergers. In particular, we focused on head-on collisions of non-spinning BHs, predicted by our model to be the configuration where the tails are most strongly excited. Tails are a hereditary effect, i.e. a signal traveling well inside the light-cone, generated by the back-scattering of small frequency signals against the long-range curvature of the background. As a consequence, numerical evolutions targeted to study tails must be performed inside a computational domain extended at large distances. Moreover, both the observer radii employed in the extrapolation procedure and the outer boundary must be at large distances. The first requirement allows for successful extrapolation of the tail at null infinity, as discussed in the main text through a series of numerical experiments. The outer boundary must be far enough away from the observers to never be in causal contact with them. Otherwise, spurious numerical noise generated by the imperfect boundary condition would propagate at late times, spoiling the tail extraction. Handling these subtleties, not taken into account in standard waveform extractions, we achieved the first identification of late-time tails in non-linear numerical evolutions.

The non-linear waveforms obtained were in good agreement with perturbative ones emitted by a radial infall from the same initial separation, for a test particle at rest at past null infinity. Surprisingly, the features of the waveforms are remarkably similar along the entire post-peak portion of the signals, even at early times when in principle one could expect non-modal non-linear effects to be relevant [51, 52, 53, 54]. Late-time tails start dominating the perturbative and non-linear waveforms at the same time and with approximately the same amplitude (with respect to the waveform peak). However, the non-linear tail signal deviates from the perturbative prediction at later times. In particular, the non-linear tail decays more slowly than the perturbative one. We argued that this is the first observation of non-linear effects at late times and is intrinsic to the very nature of tails: being a hereditary effect, they can accumulate non-linearities, amplifying them.

Once a first principle understanding of the late-time signal was found, both in perturbative and non-linear settings, we have shifted our attention to earlier times and focused on the signal propagated by the QNMs Green's function. We have supplemented the standard Green's function found in Ref. [14], with a causality condition reinforcing the retarded Green's function prescription, derived by first principles. We then isolated the portion of the signal propagated by the retarded QNMs Green's function, following its evolution through the inspiral until the plunge final stages. The causality prescription regularizes the QNMs Green's function divergence at the horizon, by generating a new (regular) signal, emitted once the test particle is inside the light-ring crossing and is approaching the horizon. This signal is non-oscillatory (zero instantaneous frequency) and can be written as a superposition of exponentially damped terms, with decay rates given by multiples of the BH redshift. We predict that in a generic planar orbit in Schwarzschild, the leading redshift mode completely swamps the overtones at intermediate times

($\gtrsim 15M$ after quadrupole peak), while for a radial infall the redshift is suppressed, hence the first overtone dominates the strain until late times. The complete predicted signal incorporates a superposition of QNMs with time dependent amplitudes, growing in an activating function fashion and saturating to constant values near the light-ring crossing. This model, even if not sufficient to explain the transient behavior of numerical waveforms near the peak, allows us to naturally connect the ringdown with the inspiral-plunge motion and is the first model of time-dependent ringdown amplitudes. This is a first step towards the analytical modelling of the entire post-plunge signal.

This first principles computation allows us to solve for the dependence of the QNMs constant amplitudes on features of the inspiral. For instance, we were able to predict for the first time the dependence of the quadrupole amplitude and phase on the eccentricity, matching numerical results with high accuracy.

In Chapter 1, we argued that solving the Regge–Wheeler and Zerilli equations by feeding a non-linear trajectory into the test-particle source is not consistent with a perturbative expansion. This is the strategy behind some of the results in Chapters 5 and 7. While we already motivated the validity of this approach in Chapter 1, here we discuss in more detail what it entails for the results derived within this framework.

The focus of Chapter 7 is on the final stages of the plunge, where the impact of radiation reaction on the trajectory is negligible. Although a hereditary component in the QNMs signal is present, it mainly receives contributions near the light-ring crossing. As a consequence, we expect that switching off dissipative effects in the trajectory will not hinder the accuracy of our semi-analytical model of the dynamical excitation of QNMs, nor of our closed-form expression for the stationary ringdown, when compared to a realistic extreme mass-ratio ringdown.

Tails are highly sensitive to the entire past history of the inspiral. As a consequence, our ability to predict their behavior in the late-time signal of a binary merger is subordinate to the inclusion of radiation-reaction effects in the inspiral. Future work will be devoted to implementing an algorithm along the lines of Ref. [102], stitching together our prediction for the late-time tail emitted by a test particle on the geodesics that osculate the trajectory at each time step. This will allow us to improve our current model so that it remains consistent with first-order perturbation theory, while retaining the same level of accuracy.

The mechanism behind enhanced or suppressed tail emission, which explains the scaling of the post-merger tail amplitude with inspiral eccentricity, is completely general and can be applied to geodesics. In fact, the same scaling was also observed in the independent study of Ref. [213], which considered only geodesics and provided a similar argument for tail enhancement with eccentricity. The closed-form expression for late-time tails as a superposition of an infinite number of inverse power laws was derived using a generic trajectory. The argument that a larger number of power laws are excited the longer the inspiral lasts was verified through tests on different inspiral trajectories, including radial infall, which can be considered geodesic. In fact, radiation reaction in this configuration is negligible, as its impact on the trajectory is of order $\sim 10^{-6}$. To conclude, the aforementioned results also hold for geodesic trajectories, confirming their consistency with first-order perturbation theory.

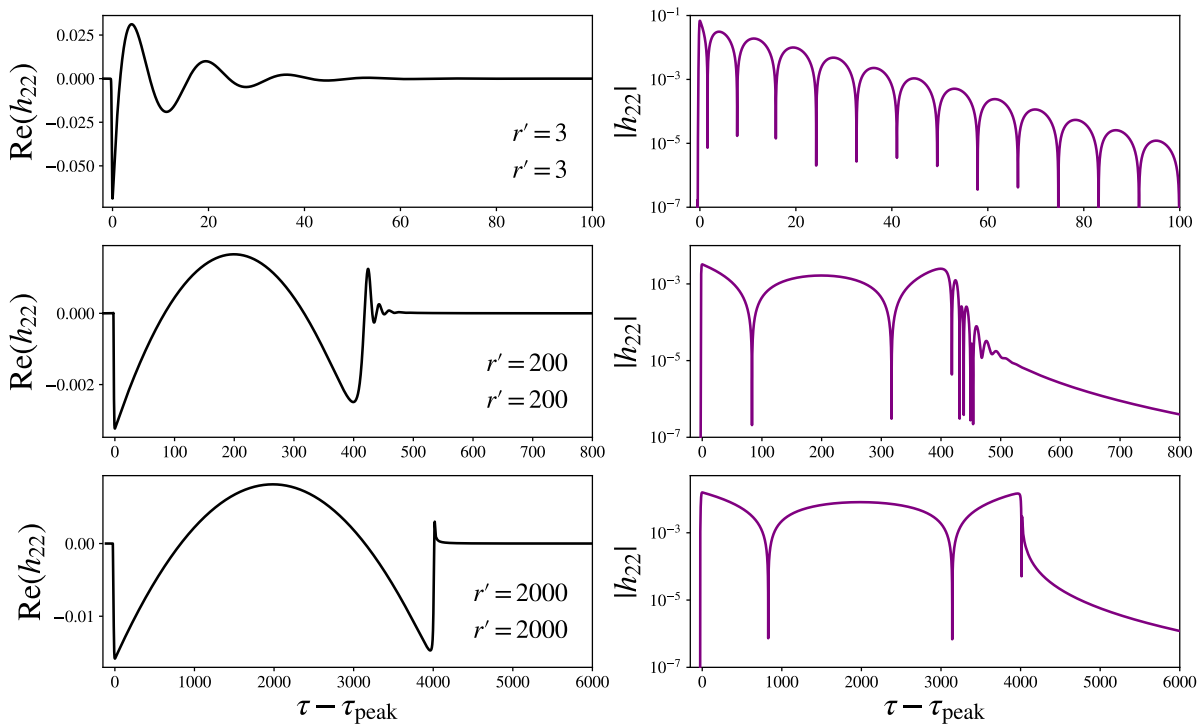

Figure 8.1: Numerical quadrupolar waveform (left) and its amplitude (right), solution of the Zerilli equation with source $\delta(t)\delta(r_* - r_*(r'))$ vs the retarded time of the observer at $\mathcal{I}^+$, translated with respect to the retarded time at which the amplitude peaks. Results obtained through the RWZHyp code [93, 94]. At early times, the numerical Green's function is dominated by a parabolic-like behavior in the retarded time. The duration of this behavior depends on the location of the source: the further away from the BH, the longer the prompt signal.

In agreement with initial intuition, once the inspiral two-body dynamics is taken into account, the phenomenology of the post-peak waveform becomes richer, with many new features arising. Price's law gets corrected by a superposition of faster decaying power-laws, giving rise to an intermediate long transient. The infinite redshift of the event horizon is such that we never see, from the outside, a test particle crossing this surface; as a consequence, the source keeps emitting radiation quenched to null infinity as a superposition of exponentially damped redshift terms. The work presented in this thesis, however, is far from complete. This thesis is rather the starting point of a program to model analytically the post-peak waveform, in the perturbative extreme mass-ratio limit. Many directions must be explored in the future to fully achieve this goal, with a particular focus on the near-peak transient. We highlight some of them below.

While our work on the QNMs response allows us to write a first principle formula for the ringdown

excitation, smoothly connected to the plunge motion, we showed that this component is not sufficient to reproduce the amplitude and frequency growth near the light-ring crossing. Future work must compute the contribution of other spectral components of the propagator, i.e. the branch-cut and the prompt response. These calculations entail several subtleties. For instance, the tail propagator derived in Chapter 2 and used for the results in Chapter 5 is computed under the approximation of large distances, both for the source and the observer. While we can safely assume an observer at null infinity (if we are interested in real detections), the location of the source must be general to investigate the near-peak waveform. Moreover, Price's law propagator is derived under the assumptions of small frequencies. At an operational level, this means that we only consider the contribution of the branch cut near the branch point, with null real frequency and small imaginary component. Hence, the tail propagator does not oscillate in the time domain and decays slowly (i.e. travels well inside the light-cone). We speculate that the branch cut contribution for large imaginary frequency would yield a non-oscillating signal decaying fast in the time domain, traveling marginally close to the light-cone. Once a complete and general propagator associated with the branch cut is available, detailed computations of its contribution to the near-peak waveform are necessary to gauge its interaction with the signal propagated through the QNMs response.

Both the tail and the QNMs response do not travel on the light-cone, except in the limit of the test particle approaching the horizon. The prompt response, instead, is propagated on the light-cone, giving rise to the *direct signal*. Spectral investigations of Leaver [14] and Andersson [15] proposed that the time-domain prompt propagator originates from the high-frequency arcs in the Fourier domain. Andersson [15] used this argument to compute an Heaviside function propagator for the direct signal, under the approximation of large distances for both the (compact) source and the observer. We claim that this approximation cannot yield the correct Green's function, even for a (compact) source at large distances. We have performed a numerical investigation of the Green's function, solving the Regge-Wheeler and Zerilli equations with an impulsive source $\sim \delta(t-t')\delta(r_*-r'_*)$, with Dirac deltas approximated by narrow Gaussians. The results, as observed at $\mathcal{I}^+$, are shown in Fig. 8.1 for different r'_*, always fixing $t'=0$. The early times signal, propagated by the prompt response, is a zero (instantaneous) frequency component, with a parabolic-like behavior in retarded time, consistent with the analytical prediction of Ref. [107, 18]. As r'_* approaches the light-ring, the prompt is progressively shorter, but its functional form is approximately the same for $r'=200, 2000$. A better description of the prompt propagator is needed to model analytically the near-peak transient.

In this thesis, we focused on perturbations of a Schwarzschild background. More work is needed to understand the implications of late-time tails and QNMs response in future astrophysical observations and their potential to answer fundamental questions in GR.

First and foremost, astrophysical BHs have spin. Hence, it is imperative to extend our perturbative models to account for a test particle plunging into a Kerr BH through generic (potentially precessing) orbits. It is known that the radiative tail propagator is not affected by spin [89, 128], however the test-particle trajectory (hence the source), is. In a spinning background, the tail could potentially be enhanced even

further [213]. The causality condition for the Kerr QNMs propagator was derived in Chapter 7, but a detailed investigation of its convolution with the test-particle source of the Teukolsky equation is still missing.

Astrophysical BHs typically exist within *environments*, rather than in vacuum. For instance, they can be surrounded by accretion disks [286] or dark matter halos [287]. The impact of low-density environments on ringdown was recently shown to be difficult to resolve through future detections [288]. The impact on tails is potentially larger, due to their close relation to the *large scale structure* of the background, which is modified by extended astrophysical environments. An investigation in this direction could open new possibilities for environmental studies in the post-merger waveform.

In Chapter 5, a closed-form expression for the late-time tail was introduced; however, it requires a large number of terms to accurately approximate the signal by the time the tail begins to dominate over the QNMs. As a result, this functional form may not be well-suited for parameter inference, should a tail signal be observed. Future research will be devoted to deriving a more compact closed-form expression for this signal that is better suited to this task. We identify two directions to achieve this goal. The first focuses on radial infall, for which the radiation reaction impact on the trajectory is negligible. As a consequence, the orbital evolution can be described through a simple closed-form geodesic trajectory, which might allow for analytical integration of the late-time tail contribution. In highly eccentric mergers, the tail observed at retarded times close to $\tau_{\rm trans}$, when the post-merger signal transitions from a QNMs to a tail-dominated behavior, is emitted primarily near the last apastron, as discussed in Chapter 5. By expanding the trajectory around this location, direct integration of the tail integral might be possible, yielding an approximate closed-form expression for the tail valid within a narrow time window around $\tau_{\rm trans}$.

Results in Chapter 6 show the presence of non-linearities in the late-time portion of the signal. We propose three different mechanisms to explain this effect. First, we mention the results of Ref. [50, 55, 56, 57], predicting the existence of a non-linear tail decaying slower than Price's law propagating to late-time. This non-linear tail originates from two QNMs coupled in the second-order source, and propagated by the prompt response Green's function. As a result, it is not a hereditary effect but is instantaneous, i.e. travels on the light-cone. An accurate comparison of fully non-linear waveforms against perturbative predictions, both at linear and second order, is needed to probe the relevance of this new effect. A second mechanism could be generated by the dynamical evolution of the background; since the tail propagator chiefly depends on the background mass monopole, it could potentially be affected by third-order non-linear effects [54] relevant for mass ratios $q \approx 1$. Lastly, (linear) tails are a hereditary effect that can accumulate non-linearities present in the source, amplifying them. Accounting for finite-size effects in the inspiral-plunge source, i.e. higher corrections in the mass-ratio, when computing the convolution with Price's law propagator, could potentially impact the late-time signal. With this mechanism, at late times we could extract information about the inspiral non-linear features. In-depth investigations of these three mechanisms for the non-linear tail enhancement will allow us to understand and model the leading non-linear effect present in the late-time signal.

The research direction outlined above would allow us to improve our models for the late-time tails and the

QNMs response. Future observational goals would be to estimate the tail detectability with LISA and understand which physics can be extracted from an eventual tail observation. Refined predictions for the QNMs and redshift modes excitation in a Kerr background will grant more control of fully non-linear waveforms: better understood templates, devoid of overfitting issues, and more strict priors could greatly improve black hole spectroscopy. Indeed, most of the recent debates sparked by our poor analytical understanding of the near-peak waveform [289]. This could allow improved studies of the non-linear, non-modal content of numerical mergers, a fundamental step to understand why waveforms emitted by comparable-mass mergers share so many similar features with perturbative ones.

Finally, extending waveforms predictions through numerical relativity simulations for a wide class of beyond-GR theories, and in the presence of a generic non-vacuum environment, would likely require an unfeasible amount of computational power. Achieving the full potential of gravitational-wave astronomy as a probe of complex astrophysical environments and fundamental physics phenomena will thus require complete inspiral-merger-ringdown *analytical* predictions, in which new effects can be added in a well-understood way.

Appendix A

Test-particle source

We focus on a test-particle evolving on top of a Schwarzschild BH geometry on a planar orbit $\theta = \pi/2$. The stress-energy tensor of the test-particle is the following

$$T_{\mu\nu} = g^0_{\mu\alpha} g^0_{\nu\beta}\, \mu \int d\tau\, \frac{u^\alpha u^\beta}{r^2} \delta(t - t(\tau))\delta(r - r(\tau))\delta(\varphi - \varphi(\tau))\delta\left(\theta - \frac{\pi}{2}\right). \tag{A.1}$$

By means of Eq. (3.6), it is possible to change the integrating variable as $d\tau = A(r)dt/E$, the integral can then be solved by means of the Dirac delta $\delta(t - t(\tau))$. The final result is the following

$$T_{\mu\nu} = \frac{\mu}{r^2}\delta(r - r(t))\delta(\phi - \phi(t))\delta\left(\theta - \frac{\pi}{2}\right) \cdot \begin{pmatrix} E\,A(r) & -p_{r_*} & 0 & -L\,A(r) \\ * & \frac{p^2_{r_*}}{E\,A(r)} & 0 & \frac{L\,p_{r_*}}{E} \\ * & * & 0 & 0 \\ * & * & * & \frac{L^2 A(r)}{E} \end{pmatrix}. \tag{A.2}$$

We decompose the above tensor in scalar, vector and tensor spherical harmonics then separate even and odd sectors, as in Eqs. (2.16) and (2.17). The explicit expressions for each component can be found in Ref. [92]. Substituting these expressions into the source functions in Eqs. (2.27) and (2.22), we compute the Zerilli (even) and Regge-Wheeler (odd) representing a test-particle influence on the gravitational field. These sources have the general expression [100]

$$S^{(o,e)}_{\ell m}(t, r) = \tilde{f}^{(o,e)}_{\ell m}(t, r)\, \delta(r_* - r_*(t)) + \tilde{g}^{(o,e)}_{\ell m}(t, r)\, \partial_{r_*}\delta(r_* - r_*(t)), \tag{A.3}$$

where we have defined the functions $\tilde{f}_{\ell m}$, $\tilde{g}_{\ell m}$ as

$$\begin{aligned} \tilde{f}^{(e)}_{\ell m}(t, r) = &- \frac{16\pi\mu A(r) Y^*_{\ell m}}{r\hat{H}\lambda\,[r(\lambda - 2) + 6]} \left\{ -2im\, p_\varphi p_{r_*} + 5 + \frac{12\hat{H}^2 r}{r(\lambda - 2) + 6} - \frac{r\lambda}{2} + \frac{2p^2_\varphi}{r^2} \right. \\ &\left. + \frac{p^2_\varphi}{r^2(\lambda - 2)} \left[r(\lambda - 2)(m^2 - \lambda - 1) + 2(3m^2 - \lambda - 5) \right] \right\}, \end{aligned} \tag{A.4}$$

$$\tilde{g}^{(e)}_{\ell m}(t, r) = -\frac{16\pi\mu A(r) Y^*_{\ell m}}{r\hat{H}\lambda\,[r(\lambda - 2) + 6]} (p^2_\varphi + r^2), \tag{A.5}$$

for the even sector, and

$$\tilde{f}^{(o)}_{\ell m}(t,r) = \frac{16\pi\mu\partial_\theta Y^*_{\ell m}}{r\lambda(\lambda-2)}\left\{\left(\frac{\hat{p}_{r_*}\hat{p}_\varphi}{\hat{H}}\right)_{,t} - \frac{2\hat{p}_\varphi}{r}A(r) - \frac{im}{r^2}A(r)\frac{\hat{p}_{r_*}\hat{p}^2_\varphi}{\hat{H}}\right\}, \tag{A.6}$$

$$\tilde{g}^{(o)}_{\ell m}(t,r) = \frac{16\pi\mu\partial_\theta Y^*_{\ell m}}{r\lambda(\lambda-2)}\hat{p}_\varphi\left(1-\frac{p^2_{r_*}}{\hat{H}}\right), \tag{A.7}$$

for the odd sector.

The Regge-Wheeler and Zerilli test-particle sources can also be written in terms of a Dirac delta in r and its derivative (with respect to r) as

$$S^{(o,e)}_{\ell m}(t,r) = f^{(o,e)}_{\ell m}(t,r)\,\delta(r-r(t)) + g^{(o,e)}_{\ell m}(t,r)\,\partial_r\delta(r-r(t)), \tag{A.8}$$

with $f_{\ell m}$, $g_{\ell m}$ defined as

$$\begin{aligned} f^{(e)}_{\ell m}(t,r) = &-\frac{16\pi\mu A^2(r)Y^*_{\ell m}}{r\hat{H}\lambda\left[r(\lambda-2)+6M\right]}\left\{-2im\hat{p}_{r_*}\hat{p}_\varphi + 3M\left(1+\frac{4\hat{H}^2 r}{r(\lambda-2)+6M}\right) - \frac{r\lambda}{2} + \right. \\ &\left. \frac{\hat{p}^2_\varphi}{r^2(\lambda-2)}\left[r(\lambda-2)(m^2-\lambda-1)+2M(3m^2-\lambda-5)\right] + \left(\hat{p}^2_\varphi + r^2\right)\frac{4M}{r^2}\right\}, \end{aligned} \tag{A.9}$$

$$g^{(e)}_{\ell m}(t,r) = -\frac{16\pi\mu A^3(r)Y^*_{\ell m}}{r\hat{H}\lambda\left[r(\lambda-2)+6M\right]}\left(\hat{p}^2_\varphi + r^2\right), \tag{A.10}$$

for the even sector and

$$f^{(o)}_{\ell m}(t,r) = \frac{16\pi\mu\partial_\theta Y^*_{\ell m}}{r\lambda(\lambda-2)}\left\{A(r)\left(\frac{\hat{p}_{r_*}\hat{p}_\varphi}{\hat{H}}\right)_{,t} - \frac{2\hat{p}_\varphi}{r}A^2(r) + \frac{2M}{r^2}A(r)\hat{p}_\varphi\left(1-\frac{p^2_{r_*}}{\hat{H}}\right) - \frac{im}{r^2}A^2(r)\frac{\hat{p}_{r_*}\hat{p}^2_\varphi}{\hat{H}}\right\}, \tag{A.11}$$

$$g^{(o)}_{\ell m}(t,r) = \frac{16\pi\mu A^2(r)\partial_\theta Y^*_{\ell m}}{r\lambda(\lambda-2)}\hat{p}_\varphi\left(1-\frac{p^2_{r_*}}{\hat{H}}\right), \tag{A.12}$$

for the odd sector

In Eqs. (A.4)-(A.12), we have denoted with $\hat{H}$, $\hat{p}_\varphi$, $\hat{p}_{r_*}$ the μ-rescaled energy and momenta, as introduced in Sec. 5.1. We denoted $\lambda = \ell(\ell+1)$.

Appendix B

RWZHyp convergence

We now assess the convergence of the time-domain code RWZHyp by performing numerical tests on an illustrative case, the initially bound configuration with $e_0 = 0.5$. For all the grid configurations, we truncate our computational domain at $r_*^{\rm H} = -100$, locate future null infinity at $\rho_+ = 500$, and perform the hyperboloidal layer matching at $\rho_{\rm match} = 400$. This grid setup is the one typically adopted for the runs considered in this work, where we use a radial-step of $\Delta\rho = 0.015$. In this Appendix we also consider three lower resolutions, going up to $\Delta\rho = 0.12$. The amplitudes of the corresponding (2,2) waveforms are shown in the upper panel of Fig. B.1 for the different radial resolutions, together with the tail decay exponents computed according to Eq. (5.22).

To establish the convergence of the code, we consider triplets of resolutions (low/medium/high) at fixed Courant–Friedrichs–Lewy number $C = 0.5$, and rescale the difference between medium-high resolutions with the scaling factor SF(r), defined as

$$\mathrm{SF}(r) = \frac{(\Delta\rho_{\rm L})^r - (\Delta\rho_{\rm M})^r}{(\Delta\rho_{\rm M})^r - (\Delta\rho_{\rm H})^r}. \tag{B.1}$$

The order of convergence r is determined by requiring that the rescaled medium-high difference match the low-medium one. We observe a 2nd order converge for the inspiral, ringdown, and early tail. However, the convergence starts to deteriorate from 2000 after the light-ring crossing. Moreover, some artefacts in the data are visible in the tail decay exponent p at late times, where high-frequency oscillations become particularly visible for small radial steps. However, all the resolutions considered provide an accurate description of the tail, since all the relative differences on the amplitude are well below the 1% threshold. We also performed some numerical tests considering different grid options, finding that setups with larger $r_*^{\rm H}$ or smaller ρ_+ provide slightly less accurate numerical waveforms.

Finally, we highlight that the junk radiation never enters in the trajectory used in Eq. (5.15), by construction. In fact, as stressed in Sec. 5.1, the fluxes used to compute the radiation-reaction effective forces, $\hat{\mathcal{F}}_{r_*}, \hat{\mathcal{F}}_{\varphi}$ in Eq. (5.8), are analytical. Then, we argue that the agreement of our prediction with the late-time signal computed in the numerical evolutions, as shown in Fig. 5.3, 5.4 and 5.5, is a test confirming the fully negligible influence of the junk on the late-time tail.

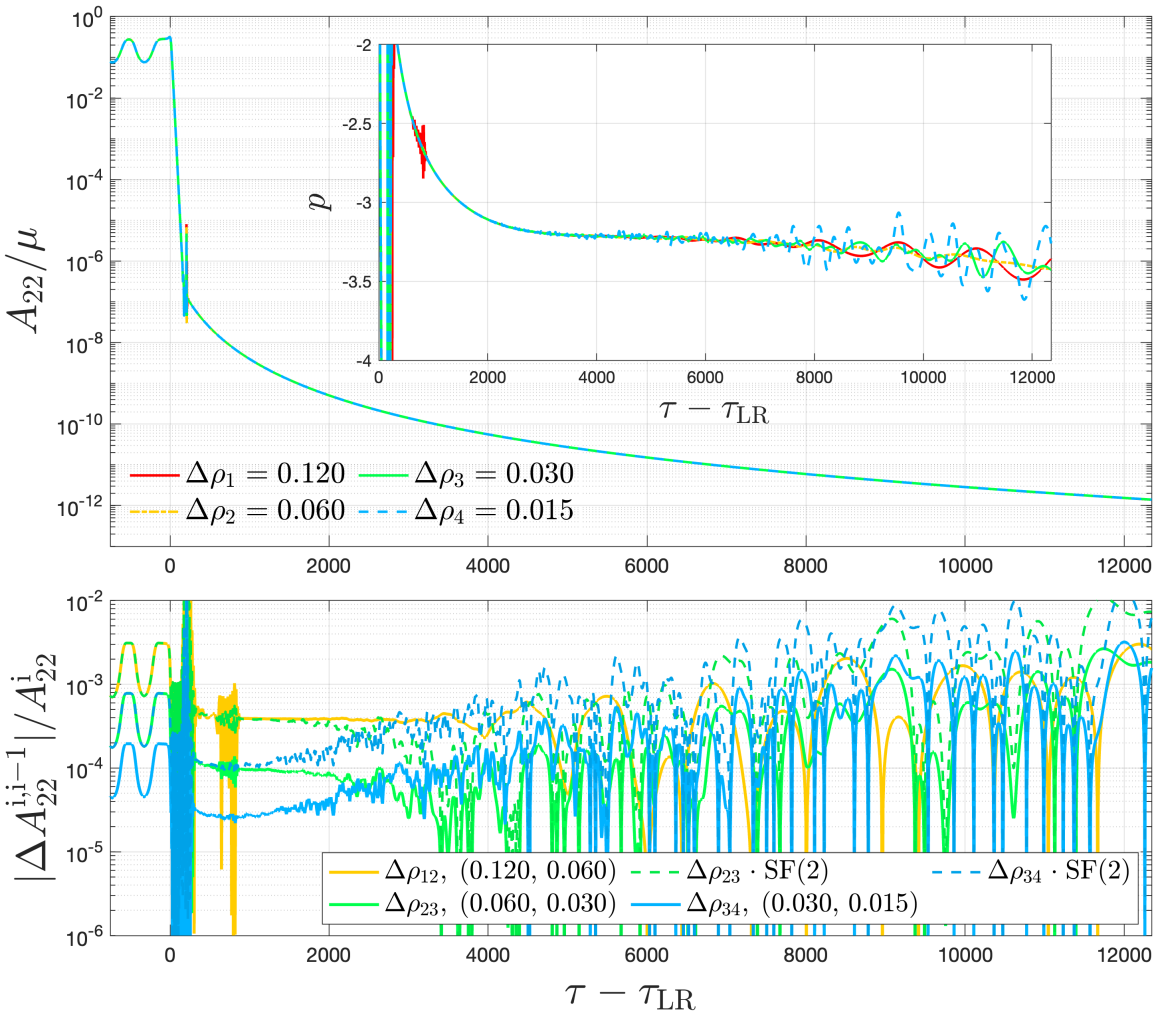

Figure B.1: Convergence test of the RWZHyp code for the configuration with $e_0 = 0.5$. Upper panel: amplitude of the (2,2) mode for different radial resolutions and corresponding tail exponent (insert) computed according to Eq. (5.22). Lower panel: relative amplitude differences among different resolutions (solid lines). We also rescale the last two with a second order rescaling factor SF(2) (dashed lines) in order to highlight the effective second-order convergence of the code.

Appendix C

Chandrasekhar's transformations between Regge-Wheeler and Zerilli modes

Consider a Regge-Wheeler mode $\tilde{u}^{\rm odd}(\omega, r_*)$ and a Zerilli one $\tilde{u}^{\rm even}(\omega, r_*)$. Following Chandraskhar [113], these modes are related through the transformation

$$\tilde{u}^{\rm even}(\omega, r_*) = \frac{1}{\kappa_\ell + 12i\omega}\left[\left(\kappa_\ell + \frac{72}{F_\ell(r)}\right)\tilde{u}^{\rm odd}(\omega, r_*) + 12A(r)\partial_r\tilde{u}^{\rm odd}(\omega, r_*)\right], \tag{C.1}$$

where we have introduced the following quantities

$$\kappa_\ell \equiv \ell^4 + 2\ell^3 - \ell^2 - 2\ell \quad , \quad F_\ell(r) \equiv \frac{r^2\left[r\ell(\ell+1) - 2r + 6\right]}{r-2}\,. \tag{C.2}$$

Following Chapters 2, 7, we write the ω-domain quasi-normal eigenfunction for an odd mode as

$$\tilde{u}^{\rm odd}(\omega_x; r_*) = e^{i\omega_x\left[r_* - 4\log\left(\frac{r-2}{r}\right)\right]}\hat{a}(\omega_x, r)\,, \tag{C.3}$$

where we defined the index $x \equiv (\ell mns)$ identifying the multipole numbers (ℓ, m), the overtone $n \geq 0$ and the regular/mirror mode $s = \pm$ index. Substituting the above expression in the transformation Eq. (C.1), we find the even quasi-normal mode as

$$\tilde{u}^{\rm even}(\omega_x; r_*) = e^{i\omega_x\left[r_* - 4\log\left(\frac{r-2}{r}\right)\right]}\hat{z}(\omega_x, r)\,, \tag{C.4}$$

where we have defined $\hat{z}(\omega, r_*)$ as

$$\hat{z}(\omega, r_*) \equiv \frac{1}{\kappa_\ell + 12i\omega}\left[\left(\kappa_\ell + \frac{72}{F(r)} + 12i\omega\frac{r^2-8}{r^2}\right)\hat{a}(\omega, r_*) + 12A(r)\partial_r\hat{a}(\omega, r_*)\right]. \tag{C.5}$$

Appendix D

Standard regularization of excitation coefficients

As discussed in Sec. 7.2.3, the quasi-normal modes excitation coefficients may be divergent should one consider initial data that extends all the way to the horizon, or a source approaching it dynamically. To handle these divergences, different regularization procedures have been introduced in the literature. In Ref. [118], Sun and Price investigated the excitation coefficients for initial data extending to the horizon. They introduced a regularization based on an analytic continuation on a deformed contour in the complex $r-$ plane. An analogous approach was used by Leaver [14]. More recently, it was shown that the excitation coefficients can be regularized by subtracting suitable counter-terms, as shown in [51, 285]. In this Appendix, we show that the two procedures are equivalent, focusing on a source with the same near horizon behavior as the one considered in Chapter 7.

Let us consider the following integral, which describes the near-horizon behavior of the excitation coefficient (7.38) of the first overtone,

$$I_H = \int_2^b (2-r)^{-4i\omega_{221}} dr\,, \tag{D.1}$$

where $b > 2$. Such integral is clearly divergent, as $-4|\omega_{221}^{\rm Im}| + 1 < 0$. The regularization procedure by Price, Sun and Leaver [14, 118] amounts to computing the integral along a complex path as the one shown in Fig. D.1 in the limit $\epsilon \to 0$. The branch cut of the integrand is placed along the real axis in the interval $r \in (2, \infty)$ and the excitation coefficient is computed as

$$I_H = \lim_{\epsilon\to 0} \frac{\int_a^b dr\Big[\Big(2-r+i\epsilon\Big)^{-4i\omega_{221}} - \Big(2-r-i\epsilon\Big)^{-4i\omega_{221}}\Big]}{(1-e^{-8\omega_{221}})}\,, \tag{D.2}$$

where $a < 2$. The denominator is due the phase change between the two sides of the branch cut. The two terms in (D.2) represent the contributions along the horizontal paths above and below the cut. Note that the contribution of the vertical path is not included, as it becomes infinitesimal in the limit $\epsilon \to 0$.

Let us now show how this expression can be rearranged to find the counter-term of regularization method

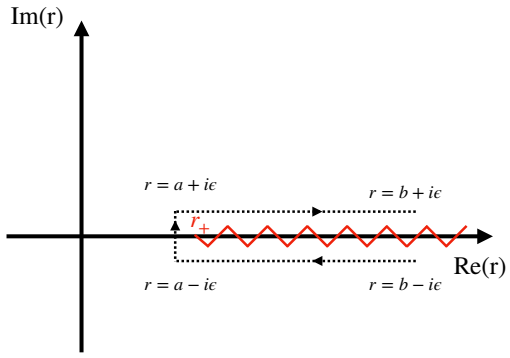

Figure D.1: Analytic continuation of the radial coordinate used to compute the regularized excitation coefficients in [118]. The zig-zag line represents the branch cut along the real axis, while the dashed line is the deformed integration contour. The integral on such contour matches the one obtained using the counter-term regularization method.

of Refs. [51, 285]. We introduce a new variable $2 < \tilde{r} < b$ such that eq. (D.2) can be rewritten as:

$$I_H = \lim_{\epsilon\to 0} \frac{\int_{\tilde{r}}^{b} dr\Big[H_+(r,\epsilon)^{-4i\omega_{221}} - H_-(r,\epsilon)^{-4i\omega_{221}}\Big]}{(1-e^{-8\omega_{221}})} - \frac{\Big[H_+(r,\epsilon)^{1-4i\omega_{221}} - H_-(r,\epsilon)^{1-4i\omega_{221}}\Big]_a^{\tilde{r}}}{(1-e^{-8\omega_{221}})(1-4i\omega_{221})}\,, \tag{D.3}$$

where we defined for compactness $H_\pm(r,\epsilon) = (2 - r \pm i\epsilon)$. Let us now take the limit $\tilde{r} \to 2$. Noting that above and below the cut we have $H_-(r,\epsilon) = H_+(r,\epsilon)e^{-8\omega_{221}}$, the first term in (D.3) can be rewritten as:

$$\lim_{\substack{\epsilon\to 0\\ \tilde{r}\to 2}} \frac{\int_{\tilde{r}}^{b} dr\Big[H_+(r,\epsilon)^{-4i\omega_{221}} - H_-(r,\epsilon)^{-4i\omega_{221}}\Big]}{(1-e^{-8\omega_{221}})} = \lim_{\substack{\epsilon\to 0^+\\ \tilde{r}\to 2}} \int_{\tilde{r}}^{b} dr\Big[H_+(r,\epsilon)^{-4i\omega_{221}}\Big] = \lim_{\tilde{r}\to 2}\int_{\tilde{r}}^{b} (-r+2)^{-4i\omega_{221}}$$

As for the second term, we have two different contributions when the function inside the square bracket is evaluated at $\tilde{r}$ and a, respectively. In the first case we have:

$$\lim_{\substack{\epsilon\to 0\\ \tilde{r}\to 2}} \frac{\Big[H_+(\tilde{r},\epsilon)^{1-4i\omega_{221}} - H_-(\tilde{r},\epsilon)^{1-4i\omega_{221}}\Big]}{(1-e^{-8\omega_{221}})(1-4i\omega_{221})} = \lim_{\substack{\epsilon\to 0^+\\ \tilde{r}\to 2}} \frac{H_+(\tilde{r},\epsilon)^{1-4i\omega_{221}}}{1-4i\omega_{221}} = \lim_{\tilde{r}\to 2} \frac{(2-\tilde{r})^{1-4i\omega_{221}}}{1-4i\omega_{221}}$$

When evaluated in $r = a$ instead, this term gives a vanishing contribution. As $a < 2$, when the limit $\epsilon \to 0$ is performed, the branch cut is not crossed and the function is continuous, and therefore $\lim_{\epsilon\to 0}\Big[H_+(r,\epsilon) - H_-(r,\epsilon)\Big] = 0$ for $r < 2$ trivially. Summing up the two terms, we can rewrite the excitation coefficient as:

$$I_H = \lim_{\tilde{r}\to 2}\Big[\int_{\tilde{r}}^{b} dr(2-r)^{-4i\omega_{221}} - \frac{(2-\tilde{r})^{1-4i\omega_{221}}}{1-4i\omega_{221}}\Big], \tag{D.4}$$

which is exactly the prescription of the counter-term regularization method. To solidify our conclusions, we verified that such equality holds by computing numerically the integral (D.1) both with the complex contour and the counter-term regularization method, obtaining the same values up to machine precision.

Bibliography

[1] Marina De Amicis, Simone Albanesi, and Gregorio Carullo. “Inspiral-inherited ringdown tails”. In: *Phys. Rev. D* 110.10 (2024), p. 104005. DOI: 10.1103/PhysRevD.110.104005. arXiv: 2406.17018 [gr-qc].

[2] Marina De Amicis et al. “Late-time tails in nonlinear evolutions of merging black holes”. In: (Dec. 2024). arXiv: 2412.06887 [gr-qc].

[3] Michele Maggiore. *Gravitational Waves. Vol. 1: Theory and Experiments*. Oxford University Press, 2007. ISBN: 978-0-19-171766-6, 978-0-19-852074-0. DOI: 10.1093/acprof:oso/9780198570745.001.0001.

[4] Valeria Ferrari, Leonardo Gualtieri, and Paolo Pani. *General Relativity and its Applications*. CRC Press, Dec. 2020. ISBN: 978-0-429-49140-5, 978-0-367-62532-0. DOI: 10.1201/9780429491405.

[5] Albert Einstein and N. Rosen. “On Gravitational waves”. In: *J. Franklin Inst.* 223 (1937), pp. 43–54. DOI: 10.1016/S0016-0032(37)90583-0.

[6] J. H. Taylor, L. A. Fowler, and P. M. McCulloch. “Measurements of general relativistic effects in the binary pulsar PSR 1913+16”. In: *Nature* 277 (1979), pp. 437–440. DOI: 10.1038/277437a0.

[7] B. P. Abbott et al. “Observation of Gravitational Waves from a Binary Black Hole Merger”. In: *Phys. Rev. Lett.* 116.6 (2016), p. 061102. DOI: 10.1103/PhysRevLett.116.061102. arXiv: 1602.03837 [gr-qc].

[8] R. Abbott et al. “GWTC-3: Compact Binary Coalescences Observed by LIGO and Virgo during the Second Part of the Third Observing Run”. In: *Phys. Rev. X* 13.4 (2023), p. 041039. DOI: 10.1103/PhysRevX.13.041039. arXiv: 2111.03606 [gr-qc].

[9] Amos Ori and Kip S. Thorne. “The Transition from inspiral to plunge for a compact body in a circular equatorial orbit around a massive, spinning black hole”. In: *Phys. Rev. D* 62 (2000), p. 124022. DOI: 10.1103/PhysRevD.62.124022. arXiv: gr-qc/0003032.

[10] Alessandra Buonanno and Thibault Damour. “Transition from inspiral to plunge in binary black hole coalescences”. In: *Phys. Rev. D* 62 (2000), p. 064015. DOI: 10.1103/PhysRevD.62.064015. arXiv: gr-qc/0001013.

[11] Lionel London, Deirdre Shoemaker, and James Healy. “Modeling ringdown: Beyond the fundamental quasinormal modes”. In: *Phys. Rev. D* 90.12 (2014). [Erratum: Phys.Rev.D 94, 069902 (2016)], p. 124032. DOI: 10.1103/PhysRevD.90.124032. arXiv: 1404.3197 [gr-qc].

[12] L. T. London. "Modeling ringdown. II. Aligned-spin binary black holes, implications for data analysis and fundamental theory". In: *Phys. Rev. D* 102.8 (2020), p. 084052. DOI: 10.1103/PhysRevD.102.084052. arXiv: 1801.08208 [gr-qc].

[13] Alessandra Buonanno, Gregory B. Cook, and Frans Pretorius. "Inspiral, merger and ring-down of equal-mass black-hole binaries". In: *Phys. Rev. D* 75 (2007), p. 124018. DOI: 10.1103/PhysRevD.75.124018. arXiv: gr-qc/0610122.

[14] Edward W. Leaver. "Spectral decomposition of the perturbation response of the Schwarzschild geometry". In: *Phys. Rev. D* 34 (1986), pp. 384–408. DOI: 10.1103/PhysRevD.34.384.

[15] Nils Andersson. "Evolving test fields in a black hole geometry". In: *Phys. Rev. D* 55 (1997), pp. 468–479. DOI: 10.1103/PhysRevD.55.468. arXiv: gr-qc/9607064.

[16] Richard H. Price. "Nonspherical perturbations of relativistic gravitational collapse. 1. Scalar and gravitational perturbations". In: *Phys. Rev. D* 5 (1972), pp. 2419–2438. DOI: 10.1103/PhysRevD.5.2419.

[17] Richard H. Price. "Nonspherical Perturbations of Relativistic Gravitational Collapse. II. Integer-Spin, Zero-Rest-Mass Fields". In: *Phys. Rev. D* 5 (1972), pp. 2439–2454. DOI: 10.1103/PhysRevD.5.2439.

[18] Leor Barack. "Late time dynamics of scalar perturbations outside black holes. 2. Schwarzschild geometry". In: *Phys. Rev. D* 59 (1999), p. 044017. DOI: 10.1103/PhysRevD.59.044017. arXiv: gr-qc/9811028.

[19] Vasco Gennari, Gregorio Carullo, and Walter Del Pozzo. "Searching for ringdown higher modes with a numerical relativity-informed post-merger model". In: *Eur. Phys. J. C* 84.3 (2024), p. 233. DOI: 10.1140/epjc/s10052-024-12550-x. arXiv: 2312.12515 [gr-qc].

[20] A.G. Doroshkevic, Ya. B. Zeldovich, and I.D. Novikov. "Gravitational collapse of non-symmetric and rotating bodies". In: *Sov. Phys. JETP 22, 122* (1966).

[21] V.L. Ginzburg and L.M. Ozernoy. "On gravitational collapse of magnetic stars". In: *Zh. Eksp. Teor. Fiz.* 147 (1964), pp. 1030–1040.

[22] Roy P. Kerr. "Gravitational field of a spinning mass as an example of algebraically special metrics". In: *Phys. Rev. Lett.* 11 (1963), pp. 237–238. DOI: 10.1103/PhysRevLett.11.237.

[23] E T. Newman et al. "Metric of a Rotating, Charged Mass". In: *J. Math. Phys.* 6 (1965), pp. 918–919. DOI: 10.1063/1.1704351.

[24] Werner Israel. "Event horizons in static vacuum space-times". In: *Phys. Rev.* 164 (1967), pp. 1776–1779. DOI: 10.1103/PhysRev.164.1776.

[25] S. W. Hawking. "Black holes in general relativity". In: *Commun. Math. Phys.* 25 (1972), pp. 152–166. DOI: 10.1007/BF01877517.

[26] D. C. Robinson. "Uniqueness of the Kerr black hole". In: *Phys. Rev. Lett.* 34 (1975), pp. 905–906. DOI: 10.1103/PhysRevLett.34.905.

[27] P. O. Mazur. “PROOF OF UNIQUENESS OF THE KERR-NEWMAN BLACK HOLE SOLUTION”. In: *J. Phys. A* 15 (1982), pp. 3173–3180. DOI: 10.1088/0305-4470/15/10/021.

[28] Jacob D. Bekenstein. “Black hole hair: 25 - years after”. In: *2nd International Sakharov Conference on Physics*. May 1996, pp. 216–219. arXiv: gr-qc/9605059.

[29] B. Carter. “Has the black hole equilibrium problem been solved?” In: *8th Marcel Grossmann Meeting on Recent Developments in Theoretical and Experimental General Relativity, Gravitation and Relativistic Field Theories (MG 8)*. Dec. 1997, pp. 136–155. arXiv: gr-qc/9712038.

[30] Pawel O. Mazur. “Black hole uniqueness theorems”. In: (Dec. 2000). arXiv: hep-th/0101012.

[31] David Robinson. “Four decades of black holes uniqueness theorems”. In: *Kerr Fest: Black Holes in Astrophysics, General Relativity and Quantum Gravity*. Aug. 2004.

[32] Piotr T. Chrusciel, Joao Lopes Costa, and Markus Heusler. “Stationary Black Holes: Uniqueness and Beyond”. In: *Living Rev. Rel.* 15 (2012), p. 7. DOI: 10.12942/lrr-2012-7. arXiv: 1205.6112 [gr-qc].

[33] Olaf Dreyer et al. “Black hole spectroscopy: Testing general relativity through gravitational wave observations”. In: *Class. Quant. Grav.* 21 (2004), pp. 787–804. DOI: 10.1088/0264-9381/21/4/003. arXiv: gr-qc/0309007.

[34] Emanuele Berti, Vitor Cardoso, and Clifford M. Will. “On gravitational-wave spectroscopy of massive black holes with the space interferometer LISA”. In: *Phys. Rev. D* 73 (2006), p. 064030. DOI: 10.1103/PhysRevD.73.064030. arXiv: gr-qc/0512160.

[35] S. Gossan, J. Veitch, and B. S. Sathyaprakash. “Bayesian model selection for testing the no-hair theorem with black hole ringdowns”. In: *Phys. Rev. D* 85 (2012), p. 124056. DOI: 10.1103/PhysRevD.85.124056. arXiv: 1111.5819 [gr-qc].

[36] J. Meidam et al. “Testing the no-hair theorem with black hole ringdowns using TIGER”. In: *Phys. Rev. D* 90.6 (2014), p. 064009. DOI: 10.1103/PhysRevD.90.064009. arXiv: 1406.3201 [gr-qc].

[37] Gregorio Carullo, Walter Del Pozzo, and John Veitch. “Observational Black Hole Spectroscopy: A time-domain multimode analysis of GW150914”. In: *Phys. Rev. D* 99.12 (2019). [Erratum: Phys.Rev.D 100, 089903 (2019)], p. 123029. DOI: 10.1103/PhysRevD.99.123029. arXiv: 1902.07527 [gr-qc].

[38] R. Abbott et al. “Tests of General Relativity with GWTC-3”. In: (Dec. 2021). arXiv: 2112.06861 [gr-qc].

[39] C. V. Vishveshwara. “Scattering of Gravitational Radiation by a Schwarzschild Black-hole”. In: *Nature* 227 (1970), pp. 936–938. DOI: 10.1038/227936a0.

[40] Vishal Baibhav et al. “Agnostic black hole spectroscopy: Quasinormal mode content of numerical relativity waveforms and limits of validity of linear perturbation theory”. In: *Phys. Rev. D* 108.10 (2023), p. 104020. DOI: 10.1103/PhysRevD.108.104020. arXiv: 2302.03050 [gr-qc].

[41] Ameya Chavda, Macarena Lagos, and Lam Hui. "The impact of initial conditions on quasi-normal modes". In: (Dec. 2024). arXiv: 2412.03435 [gr-qc].

[42] Reinaldo J. Gleiser et al. "Second order perturbations of a Schwarzschild black hole". In: *Class. Quant. Grav.* 13 (1996), pp. L117–L124. DOI: 10.1088/0264-9381/13/10/001. arXiv: gr-qc/9510049.

[43] Kunihito Ioka and Hiroyuki Nakano. "Second and higher-order quasi-normal modes in binary black hole mergers". In: *Phys. Rev. D* 76 (2007), p. 061503. DOI: 10.1103/PhysRevD.76.061503. arXiv: 0704.3467 [astro-ph].

[44] Hiroyuki Nakano and Kunihito Ioka. "Second Order Quasi-Normal Mode of the Schwarzschild Black Hole". In: *Phys. Rev. D* 76 (2007), p. 084007. DOI: 10.1103/PhysRevD.76.084007. arXiv: 0708.0450 [gr-qc].

[45] David Brizuela, Jose M. Martin-Garcia, and Manuel Tiglio. "A Complete gauge-invariant formalism for arbitrary second-order perturbations of a Schwarzschild black hole". In: *Phys. Rev. D* 80 (2009), p. 024021. DOI: 10.1103/PhysRevD.80.024021. arXiv: 0903.1134 [gr-qc].

[46] Justin L. Ripley et al. "Numerical computation of second order vacuum perturbations of Kerr black holes". In: *Phys. Rev. D* 103 (2021), p. 104018. DOI: 10.1103/PhysRevD.103.104018. arXiv: 2010.00162 [gr-qc].

[47] Mark Ho-Yeuk Cheung et al. "Nonlinear Effects in Black Hole Ringdown". In: *Phys. Rev. Lett.* 130.8 (2023), p. 081401. DOI: 10.1103/PhysRevLett.130.081401. arXiv: 2208.07374 [gr-qc].

[48] Keefe Mitman et al. "Nonlinearities in Black Hole Ringdowns". In: *Phys. Rev. Lett.* 130.8 (2023), p. 081402. DOI: 10.1103/PhysRevLett.130.081402. arXiv: 2208.07380 [gr-qc].

[49] Mark Ho-Yeuk Cheung et al. "Extracting linear and nonlinear quasinormal modes from black hole merger simulations". In: *Phys. Rev. D* 109.4 (2024). [Erratum: Phys.Rev.D 110, 049902 (2024)], p. 044069. DOI: 10.1103/PhysRevD.109.044069. arXiv: 2310.04489 [gr-qc].

[50] Satoshi Okuzumi, Kunihito Ioka, and Masa-aki Sakagami. "Possible Discovery of Nonlinear Tail and Quasinormal Modes in Black Hole Ringdown". In: *Phys. Rev. D* 77 (2008), p. 124018. DOI: 10.1103/PhysRevD.77.124018. arXiv: 0803.0501 [gr-qc].

[51] Laura Sberna et al. "Nonlinear effects in the black hole ringdown: Absorption-induced mode excitation". In: *Phys. Rev. D* 105.6 (2022), p. 064046. DOI: 10.1103/PhysRevD.105.064046. arXiv: 2112.11168 [gr-qc].

[52] Jaime Redondo-Yuste, David Pereñiguez, and Vitor Cardoso. "Ringdown of a dynamical spacetime". In: *Phys. Rev. D* 109.4 (2024), p. 044048. DOI: 10.1103/PhysRevD.109.044048. arXiv: 2312.04633 [gr-qc].

[53] Lodovico Capuano, Luca Santoni, and Enrico Barausse. "Perturbations of the Vaidya metric in the frequency domain: Quasi-normal modes and tidal response". In: (July 2024). arXiv: 2407.06009 [gr-qc].

[54] Taillte May et al. “Nonlinear effect of absorption on the ringdown of a spinning black hole”. In: (May 2024). arXiv: 2405.18303 [gr-qc].

[55] Vitor Cardoso et al. “Hushing black holes: Tails in dynamical spacetimes”. In: *Phys. Rev. D* 109.12 (2024), p. L121502. DOI: 10.1103/PhysRevD.109.L121502. arXiv: 2405.12290 [gr-qc].

[56] Siyang Ling, Sabeela Shah, and Sam S. C. Wong. “Dynamical nonlinear tails in Schwarzschild black hole ringdown”. In: (Mar. 2025). arXiv: 2503.19967 [gr-qc].

[57] Alex Kehagias and Antonio Riotto. “Nonlinear Tails of Gravitational Waves in Schwarzschild Black Hole Ringdown”. In: (Apr. 2025). arXiv: 2504.06224 [gr-qc].

[58] Alessandra Buonanno et al. “Toward faithful templates for non-spinning binary black holes using the effective-one-body approach”. In: *Phys. Rev. D* 76 (2007), p. 104049. DOI: 10.1103/PhysRevD.76.104049. arXiv: 0706.3732 [gr-qc].

[59] Matthew Giesler et al. “Black Hole Ringdown: The Importance of Overtones”. In: *Phys. Rev. X* 9.4 (2019), p. 041060. DOI: 10.1103/PhysRevX.9.041060. arXiv: 1903.08284 [gr-qc].

[60] Maximiliano Isi et al. “Testing the no-hair theorem with GW150914”. In: *Phys. Rev. Lett.* 123.11 (2019), p. 111102. DOI: 10.1103/PhysRevLett.123.111102. arXiv: 1905.00869 [gr-qc].

[61] Roberto Cotesta et al. “Analysis of Ringdown Overtones in GW150914”. In: *Phys. Rev. Lett.* 129.11 (2022), p. 111102. DOI: 10.1103/PhysRevLett.129.111102. arXiv: 2201.00822 [gr-qc].

[62] Gregorio Carullo et al. “Reply to Comment on ”Analysis of Ringdown Overtones in GW150914””. In: *Phys. Rev. Lett.* 131 (2023), p. 169002. DOI: 10.1103/PhysRevLett.131.169002. arXiv: 2310.20625 [gr-qc].

[63] Scott E. Field et al. “Fast prediction and evaluation of gravitational waveforms using surrogate models”. In: *Phys. Rev. X* 4.3 (2014), p. 031006. DOI: 10.1103/PhysRevX.4.031006. arXiv: 1308.3565 [gr-qc].

[64] Jonathan Blackman et al. “Fast and Accurate Prediction of Numerical Relativity Waveforms from Binary Black Hole Coalescences Using Surrogate Models”. In: *Phys. Rev. Lett.* 115.12 (2015), p. 121102. DOI: 10.1103/PhysRevLett.115.121102. arXiv: 1502.07758 [gr-qc].

[65] Jonathan Blackman et al. “A Surrogate Model of Gravitational Waveforms from Numerical Relativity Simulations of Precessing Binary Black Hole Mergers”. In: *Phys. Rev. D* 95.10 (2017), p. 104023. DOI: 10.1103/PhysRevD.95.104023. arXiv: 1701.00550 [gr-qc].

[66] Jonathan Blackman et al. “Numerical relativity waveform surrogate model for generically precessing binary black hole mergers”. In: *Phys. Rev. D* 96.2 (2017), p. 024058. DOI: 10.1103/PhysRevD.96.024058. arXiv: 1705.07089 [gr-qc].

[67] Vijay Varma et al. “Surrogate model of hybridized numerical relativity binary black hole waveforms”. In: *Phys. Rev. D* 99.6 (2019), p. 064045. DOI: 10.1103/PhysRevD.99.064045. arXiv: 1812.07865 [gr-qc].

[68] Vijay Varma et al. “Surrogate models for precessing binary black hole simulations with unequal masses”. In: *Phys. Rev. Research.* 1 (2019), p. 033015. DOI: 10.1103/PhysRevResearch.1.033015. arXiv: 1905.09300 [gr-qc].

[69] Lorena Magaña Zertuche et al. “High-Precision Ringdown Surrogate Model for Non-Precessing Binary Black Holes”. In: (Aug. 2024). arXiv: 2408.05300 [gr-qc].

[70] A. Buonanno and T. Damour. “Effective one-body approach to general relativistic two-body dynamics”. In: *Phys. Rev. D* 59 (1999), p. 084006. DOI: 10.1103/PhysRevD.59.084006. arXiv: gr-qc/9811091.

[71] Thibault Damour and Alessandro Nagar. “The Effective One Body description of the Two-Body problem”. In: *Fundam. Theor. Phys.* 162 (2011). Ed. by Luc Blanchet, Alessandro Spallicci, and Bernard Whiting, pp. 211–252. DOI: 10.1007/978-90-481-3015-3_7. arXiv: 0906.1769 [gr-qc].

[72] Adam Pound and Barry Wardell. “Black hole perturbation theory and gravitational self-force”. In: (Jan. 2021). DOI: 10.1007/978-981-15-4702-7_38-1. arXiv: 2101.04592 [gr-qc].

[73] Thibault Damour and Alessandro Nagar. “A new analytic representation of the ringdown waveform of coalescing spinning black hole binaries”. In: *Phys. Rev. D* 90.2 (2014), p. 024054. DOI: 10.1103/PhysRevD.90.024054. arXiv: 1406.0401 [gr-qc].

[74] Thibault Damour and Alessandro Nagar. “Faithful effective-one-body waveforms of small-mass-ratio coalescing black-hole binaries”. In: *Phys. Rev. D* 76 (2007), p. 064028. DOI: 10.1103/PhysRevD.76.064028. arXiv: 0705.2519 [gr-qc].

[75] Simone Albanesi et al. “Faithful effective-one-body waveform of small-mass-ratio coalescing black hole binaries: The eccentric, nonspinning case”. In: *Phys. Rev. D* 108.8 (2023), p. 084037. DOI: 10.1103/PhysRevD.108.084037. arXiv: 2305.19336 [gr-qc].

[76] Ioannis Kamaretsos et al. “Black-hole hair loss: learning about binary progenitors from ringdown signals”. In: *Phys. Rev. D* 85 (2012), p. 024018. DOI: 10.1103/PhysRevD.85.024018. arXiv: 1107.0854 [gr-qc].

[77] Ioannis Kamaretsos, Mark Hannam, and B. Sathyaprakash. “Is black-hole ringdown a memory of its progenitor?” In: *Phys. Rev. Lett.* 109 (2012), p. 141102. DOI: 10.1103/PhysRevLett.109.141102. arXiv: 1207.0399 [gr-qc].

[78] Vishal Baibhav et al. “Black Hole Spectroscopy: Systematic Errors and Ringdown Energy Estimates”. In: *Phys. Rev. D* 97.4 (2018), p. 044048. DOI: 10.1103/PhysRevD.97.044048. arXiv: 1710.02156 [gr-qc].

[79] Ssohrab Borhanian et al. “Comparison of post-Newtonian mode amplitudes with numerical relativity simulations of binary black holes”. In: *Class. Quant. Grav.* 37.6 (2020), p. 065006. DOI: 10.1088/1361-6382/ab6a21. arXiv: 1901.08516 [gr-qc].

[80] Hengrui Zhu et al. “Black hole spectroscopy for precessing binary black hole coalescences”. In: *Phys. Rev. D* 111.6 (2025), p. 064052. DOI: 10.1103/PhysRevD.111.064052. arXiv: 2312.08588 [gr-qc].

[81] Gregorio Carullo. “Ringdown amplitudes of nonspinning eccentric binaries”. In: *JCAP* 10 (2024), p. 061. DOI: 10.1088/1475-7516/2024/10/061. arXiv: 2406.19442 [gr-qc].

[82] Costantino Pacilio et al. “Flexible mapping of ringdown amplitudes for nonprecessing binary black holes”. In: *Phys. Rev. D* 110.10 (2024), p. 103037. DOI: 10.1103/PhysRevD.110.103037. arXiv: 2408.05276 [gr-qc].

[83] Francesco Nobili et al. “Ringdown mode amplitudes of precessing binary black holes”. In: (Apr. 2025). arXiv: 2504.17021 [gr-qc].

[84] Keefe Mitman et al. “Probing the ringdown perturbation in binary black hole coalescences with an improved quasi-normal mode extraction algorithm”. In: (Mar. 2025). arXiv: 2503.09678 [gr-qc].

[85] Linqing Wen. “On the eccentricity distribution of coalescing black hole binaries driven by the Kozai mechanism in globular clusters”. In: *Astrophys. J.* 598 (2003), pp. 419–430. DOI: 10.1086/378794. arXiv: astro-ph/0211492.

[86] Johan Samsing. “Eccentric Black Hole Mergers Forming in Globular Clusters”. In: *Phys. Rev. D* 97.10 (2018), p. 103014. DOI: 10.1103/PhysRevD.97.103014. arXiv: 1711.07452 [astro-ph.HE].

[87] V. Gayathri et al. “Eccentricity estimate for black hole mergers with numerical relativity simulations”. In: *Nature Astron.* 6.3 (2022), pp. 344–349. DOI: 10.1038/s41550-021-01568-w. arXiv: 2009.05461 [astro-ph.HE].

[88] Rossella Gamba et al. “GW190521 as a dynamical capture of two nonspinning black holes”. In: *Nature Astron.* 7.1 (2023), pp. 11–17. DOI: 10.1038/s41550-022-01813-w. arXiv: 2106.05575 [gr-qc].

[89] Eric Poisson. “Radiative falloff of a scalar field in a weakly curved space-time without symmetries”. In: *Phys. Rev. D* 66 (2002), p. 044008. DOI: 10.1103/PhysRevD.66.044008. arXiv: gr-qc/0205018.

[90] Vitor Cardoso and Gaurav Khanna. “Black holes in anti–de Sitter spacetime: Quasinormal modes, tails, and flat spacetime”. In: *Phys. Rev. D* 91.2 (2015), p. 024031. DOI: 10.1103/PhysRevD.91.024031. arXiv: 1501.00977 [gr-qc].

[91] Dejan Gajic and Leonhard M. A. Kehrberger. “On the relation between asymptotic charges, the failure of peeling and late-time tails”. In: *Class. Quant. Grav.* 39.19 (2022). [Erratum: Class.Quant.Grav. 41, 119501 (2024)], p. 195006. DOI: 10.1088/1361-6382/ac8863. arXiv: 2202.04093 [gr-qc].

[92] Alessandro Nagar and Luciano Rezzolla. "Gauge-invariant non-spherical metric perturbations of Schwarzschild black-hole spacetimes". In: *Class. Quant. Grav.* 22 (2005). [Erratum: Class.Quant.Grav. 23, 4297 (2006)], R167. DOI: 10.1088/0264-9381/22/16/R01. arXiv: gr-qc/0502064.

[93] Sebastiano Bernuzzi and Alessandro Nagar. "Binary black hole merger in the extreme-mass-ratio limit: a multipolar analysis". In: *Phys. Rev. D* 81 (2010), p. 084056. DOI: 10.1103/PhysRevD.81.084056. arXiv: 1003.0597 [gr-qc].

[94] Sebastiano Bernuzzi, Alessandro Nagar, and Anil Zenginoglu. "Binary black hole coalescence in the large-mass-ratio limit: the hyperboloidal layer method and waveforms at null infinity". In: *Phys. Rev. D* 84 (2011), p. 084026. DOI: 10.1103/PhysRevD.84.084026. arXiv: 1107.5402 [gr-qc].

[95] Mark A. Scheel et al. "High-accuracy waveforms for binary black hole inspiral, merger, and ringdown". In: *Phys. Rev. D* 79 (2009), p. 024003. DOI: 10.1103/PhysRevD.79.024003. arXiv: 0810.1767 [gr-qc].

[96] Bela Szilagyi, Lee Lindblom, and Mark A. Scheel. "Simulations of Binary Black Hole Mergers Using Spectral Methods". In: *Phys. Rev. D* 80 (2009), p. 124010. DOI: 10.1103/PhysRevD.80.124010. arXiv: 0909.3557 [gr-qc].

[97] Daniel A. Hemberger et al. "Dynamical Excision Boundaries in Spectral Evolutions of Binary Black Hole Spacetimes". In: *Class. Quant. Grav.* 30 (2013), p. 115001. DOI: 10.1088/0264-9381/30/11/115001. arXiv: 1211.6079 [gr-qc].

[98] Serguei Ossokine, Lawrence E. Kidder, and Harald P. Pfeiffer. "Precession-tracking coordinates for simulations of compact-object-binaries". In: *Phys. Rev. D* 88 (2013), p. 084031. DOI: 10.1103/PhysRevD.88.084031. arXiv: 1304.3067 [gr-qc].

[99] https://www.black-holes.org/SpEC.html.

[100] Alessandro Nagar, Thibault Damour, and Angelo Tartaglia. "Binary black hole merger in the extreme mass ratio limit". In: *Class. Quant. Grav.* 24 (2007). Ed. by Manuela Campanelli and Luciano Rezzolla, S109–S124. DOI: 10.1088/0264-9381/24/12/S08. arXiv: gr-qc/0612096.

[101] Simone Albanesi, Alessandro Nagar, and Sebastiano Bernuzzi. "Effective one-body model for extreme-mass-ratio spinning binaries on eccentric equatorial orbits: Testing radiation reaction and waveform". In: *Phys. Rev. D* 104.2 (2021), p. 024067. DOI: 10.1103/PhysRevD.104.024067. arXiv: 2104.10559 [gr-qc].

[102] Scott A. Hughes et al. "Adiabatic waveforms for extreme mass-ratio inspirals via multivoice decomposition in time and frequency". In: *Phys. Rev. D* 103.10 (2021). [Erratum: Phys.Rev.D 107, 089901 (2023)], p. 104014. DOI: 10.1103/PhysRevD.103.104014. arXiv: 2102.02713 [gr-qc].

[103] Alessandro Nagar et al. "Numerical-relativity validation of effective-one-body waveforms in the intermediate-mass-ratio regime". In: *Phys. Rev. D* 105.12 (2022), p. 124061. DOI: 10.1103/PhysRevD.105.124061. arXiv: 2202.05643 [gr-qc].

[104] E. W. Leaver. "An Analytic representation for the quasi normal modes of Kerr black holes". In: *Proc. Roy. Soc. Lond. A* 402 (1985), pp. 285–298. DOI: 10.1098/rspa.1985.0119.

[105] E. W. Leaver. "Solutions to a generalized spheroidal wave equation: Teukolsky's equations in general relativity, and the two-center problem in molecular quantum mechanics". In: *J. Math. Phys.* 27.5 (1986), p. 1238. DOI: 10.1063/1.527130.

[106] Hideki Asada and Toshifumi Futamase. "Propagation of gravitational waves from slow motion sources in Coulomb type potential". In: *Phys. Rev. D* 56 (1997), R6062–R6066. DOI: 10.1103/PhysRevD.56.R6062. arXiv: gr-qc/9711009.

[107] Leor Barack. "Late time dynamics of scalar perturbations outside black holes. 1. A Shell toy model". In: *Phys. Rev. D* 59 (1999), p. 044016. DOI: 10.1103/PhysRevD.59.044016. arXiv: gr-qc/9811027.

[108] Emanuele Berti et al. "Black hole spectroscopy: from theory to experiment". In: (May 2025). arXiv: 2505.23895 [gr-qc].

[109] Jon Mathews. "Gravitational Multipole Radiation". In: *Journal of the Society for Industrial and Applied Mathematics* 10.4 (1962), pp. 768–780. ISSN: 03684245. URL: http://www.jstor.org/stable/2098922 (visited on 04/01/2025).

[110] Frank J. Zerilli. "Tensor Harmonics in Canonical Form for Gravitational Radiation and Other Applications". In: *Journal of Mathematical Physics* 11 (1970), pp. 2203–2208. URL: https://api.semanticscholar.org/CorpusID:122923687.

[111] Charles W. Misner, K. S. Thorne, and J. A. Wheeler. *Gravitation*. San Francisco: W. H. Freeman, 1973. ISBN: 978-0-7167-0344-0, 978-0-691-17779-3.

[112] L. D. Landau and E. M. Lifschits. *The Classical Theory of Fields*. Vol. Volume 2. Course of Theoretical Physics. Oxford: Pergamon Press, 1975. ISBN: 978-0-08-018176-9.

[113] Subrahmanyan Chandrasekhar. *The mathematical theory of black holes*. 1985. ISBN: 978-0-19-850370-5.

[114] Walter Gautschi. "Computational Aspects of Three-Term Recurrence Relations". In: *SIAM Review* 9.1 (1967), pp. 24–82. ISSN: 00361445. URL: http://www.jstor.org/stable/2027410 (visited on 04/27/2025).

[115] M. Abramowitz and I.A. Stegun. *Handbook of mathematical functions with formulas, graphs, and mathematical tables*. New York: Dover, 1964.

[116] Valeria Ferrari and Bahram Mashhoon. "Oscillations of a Black Hole". In: *Phys. Rev. Lett.* 52.16 (1984), p. 1361. DOI: 10.1103/PhysRevLett.52.1361.

[117] Valeria Ferrari and Bahram Mashhoon. "New approach to the quasinormal modes of a black hole". In: *Phys. Rev. D* 30 (1984), pp. 295–304. DOI: 10.1103/PhysRevD.30.295.

[118] Y. Sun and R. H. Price. "Excitation of Quasinormal Ringing of a Schwarzschild Black Hole". In: *Phys. Rev. D* 38 (1988), pp. 1040–1052. DOI: 10.1103/PhysRevD.38.1040.

[119] Emanuele Berti and Vitor Cardoso. "Quasinormal ringing of Kerr black holes. I. The Excitation factors". In: *Phys. Rev. D* 74 (2006), p. 104020. DOI: 10.1103/PhysRevD.74.104020. arXiv: gr-qc/0605118.

[120] Lam Hui, Daniel Kabat, and Sam S. C. Wong. "Quasinormal modes, echoes and the causal structure of the Green's function". In: *JCAP* 12 (2019), p. 020. DOI: 10.1088/1475-7516/2019/12/020. arXiv: 1909.10382 [gr-qc].

[121] Richard H. Price. "Nonspherical Perturbations of Relativistic Gravitational Collapse. I. Scalar and Gravitational Perturbations". In: *Phys. Rev. D* 5 (10 1972), pp. 2419–2438. DOI: 10.1103/PhysRevD.5.2419. URL: https://link.aps.org/doi/10.1103/PhysRevD.5.2419.

[122] Carsten Gundlach, Richard H. Price, and Jorge Pullin. "Late time behavior of stellar collapse and explosions: 1. Linearized perturbations". In: *Phys. Rev. D* 49 (1994), pp. 883–889. DOI: 10.1103/PhysRevD.49.883. arXiv: gr-qc/9307009.

[123] Carsten Gundlach, Richard H. Price, and Jorge Pullin. "Late time behavior of stellar collapse and explosions: 2. Nonlinear evolution". In: *Phys. Rev. D* 49 (1994), pp. 890–899. DOI: 10.1103/PhysRevD.49.890. arXiv: gr-qc/9307010.

[124] Lior M. Burko and Amos Ori. "Late time evolution of nonlinear gravitational collapse". In: *Phys. Rev. D* 56 (1997), pp. 7820–7832. DOI: 10.1103/PhysRevD.56.7820. arXiv: gr-qc/9703067.

[125] Anil Zenginoglu. "A Hyperboloidal study of tail decay rates for scalar and Yang-Mills fields". In: *Class. Quant. Grav.* 25 (2008), p. 175013. DOI: 10.1088/0264-9381/25/17/175013. arXiv: 0803.2018 [gr-qc].

[126] Anil Zenginoglu. "Asymptotics of black hole perturbations". In: *Class. Quant. Grav.* 27 (2010), p. 045015. DOI: 10.1088/0264-9381/27/4/045015. arXiv: 0911.2450 [gr-qc].

[127] Richard H. Price and Lior M. Burko. "Late time tails from momentarily stationary, compact initial data in Schwarzschild spacetimes". In: *Phys. Rev. D* 70 (2004), p. 084039. DOI: 10.1103/PhysRevD.70.084039. arXiv: gr-qc/0408077.

[128] Romeo Felice Rosato and Paolo Pani. "On the universality of late-time ringdown tail". In: (May 2025). arXiv: 2505.08877 [gr-qc].

[129] E. S. C. Ching et al. "Late time tail of wave propagation on curved space-time". In: *Phys. Rev. Lett.* 74 (1995), pp. 2414–2417. DOI: 10.1103/PhysRevLett.74.2414. arXiv: gr-qc/9410044.

[130] E. S. C. Ching et al. "Wave propagation in gravitational systems: Late time behavior". In: *Phys. Rev. D* 52 (1995), pp. 2118–2132. DOI: 10.1103/PhysRevD.52.2118. arXiv: gr-qc/9507035.

[131] Shahar Hod. "How pure is the tail of gravitational collapse?" In: *Class. Quant. Grav.* 26 (2009), p. 028001. DOI: 10.1088/0264-9381/26/2/028001. arXiv: 0902.0237 [gr-qc].

[132] Luc Blanchet and Thibault Damour. "Tail Transported Temporal Correlations in the Dynamics of a Gravitating System". In: *Phys. Rev. D* 37 (1988), p. 1410. DOI: 10.1103/PhysRevD.37.1410.

[133] Thibault Damour, Bala R. Iyer, and B. S. Sathyaprakash. "Improved filters for gravitational waves from inspiralling compact binaries". In: *Phys. Rev. D* 57 (1998), pp. 885–907. DOI: 10.1103/PhysRevD.57.885. arXiv: gr-qc/9708034.

[134] Eric Poisson and Clifford M. Will. *Gravity: Newtonian, Post-Newtonian, Relativistic*. Cambridge University Press, 2014.

[135] Thibault Damour and Nathalie Deruelle. "Radiation Reaction and Angular Momentum Loss in Small Angle Gravitational Scattering". In: *Phys. Lett. A* 87 (1981), p. 81. DOI: 10.1016/0375-9601(81)90567-3.

[136] Bala R. Iyer and C. M. Will. "PostNewtonian gravitational radiation reaction for two-body systems". In: *Phys. Rev. Lett.* 70 (1993), pp. 113–116. DOI: 10.1103/PhysRevLett.70.113.

[137] Bala R. Iyer and C. M. Will. "PostNewtonian gravitational radiation reaction for two-body systems: Nonspinning bodies". In: *Phys. Rev. D* 52 (1995), pp. 6882–6893. DOI: 10.1103/PhysRevD.52.6882.

[138] Eric Poisson and Misao Sasaki. "Gravitational radiation from a particle in circular orbit around a black hole. 5: Black hole absorption and tail corrections". In: *Phys. Rev. D* 51 (1995), pp. 5753–5767. DOI: 10.1103/PhysRevD.51.5753. arXiv: gr-qc/9412027.

[139] Hideyuki Tagoshi, Shuhei Mano, and Eiichi Takasugi. "PostNewtonian expansion of gravitational waves from a particle in circular orbits around a rotating black hole: Effects of black hole absorption". In: *Prog. Theor. Phys.* 98 (1997), pp. 829–850. DOI: 10.1143/PTP.98.829. arXiv: gr-qc/9711072.

[140] Kashif Alvi. "Energy and angular momentum flow into a black hole in a binary". In: *Phys. Rev. D* 64 (2001), p. 104020. DOI: 10.1103/PhysRevD.64.104020. arXiv: gr-qc/0107080.

[141] J. L. Anderson et al. "DIVERGENT INTEGRALS OF POSTNEWTONIAN GRAVITY: NONANALYTIC TERMS IN THE NEAR ZONE EXPANSION OF A GRAVITATIONALLY RADIATING SYSTEM FOUND BY MATCHING". In: *Phys. Rev. D* 25 (1982), pp. 2038–2048. DOI: 10.1103/PhysRevD.25.2038.

[142] T. Apostolatos et al. "Gravitational radiation from a particle in circular orbit around a black hole. 3: Stability of circular orbits under radiation reaction". In: *Phys. Rev. D* 47 (1993), pp. 5376–5388. DOI: 10.1103/PhysRevD.47.5376.

[143] C. Cutler, D. Kennefick, and Eric Poisson. "Gravitational radiation reaction for bound motion around a Schwarzschild black hole". In: *Phys. Rev. D* 50 (1994), pp. 3816–3835. DOI: 10.1103/PhysRevD.50.3816.

[144] Amos Ori. "Radiative evolution of orbits around a Kerr black hole". In: *Phys. Lett. A* 202 (1995), pp. 347–351. DOI: 10.1016/0375-9601(95)00333-X. arXiv: gr-qc/9507048.

[145] Amos Ori. "Radiative evolution of the Carter constant for generic orbits around a Kerr black hole". In: *Phys. Rev. D* 55 (1997), pp. 3444–3456. DOI: 10.1103/PhysRevD.55.3444.

[146] Leor Barack and Amos Ori. "Mode sum regularization approach for the selfforce in black hole space-time". In: *Phys. Rev. D* 61 (2000), p. 061502. DOI: 10.1103/PhysRevD.61.061502. arXiv: gr-qc/9912010.

[147] Danilo Chiaramello and Alessandro Nagar. "Faithful analytical effective-one-body waveform model for spin-aligned, moderately eccentric, coalescing black hole binaries". In: *Phys. Rev. D* 101.10 (2020), p. 101501. DOI: 10.1103/PhysRevD.101.101501. arXiv: 2001.11736 [gr-qc].

[148] C. Cutler et al. "Gravitational radiation from a particle in circular orbit around a black hole. 2: Numerical results for the nonrotating case". In: *Phys. Rev. D* 47 (1993), pp. 1511–1518. DOI: 10.1103/PhysRevD.47.1511.

[149] Eric Poisson. "Gravitational radiation from a particle in circular orbit around a black hole. 6. Accuracy of the postNewtonian expansion". In: *Phys. Rev. D* 52 (1995). [Addendum: Phys.Rev.D 55, 7980–7981 (1997)], pp. 5719–5723. DOI: 10.1103/PhysRevD.52.5719. arXiv: gr-qc/9505030.

[150] Thibault Damour and Alessandro Nagar. "Comparing Effective-One-Body gravitational waveforms to accurate numerical data". In: *Phys. Rev. D* 77 (2008), p. 024043. DOI: 10.1103/PhysRevD.77.024043. arXiv: 0711.2628 [gr-qc].

[151] Thibault Damour, Bala R. Iyer, and Alessandro Nagar. "Improved resummation of post-Newtonian multipolar waveforms from circularized compact binaries". In: *Phys. Rev. D* 79 (2009), p. 064004. DOI: 10.1103/PhysRevD.79.064004. arXiv: 0811.2069 [gr-qc].

[152] Donato Bini and Thibault Damour. "Gravitational radiation reaction along general orbits in the effective one-body formalism". In: *Phys. Rev. D* 86 (2012), p. 124012. DOI: 10.1103/PhysRevD.86.124012. arXiv: 1210.2834 [gr-qc].

[153] John G. Baker et al. "Gravitational wave extraction from an inspiraling configuration of merging black holes". In: *Phys. Rev. Lett.* 96 (2006), p. 111102. DOI: 10.1103/PhysRevLett.96.111102. arXiv: gr-qc/0511103.

[154] Manuela Campanelli et al. "Accurate evolutions of orbiting black-hole binaries without excision". In: *Phys. Rev. Lett.* 96 (2006), p. 111101. DOI: 10.1103/PhysRevLett.96.111101. arXiv: gr-qc/0511048.

[155] Frans Pretorius. "Evolution of binary black hole spacetimes". In: *Phys. Rev. Lett.* 95 (2005), p. 121101. DOI: 10.1103/PhysRevLett.95.121101. arXiv: gr-qc/0507014.

[156] The SXS Collaboration. *SXS Gravitational Waveform Database*. 2019. URL: http://www.black-holes.org/waveforms/.

[157] Manuela Campanelli et al. *CCRG@RIT Catalog of Numerical Simulations*. 2022. URL: http://ccrg.rit.edu/~RITCatalog/.

[158] Karan Jani et al. *Georgia Tech catalog of binary black hole simulations*. 2016. URL: http://www.einstein.gatech.edu/catalog/.

[159] Eleanor Hamilton et al. “Catalog of precessing black-hole-binary numerical-relativity simulations”. In: *Phys. Rev. D* 109.4 (2024), p. 044032. DOI: 10.1103/PhysRevD.109.044032. arXiv: 2303.05419 [gr-qc].

[160] Roman Gold and Bernd Brügmann. “Eccentric black hole mergers and zoom-whirl behavior from elliptic inspirals to hyperbolic encounters”. In: *Phys. Rev. D* 88.6 (2013), p. 064051. DOI: 10.1103/PhysRevD.88.064051. arXiv: 1209.4085 [gr-qc].

[161] James Healy and Carlos O. Lousto. “Fourth RIT binary black hole simulations catalog: Extension to eccentric orbits”. In: *Phys. Rev. D* 105.12 (2022), p. 124010. DOI: 10.1103/PhysRevD.105.124010. arXiv: 2202.00018 [gr-qc].

[162] Tomas Andrade et al. “Toward numerical-relativity informed effective-one-body waveforms for dynamical capture black hole binaries”. In: *Phys. Rev. D* 109.8 (2024), p. 084025. DOI: 10.1103/PhysRevD.109.084025. arXiv: 2307.08697 [gr-qc].

[163] Simone Albanesi et al. “Scattering and dynamical capture of two black holes: Synergies between numerical and analytical methods”. In: *Phys. Rev. D* 111.2 (2025), p. 024069. DOI: 10.1103/PhysRevD.111.024069. arXiv: 2405.20398 [gr-qc].

[164] Gabriele Bozzola and Vasileios Paschalidis. “Initial data for general relativistic simulations of multiple electrically charged black holes with linear and angular momenta”. In: *Phys. Rev. D* 99.10 (2019), p. 104044. DOI: 10.1103/PhysRevD.99.104044. arXiv: 1903.01036 [gr-qc].

[165] Gabriele Bozzola and Vasileios Paschalidis. “Numerical-relativity simulations of the quasicircular inspiral and merger of nonspinning, charged black holes: Methods and comparison with approximate approaches”. In: *Phys. Rev. D* 104.4 (2021), p. 044004. DOI: 10.1103/PhysRevD.104.044004. arXiv: 2104.06978 [gr-qc].

[166] Helvi Witek et al. “Black holes and binary mergers in scalar Gauss-Bonnet gravity: scalar field dynamics”. In: *Phys. Rev. D* 99.6 (2019), p. 064035. DOI: 10.1103/PhysRevD.99.064035. arXiv: 1810.05177 [gr-qc].

[167] Maria Okounkova. “Numerical relativity simulation of GW150914 in Einstein dilaton Gauss-Bonnet gravity”. In: *Phys. Rev. D* 102.8 (2020), p. 084046. DOI: 10.1103/PhysRevD.102.084046. arXiv: 2001.03571 [gr-qc].

[168] Maria Okounkova et al. “Numerical binary black hole collisions in dynamical Chern-Simons gravity”. In: *Phys. Rev. D* 100.10 (2019), p. 104026. DOI: 10.1103/PhysRevD.100.104026. arXiv: 1906.08789 [gr-qc].

[169] William E. East and Justin L. Ripley. “Dynamics of Spontaneous Black Hole Scalarization and Mergers in Einstein-Scalar-Gauss-Bonnet Gravity”. In: *Phys. Rev. Lett.* 127.10 (2021), p. 101102. DOI: 10.1103/PhysRevLett.127.101102. arXiv: 2105.08571 [gr-qc].

[170] Maxence Corman, Justin L. Ripley, and William E. East. “Nonlinear studies of binary black hole mergers in Einstein-scalar-Gauss-Bonnet gravity”. In: *Phys. Rev. D* 107.2 (2023), p. 024014. DOI: 10.1103/PhysRevD.107.024014. arXiv: 2210.09235 [gr-qc].

[171] Justin L. Ripley. "Numerical relativity for Horndeski gravity". In: *Int. J. Mod. Phys. D* 31.13 (2022), p. 2230017. DOI: 10.1142/S0218271822300178. arXiv: 2207.13074 [gr-qc].

[172] Tamara Evstafyeva, Michalis Agathos, and Justin L. Ripley. "Measuring the ringdown scalar polarization of gravitational waves in Einstein-scalar-Gauss-Bonnet gravity". In: *Phys. Rev. D* 107.12 (2023), p. 124010. DOI: 10.1103/PhysRevD.107.124010. arXiv: 2212.11359 [gr-qc].

[173] Llibert Aresté Saló, Katy Clough, and Pau Figueras. "Well-Posedness of the Four-Derivative Scalar-Tensor Theory of Gravity in Singularity Avoiding Coordinates". In: *Phys. Rev. Lett.* 129.26 (2022), p. 261104. DOI: 10.1103/PhysRevLett.129.261104. arXiv: 2208.14470 [gr-qc].

[174] Llibert Aresté Saló, Katy Clough, and Pau Figueras. "Puncture gauge formulation for Einstein-Gauss-Bonnet gravity and four-derivative scalar-tensor theories in d+1 spacetime dimensions". In: *Phys. Rev. D* 108.8 (2023), p. 084018. DOI: 10.1103/PhysRevD.108.084018. arXiv: 2306.14966 [gr-qc].

[175] Ramiro Cayuso et al. "Modelling self-consistently beyond General Relativity". In: *Phys. Rev. Lett.* 131 (Mar. 2023), p. 111403. arXiv: 2303.07246 [gr-qc].

[176] Nils Deppe et al. *SpECTRE v2024.09.29*. 10.5281/zenodo.13858965. Version 2024.09.29. Sept. 2024. DOI: 10.5281/zenodo.13858965. URL: https://spectre-code.org.

[177] Emanuele Berti et al. "Inspiral, merger and ringdown of unequal mass black hole binaries: A Multipolar analysis". In: *Phys. Rev. D* 76 (2007), p. 064034. DOI: 10.1103/PhysRevD.76.064034. arXiv: gr-qc/0703053.

[178] Sizheng Ma and Huan Yang. "Excitation of quadratic quasinormal modes for Kerr black holes". In: *Phys. Rev. D* 109.10 (2024), p. 104070. DOI: 10.1103/PhysRevD.109.104070. arXiv: 2401.15516 [gr-qc].

[179] John G. Baker et al. "Mergers of non-spinning black-hole binaries: Gravitational radiation characteristics". In: *Phys. Rev. D* 78 (2008), p. 044046. DOI: 10.1103/PhysRevD.78.044046. arXiv: 0805.1428 [gr-qc].

[180] Saul A. Teukolsky. "Perturbations of a rotating black hole. 1. Fundamental equations for gravitational electromagnetic and neutrino field perturbations". In: *Astrophys. J.* 185 (1973), pp. 635–647. DOI: 10.1086/152444.

[181] Emanuele Berti, Vitor Cardoso, and Marc Casals. "Eigenvalues and eigenfunctions of spin-weighted spheroidal harmonics in four and higher dimensions". In: *Phys. Rev. D* 73 (2006). [Erratum: Phys.Rev.D 73, 109902 (2006)], p. 024013. DOI: 10.1103/PhysRevD.73.109902. arXiv: gr-qc/0511111.

[182] Bernard J. Kelly and John G. Baker. "Decoding mode mixing in black-hole merger ringdown". In: *Phys. Rev. D* 87.8 (2013), p. 084004. DOI: 10.1103/PhysRevD.87.084004. arXiv: 1212.5553 [gr-qc].

[183] Emanuele Berti and Antoine Klein. "Mixing of spherical and spheroidal modes in perturbed Kerr black holes". In: *Phys. Rev. D* 90.6 (2014), p. 064012. DOI: 10.1103/PhysRevD.90.064012. arXiv: 1408.1860 [gr-qc].

[184] William H. Press and Saul A. Teukolsky. "Perturbations of a Rotating Black Hole. II. Dynamical Stability of the Kerr Metric". In: *Astrophys. J.* 185 (1973), pp. 649–674. DOI: 10.1086/152445.

[185] Luc Blanchet. "Post-Newtonian Theory for Gravitational Waves". In: *Living Rev. Rel.* 17 (2014), p. 2. DOI: 10.12942/lrr-2014-2. arXiv: 1310.1528 [gr-qc].

[186] Yi Pan et al. "Post-Newtonian factorized multipolar waveforms for spinning, non-precessing black-hole binaries". In: *Phys. Rev. D* 83 (2011). [Erratum: Phys.Rev.D 87, 109901 (2013)], p. 064003. DOI: 10.1103/PhysRevD.83.064003. arXiv: 1006.0431 [gr-qc].

[187] Luc Blanchet et al. "The Third post-Newtonian gravitational wave polarisations and associated spherical harmonic modes for inspiralling compact binaries in quasi-circular orbits". In: *Class. Quant. Grav.* 25 (2008). [Erratum: Class.Quant.Grav. 29, 239501 (2012)], p. 165003. DOI: 10.1088/0264-9381/25/16/165003. arXiv: 0802.1249 [gr-qc].

[188] Peter James Nee, Sebastian H. Völkel, and Harald P. Pfeiffer. "Role of black hole quasinormal mode overtones for ringdown analysis". In: *Phys. Rev. D* 108.4 (2023), p. 044032. DOI: 10.1103/PhysRevD.108.044032. arXiv: 2302.06634 [gr-qc].

[189] Thibault Damour et al. "Accurate Effective-One-Body waveforms of inspiralling and coalescing black-hole binaries". In: *Phys. Rev. D* 78 (2008), p. 044039. DOI: 10.1103/PhysRevD.78.044039. arXiv: 0803.3162 [gr-qc].

[190] Alessandra Buonanno et al. "Effective-one-body waveforms calibrated to numerical relativity simulations: Coalescence of non-spinning, equal-mass black holes". In: *Phys. Rev. D* 79 (2009), p. 124028. DOI: 10.1103/PhysRevD.79.124028. arXiv: 0902.0790 [gr-qc].

[191] Yi Pan et al. "Inspiral-merger-ringdown multipolar waveforms of nonspinning black-hole binaries using the effective-one-body formalism". In: *Phys. Rev. D* 84 (2011), p. 124052. DOI: 10.1103/PhysRevD.84.124052. arXiv: 1106.1021 [gr-qc].

[192] D. S. Sivia and J. Skilling. *Data Analysis - A Bayesian Tutorial*. 2nd. Oxford Science Publications. Oxford University Press, 2006.

[193] Gregorio Carullo, Marina De Amicis, and Jaime Redondo-Yuste. *bayRing*. github.com/GCArullo/bayRing. Version 1.0.0. Aug. 2023. DOI: 10.5281/zenodo.8284026. URL: https://doi.org/10.5281/zenodo.8284026.

[194] Walter Del Pozzo and John Veitch. *CPNest: an efficient python parallelizable nested sampling algorithm*. https://github.com/johnveitch/cpnest. 2015.

[195] Frank Loffler et al. "The Einstein Toolkit: A Community Computational Infrastructure for Relativistic Astrophysics". In: *Class. Quant. Grav.* 29 (2012), p. 115001. DOI: 10.1088/0264-9381/29/11/115001. arXiv: 1111.3344 [gr-qc].

[196] Oscar J. C. Dias et al. “Eigenvalue repulsions in the quasinormal spectra of the Kerr-Newman black hole”. In: *Phys. Rev. D* 105.8 (2022), p. 084044. DOI: 10.1103/PhysRevD.105.084044. arXiv: 2109.13949 [gr-qc].

[197] Vitor Cardoso et al. “Black holes and gravitational waves in models of minicharged dark matter”. In: *JCAP* 05 (2016). [Erratum: JCAP 04, E01 (2020)], p. 054. DOI: 10.1088/1475-7516/2016/05/054. arXiv: 1604.07845 [hep-ph].

[198] Luc Blanchet and Thibault Damour. “Hereditary effects in gravitational radiation”. In: *Phys. Rev. D* 46 (1992), pp. 4304–4319. DOI: 10.1103/PhysRevD.46.4304.

[199] L. Blanchet and Gerhard Schaefer. “Gravitational wave tails and binary star systems”. In: *Class. Quant. Grav.* 10 (1993), pp. 2699–2721. DOI: 10.1088/0264-9381/10/12/026.

[200] Luc Blanchet and B. S. Sathyaprakash. “Detecting the tail effect in gravitational wave experiments”. In: *Phys. Rev. Lett.* 74 (1995), pp. 1067–1070. DOI: 10.1103/PhysRevLett.74.1067.

[201] Eric Poisson. “Gravitational radiation from a particle in circular orbit around a black hole. 1: Analytical results for the nonrotating case”. In: *Phys. Rev. D* 47 (1993), pp. 1497–1510. DOI: 10.1103/PhysRevD.47.1497.

[202] Frank J. Zerilli. “Effective potential for even parity Regge-Wheeler gravitational perturbation equations”. In: *Phys. Rev. Lett.* 24 (1970), pp. 737–738. DOI: 10.1103/PhysRevLett.24.737.

[203] Gregorio Carullo et al. “Unveiling the Merger Structure of Black Hole Binaries in Generic Planar Orbits”. In: *Phys. Rev. Lett.* 132.10 (2024), p. 101401. DOI: 10.1103/PhysRevLett.132.101401. arXiv: 2309.07228 [gr-qc].

[204] Alessandro Nagar et al. “Effective-one-body waveforms from dynamical captures in black hole binaries”. In: *Phys. Rev. D* 103.6 (2021), p. 064013. DOI: 10.1103/PhysRevD.103.064013. arXiv: 2009.12857 [gr-qc].

[205] Paul Virtanen *et al* (Contributors). “SciPy 1.0: Fundamental Algorithms for Scientific Computing in Python”. In: *Nature Methods* (2020).

[206] Gregorio Carullo and Marina De Amicis. “Late-time tails in nonlinear evolutions of merging black hole binaries”. In: (Oct. 2023). arXiv: 2310.12968 [gr-qc].

[207] Sebastiano Bernuzzi, Alessandro Nagar, and Anil Zenginoglu. “Horizon-absorption effects in coalescing black-hole binaries: An effective-one-body study of the non-spinning case”. In: *Phys. Rev. D* 86 (2012), p. 104038. DOI: 10.1103/PhysRevD.86.104038. arXiv: 1207.0769 [gr-qc].

[208] Arnab Priya Saha, Biswajit Sahoo, and Ashoke Sen. “Proof of the classical soft graviton theorem in $D = 4$”. In: *JHEP* 06 (2020), p. 153. DOI: 10.1007/JHEP06(2020)153. arXiv: 1912.06413 [hep-th].

[209] Biswajit Sahoo and Ashoke Sen. “Classical soft graviton theorem rewritten”. In: *JHEP* 01 (2022), p. 077. DOI: 10.1007/JHEP01(2022)077. arXiv: 2105.08739 [hep-th].

[210] Andrea Placidi et al. “Exploiting Newton-factorized, 2PN-accurate waveform multipoles in effective-one-body models for spin-aligned noncircularized binaries”. In: *Phys. Rev. D* 105.10 (2022), p. 104030. DOI: 10.1103/PhysRevD.105.104030. arXiv: 2112.05448 [gr-qc].

[211] Simone Albanesi. “Real modes and null memory contributions in effective-one-body models”. In: (Nov. 2024). arXiv: 2411.04024 [gr-qc].

[212] Keefe Mitman et al. “A Review of Gravitational Memory and BMS Frame Fixing in Numerical Relativity”. In: (May 2024). arXiv: 2405.08868 [gr-qc].

[213] Tousif Islam et al. “Phenomenology and origin of late-time tails in eccentric binary black hole mergers”. In: (July 2024). arXiv: 2407.04682 [gr-qc].

[214] Enno Harms, Sebastiano Bernuzzi, and Bernd Brügmann. “Numerical solution of the 2+1 Teukolsky equation on a hyperboloidal and horizon penetrating foliation of Kerr and application to late-time decays”. In: *Class. Quant. Grav.* 30 (2013), p. 115013. DOI: 10.1088/0264-9381/30/11/115013. arXiv: 1301.1591 [gr-qc].

[215] Elspeth W. Allen et al. “Radiation tails and boundary conditions for black hole evolutions”. In: *Phys. Rev. D* 70 (2004), p. 044038. DOI: 10.1103/PhysRevD.70.044038. arXiv: gr-qc/0401092.

[216] Mihalis Dafermos and Igor Rodnianski. “A Note on boundary value problems for black hole evolutions”. In: (Mar. 2004). arXiv: gr-qc/0403034.

[217] Leonardo Gualtieri et al. “Transformation of the multipolar components of gravitational radiation under rotations and boosts”. In: *Phys. Rev. D* 78 (2008), p. 044024. DOI: 10.1103/PhysRevD.78.044024. arXiv: 0805.1017 [gr-qc].

[218] Demetrios Christodoulou and Remo Ruffini. “Reversible Transformations of a Charged Black Hole”. In: *Phys. Rev. D* 4 (12 1971), pp. 3552–3555. DOI: 10.1103/PhysRevD.4.3552. URL: https://link.aps.org/doi/10.1103/PhysRevD.4.3552.

[219] Abdul H. Mroué et al. “Catalog of 174 Binary Black Hole Simulations for Gravitational Wave Astronomy”. In: *Phys. Rev. Lett.* 111 (24 2013), p. 241104. DOI: 10.1103/PhysRevLett.111.241104. arXiv: gr-qc/0512093 [gr-qc]. URL: https://link.aps.org/doi/10.1103/PhysRevLett.111.241104.

[220] Michael Boyle et al. “The SXS Collaboration catalog of binary black hole simulations”. In: *Class. Quant. Grav.* 36.19 (2019), p. 195006. DOI: 10.1088/1361-6382/ab34e2. arXiv: 1904.04831 [gr-qc].

[221] Geoffrey Lovelace et al. “Binary-black-hole initial data with nearly-extremal spins”. In: *Phys. Rev. D* 78 (2008), p. 084017. DOI: 10.1103/PhysRevD.78.084017. arXiv: 0805.4192 [gr-qc].

[222] Luisa T. Buchman et al. “Simulations of non-equal mass black hole binaries with spectral methods”. In: *Phys. Rev.* D86 (2012), p. 084033. DOI: 10.1103/PhysRevD.86.084033. arXiv: 1206.3015 [gr-qc].

[223] Gregory B. Cook and Harald P. Pfeiffer. "Excision boundary conditions for black hole initial data". In: *Phys. Rev.* D70 (2004), p. 104016. DOI: 10.1103/PhysRevD.70.104016. arXiv: gr-qc/0407078 [gr-qc].

[224] Harald P. Pfeiffer et al. "A Multidomain spectral method for solving elliptic equations". In: *Comput. Phys. Commun.* 152 (2003), pp. 253–273. DOI: 10.1016/S0010-4655(02)00847-0. arXiv: gr-qc/0202096.

[225] Harald P. Pfeiffer and James W. York. "Extrinsic curvature and the Einstein constraints". In: *Phys. Rev. D* 67 (4 2003), p. 044022. DOI: 10.1103/PhysRevD.67.044022. arXiv: gr-qc/0207095 [gr-qc]. URL: https://link.aps.org/doi/10.1103/PhysRevD.67.044022.

[226] Lee Lindblom et al. "A New generalized harmonic evolution system". In: *Class.Quant.Grav.* 23 (2006), S447–S462. DOI: 10.1088/0264-9381/23/16/S09. arXiv: gr-qc/0512093 [gr-qc].

[227] Lee Lindblom and Béla Szilágyi. "Improved gauge driver for the generalized harmonic Einstein system". In: *Physical Review D* 80.8 (Oct. 2009). ISSN: 1550-2368. DOI: 10.1103/physrevd.80.084019. arXiv: 0904.4873 [gr-qc]. URL: http://dx.doi.org/10.1103/PhysRevD.80.084019.

[228] O Rinne. "Stable radiation-controlling boundary conditions for the generalized harmonic Einstein equations". In: *Classical and Quantum Gravity* 23.22 (2006), p. 6275. DOI: 10.1088/0264-9381/23/22/013. arXiv: gr-qc/0606053 [gr-qc]. URL: https://dx.doi.org/10.1088/0264-9381/23/22/013.

[229] Oliver Rinne, Lee Lindblom, and Mark A Scheel. "Testing outer boundary treatments for the Einstein equations". In: *Classical and Quantum Gravity* 24.16 (2007), p. 4053. DOI: 10.1088/0264-9381/24/16/006. arXiv: 0704.0782 [gr-qc]. URL: https://dx.doi.org/10.1088/0264-9381/24/16/006.

[230] Anil Zenginoglu. "Hyperboloidal foliations and scri-fixing". In: *Class. Quant. Grav.* 25 (2008), p. 145002. DOI: 10.1088/0264-9381/25/14/145002. arXiv: 0712.4333 [gr-qc].

[231] Anil Zenginoglu. "Hyperboloidal layers for hyperbolic equations on unbounded domains". In: *J. Comput. Phys.* 230 (2011), pp. 2286–2302. DOI: 10.1016/j.jcp.2010.12.016. arXiv: 1008.3809 [math.NA].

[232] Dante A. B. Iozzo et al. "Extending gravitational wave extraction using Weyl characteristic fields". In: *Phys. Rev. D* 103 (2 2021), p. 024039. DOI: 10.1103/PhysRevD.103.024039. arXiv: 2010.15200 [gr-qc]. URL: https://link.aps.org/doi/10.1103/PhysRevD.103.024039.

[233] Mike Boyle, Dante Iozzo, and Leo C. Stein. *moble/scri: v1.2*. 10.5281/zenodo.4041972. Version v1.2. Sept. 2020. DOI: 10.5281/zenodo.4041972. URL: https://doi.org/10.5281/zenodo.4041972.

[234] *The Scri package*. https://github.com/sxs-collaboration/scri.

[235] Michael Boyle. "Angular velocity of gravitational radiation from precessing binaries and the corotating frame". In: *Phys. Rev. D* 87 (10 Sept. 2013), p. 104006. DOI: 10.1103/PhysRevD.87.104006. URL: http://link.aps.org/doi/10.1103/PhysRevD.87.104006.

[236] Michael Boyle et al. *Gravitational-wave modes from precessing black-hole binaries*. Sept. 2014. arXiv: 1409.4431 [gr-qc].

[237] Michael Boyle. "Transformations of asymptotic gravitational-wave data". In: *Phys. Rev. D* 93 (8 2016), p. 084031. DOI: 10.1103/PhysRevD.93.084031. URL: http://link.aps.org/doi/10.1103/PhysRevD.93.084031.

[238] SXS Collaboration. *Binary black-hole simulation SXS:BBH:3991*. https://data.caltech.edu/doi/10.26138/SXS:BBH:3991v3.0. Version v1. 2025. DOI: 10.26138/SXS:BBH:3991v3.0. URL: https://doi.org/10.26138/10.26138/SXS:BBH:3991v3.0.

[239] SXS Collaboration. *Binary black-hole simulation SXS:BBH:3997*. https://data.caltech.edu/doi/10.26138/SXS:BBH:3997v3.0. Version v1. 2025. DOI: 10.26138/SXS:BBH:3997v3.0. URL: https://doi.org/10.26138/10.26138/SXS:BBH:3997v3.0.

[240] SXS Collaboration. *Binary black-hole simulation SXS:BBH:3998*. https://data.caltech.edu/doi/10.26138/SXS:BBH:3998v3.0. Version v1. 2025. DOI: 10.26138/SXS:BBH:3998v3.0. URL: https://doi.org/10.26138/10.26138/SXS:BBH:3998v3.0.

[241] SXS Collaboration. *Binary black-hole simulation SXS:BBH:3994*. https://data.caltech.edu/doi/10.26138/SXS:BBH:3994v3.0. Version v1. 2025. DOI: 10.26138/SXS:BBH:3994v3.0. URL: https://doi.org/10.26138/10.26138/SXS:BBH:3994v3.0.

[242] SXS Collaboration. *Binary black-hole simulation SXS:BBH:3995*. https://data.caltech.edu/doi/10.26138/SXS:BBH:3995v3.0. Version v1. 2025. DOI: 10.26138/SXS:BBH:3995v3.0. URL: https://doi.org/10.26138/10.26138/SXS:BBH:3995v3.0.

[243] SXS Collaboration. *Binary black-hole simulation SXS:BBH:3996*. https://data.caltech.edu/doi/10.26138/SXS:BBH:3996v3.0. Version v1. 2025. DOI: 10.26138/SXS:BBH:3996v3.0. URL: https://doi.org/10.26138/10.26138/SXS:BBH:3996v3.0.

[244] SXS Collaboration. *Binary black-hole simulation SXS:BBH:3985*. https://data.caltech.edu/doi/10.26138/SXS:BBH:3985v3.0. Version v1. 2025. DOI: 10.26138/SXS:BBH:3985v3.0. URL: https://doi.org/10.26138/10.26138/SXS:BBH:3985v3.0.

[245] SXS Collaboration. *Binary black-hole simulation SXS:BBH:3986*. https://data.caltech.edu/doi/10.26138/SXS:BBH:3986v3.0. Version v1. 2025. DOI: 10.26138/SXS:BBH:3986v3.0. URL: https://doi.org/10.26138/10.26138/SXS:BBH:3986v3.0.

[246] SXS Collaboration. *Binary black-hole simulation SXS:BBH:3987*. https://data.caltech.edu/doi/10.26138/SXS:BBH:3987v3.0. Version v1. 2025. DOI: 10.26138/SXS:BBH:3987v3.0. URL: https://doi.org/10.26138/10.26138/SXS:BBH:3987v3.0.

[247] SXS Collaboration. *Binary black-hole simulation SXS:BBH:3988*. https://data.caltech.edu/doi/10.26138/SXS:BBH:3988v3.0. Version v1. 2025. DOI: 10.26138/SXS:BBH:3988v3.0. URL: https://doi.org/10.26138/10.26138/SXS:BBH:3988v3.0.

[248] SXS Collaboration. *Binary black-hole simulation SXS:BBH:3989*. https://data.caltech.edu/doi/10.26138/SXS:BBH:3989v3.0. Version v1. 2025. DOI: 10.26138/SXS:BBH:3989v3.0. URL: https://doi.org/10.26138/10.26138/SXS:BBH:3989v3.0.

[249] SXS Collaboration. *Binary black-hole simulation SXS:BBH:3990*. https://data.caltech.edu/doi/10.26138/SXS:BBH:3990v3.0. Version v1. 2025. DOI: 10.26138/SXS:BBH:3990v3.0. URL: https://doi.org/10.26138/10.26138/SXS:BBH:3990v3.0.

[250] SXS Collaboration. *Binary black-hole simulation SXS:BBH:3992*. https://data.caltech.edu/doi/10.26138/SXS:BBH:3992v3.0. Version v1. 2025. DOI: 10.26138/SXS:BBH:3992v3.0. URL: https://doi.org/10.26138/10.26138/SXS:BBH:3992v3.0.

[251] SXS Collaboration. *Binary black-hole simulation SXS:BBH:3993*. https://data.caltech.edu/doi/10.26138/SXS:BBH:3993v3.0. Version v1. 2025. DOI: 10.26138/SXS:BBH:3993v3.0. URL: https://doi.org/10.26138/10.26138/SXS:BBH:3993v3.0.

[252] Michael Boyle and Mark Scheel. *The sxs package*. github.com/sxs-collaboration/sxs/. Version v2025.0.9. Nov. 2025. DOI: 10.5281/zenodo.15232143. URL: https://doi.org/10.5281/zenodo.15232143.

[253] Abraham Savitzky and M. J. E. Golay. "Smoothing and Differentiation of Data by Simplified Least Squares Procedures". In: *Analytical Chemistry* 36.8 (1964), pp. 1627–1639. ISSN: 0003-2700. DOI: 10.1021/ac60214a047. URL: https://doi.org/10.1021/ac60214a047.

[254] Enrico Barausse et al. "Modeling multipolar gravitational-wave emission from small mass-ratio mergers". In: *Phys. Rev. D* 85 (2012), p. 024046. DOI: 10.1103/PhysRevD.85.024046. arXiv: 1110.3081 [gr-qc].

[255] Barry Wardell et al. "Gravitational Waveforms for Compact Binaries from Second-Order Self-Force Theory". In: *Phys. Rev. Lett.* 130.24 (2023), p. 241402. DOI: 10.1103/PhysRevLett.130.241402. arXiv: 2112.12265 [gr-qc].

[256] Tousif Islam and Gaurav Khanna. "Interplay between numerical relativity and perturbation theory: Finite size effects". In: *Phys. Rev. D* 108.4 (2023), p. 044012. DOI: 10.1103/PhysRevD.108.044012. arXiv: 2306.08767 [gr-qc].

[257] Hengrui Zhu et al. "Imprints of Changing Mass and Spin on Black Hole Ringdown". In: (Apr. 2024). arXiv: 2404.12424 [gr-qc].

[258] Jordan Moxon, Mark A. Scheel, and Saul A. Teukolsky. "Improved Cauchy-characteristic evolution system for high-precision numerical relativity waveforms". In: *Phys. Rev. D* 102.4 (2020), p. 044052. DOI: 10.1103/PhysRevD.102.044052. arXiv: 2007.01339 [gr-qc].

[259] Jordan Moxon et al. “SpECTRE Cauchy-characteristic evolution system for rapid, precise waveform extraction”. In: *Phys. Rev. D* 107.6 (2023), p. 064013. DOI: 10.1103/PhysRevD.107.064013. arXiv: 2110.08635 [gr-qc].

[260] Keefe Mitman et al. “Fixing the BMS frame of numerical relativity waveforms”. In: *Phys. Rev. D* 104.2 (2021), p. 024051. DOI: 10.1103/PhysRevD.104.024051. arXiv: 2105.02300 [gr-qc].

[261] Lorena Magaña Zertuche et al. “High precision ringdown modeling: Multimode fits and BMS frames”. In: *Phys. Rev. D* 105.10 (2022), p. 104015. DOI: 10.1103/PhysRevD.105.104015. arXiv: 2110.15922 [gr-qc].

[262] Keefe Mitman et al. “Fixing the BMS frame of numerical relativity waveforms with BMS charges”. In: *Phys. Rev. D* 106.8 (2022), p. 084029. DOI: 10.1103/PhysRevD.106.084029. arXiv: 2208.04356 [gr-qc].

[263] Jonathan Luk and Sung-Jin Oh. “Late time tail of waves on dynamic asymptotically flat spacetimes of odd space dimensions”. In: (Apr. 2024). arXiv: 2404.02220 [gr-qc].

[264] Nigel T. Bishop et al. “Cauchy characteristic matching”. In: *Black Holes, Gravitational Radiation and the Universe: Essays in Honor of C.V. Vishveshwara*. Ed. by Bala R. Iyer and B. Bhawal. Jan. 1998, pp. 383–408. DOI: 10.1007/978-94-017-0934-7_24. arXiv: gr-qc/9801070.

[265] Bela Szilagyi. “Cauchy characteristic matching in general relativity”. Other thesis. June 2000. arXiv: gr-qc/0006091.

[266] Sizheng Ma et al. “Fully relativistic three-dimensional Cauchy-characteristic matching for physical degrees of freedom”. In: *Phys. Rev. D* 109.12 (2024), p. 124027. DOI: 10.1103/PhysRevD.109.124027. arXiv: 2308.10361 [gr-qc].

[267] Alex Vañó-Viñuales, Sascha Husa, and David Hilditch. “Spherical symmetry as a test case for unconstrained hyperboloidal evolution”. In: *Class. Quant. Grav.* 32.17 (2015), p. 175010. DOI: 10.1088/0264-9381/32/17/175010. arXiv: 1412.3827 [gr-qc].

[268] Alex Vañó-Viñuales and Sascha Husa. “Spherical symmetry as a test case for unconstrained hyperboloidal evolution II: gauge conditions”. In: *Class. Quant. Grav.* 35.4 (2018), p. 045014. DOI: 10.1088/1361-6382/aaa4e2. arXiv: 1705.06298 [gr-qc].

[269] Alex Vañó-Viñuales. “Spherically symmetric black hole spacetimes on hyperboloidal slices”. In: *Frontiers in Applied Mathematics and Statistics* 9 (Aug. 2023), p. 1206017. ISSN: 2297-4687. DOI: 10.3389/fams.2023.1206017. arXiv: 2304.05384 [gr-qc]. URL: http://dx.doi.org/10.3389/fams.2023.1206017.

[270] Christian Peterson et al. “Spherical Evolution of the Generalized Harmonic Gauge Formulation of General Relativity on Compactified Hyperboloidal Slices”. In: (Sept. 2024). arXiv: 2409.02994 [gr-qc].

[271] Sizheng Ma et al. *Merging black holes with Cauchy-characteristic matching: Computation of late-time tails*. Dec. 2024. arXiv: 2412.06906 [gr-qc].

[272] B. Carter. “Axisymmetric Black Hole Has Only Two Degrees of Freedom”. In: *Phys. Rev. Lett.* 26 (1971), pp. 331–333. DOI: 10.1103/PhysRevLett.26.331.

[273] Richard H. Price, Sourabh Nampalliwar, and Gaurav Khanna. “Black hole binary inspiral: Analysis of the plunge”. In: *Phys. Rev. D* 93.4 (2016), p. 044060. DOI: 10.1103/PhysRevD.93.044060. arXiv: 1508.04797 [gr-qc].

[274] Richard H. Price and Jorge Pullin. “Colliding black holes: The Close limit”. In: *Phys. Rev. Lett.* 72 (1994), pp. 3297–3300. DOI: 10.1103/PhysRevLett.72.3297. arXiv: gr-qc/9402039.

[275] Jorge Pullin. “The Close limit of colliding black holes: An Update”. In: *Prog. Theor. Phys. Suppl.* 136 (1999). Ed. by T. Nakamura and H. Kodama, pp. 107–120. DOI: 10.1143/PTPS.136.107. arXiv: gr-qc/9909021.

[276] Zhongyang Zhang, Emanuele Berti, and Vitor Cardoso. “Quasinormal ringing of Kerr black holes. II. Excitation by particles falling radially with arbitrary energy”. In: *Phys. Rev. D* 88 (2013), p. 044018. DOI: 10.1103/PhysRevD.88.044018. arXiv: 1305.4306 [gr-qc].

[277] Mihalis Dafermos and Igor Rodnianski. “The Red-shift effect and radiation decay on black hole spacetimes”. In: *Commun. Pure Appl. Math.* 62 (2009), pp. 859–919. arXiv: gr-qc/0512119.

[278] Yasushi Mino and Jeandrew Brink. “Gravitational Radiation from Plunging Orbits: Perturbative Study”. In: *Phys. Rev. D* 78 (2008), p. 124015. DOI: 10.1103/PhysRevD.78.124015. arXiv: 0809.2814 [gr-qc].

[279] Aaron Zimmerman and Yanbei Chen. “New Generic Ringdown Frequencies at the Birth of a Kerr Black Hole”. In: *Phys. Rev. D* 84 (2011), p. 084012. DOI: 10.1103/PhysRevD.84.084012. arXiv: 1106.0782 [gr-qc].

[280] N. Andersson. “Excitation of Schwarzschild black hole quasinormal modes”. In: *Phys. Rev. D* 51 (1995), pp. 353–363. DOI: 10.1103/PhysRevD.51.353.

[281] Rodrigo Panosso Macedo, José Luis Jaramillo, and Marcus Ansorg. “Hyperboloidal slicing approach to quasi-normal mode expansions: the Reissner-Nordström case”. In: *Phys. Rev. D* 98.12 (2018), p. 124005. DOI: 10.1103/PhysRevD.98.124005. arXiv: 1809.02837 [gr-qc].

[282] Rodrigo Panosso Macedo. “Hyperboloidal approach for static spherically symmetric spacetimes: a didactical introductionand applications in black-hole physics”. In: *Phil. Trans. Roy. Soc. Lond. A* 382.2267 (2024), p. 20230046. DOI: 10.1098/rsta.2023.0046. arXiv: 2307.15735 [gr-qc].

[283] Rodrigo Panosso Macedo and Anil Zenginoglu. “Hyperboloidal approach to quasinormal modes”. In: *Front. in Phys.* 12 (2024), p. 1497601. DOI: 10.3389/fphy.2024.1497601. arXiv: 2409.11478 [gr-qc].

[284] Robert M. Wald. *General Relativity*. The University od Chicago Press, 1984.

[285] Enrico Cannizzaro et al. “Relativistic Perturbation Theory for Black-Hole Boson Clouds”. In: *Phys. Rev. Lett.* 132.5 (2024), p. 051401. DOI: 10.1103/PhysRevLett.132.051401. arXiv: 2309.10021 [gr-qc].

[286] P. Kotlařík, O. Semerák, and P. Čížek. “Schwarzschild black hole encircled by a rotating thin disc: Properties of perturbative solution”. In: *Phys. Rev. D* 97.8 (2018), p. 084006. DOI: 10.1103/PhysRevD.97.084006. arXiv: 1804.02010 [gr-qc].

[287] Vitor Cardoso et al. “Gravitational Waves from Extreme-Mass-Ratio Systems in Astrophysical Environments”. In: *Phys. Rev. Lett.* 129.24 (2022), p. 241103. DOI: 10.1103/PhysRevLett.129.241103. arXiv: 2210.01133 [gr-qc].

[288] Thomas F. M. Spieksma et al. “Black Hole Spectroscopy in Environments: Detectability Prospects”. In: *Phys. Rev. Lett.* 134.8 (2025), p. 081402. DOI: 10.1103/PhysRevLett.134.081402. arXiv: 2409.05950 [gr-qc].

[289] Gregorio Carullo. “Black hole spectroscopy: status report”. In: *Gen. Rel. Grav.* 57.5 (2025), p. 76. DOI: 10.1007/s10714-025-03408-y.